Synthesis and Electronic Ordering Phenomena of Calcium Ruthenate Thin Films

Von der Fakultät Mathematik und Physik der Universität Stuttgart
zur Erlangung der Würde eines Doktors der
Naturwissenschaften (Dr. rer. nat.) genehmigte Abhandlung

Vorgelegt von
Christopher Johannes Dietl
aus Tübingen

Hauptberichter:	Prof. Dr. Bernhard Keimer
Mitberichter:	Prof. Dr. Jörg Wrachtrup
Prüfungsvorsitzende:	Prof. Dr. Maria Daghofer

Tag der Einreichung:	27.06.2018
Tag der mündlichen Prüfung:	25.07.2018

Universität Stuttgart
Max-Planck-Institut für Festkörperforschung
Stuttgart 2018

Contents

Abstract

The prospect to harness the wide range of electronic phenomena found in transition metal oxides by synthesizing thin film structures and their implementation into next-generation technologies has sparked a research activity of ever increasing pace. Most prominent are thin film techniques such as heterostructuring and strain engineering, which have been shown to open up new paths to study the rich physics in these compounds.

This work constitutes a study of the thin film synthesis of the layered orthorhombic transition metal oxide compound Ca_2RuO_4 (CRO) and of the impact of biaxial epitaxial strain on the magnetic and orbital ordering phenomena previously found by spectroscopic methods. The electronic structure of CRO and other transition metal oxides with 4*d*-valence electrons is of significant topical interest, because the energy scales of spin-orbit-coupling, exchange energy and crystal field are comparable. As a result, the antiferromagnetic Mott insulator CRO plays host to an array of novel ground states and is highly susceptible to external perturbations as has been shown by numerous studies on single crystals involving e.g pressure, chemical substitution and electrical current.

Embarking on the strategy to exploit this sensitivity of CRO, we employ strain engineering via thin film growth to tune its properties. The details of the synthesis route using pulsed laser deposition are presented. Growth was accomplished with two distinct sets of high-quality samples – a-axis oriented films on $LaSrAlO_4$ and $NdCaAlO_4$ substrates with (110) cut and c-axis oriented films on $LaAlO_3$, $LaSrAlO_4$ and $YAlO_3$ substrates with (001) cut. Structural characterization shows that the epitaxy exerts strains of 1 %–3 % on the lattice constants of CRO compared to the bulk system. These large distortions manifest themselves in the electrical transport properties, which shows that the electronic state can be profoundly tuned from an insulator to a metal.

Comprehensive resonant elastic X-ray scattering and magnetometry studies confirm the presence of antiferromagnetism in CRO on $LaAlO_3$, $NdCaAlO_4$ and $LaSrAlO_4(110)$ at $T_N = 150\,\mathrm{K}$, similar to the antiferromagnetic state found in bulk. Detailed polarization analysis of resonant peaks reveals a b-axis oriented magnetic moment for CRO on $LaSrAlO_4(110)$, as found in bulk. On the other side, CRO on $NdCaAlO_4$ shows an unusual signal that is compatible with a mag-

netic moment 45° away from the c-axis, approximately along the $(\bar{1}02)$ direction of the orthorhombic unit cell of CRO, which has not been reported for the bulk system. Furthermore, magnetoresistance and magnetometry measurements show a weak ferromagnetic signal along the c-axis within the antiferromagnetic phases. We show that, while a moment direction along the b-axis is compatible with a representation analysis of the bulk Pbca space group, the presence of a weak ferromagnetic component along the c-axis and the peculiar magnetic moment direction along the $(\bar{1}02)$ for CRO on $NdCaAlO_4$ cannot be described by a single irreducible representation of the space group Pbca. Thus, we suggest either an exotic scenario with more than one critical irreducible representation or that the thin films exhibit an unusual symmetry reduction from the bulk space group Pbca. The finding of a strain-induced moment direction switching points to a non-trivial effect of epitaxial strain on the magnetic interactions in CRO.

Magnetometry, magnetoresistance and polarized neutron reflectometry experiments were conducted to investigate a low-temperature ferromagnetic phase in the c-axis oriented samples. Similar to pressurized bulk, we find ferromagnetic moment amplitudes of the order $0.1\,\mu_B$/Ru and an enhancement under compressive strain. Polarized neutron reflectometry was used to exclude impurity phases or surface effects as the underlying mechanism. Analogous to the pressurized bulk system, we found a giant positive magnetoresistance in CRO on $LaAlO_3$.

Moreover, a combined nuclear magnetic resonance and resonant elastic X-ray scattering study was dedicated to study the impact of epitaxial strain on quadrupolar order previously found in bulk CRO. Due to the small mass of the thin films, the nuclear magnetic resonance experiments were conducted using the βNMR-technique, which detects the spin lattice relaxation through the asymmetry of the β-decay of highly-polarized ^{8}Li-isotopes. The temperature dependence of the relaxation rate of the c-axis oriented films showed an increase towards higher temperatures, starting at $\approx 200\,\mathrm{K}$. More detailed measurements on metallic CRO on $LaSrAlO_4(001)$ revealed an anomaly at 300 K, which is reminiscent of a phase transition. Since resonant X-ray scattering on bulk CRO showed orbital ordering phenomena in the same temperature range, we similarly searched for quadrupolar ordering using synchrotron radiation tuned to the Ru-L absorption edges.

However, the resonant peaks detected in our experiments could be fully described by Templeton scattering, a phenomenon arising from purely structural effects. For reference purposes, we performed a similar analysis for the single crystal showing that the results previously interpreted as antiferro-orbital order bear many signatures of Templeton scattering as well. Thus, this work motivates a reevaluation of the original scattering study. An alternative scenario for the βNMR anomaly based on diffusion of the ^{8}Li-ions is discussed.

The synthesis of CRO on a variety of substrates enables further studies of the influence of large structural distortions on the electronic states in CRO, which are currently inaccessible by pressure techniques for single crystals. This opens up new opportunities to test theories regarding the electronic states in CRO, which are intensively debated due to multiple competing energy scales. Specifically, a recently proposed strong spin-orbit coupling picture for CRO predicts a high sensitivity towards the crystal field splitting in this material, which is directly tuned via the epitaxial strain. The large tunability of the electronic properties CRO by epitaxial strain might be useful for future thin film devices.

Deutsche Zusammenfassung

Die Aussicht, das weite Spektrum an elektronischen Eigenschaften in Übergangsmetalloxiden durch Dünnfilmwachstum zu nutzen, und deren Integration in Zukunftstechnologien hat eine ständig steigende Forschungsaktivität in der Festkörperphysik ausgelöst. In diesem Zuge haben Dünnfilmtechniken wie Heterostrukturierung und *strain engineering* von Übergangsmetalloxiden neue Möglichkeiten eröffnet, die vielfältige Physik in solchen Materialien zu untersuchen.

Die vorliegende Arbeit befasst sich mit der Dünnfilmsynthese des geschichteten orthorhombischen Übergangsmetalloxidsystems Ca_2RuO_4(CRO) und der Untersuchung des Einflusses von biaxialer epitaktischer Verspannung auf die vom Bulk-System bekannten magnetischen und orbitalen Ordnungsphänomene unter Verwendung spektroskopischer Methoden.

Die elektronische Struktur von CRO und anderen Übergangsmetalloxiden mit 4*d*-Valenzelektronen ist von hoher wissenschaftlicher Relevanz, da die Energieskalen von Spin-Bahn-Kopplung, Austauschenergie und Kristallfeld die gleiche Größenordnung aufweisen. Daraus ergibt sich eine Vielzahl neuartiger Grundzustände im antiferromagnetischen Mott-Isolator CRO und eine hohe Empfindlichkeit gegenüber äußeren Einflüssen. Letzteres wurde durch viele Arbeiten an Einkristallen demonstriert, die unter anderem den Effekt von Druck, chemischer Substituierung und elektrischen Strömen untersuchen.

Um diese besondere Empfindlichkeit von CRO zu nutzen, setzen wir *strain engineering* mittels Dünnfilmwachstums ein und verändern gezielt und kontrolliert die Eigenschaften von CRO. Details der hierbei genutzten Laserverdampfungsmethode (*pulsed laser deposition*) werden beschrieben. Dieses Verfahren ermöglicht das Wachstum verschiedener Arten von hochqualitativen Filmen: a-Achsen-orientierte Schichten auf $LaSrAlO_4$ und $NdCaAlO_4$ Substraten mit (110)-Oberflächenorientierung und c-Achsen-orientierte Filme auf $LaAlO_3$, $LaSrAlO_4$ und $YAlO_3$ Substraten mit (001)-Orientierung. Eine strukturelle Charakterisierung zeigt, dass die Epitaxie 1 %–3 % Verspannung relativ zu dem Bulk-System verursacht. Diese großen Verzerrungen werden durch erhebliche Veränderungen im elektrischen Transport ersichtlich, die zeigen, dass CRO von einem Isolator zu einem Metall modifiziert werden kann.

Eine umfassende Untersuchung mittels resonanter elastischer Röntgenstreuung und Magnetometrie bestätigt eine antiferromagnetische

Ordnung der Valenzelektronen von CRO auf $LaAlO_3$, $NdCaAlO_4$ und $LaSrAlO_4(110)$ mit $T_N = 150\,\mathrm{K}$, ähnlich der antiferromagnetischen Ordnung im Bulk-System. Eine umfangreiche Polarisationsanalyse eines resonanten Reflexes von CRO auf $LaSrAlO_4(110)$ zeigt ein magnetisches Moment entlang der b-Achse, was sich mit den Erkenntnissen aus dem Bulk-System deckt. Im Gegensatz dazu zeigt die gleiche Analyse für CRO auf $NdCaAlO_4$ ein ungewöhnliches Signal, das mit einem um 45° relativ zur c-Achse verkippten magnetischen Moment kompatibel ist. Dieses Moment zeigt ungefähr entlang der $(\bar{1}02)$ Richtung der orthorhombischen Einheitszelle von CRO, was bisher noch nicht im Bulk-System beobachtet wurde. Mittels zusätzlicher Magnetowiderstands- und Magnetometriemessungen kann ein Signal verbunden mit schwachem Ferromagnetismus entlang der c-Achse in den antiferromagnetisch geordneten Phasen nachgewiesen werden. Eine Analyse der magnetischen Symmetrie mittels Darstellungstheorie zeigt auf, dass zwar das magnetische Moment entlang der b-Achse für CRO auf $LaSrAlO_4(110)$ mit der Bulk-Raumgruppe Pbca kompatibel ist, dass aber der schwache FM entlang der c-Achse und die ungewöhnliche Richtung des magnetischen Moments entlang der $(\bar{1}02)$ Richtung für CRO auf $NdCaAlO_4$ nicht mit einer einzigen irreduziblen Darstellung vereinbar sind. Daher wird impliziert, dass entweder ein exotisches System mit mehr als einer kritischen irreduziblen Darstellung vorliegt oder dass die Filme eine ungewöhnliche Symmetriereduktion der Bulk-Raumgruppe Pbca besitzen. Die Erkenntnis eines verspannungsinduzierten Wechselns der Richtung des magnetischen Moments deutet auf einen nicht-trivialen Zusammenhang zwischen epitakischer Verspannung und magnetischer Wechselwirkung in CRO hin.

Mittels Magnetometrie, Magnetowiderstandsmessungen und polarisierter Neutronenreflektometrie wird eine ferromagnetische Niedrigtemperaturphase in den c-Achsen orientierten Proben untersucht. Ähnlich zu Messungen von Bulk-CRO unter Druck werden magnetische Momente der Größenordnung $0.1\,\mu_\mathrm{B}/\mathrm{Ru}$ und deren Verstärkung unter Verspannung gefunden. Durch polarisierte Neutronenreflektometrie kann der Einfluss einer Verunreinigung oder eines Oberflächeneffekts ausgeschlossen werden. Analog zum Bulk-System wurde ein positiver Riesenmagnetowiderstand (giant magnetoresistance, GMR) in dieser Phase für CRO auf $LaAlO_3$ festgestellt.

Die Techniken Kernspinresonanz und resonante elastische Röntgenstreuung werden genutzt, um den Einfluss epitaktischer

Verspannung auf die Orbitalordnung, die aus dem Bulk-System bekannt ist, zu ergründen. Auf Grund der kleinen Masse der Dünnfilme werden die Kernspinresonanzexperimente mittels der βNMR-Methode durchgeführt. Diese Technik detektiert die Spin-Relaxationszeit (spin lattice relaxation time, SLR) durch die Asymmetrie des Beta-Zerfalls von hoch-polarisierten ^{8}Li-Isotopen. Die Temperaturabhängigkeit der Relaxationszeit der c-Achsen-orientieren Filme zeigt ein bei $\approx 200\,\mathrm{K}$ beginnendes Anwachsen zu hohen Temperaturen hin. Detailliertere Messungen von metallischem CRO auf $LaSrAlO_4(001)$ zeigen eine Anomalie bei 300 K auf, die einem Phasenübergang ähnelt. Da durch resonante Röntgenstreuung an den Ru-L-Kanten an Bulk-CRO Orbitalordnungsphänomene in einem ähnlichen Temperaturbereich beobachtet werden, wurden entsprechende Streuungsexperimente durchgeführt, die darauf abzielten, eine ähnliche Quadrupolordnung in den Filmen zu finden. Allerdings können die beobachteten resonante Reflexe durch Templeton-Streuung erklärt werden, einem Effekt, der vollständig durch strukturelle Symmetrie erklärt werden kann. Zu Referenzzwecken wird ein Einkristall analysiert. Hier wird aufgezeigt, dass auch die Ergebnisse, die in früheren Arbeiten als Antiferro-Orbitalordnung interpretiert wurden, viele Merkmale von Templetonstreuung tragen. Daher legt diese Arbeit nahe, die ursprünglichen Streudaten nochmals zu überprüfen. Eine alternative Interpretation für die βNMR-Anomalie, die auf Diffusion der ^{8}Li-Atome basiert, wird diskutiert.

Die Synthese von CRO auf einer Vielzahl von Substraten ermöglicht weitergehende Untersuchungen des Einflusses von strukturellen Verzerrungen auf die elektronischen Zustände in CRO, die momentan über konventionelle Druckzellen für das Bulk-Material nicht zugänglich sind. Die Beschreibung der elektronischen Zustände in CRO wird derzeit intensiv diskutiert. CRO-Dünnfilme eröffnen neue Möglichkeiten, Erkenntnisse für die theoretische Behandlung zu gewinnen. Ein kürzlich veröffentlichtes Modell, das auf einer großen Spin-Bahn-Kopplung basiert, sagt eine hohe Empfindlichkeit gegenüber der Kristallfeldaufspaltung in diesem Material voraus. Das Kristallfeld wird direkt durch die epitakische Verspannung beeinflusst, weshalb Dünnfilme eine experimentelle Validierung erlauben könnten. Die große Modifizierbarkeit von CRO durch epitaktische Verspannung bietet vielfältige Perspektiven für den Einsatz in zukünftigen elektronischen Dünnfilm-Bauelementen.

1 Introduction

Transition-Metal-Oxides (TMOs) have been at the forefront of condensed matter research during the last decades because they provide a rich platform for fundamental research and a large potential for applications [1, 2]. At the root of the wealth of physics found in TMOs is the fact that the oxygen strips the metal ion off its outer s-shell, creating a valence shell consisting of d-electrons. s- and p-orbitals typically have a large overlap with neighboring atoms giving rise to large bandwidths, while f-electrons are much more localized at the nucleus. Electrons in d-orbitals represent the intermediate case, which can have itinerant and localized properties [3]. This forms the basis for the notion of *correlated* electrons, since spin, charge and orbital degrees of freedom can still be described in a localized picture, but are able to interact with neighboring ions. The resulting intricate interplay of electrons in the d-states is the underlying origin for complex phenomena in TMOs such as high-T_C superconductivity, metal-to-insulator transitions, spin and orbital orders, colossal magnetoresistance and quantum criticality [4–7].

A classic TMO is the compound NiO, which has been a subject of TMO research since its beginning in the 1930s and is still actively investigated today [8, 9]. It was realized early on that its poor conductance cannot be reconciled with its partially filled $3d$ valence band, which should allow good conduction according to standard band theory. A solution was found in the notion that electrostatic forces be-

tween the electrons might be responsible for explaining the insulating state [8, 10]. These ideas culminated in the formulation of the Mott-Hubbard-model [11]. Here, the ground state of the system results from a competition of the local Coulomb repulsion U between electrons and a hopping integral t, which describes the ability of an electron to transfer from one site to the next. This model successfully explains many properties of TMOs. If $U \gg t$, the electrons localize and an insulating ground state is stabilized, although a band picture would suggest a metallic state. Many such *Mott insulators* are also magnetic, which naturally results from this model, when it is reformulated in terms of a Heisenberg-Hamiltonian with an exchange coupling $J_{\mathrm{ex}} = 2t^2/U$ [1]. One interesting case is the crossover between $U > t$ and $U < t$, a.k.a. metal-to-insulator transition (MIT), where typically the resistivity shows huge changes over tens of orders of magnitude [5].

A prominent example is VO_2, which shows a MIT at 340 K [12]. Furthermore, it has been shown that its MIT can be controlled electrically [13]. Although the mechanism behind the field-effect is not yet fully clarified [14], the electric-field tunability and the proximity to room temperature make VO_2 a typical showcase-material for the potential of oxide electronics. In fact, many aspirations for electric field devices rely on TMOs. A tunable MIT might enable phase-transition transistors [15], and the control of the magnetization via electric field in e.g. $BiMnO_3$ might allow new memory devices [16].

The predictive power of Hubbard model despite its simplicity is remarkable. However, it was soon realized that the Hamiltonian for TMOs often requires additional energy scales besides U and t to describe the intricacies of particular compounds. For many TMOs, the hybridization between the metal and the oxygen states can put filled oxygen $2p$-orbitals closer to the conduction band than the d-valence band of the metal ion. Such a type of insulator is called *charge-transfer (CT) insulator* and its description requires the extension of the Hubbard model to also capture effects from the oxygen $2p$-orbitals by including an additional *charge transfer gap* Δ_{CT}[5]. A prominent example for such a type of insulator is the classic high-T_C superconductor La_2CuO_4, where the difference of CT-picture vs. Mott insulator has a profound impact on the physics of the system under doping [17].

The coordination with oxygen atoms can also have drastic effects on the degeneracy of the metal d-orbitals. The electric field of the surrounding lattice, the so called *crystal electric field* (CEF) Δ, per-

turbs the typical scheme of distributing the electrons on the d-orbitals according to Hund's rules. Hund's rules minimize first the intraionic Coulomb repulsion between electrons and then assume *spin-orbit-coupling* (SOC) as the next most important scale to energetically optimize $\lambda \boldsymbol{S} \cdot \boldsymbol{L}$, the product of the SOC coupling constant λ, spin $\boldsymbol{S}$ and angular momentum $\boldsymbol{L}$. Many TMOs that have been in the limelight of condensed matter research are based on ions with a $3d$-valence shell(e.g. Mn,Fe,Ni,Cu). The CEF in these systems is typically much stronger than the SOC and the orbital occupation of the ion results primarily from a competition between intraatomic Coulomb repulsion and Δ. The often encountered octahedral oxygen coordination of the metal ion manifests itself in the splitting of the fivefold degenerate d-orbitals into threefold t_{2g} and twofold e_g manifolds. This can have substantial consequences for the magnetic moment of a material, e.g. a $3d^6$ configuration as found for Fe^{2+} can have either $S = 0$ (*low-spin*) or $S = 2$ (*high-spin*) depending on the strength of the CEF. Due to its weakness in these compounds, the SOC was thus merely seen as a perturbation for TMO physics.

However, seminal findings during the last decade led to a resurgence of interest in the SOC. Most prominent are *topological insulators*, where SOC is a crucial ingredient to achieve a band inversion of conduction and valence band to create a state that is topologically different from regular band insulators [18]. Since λ is proportional to the square of the atomic number, these effects were mainly investigated using heavy elements such as Hg or Bi outside of the realm of typical oxides. However, as oxide research progressed towards heavier $4d$ and $5d$ transition metal ions as well, the effects of spin-orbit coupling became more apparent.

A prime example is Sr_2IrO_4 (SIO) with its $5d^5$ Ir^{4+} ion, where the finding of a profound impact of SOC generated a surge in research activity. The $5d$-orbitals are more extended than the $3d$-orbitals of typical TMOs and thus the case $U \ll t$ with lower on-site Coulomb repulsion and metallic conductance was expected. Therefore, the insulating state of SIO was at first puzzling. However, a comprehensive spectroscopic study of the compound was able to show the impact of the strong SOC in the material in stabilizing an insulating state [20]. If one considers a strong CEF splitting and applies Russel-Saunders-coupling, a half-filled $J_{\text{eff}} = 1/2$ conduction band is found. The insulating state is then induced by a further splitting of this band by U.

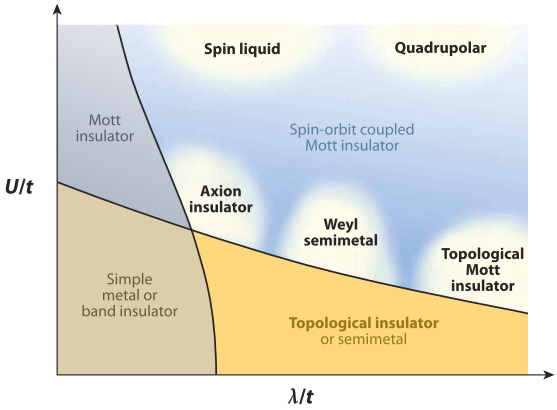

Figure 1.1: Generic phase diagram capturing the essential trends by adding the energy scale of spin-orbit-coupling λ to the Coulomb repulsion U and the hopping integral t of the Hubbard model. Many exotic ground states are predicted for the spin-orbit coupled regime. Taken from [19].

The J_{eff} stands for an *effective* total angular momentum and incorporates the effect of the CEF to partially quench the orbital angular momentum. Since the SOC plays a vital role in assisting an insulating state, compounds such as SIO are also called *relativistic Mott insulators* or *spin-orbit Mott insulators*. Furthermore, the inclusion of SOC in the spin-orbit Mott insulator model is predicted to lead to exotic ground states, which are different from paradigms known from non-relativistic Mott insulators (Fig. 1.1). The pyrochlore $R_2\text{Ir}_2\text{O}_7$ compounds, where R is a rare-earth ion, are predicted to be Weyl semimetals [19, 21], which host highly relativistic quasiparticles with photon-like linear dispersions similar to the Dirac-cones found in graphene. The honeycomb $(\text{Na}, \text{Li})_2\text{IrO}_3$ compounds are regarded as candidates for a highly frustrated *quantum spin liquid* ground state [22]. Such a state can be described within a Kitaev model, which contains several properties possibly useful for quantum computing [23].

The significance of SOC in the Ir compounds also led to a reevaluation of the systems between the conventional and relativistic Mott insulators. Currently, a very active research effort surrounds the single-layer ruthenate Ca_2RuO_4(CRO), which is the topical focus of this thesis. CRO is regarded as the antiferromagnetic Mott insula-

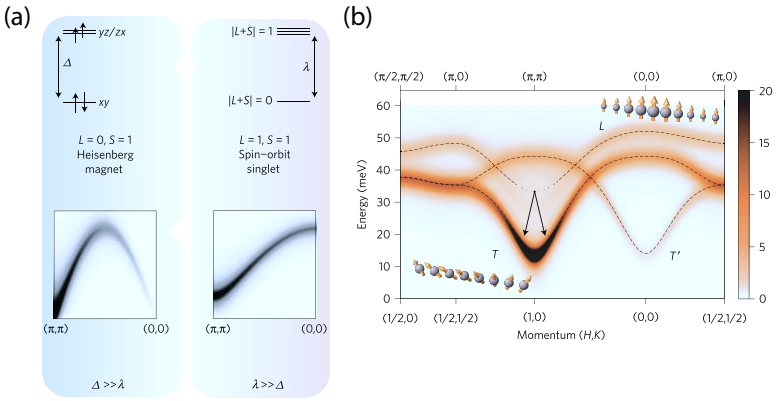

Figure 1.2: (a) The electronic states in CRO represent an intermediate case of the two depicted ground states. For large crystal field splitting Δ vs. spin-orbit-coupling λ, a $S = 1$ Heisenberg Hamiltonian results. In the opposite case with $\lambda \gg \Delta$, a non-magnetic $|L+S| = 0$ singlet is stabilized. Each case gives a distinct dispersion of the magnetic excitations. (b) Representation of the magnetic dispersions in CRO measured by inelastic neutron scattering data, which shows the strong influence of spin-orbit coupling in comparison with panel (a). Model calculations (dashed lines) identify transverse modes (T) and a high-energy longitudinal mode (*Higgs*). The arrows indicate the decay of the longitudinal mode into transverse modes at (π,π). Taken from [24, 25].

tor analogue of the unconventional superconductor Sr_2RuO_4(SRO). The superconductivity in SRO is one of the main topics of condensed matter research as it is regarded as a strong candidate for p-wave triplet superconductivity, an exotic phase similar to the A-phase in superfluid ^{3}He[26, 27]. Thus, early research on CRO was primarily focused on unraveling the connection between the electronic states in CRO and SRO, but recent findings have revealed rich SOC physics in CRO, which in itself is attracting considerable interest [28]. CRO represents an intermediate case to the 3d- and 5d-systems discussed above, since on-site Coulomb repulsion U, the spin-orbit-coupling λ, crystal field Δ and the exchange coupling $J_{\mathrm{ex}} = 2t^2/U$ are comparable. In a weak SOC picture, the Ru^{4+} ion in CRO has a low-spin t_{2g}^4 configuration with $S = 1$ and $L = 0$, as the orbital angular momentum L is expected to be completely quenched by Δ. On one hand, angular-resolved photo emission spectroscopy (ARPES) and X-ray ab-

sorption spectroscopy measurements indicated early on an active SOC in the system [29], which would motivate the inclusion of SOC in the description of its electronic states. On the other hand, the S and L coupling scheme as it was employed for the iridates yields a non-magnetic $J_{\text{eff}} = 0$ ground state, which is in obvious disagreement with the antiferromagnetism observed in the system. A recent model coined *excitonic magnetism* successfully remedies this discrepancy by proposing an intermediate state between the classical Heisenberg-type and the spin-orbit-type Mott insulator. Here, one conceptually starts in a strong SOC picture with a non-magnetic $J_{\text{eff}} = 0$ singlet and magnetic $J_{\text{eff}} = 1$ triplet. The splitting between the triplet and singlet states is on the order of the exchange coupling, which makes it favorable for excited triplet states to condense into the ground state, similar to a Van-Vleck-type magnetism. As such singlet-triplet excitations are bosonic magnons, the emergence of magnetic long-range order can also be interpreted as a Bose-Einstein-condensate (BEC). This state is part of a growing number of "condensed matter BECs" that have been found recently [30]. The natural proximity of the excitonic model to a quantum critical point has stimulated the prediction of soft amplitude fluctuations of the magnetic moment, the so called *Higgs-mode* in the parlance of spontaneous symmetry breaking known from high-energy physics. Such a mode has indeed been observed by inelastic neutron scattering (Fig. 1.2) and Raman scattering, underlining the validity of this model [31]. In such a type of magnetism, the gap between between triplet and singlet states can be controlled by the CEF, which might allow an avenue to study the quantum criticality of the system via the films synthesized within this work.

The reevaluation of the role SOC in ruthenates was not limited to CRO, but also evidence has been accumulated for a considerable SOC contribution in SRO [36]. Comprehensive ab-initio band structure calculations and ARPES measurements predicted theoretically and confirmed experimentally the presence of substantial SOC in CRO [37, 38]. SOC leads to a mixing of the t_{2g} manifold and yields complex spin-orbit entangled states, with a strong $\boldsymbol{k}$-dependence of the orbital character along the Fermi surface. A separate classification of the orbital and the spin component of the superconducting order parameter such "p-wave triplet" becomes invalid in light of these results and the symmetry is more accurately described in terms of the parity. The integration of SOC into models for the superconductivity is one of the

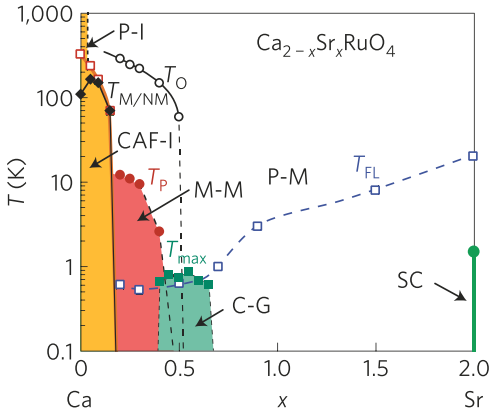

Figure 1.3: Phase diagram of presenting the wide variety of electronic phases in $Ca_{2-x}Sr_xRuO_4$. P-I: Paramagnetic-insulating, P-M: Paramagnetic-metallic, CAF-I: commensurate antiferromagnetic insulator, M-M: Metallic-magnetic state with an anomaly in the magnetization, C-G: Cluster-glass, SC: Superconducting phase. $T_{M/NM}$: MIT (red empty squares), T_O: High-temperature structural transition. Below T_{FL}, Fermi-liquid behavior is observed. Taken from [32] and includes data from [33–35].

current quests for SRO and might yield a solution for discrepancies between experimental data and earlier models for the order parameter of the superconducting phase [36].

The multiple competing energy scales make CRO an archetypal TMO system with a strong tunability of its properties. A prominent feature of CRO is its MIT at 360 K, which is accompanied by large structural changes that typically shatter single crystals. Pressure, chemical substitution and the application of current allow control of the MIT and drive the system from an insulator to a metal and from an antiferromagnetic state towards a ferromagnetic state (Fig. 1.3, Refs. [39–44]). Establishing a connection between the complex phenomena found in CRO and the superconductivity in SRO might allow new insights into the mechanism of its Cooper pairing. Ca is isovalent to Sr, thus the drastic differences between the systems arise solely from structural distortions. Indeed, it was realized early on that the electronic changes in the $Ca_{2-x}Sr_xRuO_4$ phase diagram are strongly tied to structural details [45]. Moderate pressures already suffice to suppress the antiferromagnetic insulating ground state and stabilize a metallic state as in SRO [40]. The strong susceptibility of

the ground state to structural distortions is a key feature we set out to exploit by applying epitaxial strain to CRO.

Notably, CRO exhibits also tunability of its ground-state via electrical current, which is a highly sought-after property for oxide electronics. The application of current also revealed a so far unknown phase hosting giant diamagnetism comparable with superconducting phases [39]. Besides the implications for possible electronic devices, this peculiar property opens up a new avenue to probe non-equilibrium physics in proximity to a Mott transition.

The rich repertoire of electronic phenomena in TMO make them attractive for applications. A key requirement to harness the properties of TMO in devices is their synthesis as thin films as it greatly facilitates the integration into electronic circuits. One milestone that sparked a burst of activity in this area is the realization of high critical current $YBa_2Cu_3O_7$ thin films soon after the finding of high T_C superconductivity in the bulk material using the Pulsed Laser Deposition (PLD) technique [46].

However, the motivation to grow thin films arises not only from the goal of direct application, but also from a fundamental physics perspective. One of the basic tools to manipulate the properties of single crystals is *epitaxial* growth. Here, films are grown on a single-crystalline substrate and adapt their lattice to it. This way, a large strain of the order of 1 % can be exerted on the lattice constants, which exceeds the capability of most methods used for bulk crystals. This so called *strain engineering* can alter profoundly the properties of the film [47]. Another powerful tool available for thin films is the method of *heterostructuring*, i.e. growing two different materials on top of each other. Such an approach can reveal new physics at the interface due to reconstruction of the interaction of spin, charge and orbital degrees of freedom [48]. A well-known case of interface physics is the superconducting high-mobility 2D-electron gas found in $LaAlO_3$-$SrTiO_3$ heterostructures, which consists of two wide-bandgap insulators [49, 50]. The power of interface physics has also been underlined recently by growing superconducting FeSe monolayers on a $SrTiO_3$ substrate, which led to a large boost in the T_C from 8 K to 65 K[51, 52].

For several systems, thin film deposition enables a route to stabilize the growth of single-crystalline films, while the synthesis of bulk single crystals is difficult. A typical example are the perovskite rare-earth nickelates, where the synthesis of thin films and heterostructures has

been mastered by several groups, but attempts to grow high-quality single crystals have not been fruitful. Most information of this system has thus actually been gained by studies on thin films [53]. This system also serves as a case, where basic synthesis routes have been established and the field has moved on to a more targeted synthesis of thin film structures, which enable deliberate control of orbital, charge and spin degrees of freedom(e.g. [54, 55]). Generally, however, the synthesis of TMO thin films, which often comprise three or more elements, is notoriously complex. SRO is a notable example. Despite the fact that the superconductivity in SRO was discovered in 1994 and despite continuous effort by leading thin-film groups, only recently has growth been optimized to a level where superconductivity can be achieved in thin films [56–66]. This finally paves the way to test many predictions such as half-quantum vortices [67] or new ways to probe the order parameter symmetry of the superconducting phase [68].

A similar situation exists for CRO where, despite a rich phase diagram and tunability, reports of successful thin film synthesis remain rare and most of the work was conducted on single crystals. This thesis attempts to fill this gap by presenting a PLD synthesis route yielding high-quality samples. In particular, we can show that this procedure allows us to grow on multiple substrates and thus employ a varying degree of strain engineering. This expands previous reports, which only show epitaxial growth on the substrate $LaAlO_3(100)$. A comprehensive spectroscopic study employing Resonant Elastic X-ray Scattering (REXS) and Beta Nuclear Magnetic Resonance (βNMR) is presented studying the impact of epitaxy on the ordering phenomena found in bulk CRO single crystals.

Specifically, the thesis is organized as follows:

Chapter 2 In this chapter we give an overview of the basic properties of single-layer ruthenates, which have been established through various experimental and theoretical approaches. A brief summary of previous studies of CRO films is included.

Chapter 3 The sections within chapter 2 introduce the fundamentals of REXS and βNMR, the spectroscopic techniques which have been most insightful for the investigation the CRO films.

Chapter 4 After a brief preface, which is aimed at familiarizing the reader with the basic ideas of PLD thin film growth and RHEED diagnostics, we present a detailed summary of the optimization process that led to the growth of high-quality CRO films. These sections

are the result of over 400 sample growths and comprise the bulk of the PhD work. We highlight pitfalls in the hope to facilitate future synthesis attempts. Additionally, we show the result of the basic structural characterization we have collected using laboratory X-ray diffraction (XRD), synchrotron XRD, Oxygen K-edge X-ray absorption spectroscopy and Raman spectroscopy. Electrical transport measurements are presented, which readily exhibit the impact of epitaxial strain on the system.

Chapter 5 This chapter is devoted to the clarification of the magnetic properties of CRO films using magnetoresistance (MR), magnetometry and resonant magnetic elastic X-ray scattering at synchrotron sources. Specifically, we show how polarisation analysis can be used to determine the magnetic moment direction in the antiferromagnetic phase of CRO on LSAO(110) and NCAO(110).

Chapter 6 Within this part of the thesis, we show the results of a combined study of βNMR and REXS designed to address the question regarding the possibility of quadrupolar ordering in the films. In light of the results, we critically discuss the results concerning a proposed antiferro-orbital ordering in CRO single crystals.

2

Single Layer Ruthenates

Within this section, we give a brief overview over the current understanding of the bulk Ca_2RuO_4(CRO) system. After introducing the basic properties, we will present studies of the crystallographic structure of CRO, which is intimately connected to the electronic properties in this system. This also covers aspects regarding the tunability under chemical substitution with Sr and pressure studies in view of the strain engineering performed in the course of this work. Then we will turn to the electronic structure, where we also include new developments regarding a new description in terms of a strong spin-orbit-coupling (SOC) picture. We will conclude with a short review of previous reports of CRO thin films.

2.1 The Superconductivity in Sr_2RuO_4

One of the key drivers of the research into single-layer ruthenates was the discovery of superconductivity in metallic Sr_2RuO_4 [69]. After the discovery of High-T_C superconductivity in the cuprates, this marked the first single-layer perovskite system without copper [27]. The $S = 1$ state of the system and the fact that the closely related perovskite $SrRuO_3$ is a ferromagnet led to the notion that the system is a triplet-superconductor where the two spins of the Cooper pair are aligned parallel analogous to the p-wave mediated pairing found

in the superfluid ^{3}He[70]. Indeed, μSRexperiments showed that the superconducting state [71] breaks time-reversal symmetry and that the spin susceptibility determined by ^{17}O-Knight-shift measurements remains unaffected by the superconducting transition [72].

However, it was later found that the system is indeed more complicated than the p-wave triplet superfluidity in ^{3}He. SRO as a 2D-analogue for the 3D Fermi liquid ^{3}He is expected to host a fully gapped Fermi surface [73]. However, a variety of experimental evidence was collected using specific heat [74], NQR [75], thermal conductivity [76, 77], penetration depth [78] and ultrasound attenuation [79] that suggest only a partially gapped Fermi surface in the superconducting state.

It was realized that the multiband nature of single-layer-ruthenates (see below) was crucial to explain the discrepancy of the data and the p-wave scenario. Single-layer ruthenates form three bands derived from the three 4d t_{2g}-states hybridized with O-2p orbitals: α/β (d_{yz},d_{xz}) and γ (d_{xy})[80, 81] (see sec. 2.5). Taking into account the different contributions to the pairing mechanism due to different symmetries of each band, reconciled the experimental datasets again with a p-wave order parameter, although many aspects of this issue remain under investigation [82, 83]. Here, the γ-band (denoted as "active") hosts a robust gap, whereas the α and β bands (denoted as "passive") host weaker gaps, which allows low-lying quasiparticle excitations.

Spin fluctuations in the paramagnetic state, so called paramagnons, were suggested as an essential ingredient for enhancing the superfluidity in ^{3}He[84]. Because of the closeness to ferromagnetism, this lead to the suggestion that ferromagnetic spin fluctuations might be the "glue" for superconductivity in SRO in lieu of the phonons in the BCS theory [26]. However, inelastic neutron scattering revealed that the magnetic correlations in SRO are predominantly incommensurate and antiferromagnetic, which spoke against such a kind of pairing mechanism [85]. A variety of alternative pairing mechanisms (e.g. Hund's rule coupling among the 4d-electrons [86] or charge or orbital fluctuations [87]) was suggested, but none of them could settle the debate [26]. Thus, this question remains currently open. A recent ARPES study indicated the important role of SOC in SRO, which breaks down the description in terms of a spin-triplet and requires invoking mixed spin-orbit-states [37]. This further demonstrates that the unconventional superconductivity in SRO is far from understood and that it, similarly

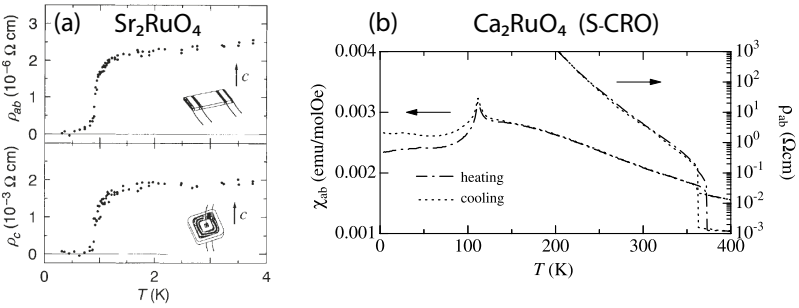

Figure 2.1: (a) In-plane and out-of-plane transport of SRO showing the transition to a superconducting state. Taken from Ref. [69] (b) In-plane susceptibility and resistivity for S-CRO depicting the MIT around 360 K and the antiferromagnetic transition at 110 K. Taken from [89].

to the cuprates, will continue being an important topics in condensed matter research.

CRO is an antiferromagnetic Mott-insulator, which can gradually be tuned toward SRO by either Sr-substitution or pressure [33, 40]. In analogy to the doping studies on the cuprates [88], the research effort surrounding the evolution of the electronic states of CRO toward the superconducting metallic SRO is hoped to bring clarification to the subject.

2.2 Structural, Electronic and Magnetic Properties

The first CRO studies were conducted on polycrystals, where it was found that, in contrast to SRO, CRO crystallizes in two variants with distinct electronic and structural properties: Stoichiometric S-CRO and oxygen-excess O-CRO [90, 91]. The O-CRO phase is also sometimes referred to as "L-Phase" because of the longer c-axis at room temperature. If not explicitly stated, we refer to the stoichiometric phase of CRO in this thesis. Most research has been devoted to S-CRO, since it proved to be impossible to synthesize O-CRO single crystals up to this date due to reasons that will become clear be-

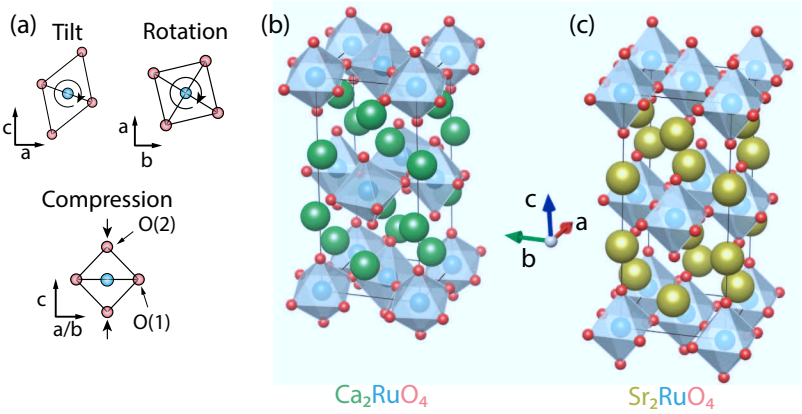

Figure 2.2: (a) Distortion modes of the RuO_6 octahedra. Tilt about the b-axis, rotation about the c-axis and compression of the octahedron. The labels denote the apical oxygen site O(2) and the basal plane oxygen site O(1). (b) Unit cell of CRO at 295 K based on Ref. [90]. (c) Illustration of tetragonal SRO using the orthorhombic unit cell of CRO. Based on Ref. [93].

low. While SRO exhibits metallicity and superconductivity at around 1 K[69], CRO was found to be insulating and antiferromagnetic at 110 K (Fig. 2.1)[91]. The insulating state in CRO is abruptly destroyed at a metal-to-insulator transition at around 360 K, which occurs together with large structural changes [92]. The volume change during the transition is so severe that the crystals shatter to many small fragments, which prohibits the growth of large crystals as for SRO. Heating CRO again through the transition after the growth usually destroys a sample completely making the study of the MIT with single crystals quite difficult.

O-CRO shows a suppressed MIT at about 150 K with a concomitant AFM transition. Thus, the suppression of the MIT by intercalation of oxygen prevents the synthesis of O-CRO single crystals since this inevitably triggers the MIT and thus leads to the destruction of the sample [90].

Refinements of the crystal structure of SRO via X-ray and neutrons showed that the compound is of the K_2NiF_4-type [93, 94] with the tetragonal space group I/4mmm (no. 13). The Ru-atoms are each coordinated with O-atoms forming an octahedron. The RuO-planes consist of corner-sharing octahedra that are stacked in a staggered

fashion. Rocksalt-type SrO-layers are sandwiched in between the RuO-planes (Fig. 2.2).

In contrast, neutron studies on CRO polycrystals revealed that the structure of Ca_2RuO_4 shows strong distortions [45, 90]. The structural refinement concluded that the best description of the crystal structure is given by the orthorhombic Pbca space group (no. 61). Here, the RuO_6 octahedra are tilted about the b-axis and rotated about the c-axis (Fig. 2.2). In SRO, the octahedra are elongated along the Ru-O2 distance, whereas in CRO they are compressed and are more regular at room temperature.

The diffraction studies revealed strong structural activity with temperature in CRO (Fig. 2.3). Especially at the MIT, CRO shows dramatic changes. On one hand, the transition itself is not linked to a symmetry reduction, i.e. the structure can be refined above and below the MIT with the Pbca space group. On the other hand, large jumps in the lattice constants and the octahedral distortions are observed. The c-lattice constant shrinks suddenly by $\approx 1\,\%$, while an increase in the in-plane lattice constants can be detected. Below the MIT, the expansion is mainly limited to the b-axis which leads to an increase of the orthorhombicity. The changes are also mirrored in the octahedral distortions. While in the metallic phase above the MIT, the octahedra are elongated as seen by $\mathrm{Ru-O2} > \mathrm{Ru-O1}$, the situation gradually inverts on cooling through the transition: $\mathrm{Ru-O2} \approx \mathrm{Ru-O1}$ around 300 K and then $\mathrm{Ru-O2} < \mathrm{Ru-O1}$ showing the compression of the octahedra at low temperatures. The rotation of the octahedra was found to be identical at 11 K and 295 K. The tilt of the octahedron can be defined i) by the plane formed by the basal oxygen atoms (O1) and the b-axis and ii) by the angle formed by the Ru-O2 axis and the c-axis (see also Fig. 6.22). We denote the former as ϑ-O1 and the latter as ϑ-O2. While ϑ-O1 shows mainly a smooth increase, ϑ-O2 shows an anomalous trend setting in at 260 K. This feature appears to be linked to the previous claim of antiferro-orbital order (see sec. 6.2.4). It is interesting to note that 260 K is also the temperature where the basal plane distances $Ru-O1 \parallel a$ and $Ru-O1 \parallel b$ invert, which appears to be connected to the different behaviors of ϑ-O1 and ϑ-O2.

The neutron powder refinement of the oxygen O-phase required the use of the monoclinic space group $P2_1/c$ for the metallic high-temperature phase, while the low-temperature phase below the MIT

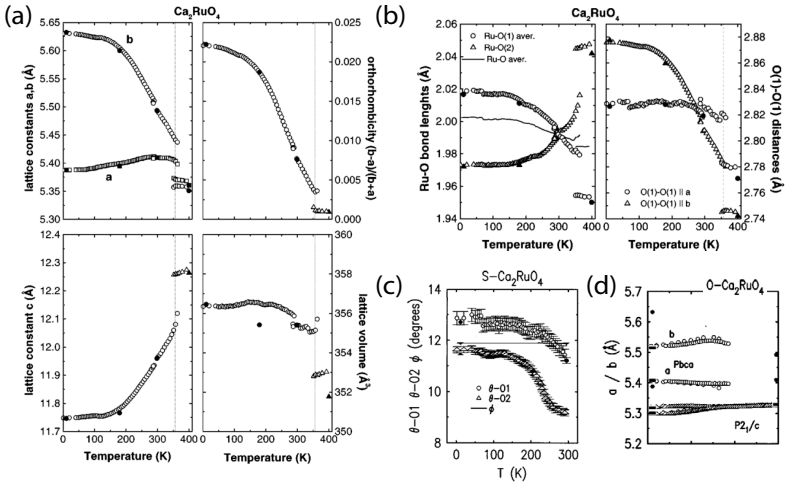

Figure 2.3: Structural changes in CRO across the MIT. (a) Changes in the lattice parameters, orthorhombicity and lattice volume. (b) Changes in the Ru-O bond distances and O-O distances. (c) Temperature dependence of the apical oxygen tilt θ-O2,basal plane oxygen θ-O1 and rotation ϕ (d) Lattice parameter changes of O-CRO with temperature. Taken from [90].

at 150 K could be again refined with the Pbca spacegroup. The refinement of the Pbca phase at 11 K is quite similar to the low-temperature refinement of the S-CRO Pbca phase at 11 K [45]. The transition from the $P2_1/c$ phase to the Pbca phase concomitant with the MIT is found to be not fully completed. Both phases are present down to the lowest temperatures. While the structural differences between the high- and low-temperature phase are large, each phase itself does not show a strong variation of the lattice. The $P2_1/c$ phase exhibits relative small tilts with ϑ-O2=4.5°,ϑ-O1=5.06°, while the rotation $\phi = 13.28°$ is larger than in S-CRO. The octahedra are quite elongated showing a Ru-O2 distance of 2.048 Å similar to SRO.

Since the $P2_1/c$ phase of O-CRO has the largest c-axis with c=12.37 Å compared with the Pbca-phases, it is also sometimes referred to as "L-Phase" (L for long). This should be not confused with the high-temperature phase of S-CRO, which is often labeled as "L-Pbca" to distinguish it from the short-c-axis "S-Pbca" phase below the MIT.

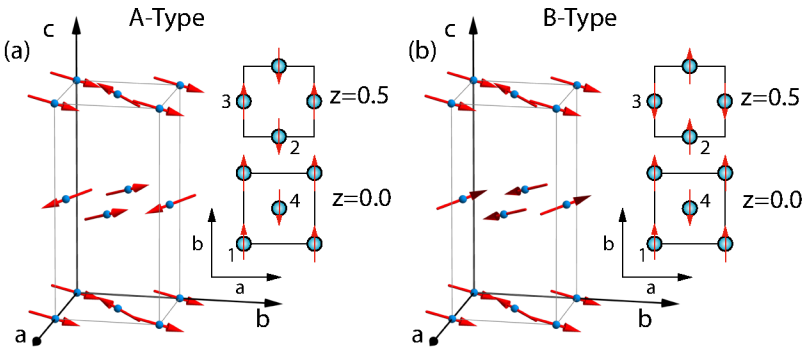

Figure 2.4: Reported Magnetic Structure for CRO in Ref. [90] (a) A-Type with propagation vector (1,0,0) (b) B-Type with propagation vector (0,1,0). The canting and rotation of the spins were not determined during the refinement, but included for completeness based on the irreducible representations for both types. Both are exaggerated for clarity. The numbers next to the Ru-atoms indicate the ordering according to the 4a-Wyckoff-position.

2.3 Magnetic Structure

Due to the magnetic moment of the neutron, neutron powder diffraction is also sensitive to the magnetic structure which makes it one of the most powerful tools to solve the magnetic structure of materials. Thus, the already mentioned studies were also sensitive to the symmetry breaking of the antiferromagnetism in CRO [45, 90].

Investigating S-CRO, two sets of structurally forbidden reflections with distinct temperature dependences appeared at temperatures below T_N. One set is of the type [(100) and (011)] and the other one (101)-type. That the sets belong to different magnetic symmetries becomes evident using simple symmetry arguments: Due to the appearance of new reflections, an antiferromagnetic arrangement of the magnetic moment is assumed and due the structure factor of the Ru 4a-Wyckoff site, there has to be an antiferromagnetic coupling within a RuO_2 plane. There are only two spin arrangements possible that satisfy this requirement (Fig. 2.4). Neither of them can cause both sets of peaks prompting the interpretation that the antiferromagnetic ordered state of S-CRO is composed of two coexisting phases. In analogy with the base-centering of Bravais-lattices, one phase is called A-

Type, the other one *B-Type*. The ordering temperatures determined by tracking the intensity of the magnetic peaks with temperature were determined to be 110 K for the A-Type ordering and 150 K for the B-Type ordering. O-CRO was determined to host only B-Type ordering with a similar $T_N = 150\,\mathrm{K}$.

For all phases, the magnetic moment direction extracted from the intensity of the magnetic peaks was compatible with the finding from magnetisation measurements, i.e. that the moments point along the b-direction.

2.4 Response to Strontium-substitution and Pressure

One of the fundamental motivations to study CRO is its connection with SRO. Analogous to the behavior in ^{3}He, SRO was thought to reside close to a nearby FM-stability. Among others, the finding of an insulating and antiferromagnetic state in the nearby CRO indicates that this notion may have been too simple and that the mechanism behind the superconductivity in SRO requires a more sophisticated model. Thus, it was the obvious next step to study the connection between CRO and SRO by investigating the substitution series $Ca_{2-x}Sr_xRuO_4$.

Typical for transition metal oxides, the phase diagram under Sr-substitution proved to be rich in physics showing a gradual stabilization of the metallic paramagnetic state in SRO (Fig. 2.5*).

The Sr-substitution reduces the transition temperature of the MIT until the sample becomes completely metallic. Concomitantly, the AFM is suppressed until it vanishes at $x = 0.2$. The AFM in the pristine CRO powder was shown to exist of A- and B-centered magnetic structures. CSRO with $x = 0.1$ shows exclusively B-Type order. Only the $x = 2$ end member SRO appears to superconduct, possibly due to the disorder induced by the substitution [33]. Neutron powder diffraction studies of the CSRO system again proved to be essential to understand the structural distortions associated with the changes in the electronic properties.

*It is unclear, why the P-I state extends up to 1000 K in this diagram at $x = 0$. Above the MIT at 360 K, CRO is regarded as metallic.

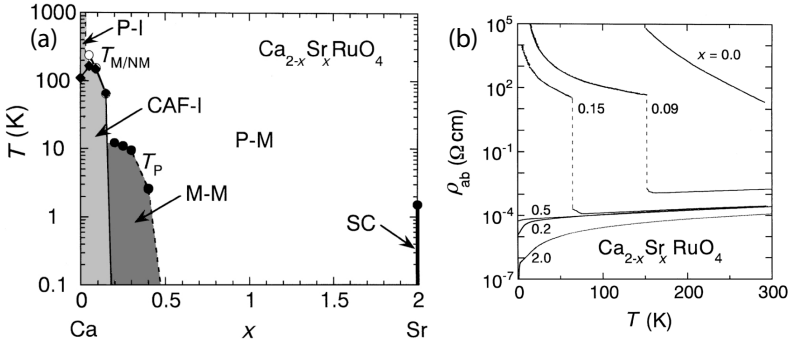

Figure 2.5: (a) $Ca_{2-x}Sr_xRuO_4$phase diagram showing magnetic and electronic properties. P-I: Paramagnetic and insulating, P-M: Paramagnetic and metallic, CAF-I: Canted antiferromagnetism and insulating, SC: Superconducting, M-M: Metallic and magnetic; The magnetic refers to an anomaly seen in the susceptibility, but no long-range order was detected. See also sec.2.6. (b) Evolution of electrical transport under stepwise Sr-substitution showing the suppression of the MIT. Both taken from Ref. [33].

The refinement of the structure revealed that the distortions of the RuO_6 octahedra are intimately connected to the electronic properties of CRO (Fig. 2.5). The only insulating and antiferromagnetic phase is S-Pbca characterized by the strongest tilt and orthorhombicity within the RuO_2-plane. Upon Sr-substitution, the octahedra are gradually rectified within the basal plane, the tilt is reduced and the Ru-O2 (apical oxygen) bond length increases. The compression of the octahedron gradually changes to an elongation. The rotation persists deep in the metallic phase until it becomes disordered and vanishes around $x = 1.5$. First-principles local density approximation (LDA) calculations agree with the structural trends shown by the neutron data [95]. The study indicates that the tilt and flattening stabilizes AF solutions, while the rotation should favor an FM instability. In contrast to the pressure phase diagram, long-range order ferromagnetism was not found in the CSRO phase diagram, but an anomaly in the magnetic susceptibility at $x = 0.5$ might indicate a ferromagnetic tendency (see also sec.2.6).

Applying hydrostatic pressures has similar effects as substituting Ca with Sr in CRO. Even moderate pressures drive CRO into a metallic state and suppress the MIT (Fig. 2.7). This follows Le Chatelier's

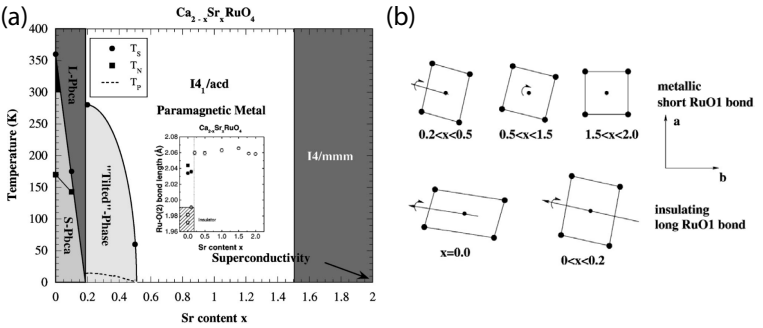

Figure 2.6: (a)$Ca_{2-x}Sr_xRuO_4$phase diagram showing the changes of the crystal structure under variation of the Sr-content x of the crystal. The $\mathrm{I4_1/acd}$ space group is tetragonal and without tilts, but still allows rotation of the RuO_6-octahedra. The inset shows the evolution of the Ru-O2 (apical oxygen) distance. (b) Tilt, rotation and bond lengths of the basal plane of the RuO_6-octahedra within the insulating and the metallic region. Both taken from [45].

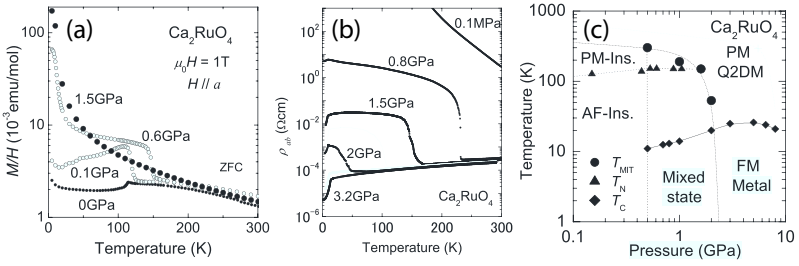

Figure 2.7: (a) Evolution of the magnetisation of a CRO single crystal with $H \| a$ under hydrostatic pressures. The data shows the shift from A-Type to B-Type AFM through the increase in T_N and the development of weak ferromagnetism below T_N. The emergence of a ferromagnetic phase around $20\,\mathrm{K}$ can be sensed. (b) Suppression of the MIT seen by in-plane electrical transport measurements under varying hydrostatic pressure. The ferromagnetic phase seen in panel a is associated with a drop in resistivity. (c) Pressure-Temperature Phase diagram of CRO derived from hydrostatic pressure experiments. All panels taken from [41].

principle since the metallic L-Pbca phase has a lower volume than the insulating S-Pbca phase ($352\,\text{Å}^3$ vs. $355\,\text{Å}^3$). The AFM switches from A-Type to B-Type with increasing pressure, which can be seen by the higher T_N and the appearance of weak ferromagnetism along the a-axis (sec. 2.3). One distinct difference compared with the CSRO phase diagram is the emergence of a ferromagnetic phase at 10 K–20 K within the metallic phase. Magnetisation measurements show a weak non-integer saturating moment of $0.35\,\mu_\text{B}$/Ru at 1.5 GPa along the a-axis within the FM phase [41]. This indicates itinerant ferromagnetism, since a localized $S = 1$ system would result in a much larger integer moment of about $2\,\mu_\text{B}$/Ru.* Additional hallmarks of itinerant magnetism were also found: In itinerant systems, the moment typically does not easily saturate in the ordered phase [97]. Also, the effective moment extracted from the Curie-law above T_C and the moment extracted from the saturation magnetization are typically not identical in itinerant systems, which is applicable here [98]. The metallic FM phase already forms at 0.5 GPa and thus protrudes into the insulating AFM part of the phase diagram. This suggests a state with coexisting metallic FM and insulating AFM CRO (mixed state in Fig. 2.7).

Neutron powder diffraction structural refinements under pressure showed also similarities with Sr-substitution. The octahedron is compressed within the ab-plane and elongates along the c-axis (Fig. 2.8). The tilt is suppressed, while the rotation almost does not change under pressure. At high pressures above 6 GPa, the tilt is completely suppressed, which allows to use the higher-symmetry space group Bbcm to refine the structure. At lower pressures, the insulating and metallic phases can be refined with the Pbca space group. The labelling L-Pbca for the metallic and S-Pbca for the insulating state is again used due to the distinct difference in the c-axis. For pressures around 1 GPa, it was found that the MIT does not fully complete to lowest temperatures, i.e. the volume percentage of both the metallic L-Pbca and the insulating S-Pbca phase is around 50 % at 2 K, which matches the mixed state found by transport and magnetization measurements.

*Having unquenched orbital momentum in CRO, the situation is less clear-cut, since L also contributes [96]. Thus, the constraint of an integer spin does not necessarily have to hold for a local model. We note, that the recent proposal of excitonic magnetism lifts this constraint, too. However, in any case, the moment is unusually weak for local magnetism.

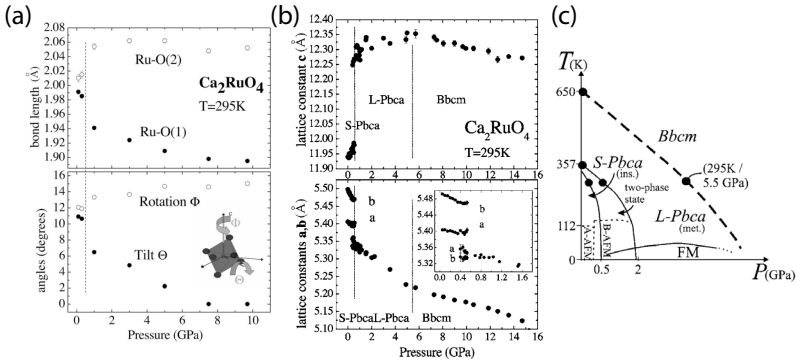

Figure 2.8: (a)RuO_6 distortions under pressure. Bond lengths Ru-O1 (basal plane oxygen) and Ru-O2 (apical oxygen). Rotation and tilt of the octahedron. The dashed line indicates the MIT. (b) Changes in the lattice constants under different pressures. The Bbcm space group is essentially a tilt-free orthorhombic version of the Pbca group. (c) Structural and magnetic phase diagram under hydrostatic pressure derived from neutron powder diffraction experiments. All panels taken from [40].

Inspecting the magnetic peaks corresponding to A-Type or B-Type AFM, it was found that the predominantly A-type AFM found in pristine samples is tuned to B-Type agreeing well with the assessment from the magnetization measurements.

2.5 Electronic Structure

Finding the correct description of the electronic states for CRO and how the orbital and spin degrees of freedom evolve under parameter changes such as doping or structural distortion toward the metallic superconducting state in SRO is at the heart of the many experimental and theoretical studies conducted on this material.

Being in the 4^{th} row of the periodic table, the Ru^{4+} ion in CRO has a $4d^4$ configuration. The 4d-orbitals are more extended than for the classic 3d-correlated systems such as the cuprates or nickelates, which reduces the Coulomb repulsion U. The volume of the 5d-orbitals is even larger reducing U further. Essentially, in a Mott-Hubbard picture, a system is a Mott-insulator, when U becomes stronger than the bandwidth W, which favors the delocalization of electrons. This explanation was found to hold for many 3d- and 4d-materials, however,

it fails to explain why e.g. the 5d-system Sr_2IrO_4 is insulating, since U is small relative to the W encountered in this material [20]. A combined spectroscopic and band calculation study was able to show that the strong spin-orbit-coupling (SOC) λ can act similarly as U in narrowing of the bands in the system and can consistently explain the insulating state. SOC is a relativistic effect and is typically treated as a perturbation for 3d-elements. Its strength is $\propto Z^2$, where Z is the atomic number [99]. Thus, it is natural to expect much stronger stronger effects for Ir with $Z = 77$ than for e.g.Cu with $Z = 29$. Ruthenates with $Z = 44$ of Ru are situated between the high U and low λ cuprates and the low U, but strong λ iridates. A priori, an intermediate scenario is then expected for ruthenates, where both U and λ have to be considered.

Another important energy scale for transition metal oxides is the so called crystal field splitting Δ. The transition metal M within an oxygen octahedron MO_6 is coordinated by six oxygen atoms, whose electrostatic field (ligand field) lifts the degeneracy of the d-states of the M-ion. Assuming a regular octahedron, the crystal-field symmetry can be described by the O_h point group in Schönflies notation. Under the assumption that the orbitals inherit the same symmetry, the rotational symmetry operations of the initially five degenerate d-orbitals can only be described by two irreducible representations of the O_h group, the two-dimensional E and three-dimensional T_2. Thus, their representation is reducible and given by $\Gamma = E \oplus T_2$([100] and references therein, also see sec. 5.3). In physical terms, the initially fivefold degenerate set is split into a twofold degenerate e_g subspace and a threefold degenerate t_{2g} subspace (Fig. 2.9). The "g", from the German *gerade* (even), was added here to denote that the corresponding base functions are even under the inversion operation $\boldsymbol{r} \rightarrow -\boldsymbol{r}$. The wavefunctions of the e_g and t_{2g} subsets are linear superpositions of the $|l^z\rangle$ eigenstates of the free ion [1, 101, 102]:

$$e_g \begin{cases} |z^2\rangle = |l^z = 0\rangle \\ |x^2 - y^2\rangle = \frac{1}{\sqrt{2}}(|2\rangle + |-2\rangle) \end{cases} \qquad t_{2g} \begin{cases} |xy\rangle = -\frac{i}{\sqrt{2}}(|2\rangle - |-2\rangle) \\ |xz\rangle = \frac{1}{\sqrt{2}}(|1\rangle - |-1\rangle) \\ |yz\rangle = \frac{i}{\sqrt{2}}(|1\rangle + |-1\rangle) \end{cases} \tag{2.1}$$

When visualizing the orbitals, one can see the reason for the split-

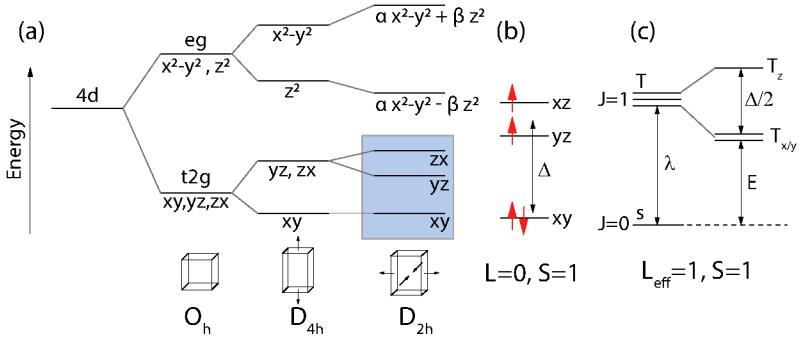

Figure 2.9: (a) Lifting of the degeneracy of the 4d-orbitals by a crystal field with cubic (O_h), tetragonal D_{4h} and orthorhombic D_{2h} symmetry. The blue rectangle represents the most relevant states for the $t_{2g}^4 e_g^0$ CRO. Based on Ref. [100]. (b) Electronic configuration without considering SOC λ. Crystal field Δ and Hund's rules stabilize a $L = 0, S = 1$ state. (c) Electronic states within a strong SOC picture with comparable λ and Δ. SOC counteracts Δ by stabilizing a nonmagnetic $J = 0$ ground state. A magnetic $J = 1$ triplet resides at λ. Its states are split by Δ in a doublet and singlet. The splitting between $J = 0$ and the T_x/T_y doublet can become comparable to the exchange energy inducing magnetic ordering (see text).

ting more clearly (Fig. 2.10): The e_g orbitals point toward the surrounding oxygen atoms, while the lobes of the t_{2g} orbitals point between them. Here, $|l^z = m\rangle$ denotes the spherical harmonics function Y_l^m with $l = 2$. The radial part of the eigenfunction is omitted for brevity, since it is not of importance for the following discussion. The crystal field has the effect to stabilize real wavefunctions, which has important implications for the angular momentum. If we assume the eigenvalues of the angular momentum operator $\hat{l^z}$ are non-degenerate, the corresponding eigenfunctions are all real. In order to see this, we need to assume a time-reversal symmetric system where ψ has to give the same eigenvalue as ψ^*. Since we assumed non-degeneracy, i.e. every eigenvalue has a unique eigenfunction, $\psi = \psi^*$, the wavefunction ψ has to be real. In fact, in the basis we chose for eq. 2.1, the e_g and t_{2g} functions are all real.

The angular momentum operator $\hat{l^\alpha}$ has an imaginary component in any α, but is also hermitian, since it is an observable. Thus, if ψ is real, this requires the expectation value $\langle\psi|\hat{l^\alpha}|\psi\rangle$ to be purely imaginary and real at the same time, which is only fulfilled if $\langle\psi|\hat{l^\alpha}|\psi\rangle = 0$.

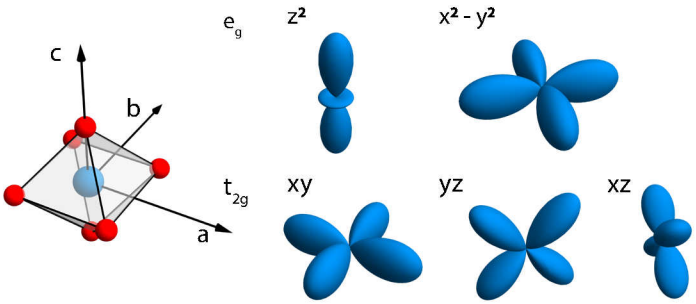

Figure 2.10: Wavefunctions of the 4d-orbitals split by a cubic crystal field. The lobes of the twofold e_g orbitals point toward the oxygen atoms, the lobes of the threefold t_{2g} point between them.

This phenomenon is also called *quenching of the orbital momentum* and is responsible for suppressing the orbital contribution to the magnetic moment for many systems [96]. A more intuitive picture is that the crystal field exerts a torque on the electrons causing them to precess. Thus, their orbital plane does not stay fixed in space and the angular momentum averages to zero [103].

However, the crystal field symmetry might be sufficiently high that some states are still degenerate. In the case of cubic symmetry, the e_g and t_{2g} orbitals retain twofold and threefold degeneracy, thus their eigenfunctions are more appropriately described by linear combinations of the states shown in eq. 2.1). In this case, it can be easily seen that the e_g manifold still does not acquire any angular momentum, since $|z^2\rangle$ does not contribute in any linear combination. For the t_{2g} states, the situation is less clear-cut. It is thus often more convenient to switch to a different basis by mapping the t_{2g} manifold onto an effective angular momentum $l_{\text{eff}} = 1$[1]:

$$t_{2g} \begin{cases} |t_{2g}^{0}\rangle = |0\rangle = |xy\rangle \\ |t_{2g}^{1}\rangle = |1\rangle = -\frac{1}{\sqrt{2}}(|xz\rangle + i\,|yz\rangle) \\ |t_{2g}^{-1}\rangle = |-1\rangle = \frac{1}{\sqrt{2}}(|xz\rangle - i\,|yz\rangle) \end{cases} \tag{2.2}$$

Here, it can be seen that the degenerate t_{2g} subset still has unquenched angular momentum, since $\langle \mp 1|\hat{l^z}|\mp 1\rangle = \mp 1$ and $\langle 0|\hat{l^z}|0\rangle = 0$.

After discussing a single particle in a d-shell, we now want to turn to CRO with its 4d t_{2g}^4 configuration. As has been shown experimentally, the O_6-octahedron surrounding the Ru-atom is not regular, but compressed at low temperatures, which reduces the symmetry from the cubic point group O_h to the tetragonal D_{4h}. The splitting between e_g and and t_{2g} is $\approx 4\,\mathrm{eV}$ and the tetragonal field splitting within the t_{2g} levels is of the order $\approx 100\,\mathrm{meV}$ [104]. Furthermore, the octahedron is also orthorhombically distorted, which reduces the crystal symmetry to the D_{2h} group and adds an additional small splitting of the xz and yz orbitals. However, the orthorhombic splitting is assumed to be relatively small, so the xz and yz states are often treated as degenerate.

Applying Hund's rules to CRO yields a so called low-spin configuration, where only the lower lying t_{2g} levels are occupied by the four electrons. Intraionic exchange coupling, the so called Hund's coupling, is small compared to the e_g-t_{2g} splitting Δ, which makes it more favorable to have two electrons with opposite spin occupying the same orbital than overcoming Δ[28]. The resulting configuration consists of three electrons with the same spin in the $|0\rangle$,$|-1\rangle$ and $|1\rangle$ states and one electron with opposite spin in the $|0\rangle$ state. In this state, $S = 1$, but the angular momentum is completely quenched $L = 0$ (Fig. 2.9b).

Now, we can turn to the role of SOC in CRO. Indeed, a combined oxygen K-edge XAS and spin-resolved ARPES study found that SOC is active in CRO by detecting a substantial orbital momentum in CRO [29]. SOC $\lambda \boldsymbol{S} \cdot \boldsymbol{L}$ stabilizes states with angular momentum, i.e. complex wavefunctions and thus counteracts the crystal field splitting [1]. If λ is sufficiently strong, $\boldsymbol{L}$ and $\boldsymbol{S}$ are not good quantum numbers anymore and the electronic states have to be described in terms of the total angular momentum J. In this case, one applies a $\boldsymbol{L} \cdot \boldsymbol{S}$ coupling scheme and yields $J = 0, 1, 2$ multiplets, whereas the $J = 0$ constitutes the ground state (Fig.2.9c).* The $J = 2$ quin-

*This may appear surprising, since we have a more than half-filled shell that should have the $J = L + S = 2$ as a ground state according to Hund's rules. [105] However, it can be shown that the mapping of the t_{2g} states on an *effective* $l = 1$ manifold is only correct, when $l = -1$ is being used. If one uses $l = 1$ instead, λ and the g-factor have to be taken negative, which changes the order [1].

tet resides at 3λ and is usually neglected in the case of CRO [106]. Thus, in the strong SOC picture, the t_{2g}^4 of CRO is described by a $J = 1$ triplet and a $J = 0$ singlet. Moreover, if $\Delta/\lambda \approx 1$, the effect of the crystal field manifests itself in a splitting of the triplet. To this end, the coupled states of the triplet $T_{\mp 1} = |J = 1, M = \mp 1\rangle$ and $T_0 = |J = 1, M = 0\rangle$ can be transformed into a Cartesian basis T_x, T_y and T_z. Similarly to the non-SOC case, the states with more in-plane character T_x/T_y are lowered compared to T_z with out-of-plane character [28].

For CRO, the fundamental question arises, which model is applicable. In the case of a large Δ, Ru carries $S = 1$, but the angular momentum is completely quenched. However, the magnetic moment detected by neutron scattering is $1.3\,\mu_\mathrm{B}$, significantly lower than the $2\,\mu_\mathrm{B}$ predicted by $S = 1$[45, 90]. Furthermore, as already mentioned, XAS and ARPES measurements indicate a substantial angular momentum, which is incompatible with the model of a dominant crystal field Δ[29]. On the other hand, the strong SOC picture has a completely nonmagnetic $J = 0$ ground state, which is seemingly nonphysical for CRO.

So far, we just considered an ion surrounded by oxygen atoms, but not the interionic superexchange (SE) interactions between Ru-atoms. By virtue of quantum mechanics, the wavefunction $|\psi_a\psi_b\rangle$ of a system of two interacting fermions $|\psi_a\rangle$ and $|\psi_b\rangle$ has to be antisymmetric. Since $|\psi_a\psi_b\rangle \propto \psi(\boldsymbol{r})\chi(\boldsymbol{r})$ is composed of a spatial part $\psi(\boldsymbol{r})$ and a spin part $\chi(\boldsymbol{r})$, the constraint of antisymmetry dictates that a symmetric $\chi(\boldsymbol{r})$ must cause an antisymmetric $\psi(\boldsymbol{r})$ and vice-versa. Thus, the spin function $\chi(\boldsymbol{r})$ can have large effect on $\psi(\boldsymbol{r})$, which determines the charge distribution and the electrostatic energy of the system. This electrostatic energy is the underlying origin of the exchange interaction and is one of the main driving forces for long-range magnetic ordering phenomena. In the case of CRO (as for many other transition metal oxides), the interaction occurs through the band overlap of the oxygen atoms between the Ru-atoms, which is coined *superexchange*(SE) interaction. In a Mott-system, the strength of the SE interaction can be quantified by $J_\mathrm{ex} = 4t^2/U$. The hopping term t characterizes the band overlap, while the Coulomb repulsion U suppresses the interaction of neighboring ions.

In CRO, the peculiar situation exists, where all energy scales λ, Δ and J_ex are of comparable scale ($\approx 100\,\mathrm{meV}$)[28]. Thus, a model

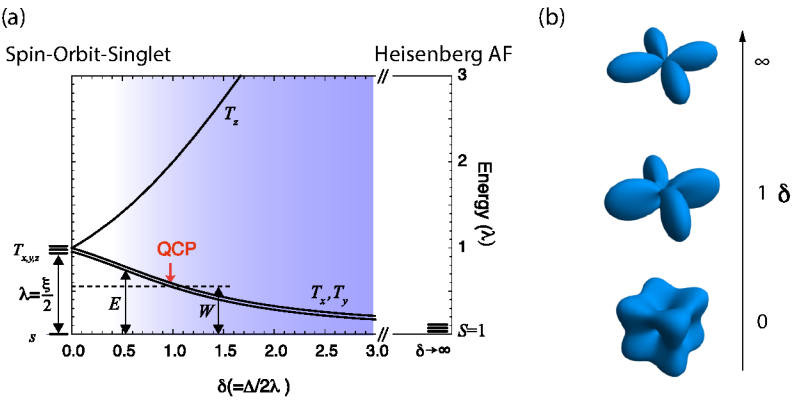

Figure 2.11: (a) Evolution of the electronic states under crystal field changes in CRO within the strong SOC picture. The $J = 1$ triplet is split into a T_x/T_y doublet and a T_z singlet with increasing Δ (corresponding to the compression of the RuO_6 octahedron). The T_x/T_y doublet is lowered until a quantum critical point (QCP) is reached. Here, the exchange energy W corresponds to the gap E between the nonmagnetic J=0 singlet $|s\rangle$ and the magnetic T_x/T_y doublet causing magnetic states to condense into the ground-state and forming magnetic long-range order (excitonic magnetism). $\delta = 0$ represents the case of dominating SOC λ and $\delta \to \infty$ of dominating crystal field Δ. Taken from [107]. (b) Evolution of the $|s\rangle$ wavefunction with varying δ. At $\delta = 0$, the state comprises xy, xz and yz contributions. At $\delta \to \infty$, $|s\rangle$ corresponds to the xy-orbital.

coined *excitonic magnetism* was proposed to provide a scenario intermediate between the strong Δ and a strong SOC model. Here, one starts in the picture of strong SOC with a $J = 0$ singlet and $J = 1$ triplet separated by λ. The $J = 1$ triplet is split by $\Delta/2$ lowering the T_x and T_y states and raising T_z (Fig. 2.11)

If the gap E between the T_x/T_y states and the singlet ground state becomes comparable to the SE energy, it becomes more favorable for the system to order magnetically, i.e. Δ and J_{ex} stabilize a magnetic ground state. This situation is reminiscent of a Van-Vleck-type mechanism, where a non-magnetic ground state becomes magnetic due to an admixture of excited states in an external magnetic field. The external field causing a Zeeman splitting of the triplet is replaced by an internal exchange field in our case. Such a type of magnetism is also called *singlet magnetism*[1]. The transitions to the magnetic states can also be seen as magnetic excitations or magnons. An intriguing

interpretation of the formation of a magnetically ordered state in such a system is the creation of a Bose-condensation of these magnons, i.e. the creation of a macroscopic number of magnons [30].

One hallmark of excitonic magnetism is the softness of the magnetic moment, i.e. the mode to excite amplitude fluctuations of the magnetic moment lies at relatively low energies compared to other magnetic systems. This results from the fact that the magnetization density is relatively low for such a type of mechanism [31]. Since the mode is connected to the amplitude fluctuations of a complex order parameter and not its phase fluctuations (*Goldstone modes*), this mode is also called *Higgs-mode* in analogy to the discussion surrounding spontaneous symmetry-breaking in high-energy physics.

The applicability of excitonic magnetism for CRO is still matter of debate. In fact, starting with a $\Delta \gg \lambda$ picture and adding SOC as a small perturbation can explain many features of CRO [108, 109]. However, recent inelastic neutron scattering and Raman scattering studies were able to directly detect the Higgs-mode in CRO [31, 107]. The distinct shape of the magnetic dispersions supports the model of excitonic magnetism [107]. The anomalously low magnetic moment in the AFM phase can also be explained by this model [28]. Thus, considerable evidence supports an excitonic magnetism in CRO.

An important implication of the excitonic magnetism model for thin films is the sensitivity toward the crystal-field-splitting Δ. Epitaxy allows one to directly tune Δ and lets us expect strong modifications of the Hamiltonian of CRO under compressive and tensile strain.

2.6 Quadrupolar Order

The report of an unquenched angular momentum in CRO sparked a flurry of predictions regarding orbital order of CRO, i.e. a long-range ordering of L separate from the one of S. Several theoretical studies tried to attack this problem and to predict possible orbital order structures. Generally, the close competition of different energy scales in CRO makes this task very complex.

The environment of the Ru-atoms does not break inversion symmetry, thus we do not expect any formation of an electrical dipole in the system. Any deviation from a spherical charge distribution, i.e. a

rotational symmetry breaking, involves the formation of an electrical quadrupolar moment. To generalize the phenomenon of orbital order, an ordering of electrical quadrupolar moments, with an effective spin quadrupolar ordering (see below) we will discuss them under the umbrella term *quadrupolar order*.

These studies include the whole arsenal of condensed matter theory (without any claim of completeness): Hartree-Fock/mean field approaches [110, 111], exact diagonalization techniques [112, 113], LSDA [95], LDA [114, 115],LDA+U [89, 109, 115–118] and Dynamical Mean Field Theory(DMFT) [119–121] and combined DMFT+LDA approaches [104, 109].

A main consensus of the studies is the double or almost double occupancy of the $|xy\rangle$ orbital of the t_{2g}^4 configuration of the Ru-ion at low temperatures in CRO stabilized by the tetragonal crystal field Δ. In these calculations, the effects of the spin-orbit-coupling λ are found to be typically too weak relative to Δ in the considered models to stabilize the discussed $J = 0$ ground-state [109]. Such an orbital polarization is also called *ferro-orbital order*(FO) in the literature, since the orbital polarization is identical on every Ru-site, similar to the spin-polarization of ferromagnetism(Fig.2.12b).* O-K-edge XAS establishing the significant presence of SOC in CRO suggested a hole population of $xy : yz/xz$ of $1/2 : 3/2$ seemingly at odds with the full electron occupation of the $|xy\rangle$ state(Ref. [29] and 4.8.4). In the original publication this was explained by an admixture of $|xz\rangle$ and $|yz\rangle$ to the $|xy\rangle$ orbital through spin-orbit-coupling. Subsequently, it was shown by an exact diagonalization approach of a 2x2 plaquette of Ru-ions, that an antiferro-orbital(AFO) order pattern could naturally explain the measured orbital polarization without the need to involve spin-orbit coupling [113]. In such a pattern, two sites would be xy-polarized, while the third would be xz- and the fourth yz-polarized. Such an AFO pattern was further corroborated by optical spectroscopy measurements, which indicated that the observed d-d-excitations are consistent with a coexistence of an FO and AFO ordering [122]. However, optical

*It may be argued, however, whether this term is appropriate for this scenario, since the analogy to ferromagnetism is suggestive of a correlation-driven phenomenon. In our case, however, the effects appear to purely arise due to crystal-field effects. To not add further confusion to this matter, we will nevertheless continue using the term ferro-orbital order describing this type of state.

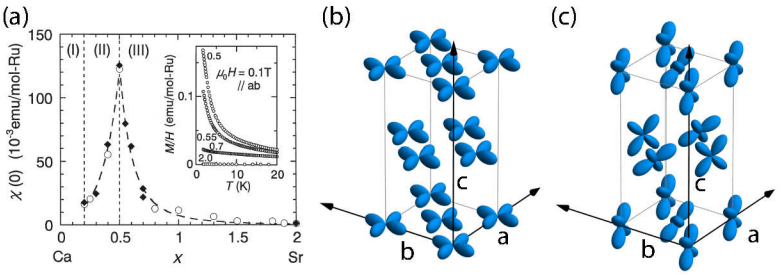

Figure 2.12: (a)Anomaly at $x = 0.5$ in the zero-temperature magnetic magnetic susceptibility $\chi(T = 0\,\mathrm{K})$ in the metallic part of the $Ca_{2-x}Sr_xRuO_4$phase diagram. Taken from [33]. (b) Minority spin orbital states of the Ru atoms in the CRO unit cell for a xy-type FO order, which was suggested for pristine CRO at low temperatures by experimental and theoretical studies. (c) Theoretically proposed[115] minority spin orbital states for localized xz/yz states for CSRO in region II shown by panel (a).

spectroscopy and LDA+U studies could show that the experimental data by Ref. [122] can be explained solely by xy-type FO ordering and that the seemingly 1/2 : 3/2-hole distribution is indeed compatible with the xy-type FO scenario if one considers the hybridization effects of the Ru 4d- with the O-2p-orbitals [89, 116]. We also note that the small size (2x2) of the system studied in Ref. [113] might lead to numerical boundary effects [111]. In addition to the O-K-edge XAS data, the FO order was confirmed by Ru-K-edge resonant elastic X-ray scattering (REXS) and nuclear magnetic resonance (NMR) experiments [123, 124]. It is interesting to note that the FO order was found to set in concomitantly with the MIT, although the octahedra are still elongated between 300 K and 360 K[45], which argues a against a simple JT-effect. Besides the xy-FO order, the only other direct evidence for orbital order is a Ru-L-edge REXS study that suggested AFO order with the same propagation vector as the antiferromagnetism in the material [125], which added confusion to the seemingly consistent xy-FO order scenario [112]. However, the reevaluation of the REXS-data (sec.6) shows that it cannot be unambiguously tied to an AFO-order-interpretations and many aspects can be explained by purely structural effects.

Besides the pristine compound, the evolution of the orbital state under Sr-substitution was investigated. Especially an anomaly in the

magnetization of the CSRO phase diagram at $x = 0.5$ attracted interest(Fig. 2.12a). While staying metallic and paramagnetic, the susceptibility at zero temperature showed a distinct peak while varying the Sr-content. Surprisingly, the moment size extracted from a Curie-fit of the susceptibility showed a magnetic moment of $1\,\mu_B$ or $S = 1/2$ [115]. A proposal to explain this feature is the scenario of an *Orbital-Selective Mott-transition (OSMT)*, where only a subset of bands at the Fermi-surface localize and generate a static magnetic moment, while the remaining bands stay itinerant and keep providing metallic electrical conductance. In the case of CRO, it was suggested that the xz and yz bands localize, while the xy-band stays itinerant at $x = 0.5$[115]. Furthermore, the localized bands were predicted to order in the fashion depicted in Fig. 2.12c. A subsequent DMFT-study refuted this scenario [120] stating that two bands coupled by electron-electron interaction are predicted to always localize simultaneously, but this study itself was called subsequently into question [119]. No definite experimental proof could be obtained so far for this scenario. Two angular-resolved photo emission spectroscopy (ARPES) experiments are seemingly contradicting each other: One report shows the localization of the xy-band [126], which is different from the theoretical prediction. Another report shows all bands at the Fermi surface [127]. High-field magnetotransport and magnetization seem to support the OSMT-scenario [35]. However, it was noted in Ref. [128] that the Drude peak measured in the optical spectroscopy studies is only weakly dependent on Sr-content, which is not expected in case of an OSMT [122]. Also, a recent DMFT-study could not reproduce the OSMT [104]. While experimental evidence remains sparse, an OSMT scenario might allow the interpretation the βNMR anomaly in the metallic CRO on LSAO(001) film as quadrupolar order(see sec. 6.1.2).

Finally, we want to address orbital order in a strong SOC picture. Within this picture, S and L are strongly coupled, thus a separate ordering of the orbital momentum cannot occur. However, in ref. [107] the term *spin-nematic phase* was assigned to the $J = 0$ ground state, which is a strong-SOC analogue of an orbitally-ordered state. In this state, we assume that the system has not yet magnetically ordered, thus no magnetic J=1 have condensed into the system. If the crystal field splitting is significant, the T_z state is considerably higher in energy such that it suffices to describe the system

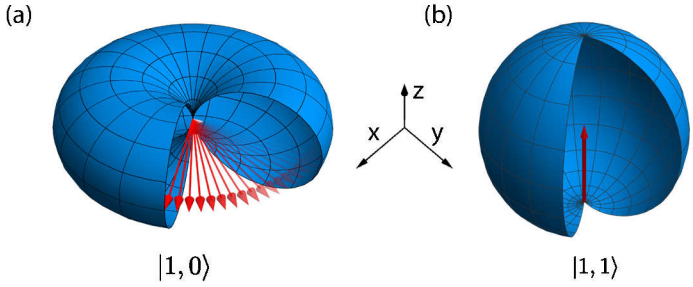

Figure 2.13: Spin distribution functions for a S=1 system. (a) $|S = 1, S_z = 0\rangle$ state, where no spin polarization,i.e. no magnetic moment is forming along the quantization axis. However, $\langle 1,0|(S_z)^2|1,0\rangle \neq \langle 1,0|(S_x)^2|1,0\rangle = \langle 1,0|(S_y)^2|1,0\rangle$, which can be thought of as a spin fluctuating in the xy-plane. (b)Fully polarized $|S = 1, S_z = 0\rangle$ state with magnetic moment along the z-axis. Based on [129].

in terms of a low energy model comprising T_x, T_y and $|s\rangle$ (see Fig. 2.11). We know that T_x, T_y are momentum-carrying, while $|s\rangle$ is not. Thus, it is convenient to map the three states onto an effective spin $\tilde{S} = 1$ manifold [107]. In this basis, the non-magnetic $|s\rangle$ state becomes $|\tilde{S} = 1, \tilde{S}_z = 0\rangle$. This state has the peculiar property that $\langle 1,0|\tilde{S}_\alpha|1,0\rangle = 0$ for $\alpha = x, y, z$. However, $\langle 1,0|(\tilde{S}_z)^2|1,0\rangle = 0$ and $\langle 1,0|(\tilde{S}_x)^2|1,0\rangle = \langle 1,0|(\tilde{S}_y)^2|1,0\rangle = 1$. In a field, the state does not exhibit any magnetic moment, i.e. a magnetic dipole, but shows fluctuations in the xy-plane. Thus, time reversal-symmetry is not broken, but the spherical rotational symmetry of the spin distribution has been lowered (Fig. 2.13). Alternatively, we can describe the state having a quadrupolar moment. Such a phase with rotational, but no time-reversal symmetry breaking, is also named *nematic*[129]. Nematic phases thus possibly allow one to reinterpret orbital order phenomena in CRO within the strong-SOC picture and motivate the search for quadrupolar order albeit classical orbital order involving L is not expected. Spin-nematic phases are predicted to be detectable by REXS [130], RIXS [131] and NMR [132], which motivates the experimental approaches taken within this work even in the case of the formation of a spin nematic and not a pure electrical quadrupole (orbital order).

2.7 Thin Films

Regarding ruthenates, most thin film studies focused on $SrRuO_3$, which can be routinely synthesized in many labs [133]. In addition, considerable effort was undertaken to produce superconducting Sr_2RuO_4 (SRO) thin films [56, 57, 59–63, 65, 134, 135]. While the stabilization of the phase appears to be mastered by multiple groups, synthesizing thin films with sufficiently low defect density to allow superconductivity to occur remains challenging. The superconducting state in SRO is infamous for its high sensitivity against impurities [136]. One report in 2010 indicated indeed superconductivity of a SRO film on LSAT [60], but the reproduction by other groups was only performed very recently [58, 64, 66]. Fewer studies were dedicated to Ca-based ruthenate thin films. Here, mostly $CaRuO_3$ films were targeted, where the growth of high-quality samples has also been established [137, 138]. On the other hand, work on epitaxial films of the single-layer Ca_2RuO_4 remains scarce albeit the growing interest in this material and the obvious sensitivity of the material toward lattice distortions (sec. 2.4). As we experienced ourselves, this is likely due to smaller thermodynamic growth windows relative to Sr_2RuO_4, which makes the growth optimization difficult(sec. 4.5).

To the best of our knowledge, the first report about single-layer CRO thin films was published by Wang et al. in 2004 [139, 140]. Here, CRO on LAO(100) was grown using pulsed laser deposition (PLD). The report mainly described the growth procedure, but transport data already showed that the film becomes metallic in contrast to bulk. An anomaly around 20 K was observed, but was left unclarified and apparently was not associated with the low-temperature itinerant ferromagnetic phase found in pressurized single crystals [42].

The second group to engage in the growth of CRO was Miao et al. [141, 142]. Similarly, the synthesis of CRO on LAO(100) via PLD was demonstrated and more characterization data was presented. Specifically, the low-temperature anomaly in transport was identified as an FM phase using magnetization measurements. The electrical transport revealed that an MIT occurs around 290 K. However, the resistivity increase is rather weak in contrast to single-crystalline CRO and shows a wide hysteresis down to the ferromagnetic phase. This was attributed the pinning of the film structure to the substrate, which suppresses the MIT and the following transformation of the electronic

structure. Additionally, a signal at 150 K in the magnetization was assigned to an AFM transition. Moreover, a detailed analysis of the harmonics of the anisotropic magnetoresistance measured at different temperatures suggested a coexistence of the FM and AFM at low temperatures. In order to show the impact of epitaxial strain on the structure, a film on LSAT(100) was also shown, but it appears the authors suffered from similar quality problems we encountered when we attempted to grow on this substrate. This is likely the reason, why no transport data was shown for films on this substrate. Furthermore, the study was expanded by substituting Sr for Ca, i.e. growing $Ca_{2-x}Sr_xRuO_4$thin films. Similar to the phase diagram for bulk, the addition of Sr led to higher metallicity and the suppression of the low-temperature ferromagnetic phase. Interestingly, the AMR data suggested a switching of the easy axis in the FM state for $x = 0.1$ similarly to CRO on LSAO(001) (see sec. 5.1.1). Unsuccessful growth attempts on substrates other than LAO were mentioned (it was not specified which substrates).

We note that the reported transport data for CRO on LAO are not fully consistent with each other. The original paper [139] reports a metallic behavior down to ≈ 100 K, Ref. [140] a completely insulating behavior, Ref. [142] an MIT at 290 K and Ref. [141] an almost completely monotonously decreasing behavior. For a discussion of this discrepancy, we refer to sec. 4.10.

Thus, we believe, this work represents the first published report of successful strain tuning of CRO using a variety of substrates other than LAO. However, we note, that during the course of this thesis we became aware of similar efforts by another group [143, 144]. Interestingly, they report the successful growth on $NdGaO_3(110)$ using molecular beam epitaxy, which we could not achieve despite multiple attempts using our PLD technique.

3
Spectroscopic Techniques

During the course of this thesis, two different resonant techniques were used to probe ordering phenomena in Ca_2RuO_4thin films: Beta Nuclear Magnetic Resonance (BNMR) is a probe for local dipolar and quadrupolar fluctuations and Resonant Elastic X-ray Scattering (REXS) measures their static long-range correlations. The techniques address the question of the ordering of the magnetic or orbital degrees of freedom from different directions. While BNMR probes the low-frequency spectrum of magnetic and electric fields through Li-ions as sensors implanted in the sample, REXS probes spatially Fourier transformed static components of the electronic density in reciprocal space. In this sense, BNMR is good for scouting for any change in the electric and magnetic internal fields of the sample, but suffers from an inherent ambiguity in the interpretation of the signal. REXS is element-specific, and thus can in our case probe directly the valence shell of Ru-ions in a film of CRO on top of a substrate, which facilitates the interpretation of data. However, one needs to know where to look in reciprocal space, i.e. which Fourier-component of the lattice might be connected to an ordering phenomenon.

This chapter will give a short introduction in both techniques and the methods used to investigate ordering phenomena in CRO thin films.

3.1 Resonant X-Ray-Scattering

3.1.1 Fundamentals of X-ray Scattering

X-ray scattering is one of the most powerful and productive techniques used in basic and applied research. Since Max von Laue's recording of the first X-ray diffraction pattern of $CuSO_4$ and the explanation of the scattering mechanism by Sir William Henry Bragg and William Lawrence Bragg at the beginning of the 20th century, many seminal findings such as the solution of the DNA structure relied on the use of X-rays [145]. With the technological advent of synchrotrons and free electron lasers, X-ray scattering will undoubtedly continue to be positioned at the scientific frontier. Because of its abundance and long history, equally abundant introductions of the topic can be found in textbooks. An excellent classic can be found in Ref. [146]. As a basis for the following chapters, we want to recall the main ideas.

Conventional X-ray scattering is based on the elastic Thomson scattering process, which can be viewed classically as a free electron oscillating in a perturbing field and emitting a spherical wave at the same frequency as the excitation. To quantify the amplitude and phase change due to the scattering, one defines the scattering length f as

$$\frac{E_{\mathrm{rad(R,t)}}}{E_{\mathrm{in}}} \propto f \frac{e^{iRt}}{R} \cos\psi \,, \tag{3.1}$$

where $E_{\mathrm{rad(R,t)}}$ is the electric field of the scattered wave, E_{in} the electric field of the incoming wave and $\cos\psi$ a polarization factor related to the dipolar nature of the process. For a free electron, $f = r_0$, the classical electron radius [146]. If one considers multiple electrons in a cloud around an atomic nucleus having an electronic density $\rho(\mathrm{r})$, then each electron emits the secondary radiation at a slightly different position leading to a phase shift and subsequently interference. In this case, we have to integrate to sum up the phase shifts $\boldsymbol{q} \cdot \boldsymbol{r}$ at each point and obtain the resulting scattering length

$$f(\boldsymbol{q}) = r_0 \int \rho(\boldsymbol{r}) e^{i\boldsymbol{q}\boldsymbol{r}} d\boldsymbol{r} \,. \tag{3.2}$$

Here, we introduced the momentum transfer $\boldsymbol{q}$ between incoming $\boldsymbol{k}_{\mathrm{in}}$ and outgoing photon momentum $\boldsymbol{k}_{\mathrm{out}}$ as $\boldsymbol{q} = \boldsymbol{k}_{\mathrm{out}} - \boldsymbol{k}_{\mathrm{in}}$. The integral

in eq.3.2 is also known as *atomic form factor*, but since they only differ in the factor r_0 the terms scattering length and form factor are often used interchangeably. In the case of forward scattering ($\boldsymbol{q} = 0$), $f = r_0 Z$, which gives an estimate for scattering of a specific element with atomic number Z. So far, we only considered a free atom, but it is easy to imagine that the bound nature of the electrons surrounding an atom affects the ability for the electrons to oscillate — similar to a damped harmonic oscillator. This is why one expands the definition by applying a dispersion correction to include changes in the amplitude and phase:

$$f(\boldsymbol{q}, \omega) = f(\boldsymbol{q}) + f'(\boldsymbol{q}, \omega) + i f''(\boldsymbol{q}, \omega) \tag{3.3}$$

The bound nature of the electrons also prompts to label the coherent elastic scattering process as *Rayleigh scattering* instead of *Thomson scattering*, which exhibits a cross-section with the well-known $\propto \omega^4$ dependence below a resonance frequency ω_0. If we now put the atoms in the periodic lattice of a crystal, we can again sum up the phase shifts using the periodicity of the unit cell and the lattice:

$$I(\boldsymbol{q}) \propto \underbrace{\left| \sum_n f_n(\boldsymbol{q}, \omega) e^{i\boldsymbol{q}\cdot\boldsymbol{r_n}} \right|^2}_{\mathrm{F}(\boldsymbol{q},\omega)} \times \underbrace{\left| \sum_m^N e^{i\boldsymbol{q}\cdot\boldsymbol{R_m}} \right|^2}_{L(\boldsymbol{q})} . \tag{3.4}$$

The term L(q) denotes the phase shift due to the interference between the unit cells with origin $\boldsymbol{R_m}$, in the crystal's lattice. It is only different from zero, if $\boldsymbol{q}$ is a *reciprocal lattice vector* $\boldsymbol{G}$, which equates to the famous Laue condition $\boldsymbol{q} = \boldsymbol{G}$. This sparked the concept of reciprocal space as a tool to rationalize the scattering from a crystal.

If we define $\boldsymbol{a_1}$,$\boldsymbol{a_1}$ and $\boldsymbol{a_1}$ as the lattice vectors of the crystal, we can define the unit cell's origin with $\boldsymbol{R_m} = n_1\boldsymbol{a_1} + n_2\boldsymbol{a_2} + n_3\boldsymbol{a_3}$ in real space. Then $\boldsymbol{q} \cdot \boldsymbol{R_m} \overset{!}{=} 2\pi n$ to yield constructive interference. From this, it follows that $\boldsymbol{q} = \boldsymbol{G} = h\boldsymbol{a_1^*} + k\boldsymbol{a_2^*} + l\boldsymbol{a_3^*}$ with

$$\boldsymbol{a_i^*} = 2\pi \frac{\boldsymbol{a_j} \times \boldsymbol{a_k}}{\boldsymbol{a_1} \cdot (\boldsymbol{a_2} \times \boldsymbol{a_3})} = 2\pi \frac{\boldsymbol{a_j} \times \boldsymbol{a_k}}{V} , \tag{3.5}$$

which defines the reciprocal lattice vectors using the unit cell volume V. Here, we also introduced the Miller indices h, k, and l for defining coordinates in reciprocal space. For $N \to \infty$, $L(\boldsymbol{q})$ represents a Delta-function, which is usually given for single crystals. However, for thin

films, this usually does not hold, since their thickness is of the order of 1 Å–1000 Å. In such a case, similar to an experiment with a finite slit in optics, this term broadens the reflections and gives additional smaller maxima based on the thickness of the film. These additional oscillations are called Laue fringes and can be used to estimate the size of the crystalline part of a thin film. They only appear if the film surface is reasonably smooth, making it a telltale sign for the quality of the thin film.

The term $F(\boldsymbol{q}, \omega)$ represents the geometric phase shift due to the scatterers within the unit cell by summing over each atom in it. This term is called the *unit cell structure factor* and depends on the scattering lengths of the atoms f_n within a unit cell and their relative phase shifts. Their symmetry can lead to a vanishing of some reflections, which are termed *forbidden reflections* in contrast to non-vanishing reflections, which are termed *allowed reflections*. By scanning systematically h, k and l, one can make some inference on the symmetry of the lattice, which allow to constrain possible space groups and sometimes non-ambiguously determine the space group.

Since the intensity is proportional to the absolute square of $F(\boldsymbol{q}, \omega)$, one cannot directly deduce the real space structure of a crystal from its diffraction image (this is also known as the *phase problem*). However, by modeling the crystal, it is possible to simulate the expected relative intensities: One varies the atomic positions and lattice parameters until a good match with the measured set of reflections is achieved. This process is called *refinement* and is a powerful tool to obtain detailed structural information. Initial experiments for exploring the structure are usually performed for polycrystals, which are unavailable for epitaxial thin films. X-ray structural refinements for single crystals are also routinely made, but the reciprocal space for thin films is contaminated by strong substrate reflexes, which restricts the number of film reflections one can study quantitatively. Due to this restriction, a structural refinement of thin films is only rarely performed.

We also want to briefly mention refraction effects of X-rays. The refractive index for X-rays is very close to unity. In fact, one usually expresses it as $n = 1 - \delta$, where δ is around 1×10^{-8} in air and 1×10^{-5} in solids. This puts the total reflection to very low angles below 1°. However, a measurement of the X-Ray Reflectivity (XRR) can yield valuable information: The wavelength of X-rays can be of the same order as the interface roughness of thin films and heterostruc-

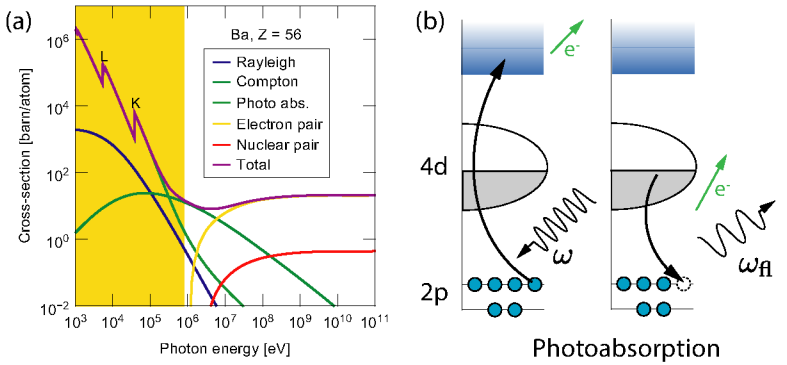

Figure 3.1: (a) Fundamental X-ray interaction cross-sections for Ba. Typical synchrotron energies are marked in yellow, where Rayleigh-scattering and photo-absorption dominates. The L- and K-edge absorption edge are marked in the total cross-section. Taken from Ref. [145] (b) Photoabsorption process at the Ru-L edge. An electron from the 2p-states is excited into the continuum and thus ejected as a photoelectron. The core-hole state decays via emission of an electron (Auger-process) or a photon (fluorescence).

tures, which allows interference effects to occur. A basic example is the interference of the air-film and film-substrate interface, which creates interference fringes in the XRR, which can accurately determine the thickness of the film. The following discussion about the dispersion correction of form factors can also be linked to refraction indices, which allows one to spatially resolve electronic effects in thin films [147].

3.1.2 Resonant Scattering Length

The interaction of X-rays with matter at low energies is dominated by photoelectric absorption(Fig. 3.1b), which is the process of exciting an electron from a bound state into the continuum. The photoelectric effect scales roughly with $\propto \omega^{-3}$, which implies an ω-dependence in penetration power [146]. This is one of the facts that motivates the different technical approaches for high and low X-ray energies: The X-ray spectrum is divided in a low energy regime ("soft"), where experiments have to be conducted in vacuum, and a high energy regime ("hard"), where air absorption is negligible and one can usually operate in air as

long no cryostat operation is required. In between a vaguely defined intermediate region (sometimes called *tender*)* around 2 keV–3 keV exists, where both technical approaches meet. The energies (Ru L2/3 edges) we used in the scattering experiments are located in this intermediate regime.

As we see in Fig. 3.1, the absorption exhibits distinct kinks. These originate from the quantized nature of bound states of the electrons within the potential of the nucleus. As we increase the energy, we cross multiple thresholds where electrons can be excited from core-levels to the continuum and thus increase the absorption cross-section. These element-specific energies are called absorption edges. Their nomenclature is based upon the core level that is being excited into the continuum: K for the 1s level, L_{I} to L_{III} for the 2s to 2p levels and M_{I} to M_{V} for the 3s to 3d levels. Slightly below the edge, one can also probe the unoccupied states of the valence shell. This process allows to access the orbital occupation and its anisotropy, which evolved to the powerful tool of X-ray Absorption Spectroscopy (XAS)(Fig. 3.2). After the absorption of a core-electron into the 4d-states, the core-hole is again "filled" by electrons from higher-energy states. These transitions emit either electrons (Auger electrons) or photons (fluorescence). Both can be used to measure the XAS signal: Experiments based on detecting the current created by the Auger-electrons is called *total electron yield*(TEY) and by detecting the emitted photons *fluorescence yield* (FY).

One may ask, what happens close to such an absorption edge in the scattering channel. Similar to a driven harmonic oscillator we expect some sort of resonance behavior in the proximity of the absorption edge. However, the dominating absorption cross-section increases also sharply at the edge, which leads to less intensity at regular Bragg peaks originating from the Thomson scattering process [124]. The symmetry of the transition probabilities into the unoccupied states that are in resonance can be lower than the symmetry of the lattice, i.e. the core electron clouds which are responsible for the Thomson scattering. In terms of magnetic scattering, one usually either excites electrons from shells, whose states are spin-polarized through spin-orbit coupling (i.e. 2p-shell), or excites into valence states, which have significant spin-orbit-coupling. This spin-polarization then gives the

*Sometimes the boundary of 1 nm for the wavelength can be found as a definition.

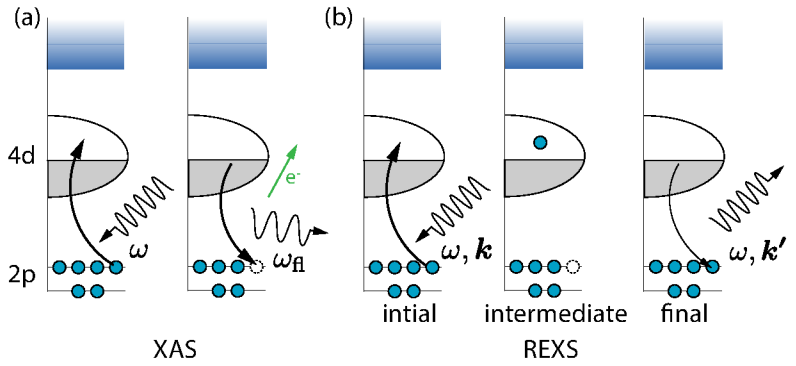

Figure 3.2: (a) XAS process at the Ru-L edges. An incoming photon is absorbed into the Fermi sea. This creates a core-hole state, which subsequently decays via emission of an electron (Auger process) or a photon (fluorescence). (b) REXS scattering process at the Ru-L edges. A photon is being absorbed exciting an electron in unoccupied states of the 4d-states. A short-lived intermediate state with a core-hole is created. The excited state decays via the emission of a photon with the same energy as the incoming photon. Based on Ref. [100].

contrast needed to observe the magnetic ordering in the valence shell. In this case, new resonant peaks can be observed at forbidden positions which can be used to monitor the symmetry breaking, e.g. due to magnetism. This is the core idea behind the resonant elastic X-ray scattering technique. In order to develop a mathematical framework for this, we have to embark on a quantum mechanical approach. The following derivation is a collection of Refs. [146, 148–151]. Aiming for a perturbation ansatz, we want to split our Hamiltonian into a part of the unperturbed system and in an perturbing part or interaction part. The Hamiltonian of an ensemble of free electrons with mass m is

$$H_0 = \sum_l \frac{\boldsymbol{p_l}^2}{2m}, \tag{3.6}$$

where we sum over the momentum operators p_l of the l-th electron surrounding an atom. If we now switch on an electromagnetic field with a vector potential operator $\boldsymbol{A}$, we replace $\boldsymbol{p_l}$ by $(\boldsymbol{p_l} - e\boldsymbol{A}/c)$[146]. If we define our total Hamiltonian as $H = H_0 + H_{\text{int}}$, we obtain the interaction term

$$H_{\text{int}} = \sum_l \left(-\frac{e}{mc} \boldsymbol{p_l} \cdot \boldsymbol{A}(\boldsymbol{r_l}) + \frac{e^2}{2mc^2} \boldsymbol{A}(\boldsymbol{r_l}) \cdot \boldsymbol{A}(\boldsymbol{r_l}) \right) . \tag{3.7}$$

Here, we neglected terms proportional to $\sigma \cdot (\nabla \times \boldsymbol{A})$ and $\sigma \cdot (\boldsymbol{E} \times \boldsymbol{A})$ describing the interaction of the electron spin σ , since the terms are tied to relativistic effects $\propto \hbar\omega/mc^2$ and thus much smaller than the above terms and not of interest for thin films, where the signal is already small due to the low amount of atoms [150]. However, these terms allow access to non-resonant magnetic scattering, which can conducted on single crystals [152]. The vector potential can be represented in a so called plane-wave expansion [150]

$$\boldsymbol{A}(\boldsymbol{r}) = \sqrt{\frac{2\pi\hbar c}{V}} \sum_{\boldsymbol{k},\boldsymbol{\varepsilon}} \sqrt{\frac{1}{k}} \left(\boldsymbol{\varepsilon} a_{\boldsymbol{k}\boldsymbol{\varepsilon}} e^{i\boldsymbol{k}\boldsymbol{r}} + \boldsymbol{\varepsilon}^* a^\dagger_{\boldsymbol{k}\boldsymbol{\varepsilon}} e^{-i\boldsymbol{k}\boldsymbol{r}} \right) . \tag{3.8}$$

Here, $a_{\boldsymbol{k}\boldsymbol{\varepsilon}}$ denotes an annihilation of a photon with with momentum $\boldsymbol{k}$ and polarization $\boldsymbol{\varepsilon}$ and $a^\dagger_{\boldsymbol{k}\boldsymbol{\varepsilon}}$ its creation. V represents the volume of the system. The transition rate between a ground state $|g\rangle = |g; \boldsymbol{k}\boldsymbol{\varepsilon}\rangle$ and final states $|f\rangle = |f; \boldsymbol{k'}\boldsymbol{\varepsilon'}\rangle$ is given by Fermi's golden rule to second order [151]:

$$W = \frac{2\pi}{\hbar} \sum_f \left| \langle f|H_{\text{int}}|g\rangle + \sum_n \frac{\langle f|H_{\text{int}}|n\rangle \langle n|H_{\text{int}}|g\rangle}{E_g - E_n} \right|^2 \times \delta(E_f - E_g) . \tag{3.9}$$

Here, we look at an initial state $|g\rangle$ that is being excited into a state $|f\rangle$. The REXS process (Fig. 3.1) involves a photonless intermediate state $|n\rangle$ in the second order term. If we now would plug H_{int} into eq. 3.9, we can state that the term $\boldsymbol{p}_l \cdot \boldsymbol{A}(\boldsymbol{r}_l, t)$ only contain terms linear in $a^\dagger_{\boldsymbol{k}\boldsymbol{\varepsilon}}$ and $a_{\boldsymbol{k}\boldsymbol{\varepsilon}}$, i.e. it will change the net number of photons in the system. The term $\propto \boldsymbol{A}(\boldsymbol{r}_l, t) \cdot \boldsymbol{A}(\boldsymbol{r}_l, t)$ is quadratic in $a_{\boldsymbol{k}\boldsymbol{\varepsilon}}$ and $a^\dagger_{\boldsymbol{k}\boldsymbol{\varepsilon}}$ and thus changes the number of photons by 0 or ± 2. Thus, one can already state that the term $\boldsymbol{p}_l \cdot A(\boldsymbol{r}_l, t)$ is important for absorption and resonant scattering. The term $\propto \boldsymbol{A}(\boldsymbol{r}_l, t) \cdot \boldsymbol{A}(\boldsymbol{r}_l, t)$ will contribute to Thomson scattering, since this process involves no change in the amount of photons. As we can see from Fig. 3.2, one would expect a mathematical relationship between the absorption and resonant scattering process. This is indeed the case as we will see after deriving the cross-sections for absorption and resonant scattering.

To express the absorption cross-section we start by plugging the term $\boldsymbol{p}_l \cdot \boldsymbol{A}(\boldsymbol{r}_l, t)$ identified as the one responsible for absorption into

Fermi's golden rule in 1st order

$$W = \frac{2\pi}{\hbar} \sum_f |\langle f|H_{\text{int}}|g\rangle|^2 \times \delta(E_f - E_g - \hbar\omega) \tag{3.10}$$

For $\boldsymbol{A}(\boldsymbol{r})$ we can use the following expression

$$\boldsymbol{A}(\boldsymbol{r}) = c\sqrt{\frac{2\pi n_{\boldsymbol{k}\boldsymbol{\varepsilon}}\hbar}{V\omega}}\boldsymbol{\varepsilon}e^{i\boldsymbol{k}\boldsymbol{r}}\,, \tag{3.11}$$

since we are annihilating a photon. The number of photons with momentum k and a specific polarisation is denoted as $n_{\boldsymbol{k}}$.* In the following, we will use the so called *dipole approximation* $e^{i\boldsymbol{k}\boldsymbol{r}} \approx 1$. This is usually justified by comparing the radius of core shells $r \approx 0.1\,\text{Å}$ to the wavelength λ. [153] For soft X-rays with an energy $\hbar\omega \leq 1000\,\text{eV}$, the wavelength correspond to $\lambda \geq 12\,\text{Å}$, which allows the approximation $2\pi/\lambda r \approx 0$. However, at the Ru L-edges ($\approx 3\,\text{keV}$ with $\lambda \approx 4\,\text{Å}$) this is generally less justified. Nevertheless, by defining the states $|g\rangle$ and $|f\rangle$ as atomic orbitals with l and m, it follows that this simplification is equivalent to only considering electric dipole transitions, which are dominant for $\Delta l = \mp 1$[154]. The Ru L edges investigated in this work constitute such a dipole transition with $2\text{p} \rightarrow 4\text{d}$, thus the approximation is applicable. The term $|\langle f|H_{int}|g\rangle|^2$ becomes

$$\begin{aligned}
|\langle f|H_{\text{int}}|g\rangle|^2 &= \left(\frac{e}{mc}\right)^2 |\langle f|\boldsymbol{p}\cdot\boldsymbol{A}|g\rangle|^2 \\
&= \left(\frac{e}{m}\right)^2 \left(\frac{2\pi n_{\boldsymbol{k}\boldsymbol{\varepsilon}}\hbar}{\omega_{\boldsymbol{k}} V}\right) |\langle f|\boldsymbol{p}\cdot\boldsymbol{\varepsilon}|g\rangle|^2 \\
&= e^2 \left(\frac{2\pi n_{\boldsymbol{k}\boldsymbol{\varepsilon}}}{\omega V\hbar}\right) |\langle f|[H_0,\boldsymbol{r}]\cdot\boldsymbol{\varepsilon}|g\rangle|^2 \\
&= e^2 \left(\frac{2\pi n_{\boldsymbol{k}\boldsymbol{\varepsilon}}\hbar\omega}{V}\right) |\langle f|\boldsymbol{\varepsilon}\cdot\boldsymbol{r}|g\rangle|^2 \\
&= \left(\frac{2\pi n_{\boldsymbol{k}\boldsymbol{\varepsilon}}\hbar\omega}{V}\right) |\langle f|\boldsymbol{\varepsilon}\cdot\boldsymbol{D}|g\rangle|^2
\end{aligned} \tag{3.12}$$

Here, we used $H^\dagger = H$, $\boldsymbol{p} = (im/\hbar)[H_0,\boldsymbol{r}]$ and the dipole operator $\boldsymbol{D} = e\cdot\boldsymbol{r}$. A cross-section is defined as $d\sigma/d\Omega = W/\Phi$, where

*We dropped the subscript ε for better readability.

$\Phi = cn_k/V$ is the photon flux. Combining eq. 3.12 and eq.3.10, we arrive at

$$\boxed{\frac{d\sigma_{\text{abs}}}{d\Omega} = \frac{4\pi^2\omega}{c} \sum_f |\langle f|\boldsymbol{\varepsilon}\cdot\boldsymbol{D}|g\rangle|^2 \times \delta(E_f - E_g - \hbar\omega)} \tag{3.13}$$

. We can transform the equation further by expanding the absolute square:

$$\frac{d\sigma_{\text{abs}}}{d\Omega} = \frac{4\pi^2\omega}{c} \sum_f \langle g|(\boldsymbol{\varepsilon}\cdot\boldsymbol{D})^\dagger|f\rangle \langle f|\boldsymbol{\varepsilon}\cdot\boldsymbol{D}|g\rangle \times \delta(E_f - E_g - \hbar\omega) \tag{3.14}$$

and use the Dirac identity relation

$$\pi\delta(E_f - E_g - \hbar\omega) = \lim_{\Gamma\to 0} \text{Im}\left(\frac{1}{E_g - E_f - \hbar\omega + i\Gamma/2}\right). \tag{3.15}$$

Similar to the damping constant for a damped harmonic oscillator, the term $i\Gamma/2$ smears out the Delta-function . Due to the energy-time uncertainty relation, this term is being named *core-hole lifetime*. This yields

$$\frac{d\sigma_{\text{abs}}}{d\Omega} = \frac{4\pi\omega}{c} \text{Im} \sum_f \frac{\langle g|(\boldsymbol{\varepsilon}\cdot\boldsymbol{D})^\dagger|f\rangle \langle f|(\boldsymbol{\varepsilon}\cdot\boldsymbol{D})|g\rangle}{E_f - E_g - \hbar\omega + i\Gamma/2}, \tag{3.16}$$

since after comparing with eq. 3.14, the only imaginary component can come from the transformation of the Delta-function.

For the scattering channel, we start at eq. 3.9. As already discussed, the term $\boldsymbol{A}\cdot\boldsymbol{A}$ only contributes to the Thomson scattering in 1st order, while the term $\boldsymbol{p}\cdot\boldsymbol{A}$ contributes to the resonant scattering in 2nd order. Following the derivation of eq.3.14, we can transform the second order term of eq. 3.9 for elastic scattering ($|f\rangle = |g\rangle$) to [150]

$$\begin{aligned}\frac{d\sigma_{\text{res}}}{d\Omega} &= \frac{2\pi}{\hbar\Phi}\left|\sum_n \frac{\langle g|H_{\text{int}}|n\rangle \langle n|H_{\text{int}}|g\rangle}{E_g - E_n - \hbar\omega + i\Gamma/2}\right|^2 \\ &= \left(\frac{\omega}{c}\right)^4 \left|\sum_n \frac{\langle g|(\boldsymbol{\varepsilon}'\cdot\boldsymbol{D})^\dagger|n\rangle \langle n|(\boldsymbol{\varepsilon}\cdot\boldsymbol{D})|g\rangle}{E_g - E_n - \hbar\omega + i\Gamma/2}\right|^2 .\end{aligned} \tag{3.17}$$

Here, we introduced again the core-hole lifetime Γ to allow for some uncertainty in the energy. Using $d\sigma/d\Omega = |f|^2$ we can formulate the resonant scattering length

$$\boxed{f_{\text{res}} = \boldsymbol{\varepsilon}'^{\dagger} \cdot \left(\frac{\omega}{c}\right)^2 \sum_n \frac{\langle g|\boldsymbol{D}^{\dagger}|n\rangle \langle n|\boldsymbol{D}|g\rangle}{E_g - E_n - \hbar\omega + i\Gamma/2} \cdot \boldsymbol{\varepsilon} = \boldsymbol{\varepsilon}'^{\dagger} \cdot \boldsymbol{F}_{\mathbf{res}} \cdot \boldsymbol{\varepsilon}\,.} \tag{3.18}$$

$\boldsymbol{F}_{\mathbf{res}}$ is the *scattering tensor* for resonant X-ray scattering and expresses the polarization dependence of the scattering. This is one of the main mathematical tools we will use to model the anisotropy of the resonant scattering data.

If one compares eqs. 3.16 and 3.18, one finds

$$\boxed{\frac{d\sigma_{\text{abs}}}{d\Omega} = \frac{4\pi}{k} \operatorname{Im}\left(f_{\text{res}}\right)} \tag{3.19}$$

This is the famous *optical theorem* formulated for resonant X-ray scattering. It allows to determine the imaginary parts of f_{res} via measuring the polarization dependence of the X-ray absorption signal. As in optical spectroscopy, the real part can then be extracted via a Kramers-Kronig transformation. This is especially useful for theoretical modelling, since X-ray absorption is a relatively simple measurement and can thus be used to determine the scattering tensor experimentally without the need to rely on assumptions for e.g. the core-hole lifetime. [150]

3.1.3 Resonant Magnetic X-Ray Scattering

The power of resonant scattering lies in the fact that it probes directly the electronic wavefunction of the valence shell. Through the spin-orbit-coupling in the initial or intermediate state, the transitions in the REXS process can be sensitive to a long range magnetic ordering in a system. If a system orders in an antiferromagnetic fashion the magnetic unit cell has a lower symmetry than the one responsible for the charge scattering. As in neutron scattering, this causes new peaks to appear in reciprocal space, which can be used to directly probe the symmetry breaking. An antiferro-quadrupolar ordering can have a similar effect. As we will see in sec.3.1.4, structural

effects can also cause additional Bragg peaks (Templeton Scattering). Since Ca_2RuO_4 hosts spin ordering, has an unquenched orbital momentum [29] and exhibits distorted RuO_6 octahedra, all effects have to be in principle considered when investigating a signal with resonant X-rays. Another very useful aspect of resonant magnetic scattering is that the anisotropy of the transitions into the intermediate state is imprinted in the scattering tensor (eq. 3.18). Thus, one can probe the magnetic moment direction of the atoms in resonance by measuring the polarization dependence of the scattering tensor by varying the incoming polarization ε in relation to the coordinates of the tensor $\boldsymbol{F}_{\mathbf{res}}$. In the following, we will establish a basic model of the polarisation dependency of the scattering length and how it can be used to deduce the magnetic moment direction. As the magnetic ordering is usually associated with a preferred magnetic moment direction through the magnetocrystalline anisotropy, Experimentally, we will probe the amplitude of the dipole transition operator $\boldsymbol{\varepsilon} \cdot \boldsymbol{r}$. i.e. we can write eq. 3.18 in terms of expectation values: [155]

$$f_{\mathrm{res}} = (\boldsymbol{\varepsilon'} \cdot \boldsymbol{r'})^{\dagger}(\boldsymbol{\varepsilon} \cdot \boldsymbol{r}) = \sum_{ij} (\varepsilon'_j)^* r_i (r'_j)^* \varepsilon_i = \boldsymbol{\varepsilon'^*} \cdot \boldsymbol{F}_{\mathbf{res}} \cdot \boldsymbol{\varepsilon} \qquad (3.20)$$

The tensor $\boldsymbol{F}_{\mathbf{res}}$ incorporates all the anisotropic properties intrinsic of our material, whereas the polarization vectors $\boldsymbol{\varepsilon'^*}$ and $\boldsymbol{\varepsilon}$ represent the particular geometry we are using the probe the elements of $\boldsymbol{F}_{\mathbf{res}}$. We will use the simplest example of a magnetic moment along a crystallographic direction in an otherwise spherical symmetric system, i.e. the only symmetry-breaking occurs through the magnetic ordering. If we assume the quantization axis and the magnetic moment lie along the z-direction, we can state that $\boldsymbol{F}_{\mathbf{res}}$ should be invariant against rotation along this axis:

$$\boldsymbol{F}_{\mathbf{res}} \overset{!}{=} R_z^{\alpha} \boldsymbol{F}_{\mathbf{res}} \left(R_z^{\alpha}\right)^{\mathrm{T}} \qquad (3.21)$$

R_z^{α} represents here the standard rotation matrix along the z axis about an angle α. It can be shown that [149]

$$\boldsymbol{F_z} = \begin{pmatrix} a - \frac{1}{3}c & b & 0 \\ -b & a - \frac{1}{3}c & 0 \\ 0 & 0 & a + \frac{2}{3}c \end{pmatrix} \qquad (3.22)$$

satisfies the eq. 3.21[155]. The entries of $\boldsymbol{F_z}$ were defined in such a way that a represents isotropic properties and b and c the anisotropy.

By applying e.g. a rotation R_x^{π}, one can see that the signs of c do not change, whereas b does change. This and eq.3.21 show that c observes the axial symmetry along z but also observes symmetry w.r.t. to the xy-plane, since the rotation about the x-axis leads to no change. This fact prompts us to label b as a vector and the terms with c as an uniaxial anisotropy.

Comparing the entries from eq. 3.20 with eq. 3.22 we can see that $\boldsymbol{F} = \boldsymbol{F}^{\dagger}$, i.e. $b^* = -b$, which shows that the vector associated with b does not obey time reversal symmetry. Applying the inversion operation U, yields the same tensor $U\boldsymbol{F_z}U^{-1} = \boldsymbol{F_z}$, thus $\boldsymbol{F_z}$ has even parity, which translates to an even parity of the vector associated with b. Electrical dipoles are odd under inversion, which is easily seen by swapping the position of the opposite charges causing the dipole moment. Magnetic dipoles are caused by current loops. If we invert the position and momentum of the electrons in the current loop, we still get the same magnetic field, i.e. a magnetic dipole has even parity. Attributing oddness in time reversal symmetry and even parity to b lets us identify b as a magnetic moment.*. If we now want to generalize the magnetic moment and put it along an arbitrary direction and not along z, we can define $m_x = \cos(\phi)\sin(\theta)$, $m_y = \sin(\phi)\sin(\theta)$, and $m_z = \cos(\theta)$ to rotate $\boldsymbol{F_z}$ for an arbitrary moment direction by applying the known rotation matrices [157]

$$R_{\phi\theta} = \begin{pmatrix} \cos(\phi) & -\sin(\phi) & 0 \\ \sin(\phi) & \cos(\phi) & 0 \\ 0 & 0 & 1 \end{pmatrix} \cdot \begin{pmatrix} \cos(\theta) & 0 & \sin(\theta) \\ 0 & 1 & 0 \\ -\sin(\theta) & 0 & \cos(\theta) \end{pmatrix}$$

$$\boldsymbol{T_{xyz}} = R_{\phi\theta}\boldsymbol{F_z}(R_{\phi\theta})^T . \tag{3.23}$$

Converting back into Cartesian coordinates, we arrive then at the tensor for a local moment $\boldsymbol{m} = (x, y, z)$ pointing in an arbitrary direction:[149]

$$\boldsymbol{F}_{xyz} = a\begin{pmatrix} 1 & 0 & 0 \\ 0 & 1 & 0 \\ 0 & 0 & 1 \end{pmatrix} + b\begin{pmatrix} 0 & m_z & -m_y \\ -m_z & 0 & m_x \\ m_y & -m_x & 0 \end{pmatrix} + c\begin{pmatrix} m_x^2 - \frac{1}{3} & m_x m_y & m_x m_z \\ m_x m_y & m_y^2 - \frac{1}{3} & m_y m_z \\ m_x m_z & m_y m_z & m_z^2 - \frac{1}{3} \end{pmatrix} \tag{3.24}$$

*This is actually corresponding to the mathematical procedure of decomposition a second rank tensor into a isotropic part , which corresponds to a scalar, a vector and a symmetric traceless part [156]

If we now multiply the polarization vectors in eq. 3.20 with F_{xyz}, we arrive at

$$f_{\mathrm{res}} = a(\boldsymbol{\varepsilon}\cdot\boldsymbol{\varepsilon'^{*}}) + b\boldsymbol{m}\cdot(\boldsymbol{\varepsilon}\times\boldsymbol{\varepsilon'^{*}}) + c[(\boldsymbol{\varepsilon}\cdot\boldsymbol{m})(\boldsymbol{\varepsilon'^{*}}\cdot\boldsymbol{m}) - \frac{1}{3}(\boldsymbol{\varepsilon}\cdot\boldsymbol{\varepsilon'^{*}})] \quad (3.25)$$

This corresponds to the formalism established by Hannon et al., which is widely used throughout the community

$$\boxed{f_{\mathrm{res}} = F^{(0)}(\boldsymbol{\varepsilon}\cdot\boldsymbol{\varepsilon'^{*}}) + iF^{(1)}\boldsymbol{m}\cdot(\boldsymbol{\varepsilon}\times\boldsymbol{\varepsilon'^{*}}) + F^{(2)}(\boldsymbol{\varepsilon}\cdot\boldsymbol{m})(\boldsymbol{\varepsilon'^{*}}\cdot\boldsymbol{m})\,.} \quad (3.26)$$

The prefactors $F^{(0)}$ and $F^{(1)}$ are defined in the original publication [158]. At this point, we can take a brief detour from scattering to look at the effect of a magnetic moment on XAS by applying the optical theorem (eq. 3.19) to eq. 3.29. In forward scattering $\varepsilon = \varepsilon'$ we obtain

$$\frac{d\sigma_{\mathrm{abs}}}{\Omega} \propto F^{''(0)} + \underbrace{iF^{''(1)}\boldsymbol{m}\cdot(\boldsymbol{\varepsilon}\times\boldsymbol{\varepsilon}^{*})}_{\mathrm{XMCD}} + \underbrace{F^{''(2)}(\boldsymbol{\varepsilon}\cdot\boldsymbol{m})(\boldsymbol{\varepsilon}^{*}\cdot\boldsymbol{m})}_{\mathrm{XMLD}}\,. \quad (3.27)$$

Here, the $''$ indicate the imaginary part of the scattering lengths defined in eq.3.26. The second term is only non-zero, if the polarisation is imaginary, i.e. circular. This corresponds to the *X-ray Magnetic Circular Dichroism* (XMCD), which can be used to study element-specific ferromagnetism. The last term corresponds to the effect of *X-ray Magnetic Linear Dichroism* (XMLD), which can be used to directly probe the anisotropy induced by a magnetic ordering. In contrast to XMCD, XMLD can also be used to study antiferromagnets with zero net momentum, since it couples quadratically to $\boldsymbol{m}$.

So far, this section was dedicated to working out mathematical tools for scattering of a magnetic atom. In diffraction, we will observe the interference of multiple atoms, which is given by the structure factor

$$I(\boldsymbol{q}) \propto \left|\sum_{n}(\boldsymbol{\varepsilon'}\cdot\boldsymbol{F}_{\mathbf{res}}\cdot\boldsymbol{\varepsilon})\cdot e^{i\boldsymbol{q}\boldsymbol{r}_{\boldsymbol{n}}}\right|^{2}. \quad (3.28)$$

As mentioned at the beginning of this section, the phase factor is given by the symmetry of the unit cell and determines the selection rules for the charge peaks. Since the moments in a ferromagnetic phase all point in the same direction, their phase factor will be identical and

the resonant reflections are coinciding with charge peak signals. Since charge peaks are usually much more intense, it is experimentally challenging to extract signals from ferro-ordering phenomena. However, antiferromagnetic ordering with alternating moments usually has a lower symmetry than the unit cell, which gives rise to magnetic peaks at positions usually forbidden by the selection rules. At such forbidden positions, the first term in eq.3.24 vanishes, since it is subject to the same selection rules as for charge peaks. The last term is quadratic in $\boldsymbol{m}$ and vanishes for the same reason. Thus, we can focus on the second term, which lets us finally arrive at the widely used formalism to model magnetic scattering for antiferromagnets:

$$I(\boldsymbol{q}) \propto \left| \sum_n \boldsymbol{\varepsilon}' \cdot \begin{pmatrix} 0 & m_z & -m_y \\ -m_z & 0 & m_x \\ m_y & -m_x & 0 \end{pmatrix} \cdot \boldsymbol{\varepsilon}\, e^{i\boldsymbol{q}\boldsymbol{r_n}} \right|^2 \tag{3.29}$$

After some algebra, we obtained with eq. 3.29 the basic toolbox for analyzing the polarisation dependence of a magnetic peak in order to extract the magnetic moment direction. Inspecting eq. 3.29 shows

$$\begin{pmatrix} 0 & m_z & -m_y \\ -m_z & 0 & m_x \\ m_y & -m_x & 0 \end{pmatrix} \cdot \boldsymbol{\varepsilon} = -\boldsymbol{m} \times \boldsymbol{\varepsilon} \perp \boldsymbol{\varepsilon}\,. \tag{3.30}$$

Thus, a magnetic scattering signal is only observed in the channel where $\boldsymbol{\varepsilon}' \perp \boldsymbol{\varepsilon}$. With the definitions for the polarization we choose later (sec. 3.2.2), it follows that for incoming $\boldsymbol{\sigma}$ polarization, we will only detect a signal in the $\boldsymbol{\pi}$ channel for scattering off magnetic peaks.

It is important to emphasize that the form of $\boldsymbol{F}_{\mathbf{res}}$ in eq.3.29 relies on the fact that only the magnetic moment is breaking the spherical symmetry of the electronic wavefunction. As we investigate not free atoms, but atoms located in a crystalline field this is not necessarily true. Lower crystal field symmetries than spherical can invalidate the approximation of eq. 3.29 and require a more involved analysis [157]. This spherical approximation is not necessarily true for Ca_2RuO_4, since the crystal field splitting in the t_{2g} manifold is quite substantial ($\approx 100\,\mathrm{meV}$)[104]. However, it can be shown that moments pointing along the high symmetry directions of a crystal give identical results in the spherical description and models for lower crystal field symmetries.

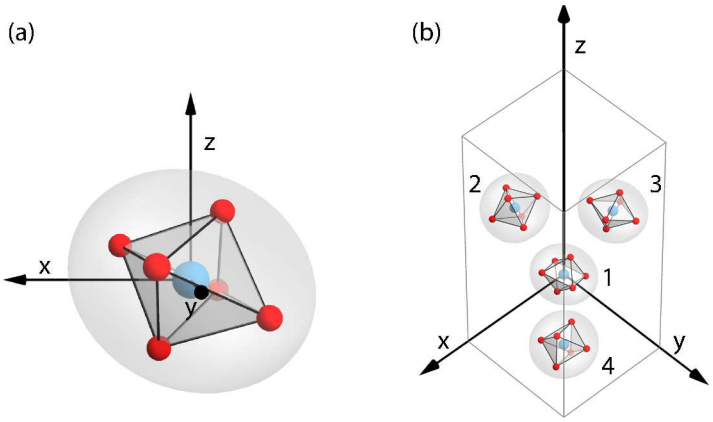

Figure 3.3: (a) Tilted, rotated and compressed RuO_6 octahedron. The grey ellipsoid illustrates the scattering tensor anisotropy. (b) Ca_2RuO_4 unit cell with the Ruthenium atoms at the sites of the 4a Wyckoff position corresponding to the Pbca space group.

3.1.4 Templeton Scattering

One phenomenon leading to resonant peaks that actually precedented resonant magnetic scattering is *Templeton scattering*, a.k.a. *Anisotropic Tensor Susceptibility*[159]. Since the origin is not related to a magnetic ordering and also not strictly speaking to an orbital ordering, it is often seen as a caveat and a nuisance for experiments that often target correlation-driven ordering phenomena. However, disentangling the different possible mechanisms (magnetic order, orbital order or Templeton scattering) behind resonant peaks is non-trivial and requires careful analysis. Ca_2RuO_4 possibly shows all three phenomena necessitating a discussion of Templeton scattering. [125]

As discussed in sec. 2.2, Ca_2RuO_4 exhibits tilted and rotated RuO_6 octahedra, which are related through the symmetry operations of the space group. The phenomenon is best explained by walking through the derivation for the Templeton scattering tensor.

In the most general form, the scattering tensor of an Ru-atom can be written as

$$f_1 = \begin{pmatrix} xx & xy & xz \\ yx & yy & yz \\ zx & zy & zz \end{pmatrix} \tag{3.31}$$

In Ca_2RuO_4, the four Ru sites are related through screw axes given by the symmetry group Pbca [90, 160]. For the anisotropy relative to the coordinate system of the unit cell, only the rotation operation is important, the translation (the different positions of the Ru-atoms) will be taken care of in the structure factor. Consequently, the scattering tensors of the other Ru sites are

$$f_2 = R_z f_1 R_z^{-1} \quad f_3 = R_y f_1 R_y^{-1} \quad f_4 = R_x f_1 R_x^{-1}\,, \tag{3.32}$$

where R_α represents the rotation matrix for a twofold rotation around the respective axis α and the number n of the atom corresponds to the labeling of the positions according to the Wyckoff position 4a of the Pbca space group (Fig. 3.3). By calculating the structure factor at structurally forbidden positions, one realizes that the structure factor indeed can become non-zero:

$$F_{100} = F_{011} = f_1 - f_2 + f_3 - f_4 = \begin{pmatrix} 0 & 0 & 4\text{xz} \\ 0 & 0 & 0 \\ 4\text{zx} & 0 & 0 \end{pmatrix} \tag{3.33}$$

$$F_{101} = F_{010} = f_1 + f_2 - f_3 - f_4 = \begin{pmatrix} 0 & 4\text{xy} & 0 \\ 4\text{yx} & 0 & 0 \\ 0 & 0 & 0 \end{pmatrix} \tag{3.34}$$

$$F_{110} = F_{001} = f_1 - f_2 - f_3 + f_4 = \begin{pmatrix} 0 & 0 & 0 \\ 0 & 0 & 4\text{yz} \\ 0 & 4\text{zy} & 0 \end{pmatrix} \tag{3.35}$$

Since the intensities only comprise off-diagonal elements, we only expect to see this effect in crystals with atoms having anisotropic form factors. CRO exhibits a tetragonal crystal field symmetry or lower due to the distorted octahedra (elongated or compressed). This is reflected in an anisotropy along the diagonal components xx,$yy = xx$ and $zz = xx + \Delta$:

$$f = \begin{pmatrix} xx & 0 & 0 \\ 0 & xx & 0 \\ 0 & 0 & xx + \Delta \end{pmatrix} \tag{3.36}$$

We now apply a rotation along the b-axis ϑ and rotation φ along the c-axis to model the distortions in Ca_2RuO_4. If we assume $\vartheta \approx \varphi$ and

small angles $\vartheta \lessapprox 10°$:

$$f_{\mathrm{Ru}} = \boldsymbol{R}_{c,\varphi}\boldsymbol{R}_{b,\vartheta} f \boldsymbol{R}^{-1}_{b,\vartheta}\boldsymbol{R}^{-1}_{c,\varphi} \approx \begin{pmatrix} \dots & \Delta\vartheta^3 & \Delta\vartheta \\ \Delta\vartheta^3 & \dots & \Delta\vartheta^2 \\ \Delta\vartheta & \Delta\vartheta^2 & \dots \end{pmatrix} . \qquad (3.37)$$

We immediately see that off-diagonal elements appear in the scattering tensor.* As eq. 3.37 shows, due to the tilt along the b-axis, the xz/zx elements are expected to be the largest in the Templeton scattering channel of Ca_2RuO_4, since ϑ<1 rad. This becomes evident in the azimuthal scans which we obtained when investigating Ca_2RuO_4 (sec. 6.2).

3.1.5 Synchrotrons as X-ray Sources

The first magnetic X-ray scattering experiments were conducted with a laboratory X-ray tube source on NiO[161]. However, the experiment were a shear tour-de-force due to the very low intensities of magnetic diffraction peaks (a factor of 1×10^8 lower than charge peaks)†. Synchrotron sources with their higher fluxes provide in principle a better tool to study magnetic peaks, but non-resonant magnetic scattering (see sec.3.1.2) has often only little advantage over neutron techniques and its low cross-section excludes its use for thin films. However, the discovery of resonant X-ray scattering exploiting the energy tunability of synchrotron experiments with its intensity enhancement of a factor of 1×10^6 brought the investigation of magnetism and valence electron phenomena in thin films using X-rays within reach [162]. In this section, we want to briefly review, how synchrotrons are used as a source for high-intensity X-ray beams with high polarisation and energy control. An often used figure-of-merit for X-ray sources is the so called *brilliance*, which defines the photon flux per unit wavelength bandwidth $\Delta\lambda/\lambda = 0.1\,\%$, unit source area and solid angle:

$$\text{Brilliance} = \frac{\text{photons/second}}{(\text{mrad})^2(\text{mm}^2 \text{ source area})(0.1\,\% \text{ bandwidth})} . \qquad (3.38)$$

*The diagonal terms are omitted here, since they don't appear at forbidden peak positions.

†The magnetic scattering detected in this experiment comes from the weak spin-dependent terms, we omitted in eq. 3.7.

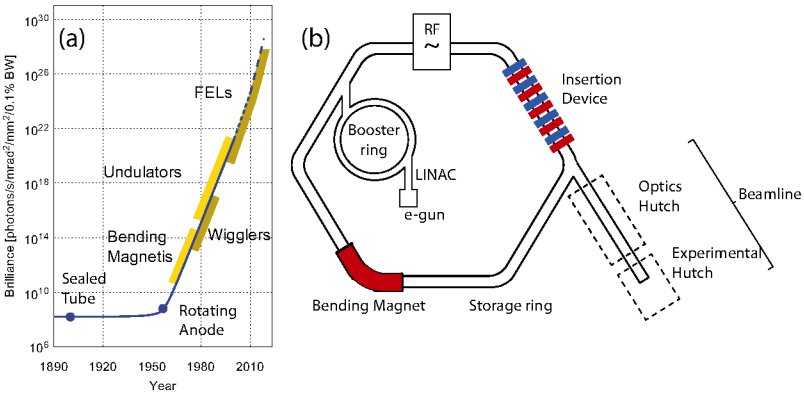

Figure 3.4: (a) Brilliance of various laboratory and synchrotron facility X-ray sources. Adapted from [145]. (b) Basic layout of a modern synchrotron facility.

A comparison of various X-ray sources is shown in Fig. 3.4a: Laboratory sources (sealed tube, rotating anode) are dwarfed by the devices employed at synchrotrons (bending magnet, wigglers and undulators). The fundamental parts of a synchrotron are sketched in Fig. 3.4b. Electrons are emitted in an electron gun and then accelerated in a linear accelerator (LINAC) to about 100 MeV. The electrons are then injected into a booster ring, where they are accelerated further to $\approx 1\,\mathrm{GeV}$ and subsequently injected into the main storage ring. The electrons are accelerated using radio-frequency (RF) cavities and are kept in a stable orbit using various magnets. The magnets curving the electron trajectory between straight sections of the storage ring are called *bending magnets*. The radiation caused by the deflection of the electrons at these points or in more sophisticated magnet arrangements, so called *insertion devices*, is then guided to the experiments (Fig. 3.6). Synchrotron X-ray *beamlines* consist usually of an optics hutch and an experimental hutch. Within the former, the beam is fine-tuned for the experimental requirements, mainly consisting of monochromatization and focusing and the latter hosts the experimental apparatus, e.g. the diffractometer in our case.

The power of the synchrotron lies in the fact that the electrons are accelerated to highly relativistic speeds. With $\beta = v/c$ and $\gamma = 1/\sqrt{1-\beta^2}$, it can be shown that the radiated power of charge moving

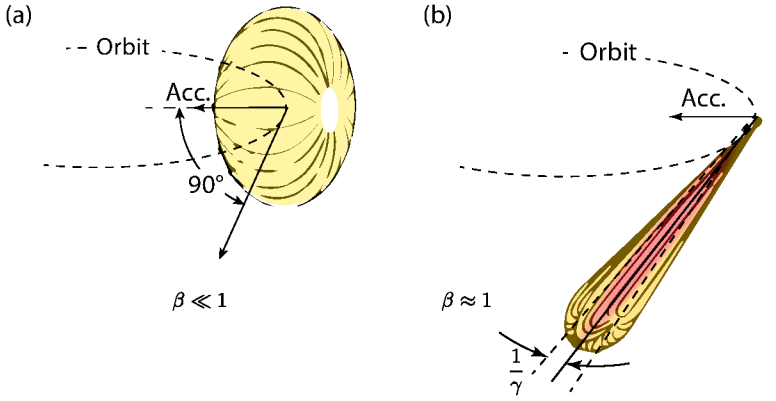

Figure 3.5: Radiation of an relativistic charged particle. (a) Regular dipole radiation at non-relativistic velocity. (b) Highly focused radiation from a particle moving at highly relativistic speeds. Based on [163].

with highly relativistic speed on a circular orbit with a bending radius R yields [164]

$$P_\gamma = \frac{2}{3} r_0 m c^3 \frac{\beta^4 \gamma^4}{R^2} \,. \tag{3.39}$$

Thus, the power increases rapidly with kinetic energy. This energy is radiated at the bending magnets in the curved sections of the synchrotron. The relativistic speeds not only are responsible for high intensity radiation, but also the substantial Lorentz contraction squeezes the dipole radiation into a narrow lobe along the moving direction of the electron (*beaming*), creating a beam with inherently low divergence of $1/\gamma$ (Fig. 3.5). Both factors give rise to the large brilliance of synchrotron radiation.

The latest generation of synchrotrons employs so called *insertion devices* in the straight sections to create even higher brilliance by forcing the electrons on an oscillatory path (Fig. 3.6). One type of insertion devices is a wiggler, which can be thought of as a series of bending magnets as the electron gets deflected similarly at each turn. In this fashion, the intensity relative to a bending magnet is enhanced by $2N$, where N constitutes the number of periods in the oscillation of the electron. In an undulator the turning points of the oscillatory motion are brought so close together that the individual radiation cones

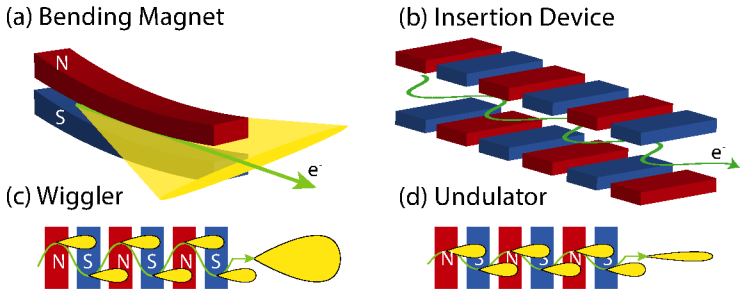

Figure 3.6: (a) Bending magnet and fundamental types of insertion devices (b) wiggler (c) undulator. In a bending magnet, the radiation is spread out in a fan as the electrons trajectory is being deflected by the magnet. A wiggler causes an oscillatory motion of the electrons accumulating radiation intensity at each turn. An undulator squeezes the sinusoidal motion in such a way that the radiation cones overlap and interfere enhancing the flux even further.

interfere with each other boosting the intensity further by a factor of N^2.

The radiation in a bending magnet spreads out in a fan with a divergence of the order of 1°, which is much larger than the natural opening angle of the radiation cone of $1/\gamma$. The horizontal divergence of a wiggler is usually of the order of $10\gamma^{-1}$. Due to the closer packing and interference effects, the spread in an undulator is reduced to $1/\gamma$ or even lower.* The observer at a beam pipe of an experiment sees the radiation appearing as flash when the electron is zipping through the bending magnet and emits radiation due to its deflection. As the pulse duration δt is very short, a broad energy spectrum can be observed (Fig. 3.7). The critical frequency ω_c denotes the high-energy cutoff this spectrum. For a pulse with width δt in the time domain, this results in $\omega_c \approx (1/\delta t)$[165]. In contrast to the continuous† energy spectrum observed at wigglers and bending magnets, the energy spectrum of undulators is bunched up in harmonics due to the interference

*In practice, however, this value is usually not reached since the real divergence is a convolution of electron and photon beam spread.

†The light pulse actually consists of many discrete frequencies corresponding to the fundamental revolution frequency of the electron in the orbit of a circular synchrotron. However, practically, the spectrum of wigglers and bending magnets is continuous due to e.g. fluctuations of the kinetic energy of the electrons [165].

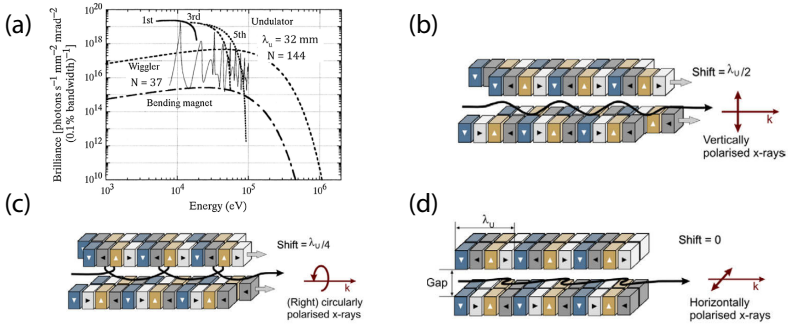

Figure 3.7: (a) Energy Spectra of synchrotron X-ray sources. The spectra for an undulator shows discrete harmonics at a specific gap. The travel range for the harmonics is also indicated which can be reached by changing the gap size of the undulator. Adapted from Ref. [166]. (b), (c), (d) Various arrangements of magnets in a helical undulator to achieve vertical, horizontal and circular polarised light. Taken from Ref. [167].

of radiation cones. Thus, the field strength of the undulator has to be adjusted when changing the incident energy to always select the harmonic with the highest intensity. This is done by changing the vertical gap between the magnetic dipole arrays.

Another beneficial property of synchrotron radiation is its excellent polarization tunability, which is well-suited to study the polarisation dependence of resonant peaks as laid out in eq. 3.29. Due to the planar geometry of the synchrotron ring, the beam is highly polarized in the horizontal plane [164]. This well-defined polarisation state also allows one to tune it either via using phase retarder plates or by introducing horizontal magnetic fields within the insertion device (Fig.3.7).

3.2 Resonant Elastic X-ray scattering at the Ru L-edges

3.2.1 The Choice of the Absorption Edge

Possible absorption edges for performing REXS of Ru-atoms are the K edge at 22.1 keV ($1s \rightarrow 5p$), M edges at 279 eV–585 eV ($3p \rightarrow 4d$)

and L edges at 2838 eV–3224 eV ($2p \rightarrow 4d$)[168].

The criteria for choosing an absorption edge are accessibility to reciprocal space and the resonance enhancement and X-ray cross-section. Also, either the initial state or the intermediate state of the REXS process requires significant spin-orbit coupling to yield spin-polarized states to give sensitivity to spin-ordering in the valence shell.

The M-edges are too low in energy to be able to reach any integer h, k, l-positions in Ca_2RuO_4 and thus not useful for REXS. We note, however, that RIXS (resonant inelastic X-Ray scattering [151]) might be interesting to explore at this energy.

The K-edges are high in energy, thus provide access to a large fraction of reciprocal space, however, the largest contribution to the resonance arises from the transition into the empty 5p shell, since the direct transition into the valence 4d-shell is dipole-forbidden. The 5p-states can still be affected by electronic order phenomena and K-edge REXS experiments have been conducted, even magnetic scattering [169, 170]. Here, one has to rely on the weak spin-orbit coupling in the intermediate 5p states. On one hand, the K-edge allows a simpler operation of an experiment at air since there is no significant air-absorption at this high energy. On the other hand, the X-ray cross section at this high energy is already substantially lower than at the other edges, which is posing a difficulty especially for thin films, where you want to concentrate the diffraction volume close to the sample surface (Fig. 3.1).

The L-edges probe directly the valence 4d shell and excite 2p-states, which due to its proximity to the nucleus have strong spin-orbit-coupling that provides a good spin-polarization to probe spin phenomena in the valence shell. The accessibility to reciprocal space is limited, but integer positions can be reached. The energies are in the intermediate X-ray regime between soft- and hard X-rays, where already substantial air-absorption can be observed. From a technical standpoint, this is the biggest drawback of using this edge: The number of beamlines that reach these energies is limited and most of them are hard-X-ray beamlines, which are not fully optimized for low-energy operation.

Previous reports of REXS experiments on bulk CRO used the K-edge and the L-edges. While the experiment at the K-edge was able to detect ferro-ordering components, it did not find forbidden peaks corresponding to antiferro-ordering [124]. In contrast, the tempera-

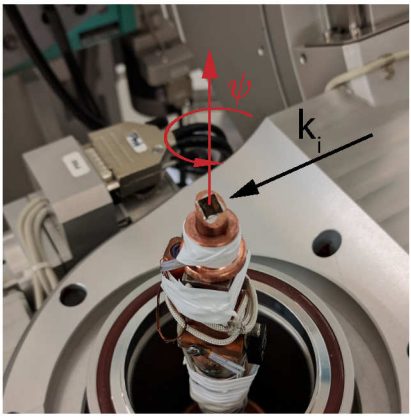

Figure 3.8: Measurement geometry at the Beamline P09 with CRO on LSAO(110) sample sitting on a 24°-wedge. The azimuthal rotation axis and the incoming beam direction k_i is depicted.

ture dependence of forbidden peaks observed at the L-edge clearly showed an intensity increase at the Neel-temperature and strong resonance enhancement of peaks at forbidden positions [125]. Thus, the Ru L2 (2.97 keV) and L3 (2.84 keV) edges were selected to study the antiferromagnetism in CRO thin films.

3.2.2 Azimuthal Scan Technique

The REXS experiments aimed at searching for the presence of forbidden peaks, their temperature dependence and polarisation dependence. To identify the underlying origin of a resonant peak, we perform a polarisation analysis based on the mathematical toolkit we laid out in sec.3.1.3. In the case of a magnetic peak, eq.3.24 was used to determine the magnetic moment orientation. In practice, this polarisation analysis is often conducted by performing a so called azimuthal scan, since few beamlines are equipped with the capability to continuously rotate the incoming polarisation at the Ru L-edges.

Fig. 3.9 and 3.8 illustrate the principle behind this technique using a scan on an a-axis oriented CRO film as an example. In the following, the polarisation will be defined by σ- and π-components. The σ-part is the component perpendicular to the scattering plane, while the π-part is the component parallel to the scattering plane. Since all our experiments were conducted with a vertical scattering plane, the σ-polarisation constitutes the natural polarisation of the synchrotron orbital plane. The scattering condition is kept fixed $\boldsymbol{q} = \boldsymbol{k_f} - \boldsymbol{k_i}$, while

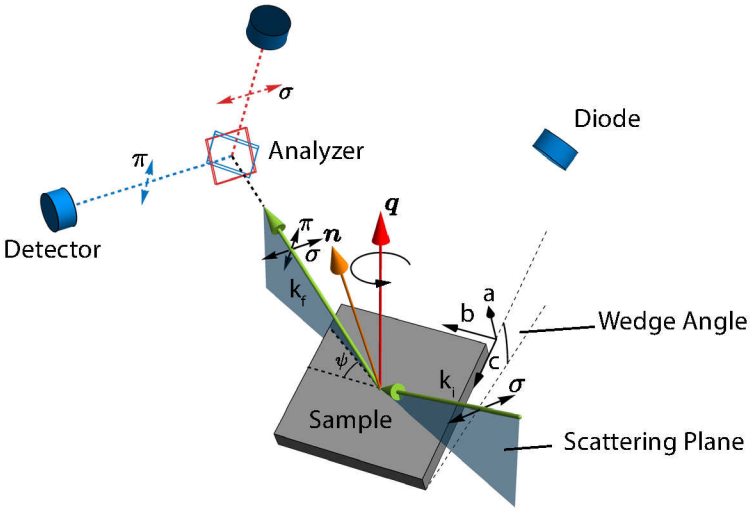

Figure 3.9: Polarisation analysis via azimuthal scan. The polarisation dependence of a reflection $\boldsymbol{q}$ (red) is probed by fixing $\boldsymbol{k_f}$ and $\boldsymbol{k_i}$ (both green) to $\boldsymbol{q} = \boldsymbol{k_f} - \boldsymbol{k_i}$ and rotating the sample around $\boldsymbol{q}$. The incoming synchrotron radiation is σ-polarised and is in this fashion rotated relative to the crystalline directions. The scattering process can turn the polarization giving it a component parallel to the scattering plane (so called π-direction). The σ- and π- components of the scattered beam can be probed separately by employing an analyzer crystal before the detector. The analyzer crystal uses the polarisation dependence of regular Thomson scattering. The illustration depicts the situation during an azimuthal scan of the (101) reflections on one of the a-axis oriented films on LSAO(110) and NCAO(110) with the b- and c-axis in the surface plane of the sample. During such a scan the surface normal $\boldsymbol{n}$ (orange) does not necessarily align with $\boldsymbol{q}$, which gives rise to intensity variations due to geometric and absorption effects (see text). In order to monitor such effects via the X-ray fluorescence signal, a diode was employed for some experiments sitting at 45° relative to the horizontal plane in the picture (the plane perpendicular to $\boldsymbol{q}$).

the sample is being rotated around $\boldsymbol{q}$. In this fashion, only the polarisation direction relative to the crystallographic direction changes. In some experiments, the polarisation of the outgoing beam is studied using an analyzer crystal, which uses the regular polarisation dependence of Thomson scattering to filter out the σ or π component of the outgoing beam. For our experiments, the Si-111 reflection was used. The scattering angle for this at the Ru-L2 edges is $2\vartheta = 83.5°$, so $\cos(2\vartheta)^2 = 0.01$, which constitutes already a significant leakage of one channel in the other. For the experiments at 4-ID-D, no analyzer compatible with the vacuum setup was available. At P09, the scattering with analyzer was conducted at the Ru-L3 edge with $\cos(2\vartheta)^2 = 0.001$. However, during all experiments studying resonant peaks from thin films with polarisation analysis, count rates not larger than 100 counts/sec were recorded making this effect irrelevant for the data analysis. The azimuthal rotation ψ is defined as the angle between a reference vector $\boldsymbol{j} \perp \boldsymbol{q}$ and the scattering plane. As depicted, we usually used the b-axis of the CRO film as $\boldsymbol{j}$. In order to define the polarization vectors, we can start in a frame, where $\boldsymbol{q}$ lies along the z-axis (lab-frame*) and define

$$\boldsymbol{\sigma}_{\mathbf{i}}^{\mathbf{lab}} = (1,0,0) \qquad \boldsymbol{\pi}_{\mathbf{i}}^{\mathbf{lab}} = (0,-\sin(\omega),\cos(\omega)) \tag{3.40}$$

$$\boldsymbol{\sigma}_{\mathbf{f}}^{\mathbf{lab}} = (1,0,0) \qquad \boldsymbol{\pi}_{\mathbf{f}}^{\mathbf{lab}} = (0,\sin(\omega),\cos(\omega))\,, \tag{3.41}$$

where $\omega = \arcsin(q\lambda/4\pi)$, the Bragg-angle for the reflection at $\boldsymbol{q}$. For convenience, we change to the coordinate frame, where the crystal axes are fixed and the polarisation rotates around $\boldsymbol{q}$ (crystal frame). This is performed by first constructing a transformation T that transforms from the crystal frame to the lab frame

$$R_1 = R^v(\boldsymbol{q},\boldsymbol{z}) \quad R_2 = R^v(R_1\boldsymbol{j},\boldsymbol{y}) \tag{3.42}$$

$$R_3 = R_z^\alpha \boldsymbol{z} \quad T = R_3 R_2 R_1 \tag{3.43}$$

Here, $R^v(\boldsymbol{u},\boldsymbol{v})$ denotes the rotation matrix that rotates the vector $\boldsymbol{u}$ into $\boldsymbol{v}$. The beam propagates along $\boldsymbol{y}$ in the lab frame, thus $\psi = 0°$, when $\boldsymbol{j}$ lies within the scattering plane. The transformation into the crystal frame is then simply performed by

$$\boldsymbol{\sigma}_{\mathrm{i}} = T^{-1}\boldsymbol{\sigma}_{\mathbf{i}}^{\mathbf{lab}} \qquad \boldsymbol{\pi}_{\mathrm{i}} = T^{-1}\boldsymbol{\pi}_{\mathbf{i}}^{\mathbf{lab}} \tag{3.44}$$

$$\boldsymbol{\sigma}_{\mathrm{f}} = T^{-1}\boldsymbol{\sigma}_{\mathbf{f}}^{\mathbf{lab}} \qquad \boldsymbol{\pi}_{\mathrm{f}} = T^{-1}\boldsymbol{\pi}_{\mathbf{f}}^{\mathbf{lab}}\,. \tag{3.45}$$

*Strictly speaking, this is not exactly the lab-frame, but the coordinate frame of the φ-circle at the diffractometer.

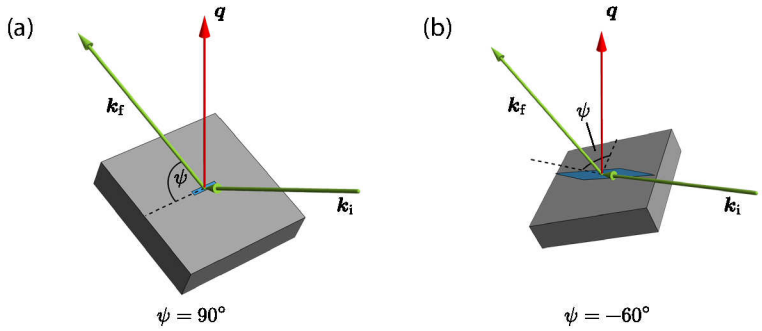

Figure 3.10: Extreme cases of geometric effects during an azimuthal scan of the (101) reflection of an a-axis oriented film on NCAO(110) and LSAO(110). (a) Highest possible incidence angle (50°) with grazing emergence angle showing a relatively small projection of the beam spot (blue). (b) Situation at $\Psi = -60^\circ$ with grazing incidence angle and a beam spot projection close to spillover.

Within the crystal frame, we then naturally have $\boldsymbol{x} \parallel \boldsymbol{a}$, $\boldsymbol{y} \parallel \boldsymbol{b}$ and $\boldsymbol{z} \parallel \boldsymbol{c}$. Generally, the reflections under study do not lie along the direction of the polished face of the substrate, i.e. are non-specular. Thus, the normal $\boldsymbol{n}$ of the surface plane of the substrate is not necessarily along $\boldsymbol{q}$. Hard-X-ray beamlines have the angular degrees of freedom (ϑ and χ) to adjust the sample tilt to keep $\boldsymbol{q}$ on a reflection in reciprocal space. However, the χ-range is restricted by the all-in-vacuum setup necessary to conduct REXS on CRO thin films (see below). Thus, one employs wedges on top of the φ-circle, the motor that performs the ψ-rotation, to tilt the sample surface in order to align $\boldsymbol{q}$ with the rotation axis of φ. Using the wedge, only the φ-motor needs to be rotated and only small adjustments in χ and ϑ have to be made to keep $\boldsymbol{q}$ at the same reciprocal space position.

3.2.3 Geometric and Absorption Effects

During the rotation, the incidence and emergence angle relative to the sample surface can change dramatically. As an example, the 101 reflection studied on the a-axis-oriented films required a wedge of $\omega = 24^\circ$, while $2\vartheta = 49.95^\circ$ and $\vartheta = 24.97^\circ$, i.e. the incident angle and correspondingly the exiting angle will vary between $\vartheta + \omega = 49^\circ$ and $\vartheta - \omega = 0.9^\circ$. These large changes in the incident and exiting angles

lead to substantial geometric and absorption effects on the intensity during an azimuthal scan [171] as we will show in the following. The penetration power of the X-rays at low-energies is dominated by the absorption process (sec. 3.1.1). X-ray absorption of photons travelling through matter with an energy-dependent attenuation length δ can be described by the Lambert-Beer-Law

$$I(x) = I_0 \exp\left(-\frac{x}{\delta}\right) , \tag{3.46}$$

where $I(x)$ denotes the intensity at the location x within the sample and I_0 the initial intensity before entering the sample. The penetration depth within the substrate and film is $\delta \approx 1\,\mathrm{m}$ at the Ru L edges, so for our films with $d_{\mathrm{film}} \approx 50\,\mathrm{nm}$, $\delta \gg d_{\mathrm{film}}$ (see also appendix A). Thus, the ratio of the volume of the film filled with photons relative to the total volume of photons within the sample varies with the incidence angle. As illustrated in Fig.3.11, $x_{\mathrm{in}}/(x_{\mathrm{in}} + x_{\mathrm{sub}}) = x_{\mathrm{in}}/\delta \propto 1/\sin(\alpha)$. This leads to an intensity modulation during an azimuthal scan, where $\boldsymbol{q} \nparallel \boldsymbol{n}$: grazing angles enhance the scattering of the film, while steeper incidence angles decrease the intensity. In addition, the projection of the beam spot scales as well with $\propto 1/\sin(\alpha)$ (Fig. 3.10). While the beam footprint change itself does not modify the intensity (the photon density does not change), it can lead to a spillover of the footprint off the sample surface, which can lead to a sudden drop in intensity at grazing incidence. The beam path within the film x_{s} can also substantially vary during an azimuthal scan. Since $\beta = 2\theta - \alpha$, we simply have

$$x_{\mathrm{s}}(\alpha, z) = x_{\mathrm{in}} + x_{\mathrm{out}} = z\left(\frac{1}{\sin(\alpha)} + \frac{1}{\sin(2\theta - \alpha)}\right) , \tag{3.47}$$

where z is the vertical axis perpendicular to the surface. At low angles, the beam path can in fact be longer than δ and the scattering volume can be completely located in the film. This leads to absorption effects of the beam intensity while it is penetrating through the film. This effect causes an additional modulation of the intensity when the beam is either exiting with a grazing angle or entering with a grazing angle. The absorption within the sample can be described by

$$\frac{I_{\mathrm{out}}(\alpha)}{I_{\mathrm{in}}} = \frac{1}{d}\int_0^d \exp\left(-\frac{x_{\mathrm{s}}(\alpha, z)}{\delta}\right) dz\,. \tag{3.48}$$

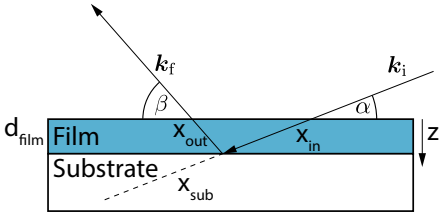

Figure 3.11: Illustration showing the geometry when scattering off a thin film grown on a much thicker substrate. The ratio x_{in}/x_{sub} can vary considerably with incidence angle α modulating the volume of the film exposed to the X-rays. The beam path length within the film varies with incidence angle α and emergence angle β giving rise to additional absorption effects.

The absorption effects and the volume change of the X-ray interaction volume within the film constitute effects that are fairly predictable assuming quantities such as the film thickness and penetration depth are well known. However, the beam spillover effect depends on the position of the beam on the sample and the dimensions of the sample, which either are hard to determine exactly from the experiment or would add unwanted additional degrees of freedom to theoretical models used to fit of the azimuthal dependence. After Ru-L-edge experiments, substantial surface contamination was found by inspecting the sample surface by eye. This is likely due to residual gases within the all-in-vacuum setups reacting with the high-intensity X-ray beam(sec.3.2.4). For low intensity reflections, such surface contaminants can add significant additional intensity variations during an azimuthal scan, which is impossible to model without prior knowledge of the exact nature of the contaminants. Several strategies exist to access the intrinsic polarisation dependence of the scattering tensor and to avoid the influence of extrinsic factors. One method is to model the ratio of two polarization channels. With a helical undulator, one can conduct two azimuthal scans with incoming σ and π polarization and then calculate the ratio [172]. No beamline used in our experiments has this capability, however. Resonant non-magnetic peaks can show σ-σ and σ-π scattering, which can be disentangled using a polarisation analyzer. In such cases, it is possible to use their ratio to get a value unaffected by the extrinsic effects mentioned above. However, using the ratio also suffers from some drawbacks: The dipolar ($\propto \sin(\psi)^2$) or quadrupolar ($\propto \sin(2\psi)^2$) dependences encountered in our systems naturally have zeros. In proximity to those, errors generally become amplified and the ratio diverges to infinity (sec. 6.2.3). Effectively,

this makes models for the ratio less distinct and complicates the analysis.

For some experiments, we employed using the X-ray fluorescence (XRF) signal as a normalization(see sec. 3.1.2). The XRF signal has the advantage that is it being subjected to similar absorption and geometric effects as the scattering signal, but its polarization dependence is small*. It can be measured simultaneously with the scattering signal and can be even used for resonant magnetic peaks, where only the $\sigma - \pi$ polarisation channel is available and thus no $\sigma - \sigma$ can be used for the normalization. The fluorescence originates from a beam impinging with the energy tuned to the Ru-L absorption edges. It is emitted after a de-excitation from an occupied state below the absorption line energy to the core-hole-level. The fluorescence radiation thus has energies below the actual absorption edge. Since the incident energy is set to the Ru-L-edges, the dominant contribution to the fluorescence is by the Ru L-emission lines (L-α, L-β and L-γ). The emission line that should give the largest absorption effect is the $L\beta 1$ (2683 eV) line, that is the highest in energy with the lowest penetration depth [173].† Thus, for the XRF signal the penetration depth is larger with $\delta_{\mathrm{Fl}} \approx 3\,\mathrm{m}$ (see appendix A).

3.2.4 Beamlines / All-in-Vacuum Setup

The experiments were conducted at the bending-magnet beamline BM28 at the European Synchrotron Radiation Facility (ESRF), Grenoble [174], and the undulator beamlines 4-ID-D at the Advanced Photon Source (APS), Chicago and P09 at the Deutsches Elektronen-Synchrotron (DESY), Hamburg [175]. Extensive technical details regarding 4-ID-D can be found in the theses by Bohnenbuck and Zegkinoglou [176, 177], regarding BM28 in Ref. [174] and regarding P09 in Ref. [175]. We want to focus here on the technical modifications allowing a low-energy operation. The setups are hard X-ray beamlines that normally operate with a beam path mostly in air. However, the air absorption is already significant at the Ru L edges

*The XRF is proportional to the XAS, which can show dichroism. However, this effects are typically smaller than the geometric or absorption effects. In CRO the films, we could not find any evidence for dichroism in the XAS (see appendix A).

†The $L-\gamma 1$ is even higher, but its relative strength is insignificant [173].

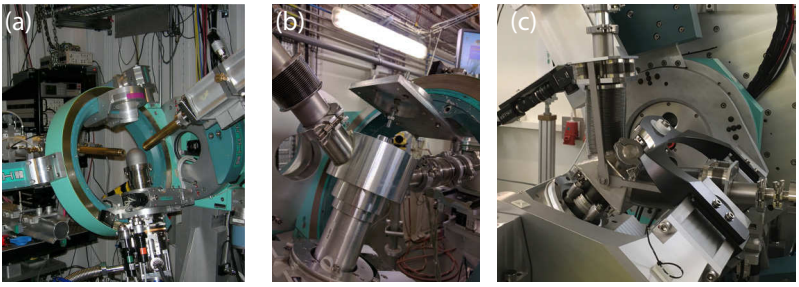

Figure 3.12: Modifications to the beamline setups to allow operation with minimal air absorption. (a) Conventional setup employed at 4-ID-D used for earlier single-crystal experiments (taken from [176]). A Be-dome seals the insulation vacuum at the cryostat. The rest of the beam path is mostly evacuated or filled with He to reduce absorption. The vacuum pipe of the incoming beam and the pipe leading to the detector are not connected to the sample chamber allowing a large angular range. (b) Vacuum chambers used at BM-28 and part of 4-ID-D experiments used within this work. (c) Vacuum chamber employed at P09. The option depicted in (c) allows for higher flexibility in ϑ and 2ϑ and has separate KF-25 flanges for attaching e.g. a diode.

(90 % attenuation over 10 cm of air [178]). The high intensity of reflections studied in previous scattering experiments on CRO single crystals allowed to keep a small part of the beam path in air. This permitted the use of a conventional Be-dome setup for creating the insulation vacuum needed to cool the sample to cryogenic temperatures (Fig.3.12). The incoming and outgoing beam pipe are not connected to the Be-dome allowing a high flexibility in the angular ranges, since the cryostat with the sample can be moved independently of the detector arm. However, trials with a 250 m thick Be-dome showed that too much flux is absorbed for studying resonant peaks coming from thin films. This prompted us to use all-in-vacuum setups developed at P09 and BM28 to mitigate air absorption for low-energy experiments. The vacuum of the incoming beam pipe is directly connected to the vacuum chamber of the sample (Fig. 3.12). Another vacuum flange at the sample vacuum chamber allows to connect a bellow towards the detector or polarisation analyzer. Using this experimental apparatus, the beam travels from the synchrotron to the detector with no or minimal air path and minimal number of Be-windows. Only the increased flux by using this method enabled the study of resonant peaks on thin films. The drawback of using such a system are the rigid vacuum con-

nections surrounding the sample chamber, which can severely restrict the accessible angular ranges. The BM28-type vacuum chamber had to be custom-made to access specific ϑ and 2ϑ Bragg angles, which is a time-consuming process if multiple reflections with different angles need to be investigated during one beam time.

In such a mode of operation the volume that needs to be evacuated is much larger and includes many parts that are not specified for ultra-high vacuum (e.g. slit systems). This resulted generally in relatively high pressures close to the sample($\approx 1 \times 10^{-3}$ mbar–1×10^{-4} mbar). The vacuum was sufficient to insulate the sample and reduce the air absorption, however we experienced sudden losses of intensity at temperatures comparable to the coldfinger of the cryostat ($\lessapprox 10$ K) we related to the condensation of residual gases on top of the sample. The loss of intensity also occurred several times even at higher temperatures, which likely were caused by small leaks that appeared after motor movements. Eg, the rotation of the φ-motor is most vulnerable in this respect, since it is only sealed with O-rings and vacuum grease.* In fact, all samples (even single crystals) had a visible residue on top after the experiment, which appears to originate from a reaction of the X-ray beam with condensed residual gases on top. Test measurements in the MARES soft-X-ray scattering chamber at the BL29 beamline at ALBA, Barcelona, under UHV-conditions did not yield a discoloring of the surface corroborating the idea of a bad vacuum as the underlying reason for the contamination. An intensity loss coming from condensation was identified via its time-dependence. The fluorescence signal proved also to be very useful to monitor for such condensation effects.

*In the conventional setup, the Be-dome can rotate with the sample. Using the all-in-vacuum setup, the vacuum chamber is kept being fixed, while the sample and the cryostat rotates. At the joint of both parts, the "bearing" is vacuum grease surrounding an O-ring. It can be easily seen that the chamber could lose its sealing capability under rotation at this point.

3.3 Beta-detected Nuclear Magnetic Resonance

3.3.1 Nuclear Energy Levels and Resonance

Nuclear Magnetic Resonance (NMR) has evolved to a versatile tool to study the dynamics of internal magnetic and electric fields in solids. It has found widespread application in physics, chemistry and medicine [96]. Conventional NMR requires typically $\approx 10^{17}$ nuclei in order to achieve good sensitivity, which rules out thin films (usually $\leq 10^{15}$ atoms) as samples for this technique. βNMR is a technique which greatly enhances this sensitivity to a lower limit of $\approx 10^{8}$ atoms, which lies well in the range for surfaces and thin films. [179] This section will briefly introduce the fundamentals of both techniques and how they are used to study order phenomena in Ca_2RuO_4 thin films. This section follows the classic NMR books by Abragam, Slichter, Cowan and Blundell. [96, 103, 180, 181]

The interaction and the size of nuclear moments is so weak that they can always regarded to be paramagnetic in the temperature ranges for phenomena related to the electrons ($>1 \times 10^{-7}$ K)[103].Thus, by applying a magnetic field, a lifting of the degeneracy of the nuclear energy states can be induced via the Zeemann effect. In contrast to the electron, nuclei can have non-spherical electric fields exhibiting an electric quadrupolar moment. It can be shown that this holds for nuclei with a spin $I \geq 1$[103]. The fact, that the probe of beta-NMR, ^{8}Li, exhibits $I = 2$, prompts the discussion about the effects of the coupling between a quadrupolar moment and electric fields.

Since its center of mass and charge are identical, a nucleus has generally no electric dipole moment. However, the existence of an electric dipole could have some interesting implications regarding PT-symmetry in particle physics prompting multiple experiments to measure it, but so far all of them turned out not be able to detect an electric dipole moment [182, 183].

The Zeemann coupling evenly splits the degenerate energy levels of a nucleus with a given nuclear magnetic moment $\boldsymbol{\mu}$ and spin I by the magnetic energy according to

$$\Delta E_m = -\boldsymbol{\mu} \cdot \boldsymbol{B_0} = -g\mu m_I B_0, \tag{3.49}$$

where g is the gyromagnetic ratio of the positively charged nucleus and m_I the magnetic quantum number. Since a quadrupole is a tensor

quantity, the derivation of its effects on the energy levels is more involved. We will provide a brief sketch here collecting the derivations from standard literature [96, 103, 180, 181]. Starting with classical electrodynamics, the electric energy of a charge distribution ρ in a potential $V(\boldsymbol{r})$ can be described by

$$E = \int \rho(\boldsymbol{r}) V(\boldsymbol{r}) d^3\boldsymbol{r}. \tag{3.50}$$

Using the usual Taylor series expansion, we can rewrite this to

$$E = \int \rho(\boldsymbol{r}) \left[V_0 + \sum_{\alpha=x,y,z} \left(\frac{\partial V}{\partial r_\alpha} \right)_0 r_\alpha \right. \tag{3.51}$$

$$\left. + \frac{1}{2} \sum_{\alpha,\beta=x,y,z} \left(\frac{\partial^2 V}{\partial r_\alpha \partial r_\beta} \right) r_\alpha r_\beta + \ldots \right] d^3 r. \tag{3.52}$$

Since nuclei do not have electric dipole moments (see above), the second term vanishes. The first term corresponds to a monopole and does not yield a line splitting. Using the conventional definition of the electric quadrupole tensor

$$Q_{\alpha\beta} = \int \rho(\boldsymbol{r})(3 r_\alpha r_\beta - \delta_{\alpha\beta} r^2) d^3 r \tag{3.53}$$

one arrives at

$$E_{Quad} = \frac{1}{6} \sum_{\alpha,\beta=x,y,z} \left(\frac{\partial^2 V}{\partial r_\alpha \partial r_\beta} \right)_0 Q_{\alpha\beta} + \frac{1}{2} \sum_{\alpha=x,y,z} \left(\frac{\partial^2 V}{\partial r_\alpha^2} \right) \int \rho(\boldsymbol{r}) r^2 d^3 r. \tag{3.54}$$

Due to Laplace's equation, $\nabla^2 V = 0$, the second term vanishes. The calculation has been purely classical so far. In order to see the role of the quantization of I, we can invoke the Wigner-Eckart-theorem, which allows us to replace $Q_{\alpha\beta}$ with its quantum mechanical counterpart. In essence, one uses the commutation relation of angular momentum and position operator. We define the components of the total nuclear angular momentum as

$$I_\alpha = \sum_k \boldsymbol{l}_{\alpha,\mathrm{k}} + \boldsymbol{s}_{\alpha,\mathrm{k}} \quad \text{with} \quad \alpha = x, y, z\,. \tag{3.55}$$

Here, we are summing over the protons of the nucleus. Now the commutation relations

$$[I_x, y_k] = iz_k \quad [I_y, z_k] = ix_k \quad [I_z, x_k] = iy_k \tag{3.56}$$

can be used to transform eq. 3.53 to (details can be found in Ref. [180])

$$Q_{\alpha\beta} = \frac{eQ}{I(2I-1)} \left(\frac{3}{2}(I_\alpha I_\beta + I_\beta I_\alpha) - \delta_{\alpha\beta} I^2 \right) \tag{3.57}$$

where Q is the scalar quadrupolar moment. In analogy to eq. 3.54 we can define the Hamiltonian

$$H_Q = \frac{1}{6} \sum_{\alpha,\beta} V_{\alpha\beta} Q_{\alpha\beta} \,. \tag{3.58}$$

This is further simplified by transforming into a coordinate frame using a set of principle axes, where the tensor $V_{\alpha\beta} = \partial^2 V / \partial(r_\alpha \partial r_\beta)$ is diagonal. In this frame, eq. 3.58 becomes

$$H_Q = \frac{eQ}{6I(2I-1)} \left[V_{xx}(3I_x^2 - I^2) + V_{yy}(3I_y^2 - I^2) + V_{zz}(3I_z^2 - I^2) \right] \tag{3.59}$$

Using the Laplace equation $\sum_\alpha V_{\alpha\alpha} = 0$ we can simplify further to

$$H_Q = \frac{eQ}{4I(2I-1)} V_{zz} \left((3I_z^2 - I^2) + \eta(I_x^2 - I_y^2) \right) \tag{3.60}$$

Here, we have introduced the asymmetry parameter $\eta = (V_{xx} - V_{yy})/V_{zz}$. By convention $|V_{zz}| \geq |V_{xx}| \geq |V_{yy}|$[103]. V_{zz} or other components $V_{\alpha\beta}$ are often denoted as the *electric field gradient (EFG)*.

From this discussion, we see that subjecting a nucleus to magnetic or to electric field gradients (in the case of $I \geq 1$) leads to a splitting of its energy levels. The case of an axially symmetric EFG with $\eta = 0$ leads to the scenario for ^{8}Li depicted in Fig. 3.13. Now that we established the influence of magnetic and electric fields on the nuclear energy levels, we will address the resonance part of NMR. It is instructive to start from a simple two-level system in a magnetic field, e.g. $I = 1/2$ (Fig. 3.14). We label the upper level with + and the lower one with −. If we now drive this system with an electromagnetic excitation, we induce excitations from the lower level to the higher level

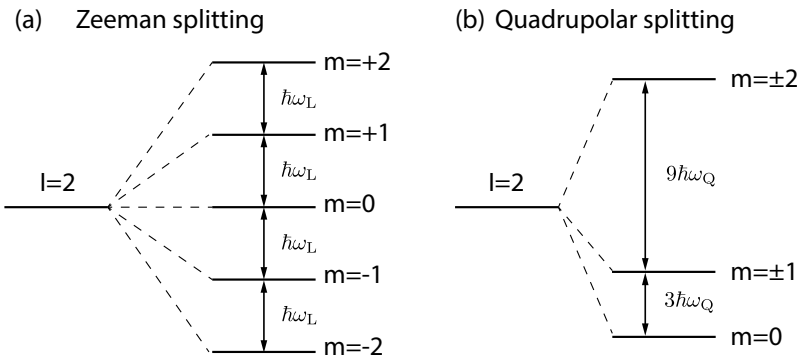

Figure 3.13: Energy level splitting for ^{8}Li in a magnetic and electric field gradient. (a) Zeeman-Splitting for ^{8}Li with $\hbar\omega_L = g\mu_N B_0$ (b) Quadrupolar splitting in zero magnetic field with $\hbar\omega_Q = eQV_{zz}/24$.

and vice versa with an equal probability W.* We can now define the following equations for the occupations:

$$\frac{dN_+(t)}{dt} = WN_-(t) - WN_+(t) \tag{3.61}$$

$$\frac{dN_-(t)}{dt} = WN_+(t) - WN_-(t) \tag{3.62}$$

If we now define a population difference of $n(t) = N_+(t) - N_-(t)$, it is straightforward to solve for

$$n(t) = n(0)e^{-2Wt}. \tag{3.63}$$

This basic result tells us that an external excitation resonant to the energy level difference gets absorbed and destroys the population difference $n(t)$. The measurements of the absorption of the nuclear energy levels is the heart of most NMR techniques: Scanning the absorption lines, measuring their positions and shape and detecting their time-dependence. This allows to extract the internal fields acting on the studied nuclei. Since these quantities are sensitive to microscopic details, they are often used as a fingerprint for chemicals. The energy scale for measuring the nuclear absorption lies in the radio frequency

*This equivalence is a natural consequence of Fermi's golden rule and the fact that the perturbing Hamiltonian $< \psi_-|H'|\psi_+ >$ is hermitian

(RF) spectrum, which makes this spectroscopic method technically very accessible, since one can use electronic oscillators to generate RF waves and monitor the absorption via induction coils [96]. This induction method corresponds to the standard NMR-experiment conducted on bulk materials. If this two level system is free from external perturbation and in thermal equilibrium in a static magnetic field $\boldsymbol{B_0}$, the system will exhibit a weak Boltzmann-distributed spin-polarisation ($\Delta E \ll k_B T$) giving

$$\frac{N_+}{N_-} = \exp\left(\frac{-\hbar\omega}{k_B T}\right) \tag{3.64}$$

If we now e.g. apply a pulse at the resonance condition we will reduce the polarisation to some extent and the system will tend to relax back to the thermal equilibrium. In this situation the transition rates from the lower state to the higher state $W_\uparrow$ and the other direction $W_\downarrow$ are not equal anymore, since this would not create the initial polarization. If we define $N = N_+ + N_-$, we can now rewrite eq. 3.62 to

$$\frac{dn}{dt} = N(W_\uparrow - W_\downarrow) - n(W_\uparrow + W_\downarrow). \tag{3.65}$$

This equation can be solved to

$$n(t) = n_0 + Ae^{-t/T_1} \tag{3.66}$$

with a constant A and

$$n_0 = N\left(\frac{W_\uparrow - W_\downarrow}{W_\uparrow + W_\downarrow}\right) \qquad \frac{1}{T_1} = (W_\uparrow + W_\downarrow). \tag{3.67}$$

Eq. 3.66 describes the exponential relaxation of the system to its equilibrium state with a population n_0. The time constant T_1 is the so called spin-lattice relaxation rate and the key quantity that was measured in the course of this thesis. It represents the time scale for the spin polarization to reach thermal equilibrium. Since this corresponds to the nuclear spin component along the quantization direction I_z, this is also called the longitudinal relaxation.

To address the vectorial nature of the interaction between spin and B-field, one can use a quantum-mechanical approach (as we did above) or a classical approach. The quantum mechanical approach is certainly more accurate, i.e. it contains the interaction of the electric

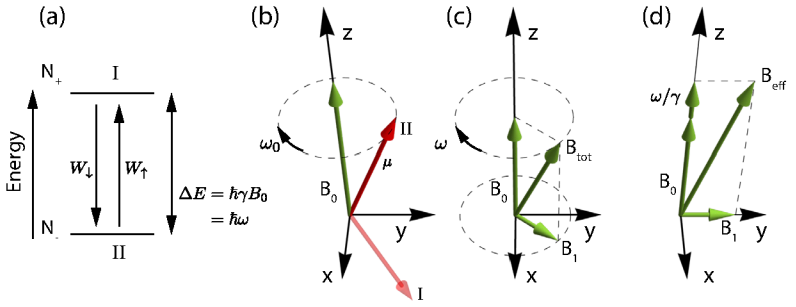

Figure 3.14: (a) Simple Two-Level system to introduce the concept behind NMR (b) Classical view of precession of a magnetic moment $\boldsymbol{\mu}$ in a static magnetic field $\boldsymbol{B_0}$. (c) Static field $\boldsymbol{B_0}$ and oscillating field $\boldsymbol{B_1}$ in the laboratory frame (d) Fields in the rotating frame. After Ref. [181]

quadrupole, but we will use the classical approach, since it allows a more intuitive approach to understand the dynamics of a magnetic dipole in magnetic field. Classically, the equation of motion of a magnetic moment μ in a static magnetic field $\boldsymbol{B_0}$ is described by

$$\dot{\mu} = \gamma \boldsymbol{\mu} \times \boldsymbol{B}\,, \tag{3.68}$$

where γ is the gyromagnetic ratio. Putting $\boldsymbol{B_0}$ along the z-direction, gives the following solutions

$$\begin{aligned} \mu_x(t) &= \mu_x(0)\cos(\gamma B_0 t) \\ \mu_y(t) &= -\mu_x(0)\sin(\gamma B_0 t) \\ \mu_z(t) &= \mu_z(0) = \text{const}\,. \end{aligned} \tag{3.69}$$

The moment will preserve its component along the z-axis, but will start to precess in the xy-plane around the magnetic field B_0 with the so called Larmor frequency $\omega_0 = \gamma B_0$ (Fig. 3.14b). This frequency corresponds exactly to the Zeeman splitting discussed above (eq.3.49) and μ_z to the population difference in the nuclear energy levels. From the cross-product in eq.3.68 we can see that M_z can only manipulated by transverse fields in the xy-plane. The fact that a transverse field $\boldsymbol{B_1}$ oscillating at the Larmor frequency ω_0 manipulates the population difference can also be understood by switching to the rotating frame of reference: If one transforms from a laboratory frame to a frame

rotating with $\boldsymbol{B_1}$ oscillating at ω, the effective stationary field sensed by the precessing nucleus is $\boldsymbol{B}_{\text{eff}} = \boldsymbol{B_1} + (\boldsymbol{B_0} + \boldsymbol{\omega}/\gamma)$[181]. Thus, if one tunes the frequency of $\boldsymbol{B_1}$ to ω_0 and, then $\boldsymbol{B}_{\text{eff}} = \boldsymbol{B_1}$, since $\boldsymbol{B_0} = -\boldsymbol{\omega_0}/\gamma$. The moment $\boldsymbol{\mu}$ will start precessing in a plane perpendicular to $\boldsymbol{B_1}$ effectively eliminating μ_z. This effect is widely used for pulsed NMR techniques. Here, sophisticated pulse sequences perturb the system away from equilibrium to e.g. start relaxation processes to extract T_1. To include relaxation effects in eq. 3.68, one expands to [96]

$$\begin{aligned} \dot{\mu_x}(t) &= \gamma|\boldsymbol{\mu} \times \boldsymbol{B}|_x - \frac{\mu_x}{T_2} \\ \dot{\mu_y}(t) &= \gamma|\boldsymbol{\mu} \times \boldsymbol{B}|_y - \frac{\mu_y}{T_2} \\ \dot{\mu_z}(t) &= \gamma|\boldsymbol{\mu} \times \boldsymbol{B}|_z + \frac{\mu_0 - \mu_z}{T_1}\,. \end{aligned} \tag{3.70}$$

These equations are known as *Bloch equations*. Here, we introduced a relaxation times T_2 for the precession in the xy-plane. T_2 is also called transverse relaxation rate or spin-spin-relaxation rate. This decay may appear as surprising at first, since the μ_x and μ_y are perpendicular to B_0 and thus it cost no energy to precess. However, one usually measures an ensemble of spins. The coherence among these nuclei can get destroyed due to a dephasing by to e.g. molecular motion, dipolar interaction or inhomogeneous external magnetic fields resulting in a decay of μ_x and μ_y, hence the name spin-spin-relaxation rate.

3.3.2 βNMR-NMR Detection through β-decay

The seminal discovery of Chien-Shiung Wu in 1957 confirmed the theoretical work of Lee and Yang the β-decay of $^{60}_{27}$Co violates parity [185, 186]. It was found that the emission of the leptons electron involved in the decay is correlated with the spin polarization of the parent $^{60}_{27}$Co radionuclide. Soon after this discovery, it was realized that the muon, which also undergoes a β-decay, could be used as an NMR-probe for magnetism in materials, a technique that is now commonly known as *muon spin rotation and relaxation* (μSR). [187] The idea being that the muon is implanted into a sample, it senses the internal fields in the sample, it undergoes β-decay and then the direction of the emitted positron can be used to probe the amplitude and time-evolution of

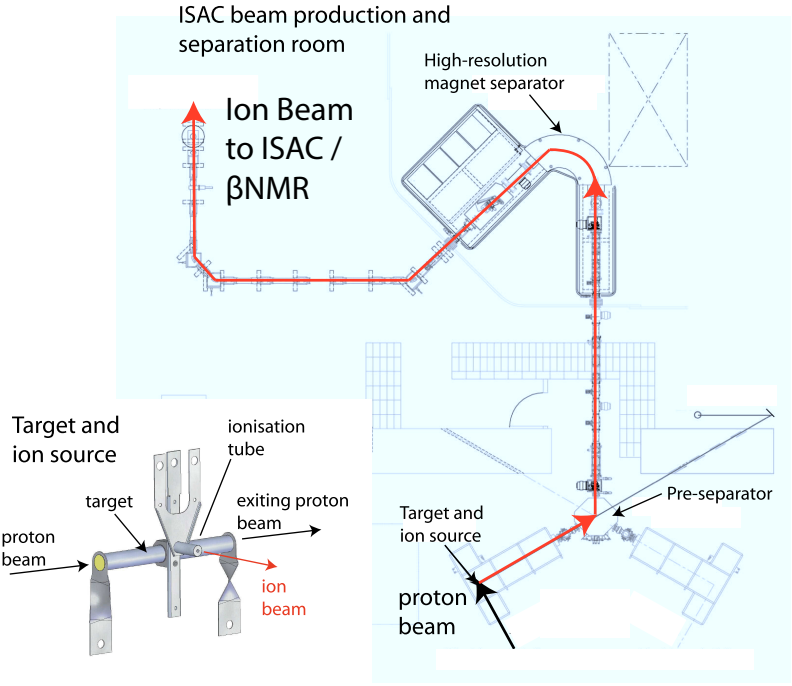

Figure 3.15: Ion production and separation at ISAC, TRIUMF. The proton beam coming from the cyclotron is injected into a target, where the radioactive isotopes are formed. The nuclei are ionized and guided toward magnetic mass separators. Subsequently they are guided to the experimental endstations. Taken from Ref. [184].

the magnetization of the muon, since the direction of the positron and the spin of the muon are coupled through the parity violation in the decay. The advantages were immediately clear: Highly spin-polarized muons can be produced by Pion decay* at cyclotrons without the need of a high magnetic field $\boldsymbol{B_0}$ as in a regular NMR setup. Their gyromagnetic ratio $\gamma = 135.5\,\mathrm{MHz\,T^{-1}}$ is high due to their low mass yielding high sensitivity to magnetic fields†. The muon is a $S = 1/2$ particle and thus has no quadrupolar moment, making it only sensitive to magnetic fields, which is often seen as an advantage in the interpretation of data when investigating magnetism. Since not all nuclei have a nuclear moment, it is often necessary to replace atoms with NMR active isotopes, e.g. ^{16}O by ^{17}O, which can disturb the system. A muon can be simply implanted in a sample and decay fully without leaving impurities. However, usual muon beams have an energy of 4 MeV giving a much too high penetration depths of the order of 1 mm to study thin films. This obstacle can be overcome by sophisticated beam conditioning (low-energy μSR) , but only with low flux and relative large lateral sample dimensions are required (typically a mosaic of four 10 mm x 10 mm substrates)[188].

The βNMR-technique used in this work is similarly exploiting the asymmetry of the β-decay of radioactive ^{8}Li in order to conduct NMR experiments. Here, a spin-polarized $^8\mathrm{Li}^+$ ion is implanted into to sample and decays anisotropically into $^8_4$Be and an electron and antineutrino. The $^8_4$Be subsequently fully decays into two α particles.

The experiments were conducted at the TRIUMF Isotope Separator and Accelerator (ISAC) facility. A proton beam is accelerated up to 500 MeV and directed onto a production target, where nuclear spallation reactions create various isotopes. For ^{8}Li, the target is typically made of a tantalum, which can be kept at high temperatures exceeding 2000 K to improve the diffusion of the isotopes out of the target. The so produced isotopes are then ionized and purified by a magnetic mass separator. Electrostatic optics guide the radioactive ion beam (RIB) toward to experimental endstation (Fig. 3.15). In contrast to muons, the RIB is not naturally polarized. For this, a sophisticated optical pumping scheme is employed that exploits the

*The pion decay is in itself also a β decay yielding a polarization of the muon.

†For comparison, ^{17}O, a frequently used NMR-isotope, exhibits $\gamma = -5.77\,\mathrm{MHz\,T^{-1}}$.

Probe	I	$T_{1/2}$ (s)	γ(MHz T^{-1})	Asymmetry	Production Rate (ions/s)
μ	1/2	2.2×10^{-6}	135.5	0.33	10^4 (low energy)
^{8}Li	2	0.84	6.013	0.33	10^8
^{11}Be	1/2	13.8	22	0.02	10^7
^{15}O	1/2	122	10.8	0.7	10^8

Table 3.1: Radioactive isotopes suitable for βNMR that can be produced at ISAC in comparison with the characteristics of a low-energy muon setup. The columns contain the nuclear moment I, half-life $T_{1/2}$, gyromagnetic ratio γ, the asymmetry (corresponding to A in eq. 3.72) and production rate. Sources:[190–193]

hyperfine coupling between the electrons and the nuclei of ^{8}Li [189]. In principle, the ISAC facility can also produce other isotopes that can be used as a βNMR–probe, but in comparison clear advantages of ^{8}Li become evident (Tab.3.1). While ^{11}Be and ^{15}O have $I = 1/2$ and thus have simpler NMR spectra as ^{8}Li, they can either be only poorly polarized or have long half-lives making them only suitable for relatively long relaxation processes.

A key difference between a muon and ^{8}Li is its lifetime τ and spin.* The muon exhibits a a lifetime $\tau_\mu = 2.2\,\mathrm{s}$, while ^{8}Li shows $\tau = 1.21\,\mathrm{s}$ [189, 194]. The lifetime defines the sampling rate of the polarisation. The short τ_μ allows to detect the precession of the muon, while the precession period of ^{8}Li is much faster than can be probed through its decay. ^{8}Li can be produced with much higher intensities than low energy muons and the beam can be focused to fit on a $5\,\mathrm{mm} \times 5\,\mathrm{mm}$. With $I = 2$, ^{8}Li exhibits an electric quadrupole moment and makes it sensitive to EFG in the sample. When studying magnetism, this is usually seen as a nuisance, since it creates additional relaxation mechanisms through fluctuating electric fields that cannot easily separated from magnetic effects. However, in the case of this work, it actually constitutes an advantage, since it makes us sensitive to EFG, which can be linked to orbital order [123]. The ^{8}Li ions typically arrive with $\approx 20\,\mathrm{keV}$ at the experimental endstation. When studying thin films, it is important to reduce the energy of the ions, so most of them get implanted into the film and not the substrate. This is done by apply a high-voltage bias to the experimental setup. The

*Lifetime is the decay of a number of radioactive isotopes to $1/e$ of the original amount, while the half-life is the decay to 1/2 of the original amount.

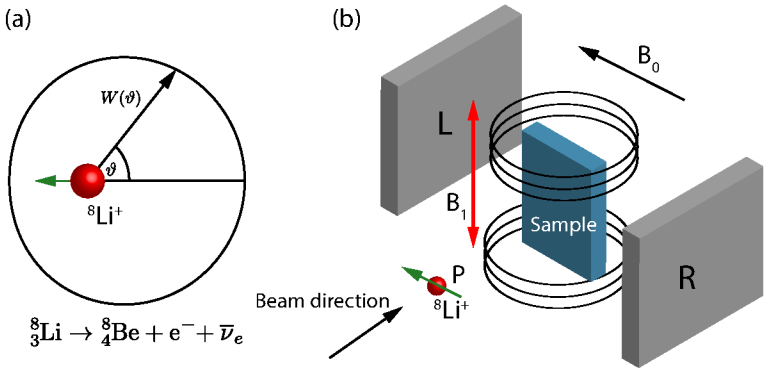

Figure 3.16: (a) The asymmetry of the β-decay of ^{8}Li (b) Beta-Nuclear-Quadrupole (BNQR) setup for studying electric quadrupolar effects and in-plane magnetic internal fields. The ^{8}Li-ions are implanted with a polarization $\boldsymbol{P}$ in the plane of the sample. Detectors left (L) and right(R) pick up the anisotropy of the angular distribution of the electrons after the decay. A static field $\boldsymbol{B}_0$ along $\boldsymbol{P}$ can be applied. In addition, the setup allows to scan resonances via a transverse dynamic field $\boldsymbol{B}_1$, however, this was not used within this work.

penetration profile and the optimal energy of the ions is usually calculated via Monte-Carlo-simulations [195]. To avoid absorption of ^{8}Li and to avoid condensation of contaminants on the sample, the whole setup is kept in ultra-high vacuum. The experiments conducted during this thesis were conducted at the β-NQR (nuclear quadrupolar resonance) endstation at ISAC, which is optimized for low magnetic fields in order to study electric quadrupolar splittings arising from EFG at the ^{8}Li stopping site. The ^{8}Li ions arrive with their spin polarization in the plane of the sample making it most sensitive to in-plane magnetic fields or EFG (Fig. 3.16). Small static fields B_0 of up to 220 G can be applied along the polarization direction [191]. In order to scan the resonance of the ^{8}Li, oscillating fields along B_1 can be applied transversely to the polarization direction. After the implantation, the ^{8}Li interacts with the sample and then decays via

$$^8_3\mathrm{Li} \rightarrow {}^8_4\mathrm{Be} + e^- + \overline{\nu}\,. \tag{3.71}$$

The asymmetry of this β-decay of ^{8}Li can be described as

$$W(\theta) = 1 + \frac{v}{c} P A \cos\vartheta\,, \tag{3.72}$$

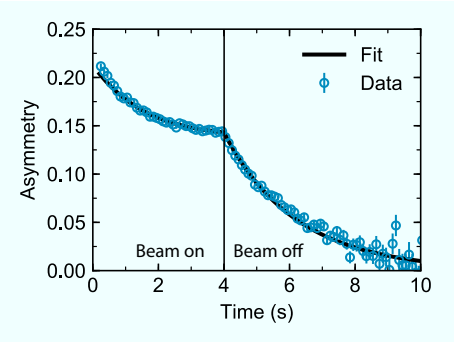

Figure 3.17: Exemplary ^{8}Li relaxation in a pulsed βNMR- experiment. While the beam is on ($t < T = 4\,\mathrm{s}$), the polarization approaches a dynamic equilibrium. After the beam is switched off, the polarization relaxes to a thermal equilibrium ≈ 0. The example shows the asymmetry for Sr_2RuO_4 at $50\,\mathrm{G}$.

where v describe the velocity of the electron, c the speed of light, P the polarisation of ^{8}Li at the moment of decay, ϑ the angle between the polarisation and the electron momentum, and the asymmetry parameter $A = 1/3$ describes an intrinsic constant of the decay of ^{8}Li. The β-decay produces electrons with a continuous energy spectrum with an endpoint of $13\,\mathrm{MeV}$[196]. Fig. 3.16 shows the case of $v/c = 1$ and $P = 1$ (for MeV electrons $v/c \approx 1$). Plastic scintillation detectors and phototubes perpendicular to the ^{8}Li polarization (left in and right of the sample) measure the emitted electrons and their asymmetry. The energy of the electrons is sufficiently high to pass through thin cryostat shielding and window ports. The experimental asymmetry is then given by

$$\mathcal{A}_\pm = \frac{R_\pm - L_\pm}{R_\pm + L_\pm} = aP_\pm + c \tag{3.73}$$

where $R_\pm$ and $L_\pm$ are the count rates of the detectors right and left (Fig. 3.16). The $\pm$ denotes different helicities of the ^{8}Li polarisation. The c term corrects for a non-asymmetry of the detectors. Note that a depends on experimental factors such as the sample itself, its position, the strength of the magnetic field B_0 etc., so usually $|a| < |A|$. Typically, the data at this setup shows [196] $a \approx -0.2$. To cancel the c term, one measures two helicities and then creates the difference $\overline{\mathcal{A}} = \mathcal{A}^+ - \mathcal{A}^-$., which constitutes the quantity that is labeled *Asymmetry* in this thesis.

The setup is operated in a pulsed mode. The relaxation is measured by implanting a beam of ^{8}Li for $T = 4\,\mathrm{s}$ in the sample and recording the asymmetry before and after T. During the beam on period, new

^{8}Li arrive, but also implanted ^{8}Li have started to relax and decay. In this state, the system approaches a dynamical equilibrium, which is seen as a plateau in the measured asymmetry (Fig. 3.17). After the beam is switched off, the system relaxes to a Boltzmann-distributed thermal equilibrium with only little polarization $\mathcal{A}_\pm \approx 0$. Assuming a general relaxation function $f(t, t_P, \lambda)$, the time evolution of the asymmetry can be described with [197]

$$\overline{\mathcal{A}}(t) = \begin{cases} \dfrac{\int_0^t e^{-(t-t_p)/\tau} f(t, t_P, \lambda) dt_p}{\int_0^t e^{-t/\tau} dt} & t \leq T, \\ \dfrac{\int_0^T e^{-(T-t_p)/\tau} f(t, t_P, \lambda) dt_p}{\int_0^T e^{-t/\tau} dt} & t > T. \end{cases} \tag{3.74}$$

Here, The relaxation function is convoluted with the radioactive decay with a lifetime τ over several implantation times t_p during the beam on period $t < T$. The simplest relaxation function is a single exponential as postulated in eq. 3.70, which corresponds to a single relaxation channel:

$$f(t, t_p, \lambda) = \mathcal{A}_0 e^{-\lambda(t-t_p)} \tag{3.75}$$

Here, $\lambda = 1/T_1$ denotes the relaxation rate and $\mathcal{A}_0$ the initial asymmetry, which is also often denoted as *amplitude*. In the case of a single exponential relaxation, eq. 3.74 is analytically solvable and becomes

$$\overline{\mathcal{A}}(t) = \begin{cases} \dfrac{\mathcal{A}_0}{\lambda'\tau} \left(\dfrac{1 - e^{-\lambda' t}}{1 - e^{-t/\tau}} \right) & t \leq T \\ \dfrac{\mathcal{A}_0}{\lambda'\tau} \left(\dfrac{1 - e^{-\lambda' T}}{1 - e^{-T/\tau}} \right) e^{-\lambda(t-T)} & t > T\,, \end{cases} \tag{3.76}$$

where $\lambda' = \lambda + 1/\tau$. However, the relaxation function does not necessarily have to be a simple exponential. For example, the ^{8}Li could have two stopping sites with with different relaxation processes. In this case, one would probably need to use at least a bi-exponential relaxation. Another notable relaxation function is the so called *stretched*

exponential or *Kohlrausch Law*[198]

$$f(t, t_p, \lambda) = \mathcal{A}_0 e^{-\lambda(t-t_p)^\beta} . \tag{3.77}$$

This function describes a distribution of multiple independent exponential relaxation channels. In such a case, the integral in eq. 3.74 has to computed numerically.

3.3.3 Phenomenology of Phase Transitions probed by Nuclear Magnetic Resonance

Second order phase transition are characterized by a diverging correlation length ξ linked to the order parameter and a critical slowing of fluctuations at the phase transition temperature (divergence in temporal correlations). For simple antiferromagnets, the order parameter is the dipole moment of spin and thus the Neel transition is accompanied with a divergence in spin fluctuations. Close to the phase transition $\xi \propto ((T - T_N)/T_N)^{-\nu}$ with the Neel temperature T_N and the critical exponent ν. Using time-dependent Ginzburg-Landau-theory, it can be derived that [132]

$$\frac{1}{T_1} \propto \xi \propto \left(\frac{T - T_N}{T_N}\right)^{-\nu} , \tag{3.78}$$

i.e. the relaxation rate diverges actually in the same way as the correlation length. Fig.3.18 shows the correlation in energy around a magnetic Bragg peak in Rb_2MnF_4 measured via inelastic Neutron scattering. The critical slowing is visible by the increasing spectral weight at low frequencies close to T_N. A nuclear Larmor frequency ω_L resides typically in MHz range, so much smaller than the THz scale associated with electronic spin fluctuations. The diverging amplitude of spin fluctuations at ω_L causes then $1/T_1$ to diverge [199].

Similar features can also be observed via electrical fluctuations in the NQR relaxation channel. An often studied ordering phenomenon using NMR is a charge-density-wave (CDW), a period modulation of the charge distribution within a crystal. In such a case, the order parameter is the charge density modulation $\Delta\rho$ and its fluctuations couple to the electrical quadrupolar moment of the nucleus. Fig. 3.19 shows an example of such an investigation in $SrPt_2As_2$. Another notable example is the CDW in cuprates [201]. Although encountered

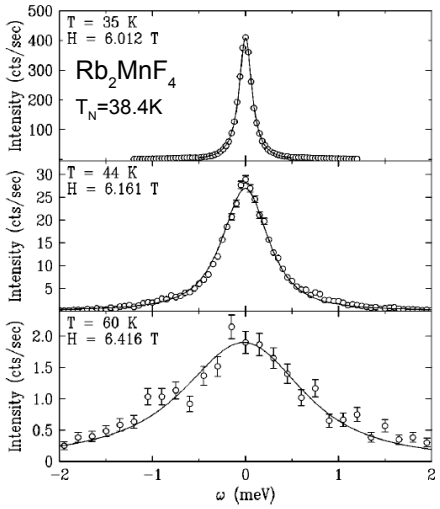

Figure 3.18: Spin fluctuations in Rb_2MnF_4 measured by Inelastic Neutron Scattering around the (010) magnetic Bragg peak. By going through the phase transition, increasing spectral weight is shifted to low energies due to critical slowing. Taken from Ref. [200].

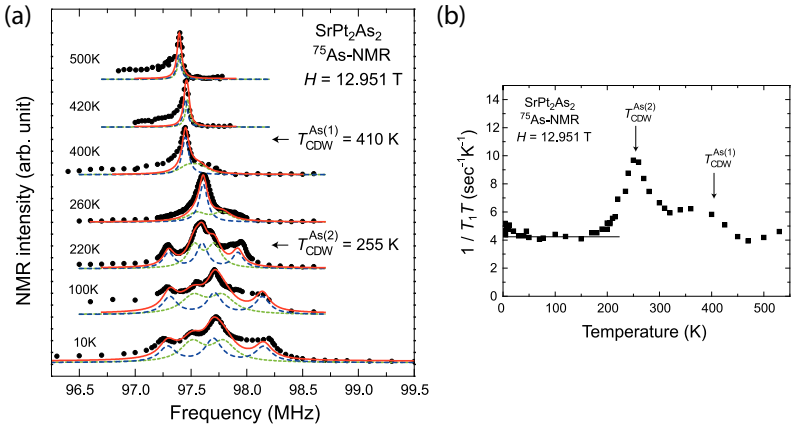

Figure 3.19: Probing charge density waves in $SrPt_2As_2$ via NMR in Ref. [202]. (a) Scanning the absorption lines, above the transition temperatures only one line is visible corresponding to the uniform Zeeman splitting. Below the transitions temperature, additional lines appear corresponding to splitting of absorption lines due to an EFG setting in (b) Anomalies in the longitudinal relaxation rates setting in at corresponding temperatures. The authors note that the nature (electric/magnetic) of the fluctuations cannot unambiguously determined, the absorption spectrum indicates that EFG-fluctuations are responsible. Figure taken from Ref. [202]

frequently, much less research has been devoted to the dynamics close to a first-order transition transition [203, 204]. Generally, the correlation length in a first-order transition is finite at the transition temperature, thus one does expect also to encounter a finite relaxation time. Anomalies, however, are also certainly expected due to the discontinuities in all thermodynamic quantities.

4

Synthesis and Characterization

In this chapter we present basic concepts of thin film growth and introduce the techniques related to pulsed laser deposition (PLD) growth of oxide thin films. We present a chronological summary of the growth optimization process in order to guide future works. Structural characterization via hard X-ray diffraction, Raman spectroscopy and Oxygen K-edge XAS reveal strongly modified structures relative to bulk CRO. Electrical transport measurements reveal the large impact of the epitaxial strain showing that it can tune the material from an insulator to a metal. Parts of this chapter have been published in *Appl. Phys. Lett.* 112, 031902 (2018).

4.1 Thermodynamics and Kinetics of Epitaxial Growth

As for single crystals, the growth of thin films is largely pursued using empirical approaches. Usually, thin film growers have to rely on systematically mapping out growth conditions until samples with satisfactory quality can be achieved. However, basic theoretical considerations can guide the growth effort. We will start by assuming an equilibrium process. Here, thermodynamics can be used to define basic scenarios regarding the growth morphology. A helpful variable

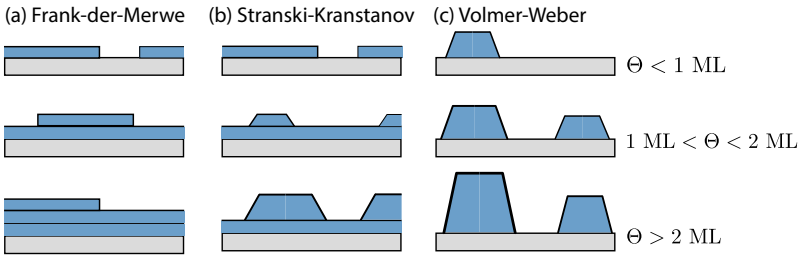

Figure 4.1: Fundamental modes of thin film growth in thermodynamic equilibrium. (a) Frank-der-Merwe or Layer-by-Layer growth (b) Stranski-Krastanov growth and (c) Volmer-Weber or Island growth . Θ denotes the number of monolayers (ML). Adapted from [206].

is the chemical potential [205]

$$\mu(n) = \left.\frac{\partial G}{\partial n}\right|_n = \mu_\infty + (\varphi_\alpha - \varphi_\alpha^{'}(n) + \epsilon_d(n) + \epsilon_e(n)) \,, \tag{4.1}$$

where G is the Gibbs energy, μ_∞ the bulk chemical potential of the film, φ_α the desorption energy of an atom of the film on film atoms, $\varphi_\alpha^{'}(n)$ the desorption energy of film atoms on the substrate, $\epsilon_d(n)$ the energy per atom of misfit dislocations, $\epsilon_e(n)$ the energy per atom related to homogeneous strain in the film and n the number of layer that has been deposited on top of the substrate.

The chemical potential μ essentially summarizes the energy balance of cohesion vs. adhesion of film atoms and the formation of misfit defects vs. accommodation of the lattice misfit via strain. When a system goes into equilibrium, G is driven to a minimum. Based on this equation one can define three different equilibrium growth modes (see Fig. 4.1):

$\partial\mu/\partial n > 0$ Frank-der-Merwe (FdM) growth mode or layer-by-layer growth mode. Adhesion forces dominate (complete wetting).

$\partial\mu/\partial n \lesseqgtr 0$ Complete wetting until a critical thickness, but then due to tendency to form dislocation defects, the sign of $\partial\mu/\partial n$ is reversed. Strain relaxation and incomplete wetting occurs. This growth is named Stranski-Krastanov (SK) growth.

$\partial\mu/\partial n < 0$ It is energetically favorable to create a new layer rather than to fill an already existing one. This results in the so called

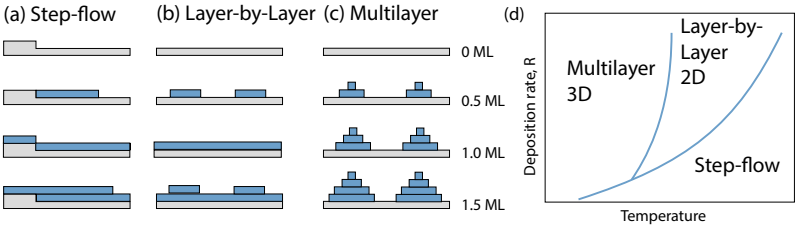

Figure 4.2: Growth Modes based on kinetic considerations. (a) Step-flow growth (b) Layer-by-Layer growth (c) 3D Multilayer or island growth. (d) Growth mode diagram. Based on [206].

Volmer-Weber (VW) growth or island growth. Cohesion forces dominate (incomplete wetting).

Because of the smoothness of the film and good surface coverage, usually layer-by-layer growth is preferred and sometime necessary for specific growth techniques (atomic-layer-by-layer molecular beam epitaxy). However, Stranski-Krastanov growth can be beneficial for creating e.g. quantum dots [207].

As the atoms being deposited (adatoms) arrive usually with a thermal energy much higher than the substrate temperature, time-dependent processes such as surface diffusion and the deposition rate also must have to be taken into account. These type of effects are labeled as *kinetic*. Thus, even if we deposit a chemical species on a substrate consisting of the identical chemical species, different growth modes can occur although thermodynamics would predict a FdM growth [206].

Substrates are most often single-crystals which have been polished to provide a smooth surface. During this polishing process, it is, however, impossible to be perfectly aligned with the crystallographic planes. This offset ("miscut") produces steps and terraces on the substrate surface. If the mobility of an impinging atom is high and the deposition rate is low, the atoms have the tendency to migrate to the steps where the nucleation rate is higher. This constitutes the so called *step flow* (Fig. 4.2). If the migration length is shorter than the terrace width, islands of adatoms nucleate. Jumping from the top of an island to the layer below requires extra energy (the so called *Ehrlich-Schwoebel-Barrier*). If this transport between layers

(interlayer-transport) is inhibited and the atoms cannot escape on top of an island, the growth will proceed with a *3D island growth*. On the other hand, sufficient interlayer-transport will yield a *layer-by-layer growth*.

Higher temperature promotes diffusion and thus interlayer mass transport. Higher deposition rates increase the tendency to nucleate, thus favoring layer-by-layer or island growth (Fig 4.2). High adatom migrations lengths and low deposition rates put the step-flow-growth mode closest to equilibrium [206].

4.2 Growth Techniques

4.2.1 RHEED

RHEED stands for Reflection High-Energy Electron Diffraction and comprises one of the standard techniques for in-situ characterization during the growth of thin film systems. In essence, it involves an electron gun, electrostatic optics and a phosphorous screen (Fig. 4.4). This simplicity allows for an easy implementation in thin film deposition setups.

Since electrons interact strongly with the other electrons, electron scattering experiments have to be conducted in vacuum, which is, however, already in place for most thin film deposition apparatuses. For RHEED, electrons are accelerated to 20 keV–40 keV and then directed at the sample surface typically at glancing angles of 1°–2° to improve the surface sensitivity. The combination of the high scattering cross-section and the low incidence angle results in a very low penetration depth of a few atomic layers, which makes it only sensitive to the first few monolayers. The electrons are then reflected and diffracted from the surface lattice. The very low penetration depth of the beam does not allow one to probe lattice periodicities along the out-of-plane direction. Thus, point-like reflections in reciprocal space as known from X-rays become rods pointing along the z-direction (Fig. 4.3). Depending on the surface morphology, e.g. island size, these rods can be significantly broadened due to the finite correlation length of the scattering. The broader the rod, the more overlap is created with the Ewald sphere allowing for a wider volume where the Laue condition for scattering is fulfilled. This causes the streak pattern seen

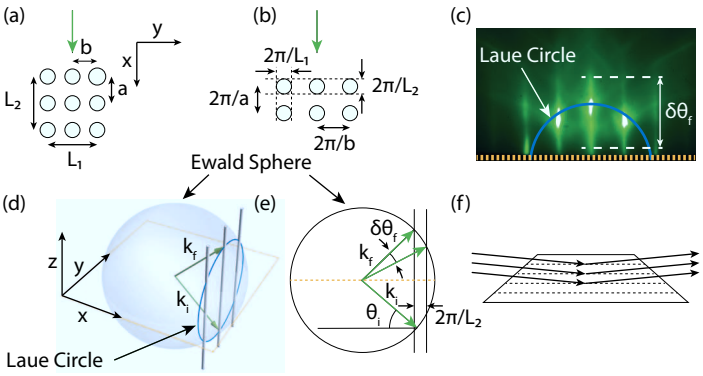

Figure 4.3: Concepts behind RHEED. (a) Real space depiction of surface lattice (b) Reciprocal space depiction of surface lattice (c) RHEED image of a $LaSrAlO_4$(001) substrate as seen on screen (d) Ewald Sphere with Reciprocal Space Rods (e) Intersection of Ewald sphere with reciprocal space rods showing the origin of streaks in the RHEED image (d) Transmission through feature of nanometer size yielding three-dimensional scattering. Based on [208] and [209].

in RHEED images, which is typical for smooth, two-dimensional film growth. If growth of 3D-islands or precipitates occurs, these features can be small enough to allow transmission of electrons. This effect allows for a correlation along the z-axis and causes spots with finite size in the diffraction pattern. Thus, a streak pattern is usually seen as a feature of a smooth, high-quality surface and spots for a rough surface populated with 3D features. One exemption to this rule are very high-quality surfaces, where the correlation length along x and y is so large that the overlap between the 2D-lattice rods and the Ewald sphere in reciprocal space becomes pointlike. This again causes a pattern of spots in the diffracted image. The 3D- or 2D-nature of spot patterns can be distinguished by whether the reflections lie on a circle or not. In case of a perfect 2D-surface the reciprocal lattice rods are infinitely thin, but the finite width of the Ewald sphere determines the location of the spots and creates a circular placement of the reflections (see Laue circle in Fig. 4.3). In the case of 3D-transmission through e.g. islands, the rods become points in reciprocal space. Since now the points determine the location of the spots in the diffracted image and not the intersection of rods with the Ewald sphere, the spots appear on a grid given by the reciprocal lattice(Fig. 4.11)

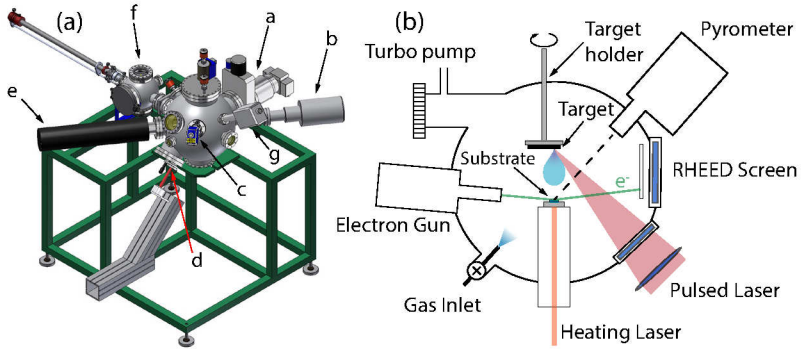

Figure 4.4: (a) Pulsed laser deposition setup used for the synthesis of the CRO thin film samples investigated within this work. Based on technical drawings by G. Cristiani. **a** Turbo pump,**b** RHEED electron gun,**c** Pyrometer, **d** Laser entry view port, **e** RHEED camera, **f** Load lock, **g** Residual Gas Analyzer (b) Simplified sketch illustrating the fundamentals of a PLD vacuum chamber.

RHEED analysis is usually constrained to a qualitative feedback during growth and surface quality. Since the inelastic mean free path of electrons is similar to the elastic one, quantitative simulations have to go beyond the kinematical approximation and are rarely being used [208].

4.2.2 Pulsed Laser Deposition

The Pulsed Laser Deposition (PLD) technique has found wide use in complex oxide research because of its flexibility and simplicity [210]. PLD uses a laser to ablate precursor materials controllably to synthesize thin films. A typical setup consists of a vacuum chamber, a laser, laser optics, a substrate heater and a so called target (Fig. 4.4). The target is a solid piece consisting of a mixture of precursors for the intended phase of the film. For this purpose, mostly sintered pellets are used. UV-Excimer lasers are popular for the growth of complex oxides, since ceramic targets absorb well at UV-wavelengths and they can easily reach the power required. The laser can be focused to such a high energy density that virtually any material can be ablated. The high local temperature of the point where the laser strikes prompts immediate ejection of the material regardless of their vapor

pressure differences. The ablated material expands as a plasma plume and condenses on a typically hot substrate. The high kinetic energy of the particles allows the vacuum chamber to be pressurized up to 1 torr[210]*. Varying the process gas allows one to tune the oxygen chemical potential and to vary the kinetic energy of the plasma plume. Typical energies for the plume species are $\approx 1\,\mathrm{eV}$ [211]. This is intermediate between the techniques of molecular beam epitaxy (MBE) ($\approx 0.1\,\mathrm{eV}$) and sputtering ($\approx 10\,\mathrm{eV}$).

For many materials this process yields a one to one (also known as congruent) transfer of the stoichiometry of the target to the film. However, this is not necessarily true for volatile species such as Li or RuO_x[212]. In such cases off-stoichiometric targets are used to compensate for the additional loss of the volatile species (sec.4.4). The oxygen stoichiometry in complex oxides is often ill-defined and hard to measure. It can be tweaked, however, by systematically adjusting the oxygen partial pressure in the background gas or by post-annealing and observing the effects on e.g. transport properties [213].

One specific issue with PLD growth is the formation of droplets due to the high energy deposited on the target. The laser can partially melt the target or eject macroscopic particles . This can cause droplets on the substrate surface, which can be detrimental for growing e.g. superlattices where a low interfacial roughness is required. It was found that targets with high densities can mitigate this issue (sec. 4.4).

The PLD chamber used in this thesis is based on a commercially available DCA PLAD 500 system (Fig. 4.4). It is suited for UHV-operation including a loadlock, which allows a relatively low base pressure for a PLD chamber of 1×10^{-8} torr. The laser is a Lambda Physik LPX305 Pro UV Excimer laser operating with KrF gas. Under this configuration it emits light with a wavelength of 248 nm and a pulse duration of 1.5 ns. The target-to-substrate distance is $\approx 50\,\mathrm{mm}$. The chamber is equipped with a differentially pumped RHEED system, which allows operation at elevated pressures and protects the filament from oxidation. The substrate is heated via an IR laser, which allows high temperatures $> 1000\,^{\circ}\mathrm{C}$. The temperature is controlled via two pyrometers(see sec. 4.7).

*760 torr $\approx$ 1013 hPa $\approx$ 1 bar

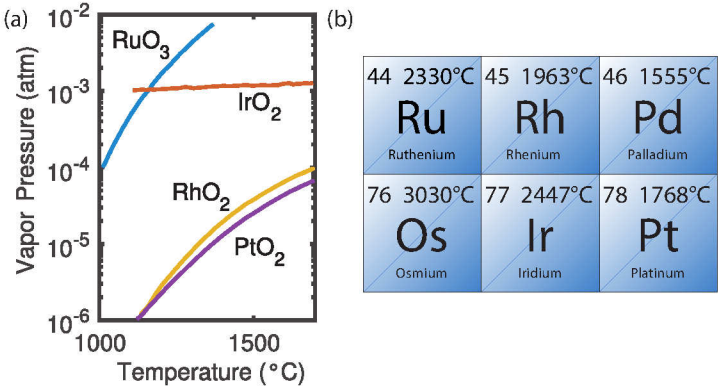

Figure 4.5: (a) Vapor pressure of oxidized platinum group metal species [214] (b) Platinum group metals with their melting point and atomic number [215].

4.3 Volatility of Ruthenium

Ruthenium belongs to the platinum group metals (PGM), which are neighboring metals in the 8th to the 10th group of the periodic table. They share common properties such as low tendency to be oxidized and a high melting point (Fig. 4.5). The high melting point is representative of the generally low vapor pressure of PGM. This is especially an issue for thermal evaporation methods such as effusion cells. On the other hand, once PGM are oxidized they can develop a substantial increase in their vapor pressure (Fig. 4.5) (water has a vapor pressure of 1×10^{-2} atm at room temperature [216]). This has to be taken into account since ruthenates have to be grown by definition at conditions where ruthenium is oxidized. In order to counter loss of Ru during the synthesis, often a Ru-excess is used when preparing the precursors for the growth of ruthenates [217].

4.4 Target Synthesis

It is desirable to have a high density PLD-target in order to avoid the formation of droplets during the ablation [219, 220]. Thus, single crystals are usually favored. However, the size of CRO single crystals

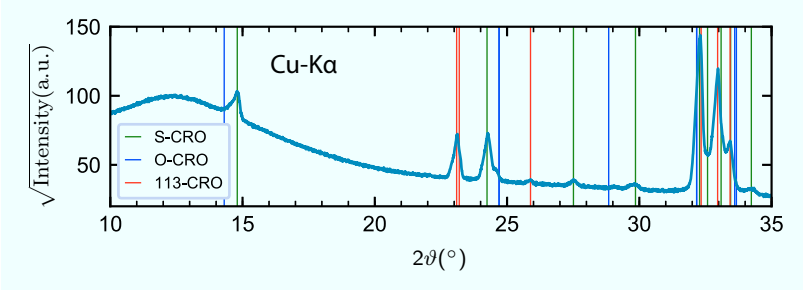

Figure 4.6: Typical powder diffractogram of a $Ca_2Ru_{1.2}O_4$ polycrystalline target synthesized with the recipe described in the text. The strongest reflections can be assigned to S-CRO and $CaRuO_3$. Faint additional peaks are visible which we ascribe to O-CRO. Lattice parameters of the O-CRO phase do not match the literature well, which might be due to different oxygen-stoichiometry. The large hump at 12° is due to the sample holder. Structural parameters taken from [90, 218].

is impractical (typically less than 1 mm) and the proximity to the MIT probably triggers shattering of the crystal under laser ablation. In addition, due to the volatility of RuO_x, we require an off-stoichiometric target with excess Ru. Ref. [142] used an array of small $Ca_3Ru_2O_7$ single crystal pieces to obtain high density and Ru-excess. However, $Ca_3Ru_2O_7$ single crystals are not much larger than CRO crystals [221], which must have caused limitations on the targets usage. Targets are typically 1 inch $\approx$ 25 mm in diameter and 1/8 inch $\approx$ 3 mm thick to distribute the wear on the targets surface over a wider area and to allow repolishing the target. We chose to undergo the route of a polycrystalline $Ca_2Ru_{1.2}O_4$ pellet as a target using the same Ru-excess as previous reports of CRO thin films [140, 141, 222] and similar to the stoichiometry of floating-zone growths of single crystals [217].

Following Ref. [217], the targets were synthesized via a typical solid-state synthesis route by mixing 99.999 % $CaCO_3$ and 99.9 % RuO_2 in a 2:1.2 ratio. The high-purity of $CaCO_3$ was deliberately chosen to avoid Sr contamination. Both powders were weighed hot due to their hygroscopy. The mixing of the precursors was conducted by using a ZrO_2 ball mill. This was especially advantageous for milling $CaCO_3$, whose hardness made manual pestling quite painstaking. After a cal-

cination step at 900 °C for 24 h in air*, the mixture was pressed uniaxially in a 30 mm diameter mold at 62 MPa. The pellet was then pressed isostatically at 640 MPa for further densification. Sintering was conducted at 1370 °C for 24 h in 1 % O_2 in Ar atmosphere using non-compressed powder of the same composition as bedding powder, since we observed as reported in Ref. [223] that CRO powders form an eutecticum with Al_2O_3crucibles.

Initially, we also explored a wet-chemistry using $Ca(NO_3)_2$ as a precursor, since we noticed that the as-purchased RuO_2 is fine enough to mix easily with other powders, but the $CaCO_3$ powder often contains tiny "rocks", which require ball-milling. Since the superconductivity in SRO is very sensitive to Si and Al_2O_3 impurities [136] and it was demonstrated that high pressure can yield superconductivity in CRO [224] and thus possibly epitaxial strain, a less pure target might already prevent us from observing such an effect. Thus, to avoid impurities from ball-milling, we dissolved $CaCO_3$ in nitric acid and added RuO_2. Since RuO_2 does not dissolve, this creates a slurry, which, however, can be well mixed. After boiling off the nitric acid, the mixture was calcinated at 900 °C for 24 h. All the mixing steps were conducted with PTFE-tools to avoid the inclusion of small glass (SiO_2) particles. Eventually, this route was not pursued further, since the toxicity and hazardousness of the substances make this process relatively time-consuming. We note, that similar methods were used for making Sr_2RuO_4 targets and the higher purity helped to improve the residual resistivity [56].

Fig. 4.6 shows a typical powder X-ray diffractogram of a polycrystal prepared using the method based on the carbonate precursors. Comparing with known structures from the literature [90, 218], S-CRO, O-CRO and $CaRuO_3$ can be identified. The phase composition of a target is not important per se, more so the stoichiometry (mainly Ca/Ru, as O can be replenished by background gas). However, it gives us the information that the system accommodates Ru excess by the formation of $CaRuO_3$, when in thermal equilibrium.

We noticed that the tube furnace contained black residue after the sintering, which we attributed to condensed RuO_x material due to the volatility of RuO_x. Thus, we suspect the Ru:Ca ratio of the sintered pellet to be less than 1.2 : 2.

*Calcination describes the process to drive off the carbon part by the formation of CO_2 at high temperatures.

The isostatic pressing turned out to be crucial to achieve good structural integrity* and good densification. However, the density of the resulting pellet was estimated to be $\approx 3.2\,\mathrm{g\,cm^{-3}}$, which is only 69 % of the single crystal density. This is slightly higher than the 65 % previously reported target-making procedures, but still offers room for improvement [222].

We briefly explored spark plasma sintering (SPS) as a way to improve the density [225]. Here, the powder is compressed while it is kept at high temperature by running a current through the sample. For this, we crushed a pellet made with the recipe described above and used it as the starting material. We note, that by the design of most SPS machines, however, the process needs to be conducted in vacuum, which might be detrimental the oxygen-stoichiometry of the system. We found that CRO reacted with the graphite crucible at the high temperatures used in this process ($\approx 1200\,^{\circ}\mathrm{C}$), which is consistent with a report in the literature [226]. A different crucible material might allow the use of the SPS method to obtain denser CRO pellets.

4.5 Phase Stabilization and Optimization

In this section, we want to provide a chronological summary of the growth optimization process and present the most important aspects of how to achieve high-quality CRO films. Thin film growth is highly empirical and approaches taken in the beginning of the synthesis may not appear sensible in hindsight.

We first focused on reproducing the reported growth recipes for CRO on LAO by Wang et al. [139] and Miao et al. [142]. LAO substrates are relatively inexpensive and easy to handle, which turned out to be quite fortunate, since many iterations of the growth conditions had to be conducted in order to arrive at a satisfactory procedure. We used a substrate size of $10\,\mathrm{mm}\times10\,\mathrm{mm}\times1\,\mathrm{mm}$ in the beginning, but we realized that the issues arising from the required high growth temperatures around 900 °C can be better managed with $5\,\mathrm{mm}\times5\,\mathrm{mm}\times1\,\mathrm{mm}$ or $5\,\mathrm{mm}\times5\,\mathrm{mm}\times0.5\,\mathrm{mm}$ substrates (see also 4.7).

Initially, we attempted to reproduce the growth conditions for CRO on LAO reported by Wang et al., i.e. we used $T_S = 920\,^{\circ}\mathrm{C}$, $p_{O2} =$

*We tested this somewhat non-scientifically by whether you can break the pellet by hand or not.

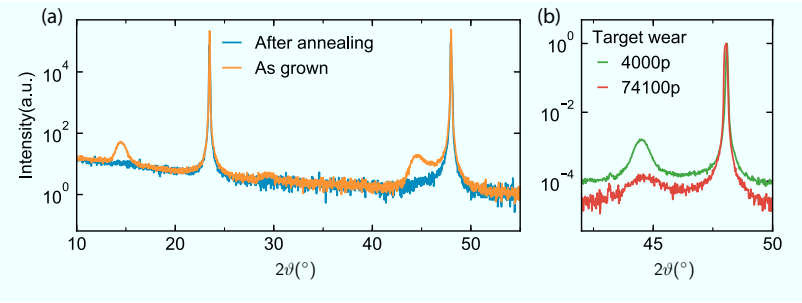

Figure 4.7: XRD ϑ-2ϑ scans of the first generation of PLD grown CRO thin films during the course of the PhD work. (a) The as grown film shows peaks, which can be clearly attributed to the Ca_2RuO_4 phase, but the faintness indicates poor quality. Annealing for 2 h at the used growth conditions destroys the phase showing the metastability of CRO films. (b) Two CRO films on LAO(100) grown under the same growth conditions, but with a different preceding target usage (given in laser pulses ablated in the legend).

20 mtorr, a laser repetition frequency $f = 10\,\mathrm{Hz}$, a fluence of $2\,\mathrm{J\,cm^{-2}}$ and a oxygen flow rate of 20 sccm. The oxygen flow rate was chosen to be larger than Wang et al., since it was shown that essentially only low flow rates are detrimental for the film quality, but no difference was observed above 7 sccm. Following the recipe, we evacuated the system after growth and quickly switched off the laser heater to rapidly quench the sample. Indeed, the subsequent XRD θ–2θ scans showed the formation of a Ca_2RuO_4 phase (Fig. 4.7). However, the film peak intensity turned out to be consistently low. The film shown was grown with 10 000 pulses, which for typical growths rates of $\approx 0.1\,\mathrm{Å\,s^{-1}}$ should yield thicker and thus typically much more intense peaks. Also, growing with higher pulse counts did not improve the peak intensity. Thus, this cannot be attributed to a low growth rate. A growth at lower temperatures around $\approx 850\,°\mathrm{C}$ yielded a mixed in $CaRuO_3$ phase prompting us to investigate higher temperatures. In addition, the fact that Miao et al. grew CRO on LAO films at higher temperatures of 1120 °C served as an indicator that higher growth temperatures might be beneficial. Furthermore, we checked whether the quenching described by both reports was actually necessary by annealing a film for 2 h at the same conditions it was grown at. We observed a disappearance of the CRO phase corroborating the metastability of the phase at the growth conditions. Thus, the rapid

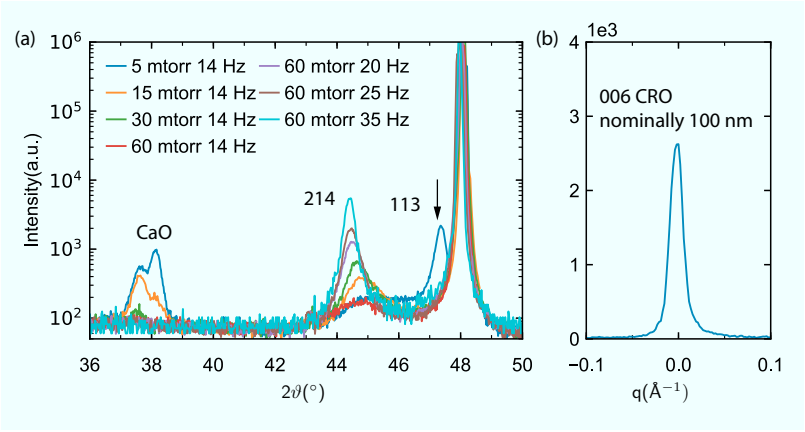

Figure 4.8: (a) Growth optimization of CRO on LAO films at a substrate temperature of 950 °C. All growth conditions except the one denoted in the legend (p_{O2} and laser repetition frequency) were kept constant(pulse counts, fluence). (b)The 006 peaks of CRO films on LAO grown at optimal conditions (60 mtorr and 35 Hz) with a nominal thickness of $\approx$ 100 nm showed a width ≈ 0.01 Å^{-1}, which is too wide for their expected thickness.

cooling was assumed to be generally beneficial for the growth. We optimized the quenching by electronically closing the gate valve to the turbo pump and opening another gate valve, which subsequently injected high-purity He-gas into the system. This allowed to bring the system from growth temperature to 600 °C in 30 s and down to 100 °C in 4 min. We note, that this also had the side-effect that the time from heating the substrate to extracting the substrate after the deposition was relatively short ($\approx$ 1 h), which allowed a relatively fast iteration of different growth conditions.

Growing at 950 °C we noticed a systematic repetition frequency dependence of the film quality (Fig. 4.8). While low p_{O2} favored the formation of the CaO and $CaRuO_3$ phases, higher p_{O2} stabilized the Ca_2RuO_4 phase. Higher frequencies consistently improved the film peak intensity. We note, that the repetition frequency of 35 Hz is extremely high, frequencies of 1 Hz–10 Hz are more typical for oxide thin film growth. We believe, that this effect might be connected to the volatility of RuOx, which creates a time-dependence of the Ru supply on the surface of the substrate available for the CRO phase formation. The higher frequency might counter the evaporation and

allow more Ru to go into the CRO phase. We note that an opposite effect was observed for $SrRuO_3$ [227], i.e. Ru-deficiency with increasing repetition rate. However, the frequency dependence at low temperatures (900 °C) corroborates an Ru-excess with increasing frequency in our case. The temperature used here is substantially higher (900 °C–950 °C) than the one used for $SrRuO_3$ in Ref. [227] (600 °C), which might be a factor for the different dependencies.

Using this method, we improved the intensity in the XRD, but we observed that it still did not scale well with thickness / pulse counts. Growing films with 10 nm thickness showed the expected intensity and widths of the peaks in the XRD pattern, but trying to grow thicker films did not yield the expected peak sharpness and intensity (Fig. 4.8).

At this stage of the process, while trying to reproduce films, we realized that there is a correlation between target use and film quality. Only repolishing the target after every run allowed us to reproduce films with similar quality (Fig. 4.7). We are not aware of any other system that shows such a strong dependence on the target usage. The description in Ref. [222] suggests, that Wang et al. might not have observed this effect, since they already repolished the target between runs to remove Ag-contaminants evaporating from the silver paste used to bond the substrate to the heater.

After lowering the growth temperature back to 900 °C, we found a significant increase in quality of the films. This was readily visible in the RHEED image, which stayed mostly streak- or spot-like (2D) till the end of the growth (see sec. 4.6) and the intensity of the reflections in the XRD patterns started to scale with the pulse count.

In order to clarify the dependence on the repetition rate, which we have noticed at 950 °C, we performed a combined XRD/Transport vs. repetition rate study in order to optimize the growth conditions. Since the films with the best quality grown at 950 °C had small thicknesses around 10 nm, we used similar pulse counts, which yields films with approximately the same thickness at 900 °C (Fig. 4.9). The electrical transport was measured in van-der-Pauw geometry applying currents of 10 A. Here, we noticed an intensity shift in the ϑ-2ϑ scans from the CRO (006) reflection toward the LAO (002) substrate reflection. Low-temperature growths ($T = 750$ °C) generally favored the $CaRuO_3$ phase. From such runs, we observed the (220) reflection of the $CaRuO_3$ phase at $2\vartheta = 46°$–$47°$. Thus the shift indicates the

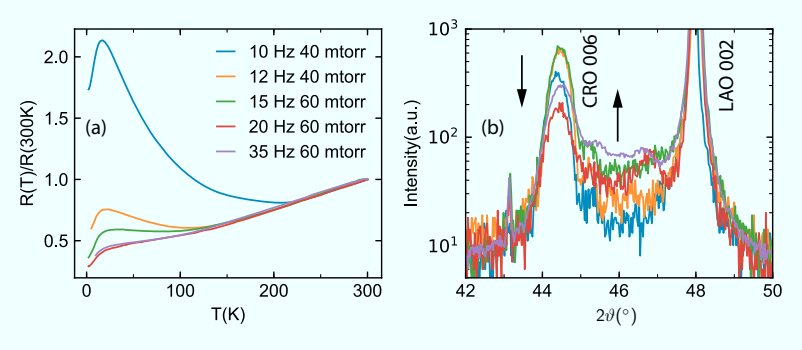

Figure 4.9: Synthesis optimization of 10 nm CRO films on LAO at 900 °C substrate temperature by inspecting of (a) Electrical transport and b) XRD ϑ-2ϑ scans in the vicinity of the CRO 006 peak. All growth conditions were kept constant except p_{O2} and the laser repetition rate as indicated in the legend. The trend in the transport and XRD suggests increasing metallicity with higher pulse repetition rate. The intensity shifts in the XRD pattern indicate the formation of the metallic $CaRuO_3$ phase at higher frequencies as the origin.

formation of $CaRuO_3$ inclusions, which is also corroborated by the increasing metallicity in the resistance. Based on this dependence we chose 11 Hz as the laser repetition rate for the deposition, which let us obtain high-quality single-phase Ca_2RuO_4 thin films according to the XRD characterization. The trend in the transport data of the $\approx$ 10 nm films presented here, is different from the thicker samples we chose to investigate in more detail. This might be related to a strain effect (see also sec. 4.10).

Combining the findings described above, we arrived at the growth conditions used for the high-quality samples that were used for the further study of the physical properties of CRO (Tab. 4.1). With these conditions and repolishing the target before every run, we were able to grow high-quality films with c-axis orientation on $LaAlO_3(100)$, $LaSrAlO_4(001)$ and $YAlO_3(001)$ and a-axis orientation on $LaSrAlO_4(110)$ and $NdCaAlO_4(110)$ (Fig. 4.10).

CRO on YAO imposes a large compressive strain on the system (Tab. 4.2). Growing films larger than $\approx$ 10 nm led to strain relaxation, which could be seen by a collapse of the c-axis in the ϑ-2ϑ scan. This is why we only investigated 10 nm films grown on this substrate type.

A-axis oriented substrates were optimized based on the peak in-

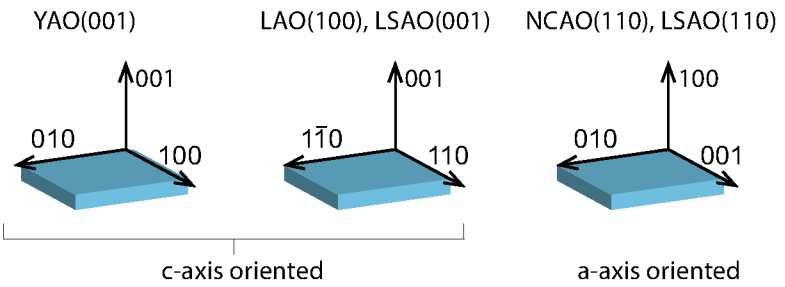

Figure 4.10: The two fundamental types of film orientations, which were grown. The crystallographic axes denote the orientation in the orthorhombic unit cell of CRO.

Type	T(°C)	f(Hz)	p_{O2}(mtorr)	F_{O2}(sccm)	Fluence (J cm^{-2})
c-axis	900	11	60	10	≈ 2
a-axis	860	11	60	10	≈ 2

Table 4.1: Optimized growth conditions used for the high-quality samples shown in Fig. 4.14. The columns denote the substrate temperature T, laser repetition frequency f, oxygen partial pressure p_{O2}, oxygen flow rate F_{O2} and laser fluence.

tensity of the (200) reflection visible in the specular ϑ-2ϑ scan. We found that the highest intensities were achieved at slightly lower temperatures ($T = 860\,°C$) than for the c-axis oriented substrates. We note that the temperature measurement is also subject to emissivity changes.

We note that we could not find evidence for the presence of $CaRuO_3$ inclusions in any of the a-axis oriented films, thus the growth window for the Ca_2RuO_4 phase on these substrates is potentially much larger. The tetragonal nature of the substrate face (long c-axis in-plane) should naturally stabilize the phase with the most similar symmetry, which is Ca_2RuO_4. A-axis oriented films might thus also be a strategy for other systems, where it might be difficult to stabilize a single-layer phase.

We also tried various approaches to stabilize the Ca_2RuO_4 phase on $NdGaO_3(110)$, $NdGaO_3(001)$ and LSAT, which should impose tensile strain on CRO, but only yielded bad quality samples consisting of Ca_2RuO_4 and $CaRuO_3$ mixtures.

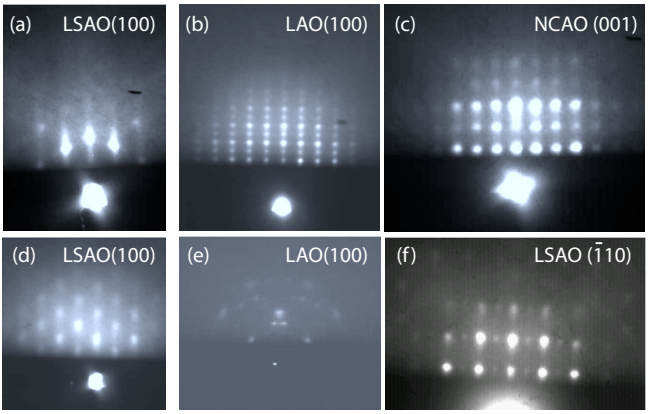

Figure 4.11: Basic RHEED patterns observed during the growth of CRO thin films. The substrate is given and its crystallographic direction parallel to the electron beam (in the tetragonal/cubic notation of the substrate). (a) Highest-quality samples with 2D-type spots and streaks. Faint Kikuchi lines are visible. (b) 3D-type spots associated with $CaRuO_3$ inclusions in c-axis oriented films. (c) & (f) Typical pattern of a-axis oriented films showing 3D-island growth along the (001) and (-110) directions. The direction was inferred from the smaller spacing of the spots along the horizontal direction, which corresponds to the longer c-axis. (d) & (e) Diffraction pattern associated with bad quality c-axis oriented samples.

4.6 RHEED Phenomenology

The RHEED system of the PLD setup turned out to be very useful to characterize the samples in-situ. Especially for the c-axis oriented samples, the correlation between quality seen in the XRD pattern and RHEED was so consistent, that it sufficed to check the RHEED diffraction image to discard bad samples. Fig. 4.11 shows typical distinct patterns obtained during the optimization process. In the following we will refer to these panels by using capital letters. **A** represents an image of one of the highest quality CRO films on LSAO(001). In such a case, the pattern stayed consistently streak- or even spot-like during growth. Faint Kikuchi-Lines are visible. Kikuchi lines arise due to inelastic scattering of electrons with phonons and plasmons. Their intensity and sharpness depends strongly on the surface morphology. Their appearance is typical for a high-quality surface [208]. **B**, **D** and **E** show "pathological" RHEED patterns, we were able to

associate with low-quality samples. The pattern in **B** was linked with the appearance of the $CaRuO_3$ phase in the XRD pattern. In case of the pattern shown in **D**, a Ca_2RuO_4 phase was found in the ϑ-2ϑ XRD scan, but the reflections had low intensity. The RHEED image corresponds to a typical transmission diffraction image of a cubic lattice seen along 110 direction [208], but we were not able to associate it with a specific phase. Based on Fig. 4.13, we tentatively associate it with a too high growth temperature. **E** was also similarly linked to low-quality films. We note that **E** bears similarity to the pattern CaO+Ru and **B** to $CaRuO_3$+RuO_2 found in Ref. [138]. If a high-quality pattern as shown in **A** was present with only a minor contribution from **D** or **E**, it was still worthwhile to inspect the film further. The effects could just be from the edges of the film and the main part of the film could still be useful.

C and **F** show the RHEED image for a CRO film on NCAO(110) and LSAO(110). Typically, spots were observed along the (001) and $(\bar{1}10)$ directions, which we associated with an island growth of the Ca_2RuO_4 phase. We could not find the same quality-indicators here. The island growth is nicely visible in the TEM images, where a wavy surface of CRO on NCAO is revealed(Fig. C.1).

4.7 Thermal Management of the Substrate

The substrates used for the growth of CRO films are all transparent in infrared and cannot be heated directly with the heating laser. Thus, the substrate needs to be attached to an IR-absorbing metal (Fig. 4.12 and 4.4). Two aspects constrain the choice of the absorber to only a few materials: The material must not have an appreciable vapor pressure at the growth temperatures and must not be easily oxidized, since we are growing with an oxygen background gas at high temperatures. These constraints led us to Ta, which has a low vapor pressure [228] and is relatively resistant to oxidation. We also briefly used small $5\,\text{mm}\times5\,\text{mm}\times0.5\,\text{mm}$ commercially available metallic Nb-doped STO substrates, but the small size was not favorable in terms of temperature homogeneity. A larger size might be more beneficial, but might be prone to cracking when quenching after growth.

For some growths a RuO_2 piece was tested as an absorber, but only yielded bad quality films, likely due to the excessive RuO_x-supply evaporating off the absorber.

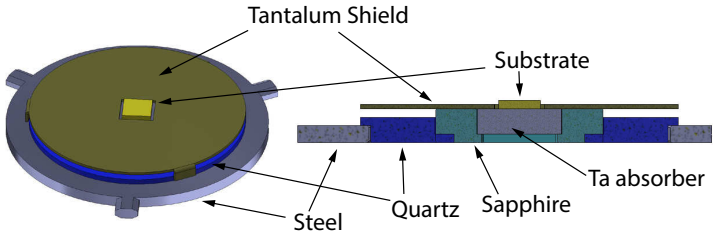

Figure 4.12: Most advanced version of the substrate holder used at the end of the growth optimization. The substrate is glued via Pt-paste to a high-purity Ta-block, which is heated by an IR-laser. The Ta-block sits in a sapphire piece, which sits on a quartz ring. The quartz ring lies on top of a steel piece, which fits in the bayonet coupling of the PLD chamber. The heat radiation coming from the substrate and absorber is masked with a tantalum shield to minimize the influence of stray radiation on the temperature detection via the pyrometer. Note that only the Ta-block and the substrate are red hot at growth temperature. Illustration based on technical drawings by G. Cristiani and B. Stuhlhofer.

We found it necessary to use a high-purity (99.999 %) Ta-piece, because a contaminant layer became visible by eye after heating cycles without deposition when using less pure material.* The Ta-block does oxidize at the growth temperature, but at a manageable rate.

The substrate was attached to the absorber as follows: After grinding off residues (oxidation layer, Pt-paste) from the Ta-block originating from previous growths, the substrate was attached to it by using a Pt-paste†. A coarse grinding paper is beneficial for this step, since it allows better contact. The high growth temperatures prohibit the use of the typically used silver paste, since its vapor pressure is too high. The Pt-paste contains organic solvents, which have to baked out before inserting in a UHV-system. We typically heated the substrate-absorber-stack at 120 °C for 10 min on a hot plate for this.

The substrate temperature in this setup is measured by a pyrometer directed at the substrate (Fig. 4.4). The measured area of the pyrometer optics is a circle of 4 mm diameter. However, by virtue of the projection due to its tilted angle relative to the substrate surface effectively the area is effectively 8 mm, which is larger than the 5 mm×5 mm substrates. The pyrometer cannot differentiate between

*This might be Nb[229], which is typically the highest impurity for Ta. We did not observe this effect when using Nb-doped STO as an absorber.

†Heraeus CL11-5100 Platinum Conductor

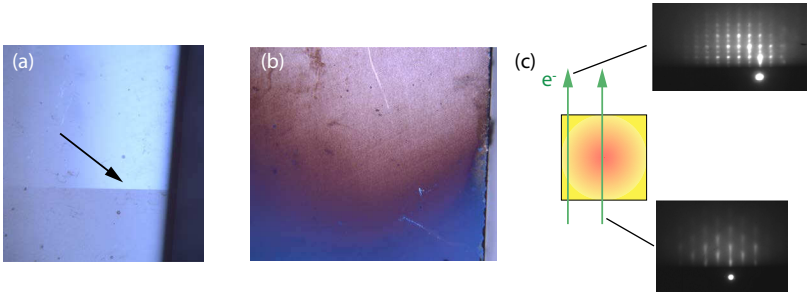

Figure 4.13: Temperature inhomogeneity issues encountered during the synthesis optimization process. (a) Discoloring of a CRO film on an LSAT substrate. Likely due to a temperature gradient, the substrate cracked (arrow). The discoloring stops directly at the crack indicating that the discoloring is related to a temperature inhomogeneity. (b) Surface discoloring of a CRO film on NGO* (c) RHEED patterns along the edge and the middle of a CRO film on LSAO(001) during growth. The pattern in the middle corresponds to a bad Ca_2RuO_4 phase, while the one along the edge corresponds to a $CaRuO_3$ phase (Fig. 4.11) consistent with a temperature gradient along the substrate.

heat radiation coming from the substrate or the heat absorber and is simply integrating over the measurement area.

The used emissivities are $\varepsilon_{\mathrm{LAO}} = 0.93$, $\varepsilon_{\mathrm{NCAO}} = \varepsilon_{\mathrm{LSAO}} = 0.92$, $\varepsilon_{\mathrm{NGO}} = \varepsilon_{\mathrm{YAO}} = 0.91$. The values are partially based on calibration measurements in a tube furnace setup. However, the accuracy used here is likely overestimated and they have to be rather regarded as process parameters.

The PLD-setup also included a second pyrometer to measure the temperature on the backside of the absorber. However, the oxidation of Ta-surface leads to changing emissivities, which did not allow us to use this method. In contrast to materials such as steel alloys [230], Ta does not create a stable surface when being oxidized, but starts flaking.

During the various growths, we often encountered a discolored surface (Fig. 4.13) of the CRO films. By rotating the substrate during the growth, we could exclude that this effect comes from a plume inhomogeneity. Thus, we attribute this issue to an inhomogeneous temperature distribution along the substrate. The Ta-block used to absorb the IR-radiation from the heating laser, sits in a Sapphire holder (Fig. 4.12). The contact surface between the two likely acts as a heat

bridge causing a temperature gradient in the Ta-block, which then gets transferred to the substrate. Thus we abandoned the use of absorbers with a similar size as the substrate and only used 5 mm×5 mm substrates on 10 mm×10 mm absorber. Originally, smaller absorbers were used, since they allowed a faster ramping to the growth temperature. In addition, for a small Ta-block the overall hot area was smaller than the pyrometer detection area, which we hoped, would improve the temperature reproducibility. In order to restrict the temperature measurement to the substrate region when using the larger absorber, we designed a substrate holder with a Ta-cover (Fig. 4.12).

Surprisingly, the homogeneity was consistently improved by applying the Pt-paste not only below the substrate, but also along the edges. Inevitably, this often caused the paste to creep up on top of the substrate. However, this did not interfere with further measurements or e.g. subsequent lithography processes. Pt-powder rings in XRD could be clearly identified.

4.8 Structural Characterization

The intricate coupling between structure and electronic properties, make the structural characterization vital for understanding the physics in CRO films. Neutron powder diffraction is the ideal technique for studying bulk samples, since it allows to access the nuclear and magnetic structure, but it is generally not applicable for thin films due to their low mass. However, as we will show below, already basic X-ray characterization techniques, Raman spectroscopy, X-ray absorption and transmission electron microscopy (TEM) can already give insightful structural information guiding further studies.

4.8.1 Hard-X-Ray Diffraction

Using Cu-K-α1 X-ray lab sources, we conducted scans along the c-axis confirm the formation of the Ca_2RuO_4 phase on the c-axis oriented LSAO(001), LAO(100),YAO(001) and on the a-axis oriented films on LSAO(110) and NCAO(110) substrates (Fig.4.14 and 4.15).

[†]At first, it seems not justified to show films on LSAT or NGO as a reference, since we could not grow good films on these substrate under any growth conditions. However, the effects shown here were also present on other substrates.

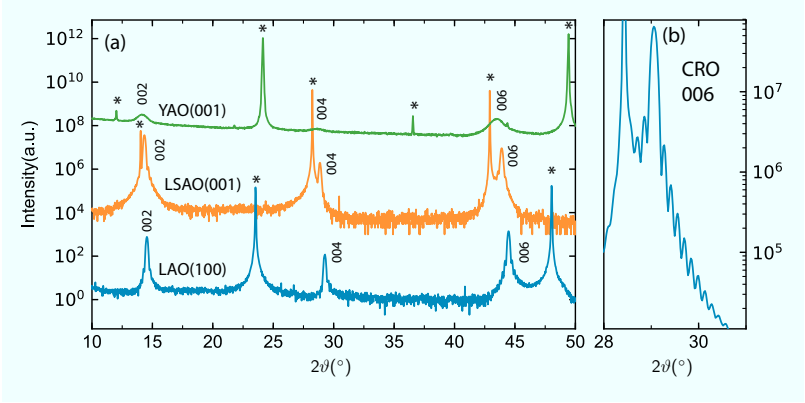

Figure 4.14: (a) Typical ϑ-2ϑ scans along the (001) direction for the set of c-axis oriented samples using a Cu-K-α1 laboratory source. Substrate peaks are denoted with an asterisk. (b) ϑ-2ϑ scan close to the 006 peak of the CRO film on LSAO(001) taken using $12\,\mathrm{keV}$ photons at the MPI-MF beamline. Thickness fringes are observed indicating a smooth surface.

Except for CRO on YAO, films similar to the samples shown were also characterized at the MPI beamline at ANKA, Karlsruhe [231]. All samples showed Bragg peaks linked to a doubling of the tetragonal unit cell indicating that the RuO_6 octahedra are tilted or rotated. Reflections found for CRO on LAO and LSAO(001) can be indexed with a twinned structure based on the selection rules for Pbca, which is the space group for bulk CRO [90]. CRO on NCAO (110) and LSAO(110) exhibits a single-domain structure, which was expected, since the c-axis of the substrate naturally constitutes a preferred direction. The out-of-plane direction is compatible with the H0L selection rule of the Pbca space group allowing us to identify it as the a-axis.

Reciprocal Space Mapping (RSM) confirms that the films on LSAO(001), LAO(100) and YAO(001) are coherently strained to the substrate (Fig.4.16). The in-plane c-axis of the film on NCAO matches the c-axis of the substrate, whilst the in-plane b-axis as the other in-plane component is only partially strained. The fact that the system can only partly accommodate the compression along b and c is also visible in the RSM showing a typical triangular relaxation (Fig. 4.17)[232]. The situation is reversed for CRO on LSAO(110): The b-axis is close to being fully strained, while the c-axis can only be partially strained due to large c-axis lattice constant mismatch of CRO vs.

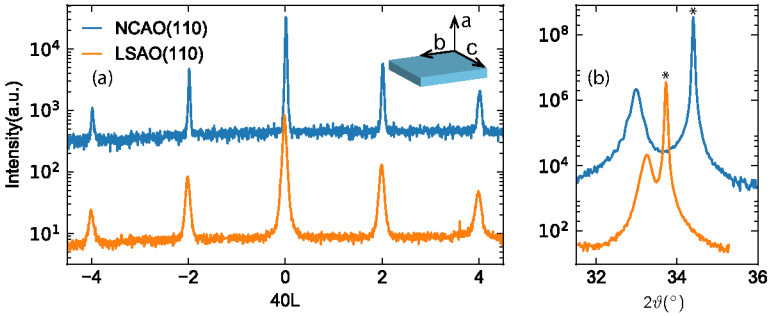

Figure 4.15: (a) Typical scans along the 40L-direction of a-axis oriented CRO films. For CRO on NCAO(110), $c = 12.12$ Å is used for the definition of L, while for CRO on LSAO(110) $c = 12.2$ Å was used. The inset shows the orientation of the orthorhombic unit cell of CRO in relation to the substrate edges. (b) ϑ-2ϑ along the specular 100 direction in proximity of the (200) reflection of CRO.

LSAO. The c-axis lattice constants of the films on LAO, LSAO and YAO were determined by the specular out-of-plane XRD scans using Nelson-Riley-fitting [233], while the in-plane constants are identical to the substrate due to the epitaxial relationship. [234–236] The a-axis lattice constant of the films on NCAO(110) and LSAO(110) were derived from a θ−2θ scan as well, while the in-plane lattice constants b and c were determined by refining a small set of film peaks (Tab. 4.2).

Evaluating the strain on CRO is not straightforward, since the lattice constants of the single crystal are highly dependent on temperature. The MIT is accompanied by large structural changes (sec. 2.2). Thus, it is a priori not clear, whether the films have to be compared to the short-c-axis or to the long-c-axis phase of CRO. We chose to show the strain in Tab. 4.2 relative to the L-Phase at high temperatures, since the strain values seem more reasonable. E.g. choosing S-CRO at 295 K as a reference would nominally yield 3.6 % strain for the b-axis for CRO on LSAO(001). In addition, calculating the unit cell volume indicates a better compatibility with the L-Phase. The Raman spectra of CRO on LAO show also a spectrum with a better compatibility with the L-Phase above the MIT(see 4.8.3).

Initially, it was confusing to us, why the longer lattice constant

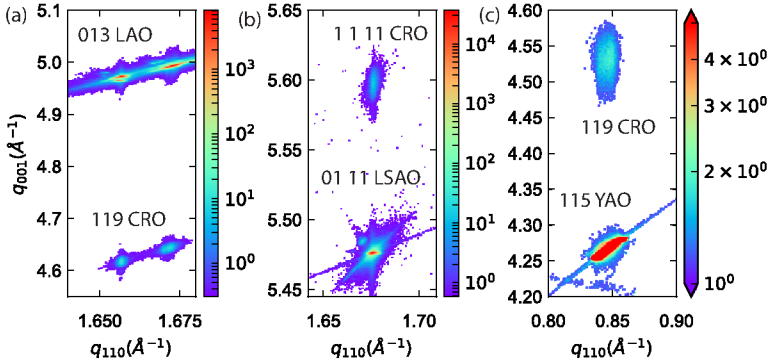

Figure 4.16: Typical Reciprocal Space Maps (RSM) of the c-axis oriented samples. The substrate peaks line up in-plane with the film peaks indicating a fully strained state. (a) (119) reflection of CRO on LAO. The double peak arises from the twin domain of LAO [234]. (b) (1 1 11) reflection of CRO on LSAO(001) (c) (119) reflection of CRO on YAO. Indices of substrate reflections refer to the unit cell of the substrate. Other crystallographic direction refer to the orthorhombic unit cell of CRO.

for the a-axis oriented samples is associated with the a-axis, since S-CRO at low temperatures shows the opposite behavior. However, one has to consider that the orientation of the axes is likely fixed at the high temperatures of the growth. At 400 K, S-CRO shows a reversed orthorhombicity with a longer a- than b-axis.

Hybrid Reflections

Besides detecting peaks corresponding to the CRO phase and substrates, we also found weak out-of-plane peaks for CRO on LAO(100) and on LSAO(001) using laboratory X-ray sources and the MPI-MF beamline at the ANKA synchrotron facility. The most prominent of these peaks was observed at a q of (0 0 1.93) for CRO films on LAO (in substrate notation, corresponding to $2\theta = 46°$ for Cu K-$\alpha 1$ radiation) (Fig. 4.18). A similar peak was found for Sr_2IrO_4, Sr_2RuO_4, Sr_2TiO_4 thin films [237–239] and in previous reports of Ca_2RuO_4 thin films [141, 240]. The position is close to the expected (220) reflection of $CaRuO_3$, which was at first confusing for the growth optimization

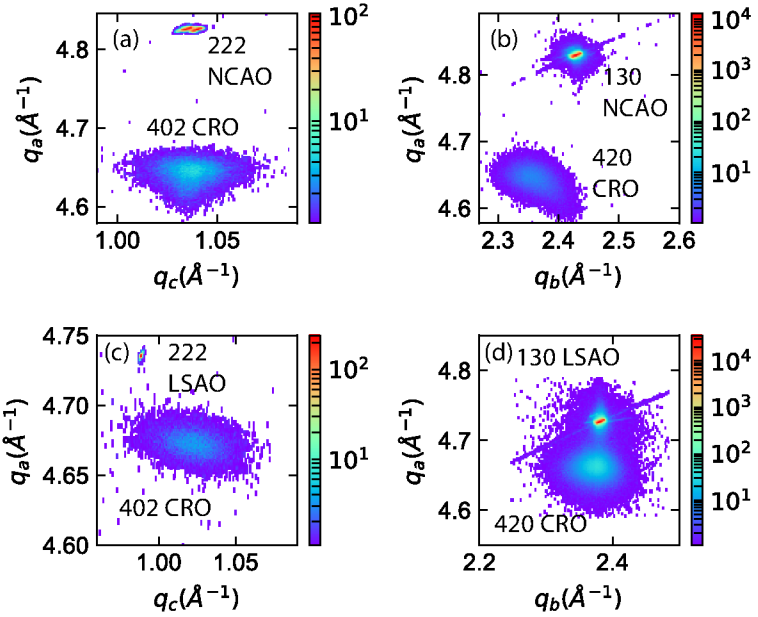

Figure 4.17: Reciprocal space maps (RSM) of a-axis oriented CRO films. (a) (H0L) plane of CRO on NCAO revealing a strained state along the c-axis. The triangular shape of the film peak indicates partial relaxation. (b)(HK0) plane of CRO on NCAO showing a relaxed lattice along the b-direction. (c) H0L plane of CRO on LSAO(110) showing a relaxed c-axis. (d) (HK0) plane of CRO on LSAO(110) revealing a strained state along the b-axis. Indices of substrate reflections refer to the unit cell of the substrate. Other crystallographic direction refer to the orthorhombic unit cell of CRO.

	a(Å)	ε_a(%)	b(Å)	ε_b(%)	c(Å)	ε_c(%)	$\lvert\frac{a-b}{a+b}\rvert$ (%)
S-CRO 400 K [45]	5.36		5.35		12.26		0.09
S-CRO 295 K [90]	5.41		5.49		11.96		0.73
O-CRO 295 K [90]	5.33		5.32		12.37		0.09
NCAO (110)	5.42	1.1	5.30	-0.95	12.11	-1.3	1.12
LSAO (110)	5.38	0.36	5.30	-0.95	12.22	-0.36	0.19
LAO (100)	5.36	-0.02	5.36	0.16	12.24	-0.19	0.00
LSAO (001)	5.31	-0.89	5.31	-0.71	12.37	0.87	0.00
YAO (001)*	5.33	-0.55	5.19	-3.1	12.45	1.5	1.39

Table 4.2: Room-temperature lattice parameters of CRO thin films compared to literature values for bulk CRO below and above the MIT. The strain relative to S-CRO at 400 K is given. Positive strain indicates tensile strain, negative strain indicates compressive strain. *The orientation of the film on YAO(001) was not determined in this thesis. Based on the tendency that the a-axis is longer than the b-axis for CRO thin films, we chose to assign the lattice constants similarly for CRO on YAO.

process. However, we find that they show an unusually sharp shape in reciprocal space and exhibit a φ-dependence (Fig.4.18), which is not expected from specular reflections involving a single crystallographic plane.

A possible explanation is the phenomenon of so called *hybrid reflections*. For single crystals, it is well-known that the Bragg scattering condition can also be fulfilled in an interlinked fashion [241, 242]: First, the photons are scattered from one set of planes of the crystal, but then it can also occur that they meet the condition for another set of planes before exiting the sample and are scattered a second time. This causes the appearance of a so called *double reflections*, which is also referred to as *Renninger effect*[241]. Here, it turns out that the reciprocal space position of the double reflection $\boldsymbol{q_D}$ corresponds simply to the sum of the momentum transfers of the first ($\boldsymbol{q_A}$) and second ($\boldsymbol{q_B}$) set of planes: $\boldsymbol{q_D} = \boldsymbol{q_A} + \boldsymbol{q_B}$. Thus, the resulting reflections are commensurate, i.e. integer positions in reciprocal space. Only $\boldsymbol{q_A}$ and $\boldsymbol{q_B}$ must obey the selection rules of the space group, but not $\boldsymbol{q_D}$. A similar effect has been found for films, where the scattering off a substrate plane and subsequently from a film plane (or vice versa) yields a double reflection [243, 244]. Here, the reflection of the film $\boldsymbol{q_f}$ and the substrate $\boldsymbol{q_s}$ do not necessarily share the same lattice constants.

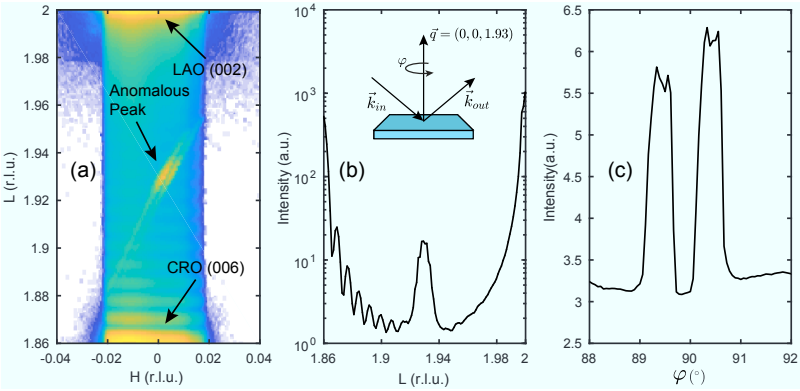

Figure 4.18: Possible hybrid reflection of CRO on LAO. Synchrotron X-ray diffraction data of an anomalous peak at the (0,0,1.93) position for a CRO film on LAO (in pseudocubic notation of LAO) (a) RSM showing the shape of the anomalous peak at $\varphi = 89.4°$ (b) Same scan integrated along the h-direction. The inset shows the measurement geometry of the φ dependence. (c) φ-dependence of the anomalous peak.

Thus, the resulting reflection $\boldsymbol{q_d}$ can be incommensurate:

$$\boldsymbol{q_f} = h_f\boldsymbol{a_f^*} + k_f\boldsymbol{b_f^*} + l_f\boldsymbol{c_f^*} \qquad \boldsymbol{q_s} = h_s\boldsymbol{a_s^*} + k_s\boldsymbol{b_s^*} + l_s\boldsymbol{c_s^*} \qquad \boldsymbol{q_d} = \boldsymbol{q_f} + \boldsymbol{q_s} \tag{4.2}$$

The observed (0 0 1.93) for CRO on LAO would fit well a combination of $q_f = (hk3)$ and $q_s = (-h-k1)$[244]. Since we assume a coherent epitaxial strain between film and substrate, the hk-values cancel each other and thus cannot be unambiguously defined. The hk components can naturally explain the φ-dependence of such a type of reflection.

4.8.2 Transmission Electron Microscopy

The microstructure of films on NCAO(110), LAO(100) and LSAO(001) was investigated using high-resolution transmission electron microscopy in High-Angle Annular Dark Field (HAADF) mode. The measurements were conducted by S. K. Sinha. High magnification images show coherent growth with only minor disorder in proximity to the interface (Fig. 4.19)

Low magnification overview images of films are shown in appendix C. While CRO on LAO and LSAO show a smooth surface, CRO

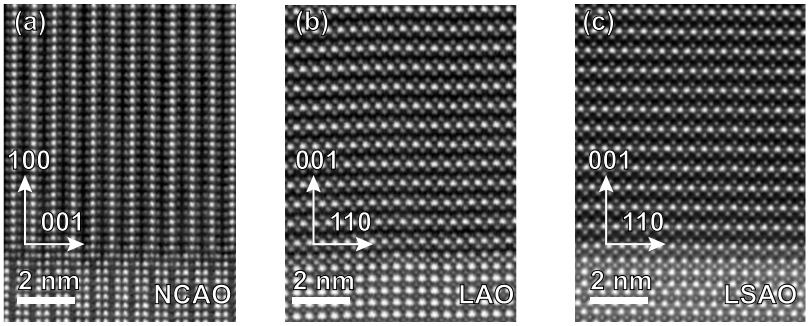

Figure 4.19: High-magnification HAADF images showing a cross-section of substrate-film interface for (a) CRO on NCAO (b) CRO on LAO and (c) CRO on LSAO(001). Crystallographic directions are referring to the orthorhombic unit cell of CRO.

on NCAO exhibits a wavy surface presumably due to island growth, which agrees well with the surface roughness of $\approx 3\,\mathrm{nm}$ obtained in X-ray reflectivity measurements. This also corresponds well to the RHEED images acquired during the growth, which are compatible with a 3D-island growth (sec. 4.6). CRO on LAO shows stacking faults similar to out-of-phase-boundaries observed in Sr_2RuO_4 thin films [57]. Such defects form due to different stacking sequence of the perovskite structure of $LaAlO_3$ and the K_2NiF_4-type structure of CRO [245]. This analysis shows that choosing a tetragonal substrate can lead to an effective suppression of such defects.

4.8.3 Raman Spectroscopy

A CRO film on LAO(100) from the generation depicted in Fig. 4.8 was investigated using Raman spectroscopy. Nominally, the film should have a thickness of 44 nm, but due to the problems of this generation of samples in the growth iteration, the effective thickness of the CRO phase might be thinner. However, the Ca_2RuO_4 phase can be clearly identified in XRD. In terms of lattice constants and strain state, the films is identical to the higher-quality films grown later. Thus, we believe that the Raman spectra are also representative for the later generation of CRO films on LAO.

The spectrum was acquired using a HORIBA JOBIN YVON LabRAM HR800 spectrometer using a wavelength of 632.8 nm. This

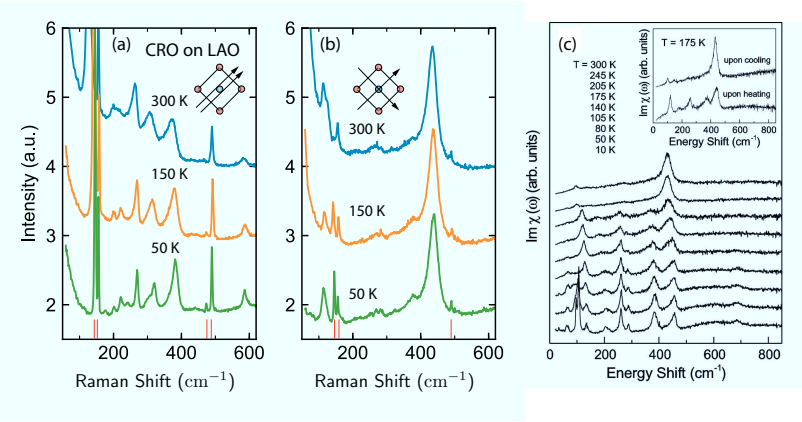

Figure 4.20: Raman spectroscopy on CRO film on LAO. (a) Crossed geometry (b) Parallel geometry. Substrate modes are indicated with red ticks. (c) Crossed channel of a $Ca_{2-x}Sr_xRuO_4$single crystal with $x = 0.09$ tracked through the MIT. [246] Vis-à-vis, the proximity of CRO on LAO to the L-Phase of CRO can be clearly seen. Interestingly, the spectrum shows no changes despite the presence of an MIT at 290 K in CRO on LAO. The polarization direction of the incoming and outgoing light relative to the Ru-atoms (blue) and O-atoms (red) is indicated in the sketches. Changes in the background are caused by contributions from the strong elastic line, which were not completely suppressed at higher temperatures.

setup allows positioning of the focus of the probing laser with submicron-precision [247]. This allowed us to selectively enhance the sensitivity toward excitations coming from the substrate and the film. A detailed description of this setup can be found in Ref. [55]. Using this technique, we can quickly identify the film modes and suppress the substrate modes (Fig. 4.20). The LAO substrate is well suited for Raman studies, since it has a large window free from phonons, where film modes can be studied.

We measured with incoming polarization along the (100)/(010) direction (CRO on LAO is twinned) and analyzed the outgoing polarization in terms of the component parallel to the incoming polarization (*parallel*) and the component perpendicular to the incoming polarization (*crossed*). The film modes in the parallel channel can be well matched with modes of the single crystal [31]. Due to the epitaxy, some film modes show a shift up to 10 % in frequency compared to

S-CRO. The crossed polarization channel has been investigated in a $Ca_{2-x}Sr_xRuO_4$ single crystal with $x = 0.09$[246]. Here, the MIT is suppressed to 220 K and thus can be studied more conveniently in typical cryostats. The Raman spectra above the MIT (L-Phase) and below the MIT (S-Phase) show striking difference in the crossed channel (Fig.4.20c). This distinct difference allows us to identify CRO on LAO as being closer to the L-Phase, which matches the lattice constants and the O-K-edge XAS showing an elongated octahedron (sec. 4.8.4). Interestingly, no large changes in the spectrum across the MIT at 290 K were observed.

Since CRO on LAO orders antiferromagnetically below 150 K (sec. 5.2.1), we also searched for single- and two-magnon excitations, which were observed in the AFM state of the CRO single crystal [31]. However, no signatures could be found.

4.8.4 Oxygen K-Edge X-Ray Absorption

A set of c-axis oriented films was investigated using X-ray absorption spectroscopy at the O-K-edge, which has proven to be a useful tool in oxide research to probe the t_{2g} and e_g orbital states of the d-valence shell through the hybridization of the 4d-orbitals with the 2p-orbitals of oxygen. Specifically, CRO O-K-edge XAS studies focused on pre-edge peaks at 528.5 eV (peak A) and 529.5 eV (peak B) (Fig.4.21). These peaks can be derived from transitions at the apical oxygen (A) and basal plane oxygen site (B) of the RuO_6-octahedra [29, 248–250]. Thus, the intensity ratio of these peaks be used to quantify the population of the xy orbital vs. the xz/yz-orbitals within the t_{2g} manifold. CRO exhibits compressed octahedra at low temperatures, thus the tetragonal crystal field lowers the xy-states relative to the xz/yz-states. In this case, the majority of the holes occupies the apical oxygen sites, which can be seen by the larger intensity at peak A than B(Fig.4.21). At 300 K, the octahedron is approximately regular, which is mirrored in the equal intensities of peak A and B [29]. Following the previous studies, we conducted a O-K-edge study on CRO films at the BL29 BOREAS beamline at the ALBA synchrotron facility, Barcelona (LAO and LSAO(001)) and at the UE46_PGM1 beamline at the BESSY synchrotron facility, Berlin(YAO). Circular polarized light was used for the measurements of CRO on LAO and LSAO, while for CRO on YAO linearly π-polarized light was used.

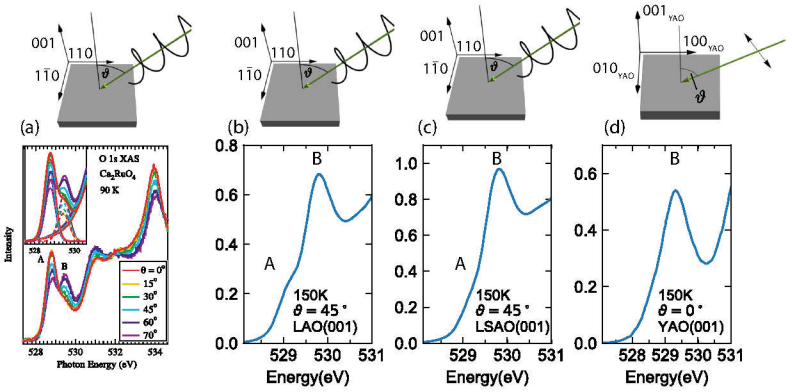

Figure 4.21: Oxygen K-edge X-ray absorption spectroscopy of bulk CRO in comparison with the CRO thin films. Spectra were taken in total electron yield (TEY) mode. (a) XAS analysis using performed in Ref. [29] of a CRO single crystal at $90\,\mathrm{K}$ showing pre-edge transitions related to the holes associated with the hybridized orbitals of the apical oxygen (A) and basal plane oxygen (B). The angle dependence reveals a large hole population at the apical sites indicating a compressed RuO_6 octahedron. (b) Grazing incidence measurement for CRO on LAO. The feature A is much weaker than B suggesting an elongated octahedron. (c) Feature A is further suppressed fro CRO on LSAO(001) until it vanished for (d) CRO on YAO. The top panels indicate the geometry and whether circular polarized or linear polarized π-light was used.

The measurements show an intensity ratio that is compatible with an elongated octahedron, since peak A is faint and peak B is prominent. Most holes reside in the states associated with the basal oxygen sites. We did not detect a change of the spectrum across the MIT in CRO on LAO. The evolution of the intensity ratio of peak A vs. B follows the compressive biaxial strain on the system, i.e. CRO on LAO shows a relatively strong peak A, while it is reduced for CRO on LSAO and then for CRO on YAO with the largest compressive strain peak A practically vanished.

4.9 Electrical Transport

Transport properties of the samples were studied using a Quantum Design PPMS setup. The standard four-point probe technique with

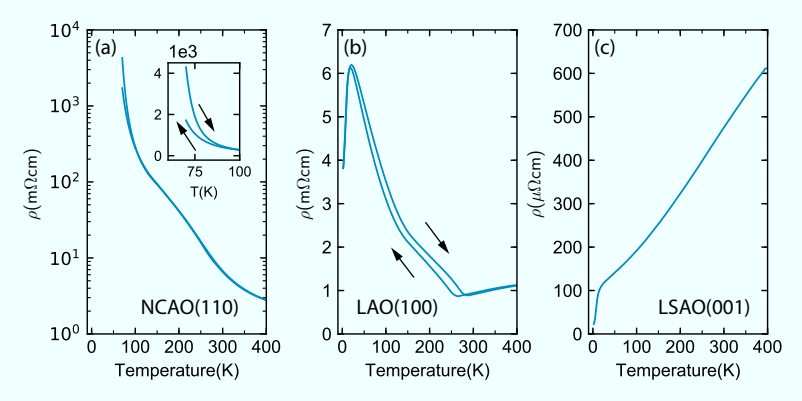

Figure 4.22: Electrical transport measurements along the ab-planes of (a) CRO on NCAO (b) CRO on LAO and (c) CRO on LSAO(001). The inset of (a) shows a magnification of the low-temperature region. Here, an hysteresis was measured, which might indicate a phase transition. CRO on LAO and LSAO(001) show a downturn at low temperatures connect to a metallic FM phase. CRO on LAO shows a hysteresis over a broad temperature range starting at a weak MIT at $290\,\mathrm{K}$ and ending at the transition to the FM phase.

sputtered Pt-contacts placed in-line was used. Applied currents range from $1\,\mathrm{A}$–$10\,\mathrm{A}$, giving current densities of $1\,\mathrm{A\,cm^{-2}}$–$100\,\mathrm{A\,cm^{-2}}$ depending on the dimensions of the sample. These current densities are by far exceeding the thresholds needed to induce an insulator-to-metal transition in the bulk [251]. Although it would highly desirable to see this electric field effect in CRO films, we could not find evidence for any dependence on current strength. This is probably related to the overall notion that the electronic structure and the crystal structure go hand-in-hand. In such a case, the pinning of the substrate might prohibit the structural changes and prevent the change in the electronic structure.

CRO on NCAO(110) films show an insulating behavior in the whole measured temperature range. To the best of our knowledge, this constitutes a novelty for CRO, since typical modifications (pressure, Sr-substitution) of CRO suppress the MIT and stabilize the metallic state of CRO. The insulating phases of CRO are associated with larger tilt and a compressed RuO_6-octahedra (see ch.2). In comparison to the other films, CRO on NCAO exhibits substantial orthorhombicity and a relatively short c-axis indicating that both distortions are present.

Despite showing no MIT up to 400 K, we reproducibly measured a hysteresis starting at ≈ 100 K, which might be connected to a phase transition in the insulating state. A kink in the temperature trend of the ϑ-position taken while investigating the antiferromagnetic peak in this material might be connected to this (sec. 5.2.3).

The result of our resistivity measurements of CRO on LAO match previously reported data on a 170 nm film [240]. We find as well that films on LAO show a MIT at $T_{\mathrm{MIT}} = 290\,\mathrm{K}$ similar to single crystals, but the magnitude of the resistivity jump at the transition is much smaller than in bulk. [92] As conjectured in previous reports [240], this might be related to the epitaxial relationship between film and substrate, which prevents CRO from completing the transition and keeps it in a metastable state as indicated by the broad hysteresis. The lattice constants of CRO on LAO in the metallic phase at room temperature are similar to the metallic phase in bulk CRO above the MIT (Tab. 4.2). Assuming that the in-plane lattice constants of CRO do not change significantly below the MIT due to the pinning of the substrate, the material can be considered to be 1 %–2 % compressively strained in the ab-plane relative to the insulating phase of the single crystal. The resistivity also shows a downturn at $T_{\mathrm{C}} \approx 20\,\mathrm{K}$ where the hysteresis concomitant with the MIT vanishes. Previous studies of CRO thin films on LAO and on pressurized single crystals attribute the cusp to a metallic ferromagnetic phase [42, 43, 240]. Except for the suppression of the MIT, its transport properties are similar to those of bulk CRO under 0.5 GPa–1 GPa hydrostatic pressure [41]. A kink at 150 K is likely associated with the AFM detected at 150 K via REXS and magnetometry (sec. 5.2.1).

The films grown on LSAO(001) substrates show a metallic temperature dependence in the temperature range 2 K–400 K. Similar to CRO on LAO, a downturn at $T_{\mathrm{C}} \approx 20\,\mathrm{K}$ is found, which we can also link to a ferromagnetic phase in magnetometry and magnetoresistance (see sec. 5.1.1). The lattice constants of films on LSAO(001) agree well with structural parameters known from metallic phases of bulk CRO [40]. Relative to the structure of insulating bulk CRO at 295 K, the films on LSAO(001) can be regarded to be 2 %–3 % compressively strained in the ab-plane. The film on LSAO exhibits a residual resistivity of $\rho(2\,\mathrm{K}) = 30\,\mu\Omega\mathrm{cm}$, which is higher than the $3\,\mu\Omega\mathrm{cm}$ measured in pressurized single crystals [42]. This difference can likely be attributed to defects caused by epitaxial strain or steps on the substrate surface

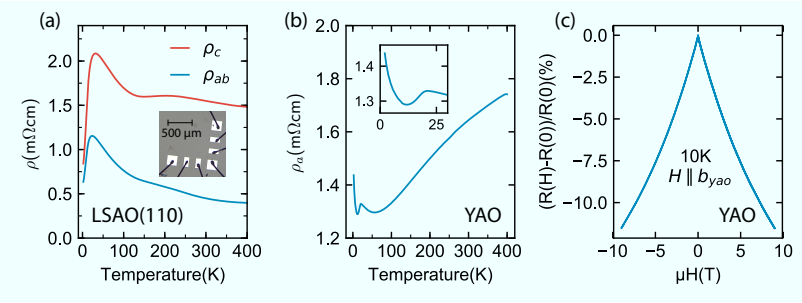

Figure 4.23: Resistivity measurements on CRO on (a) LSAO(110) and (b) CRO on YAO(001). The inset in (a) shows the contact structure used to perform measurements along the ab-plane and c-axis. The inset in (b) presents a magnification of the low-temperature upturn. (c) Transverse Magnetoresistance of CRO on YAO showing a shape reminiscent of weak localization.

and is similar to what has been observed when comparing $SrRuO_3$ thin films with their single crystal counterpart [252].

CRO films grown on LSAO(110) are most similar to CRO on LAO(100) exhibiting resistivities in the mΩcm range (Fig. 4.23). However, up to 400 K no MIT was detected. A hysteresis, if present, is close to intrinsic hysteretic behavior of the measurement system and could thus not be unambiguously detected. A downturn at $\approx$ 20 K is detected, which can be attributed to a transition into a metallic ferromagnetic phase similar to the one found in all other films except for CRO on NCAO (see 5.1.1)

Since the c-axis is in-plane for CRO on LSAO(110), we can simultaneously measure the resistivity along the c-axis ρ_c and the ab-plane ρ_{ab}. The ratio $\rho_c/\rho_{ab} \approx 2$ is relatively small compared to pressurized bulk [42] indicating that that the electronic transport along the c-axis is coherent. This is corroborated by the anomaly in both channels at $\approx$ 150 K, where we detected an antiferromagnetic transition using REXS and magnetometry (sec. 5.2.2). This dip appears to be stronger along the c-axis. The transition to a FM metallic state is visible along both directions confirming the emergence of a 3D metallic state in the material [42].

The transport of CRO on YAO was difficult to measure due to its thinness (8 nm) and the high epitaxial strain. Especially the latter likely contributes to a high defect density. One film that shows metal-

lic conductivity down to 60 K is shown in Fig. 4.23. Here, the drop in resistivity around 23 K indicates that we are again sensing the FM phase known from the other films and the pressurized single crystal. In principle, we cannot exclude an $CaRuO_3$ impurity phase to be responsible for the metallic conductivity. However, the width of the peaks in the $\vartheta - 2\vartheta$ scan (Fig. 4.14), matches the thickness measured with XRR indicating that the majority phase is indeed Ca_2RuO_4. For such a small thickness, it is hard to imagine that undetected small patches of $CaRuO_3$ can create a metallic channel. Interestingly, the sample shows an upturn at 60 K, which is interrupted by the FM transition, but then increases sharply at low temperatures. A transverse magnetoresistance (MR) measurement ($J \parallel a_{\mathrm{yao}}$, $H \parallel b_{\mathrm{yao}}$) shows a large negative MR similar to the metallic CRO in LSAO(001) (sec. 5.1.1). The shape is characteristic of so called *weak localization* (WL), which is typical for disordered systems [253, 254]. Here, electrons interfere with their own scattered wavefunction adding corrections to the electric conductivity. The interference can be perturbed by a magnetic field making it observable in the MR. Disorder is certainly expected in this film due to the high residual resistivity in the mΩcm range. Improved sample quality might show a complete metallic behavior similar to CRO on LSAO(001).

4.10 Conclusion, Discussion and Outlook

We have presented a synthesis process yielding high-quality films starting from the precursors RuO_2 and $CaCO_3$. Careful optimization of the growth conditions allowed us to grow two different types of films: One set consists of c-axis oriented films on LAO(100), LSAO(001) and YAO(001). The other set consists of a-axis oriented films on NCAO(110) and LSAO(110). Already the basic characterization shows substantial modifications of bulk CRO. By applying epitaxial strain, we can tune the resistance in the material across six orders of magnitude. The MIT found in bulk was only detected for CRO on LAO, but appears only weakly.

Oxygen K-edge XAS suggests that the RuO_6 octahedra are elongated for the c-axis oriented films, which is characteristic for metallic phases of bulk CRO. CRO on LSAO(001) shows a typical response of a metallic CRO phase, thus the XAS data is consistent with the

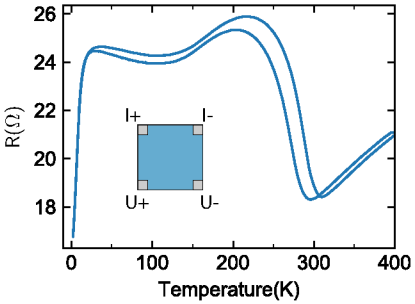

Figure 4.24: Temperature dependence of the resistivity of a high-quality 80 nm thick CRO film on LAO measured in van-der-Pauw geometry. A clear deviation from the in-line measurement of the sample shown in Fig. 4.22 can be seen.

findings for the single crystal. The transport data of CRO on YAO is less clear cut, but can be well explained by an intrinsic metallic dependence and a weak localization effect due to high disorder, making its O-K-edge XAS data also compatible with typical metallic phases of CRO. However, CRO on LAO is a peculiar case. The FM at low temperatures, the XAS and Raman data would classify it as the L-Pbca phase of CRO (metallic), while the insulating behavior and the AFM (sec. 5.2.1) would be consistent with the S-Pbca phase of CRO (insulating) below the MIT. Mixed phases of CRO were reported under pressure and also suggested for CRO on LAO in previous reports [40, 43, 142]. However, the phases would need to be structurally and electronically much closer to explain the XAS and Raman data. Thus, more research is needed to unambiguously establish a phase coexistence for CRO on LAO. One approach could include using scanning near-field optical microscopy (SNOM) to spatially resolve conducting and metallic areas [255]. High-resolution X-ray diffraction might be able to sense two different c-axes at low temperatures arising from a S- and Pbca-phase.

LDA+DMFT calculations suggest that the MIT in CRO is driven by the structural transition [104]. In turn, since we have no indication for structural changes for CRO on LAO, a purely electronic Mott-transition might be a viable scenario. This would be similar to what has been observed at the surface of $Ca_{2-x}Sr_xRuO_4$with $x = 0.1$[256].

We also want to critically assess the transport data for CRO on LAO. As we noted earlier, the electrical transport reported in the literature is somewhat inconsistent. In the report by Wang et al., the resistance of a 20 nm-film showed a metallic behavior down to 100 K where it transitioned to an insulating behavior until 20 K and then became metallic by entering the FM phase [139]. The next report

by the same group showed a film with only insulating behavior [140]. Miao et al. presented data of a 170 nm thick film, which is similar to the data presented in Fig. 4.22 [142], while in a subsequent Sr-substitution study, the transport appeared monotonously decreasing indicating a more metallic behavior [141]. Our highest-quality 50 nm-samples showed the behavior depicted in Fig. 4.22, when measured in-line. The data depicted in Fig. 4.9 suggests that the transport behavior is very sensitive to the growth conditions. Samples characterized by XRD as high-quality and measured not in-line but in van-der-Pauw geometry [257] sometimes showed a behavior similar to Fig. 4.24, which, compared to the in-line measurements, indicates a heterogeneous system. Such inhomogeneity could be intrinsic due to a mixed phase state (see above). However, the length scales of the structures to measure transport are in the 0.1 mm–1 mm range, which should be larger than the length scale of individual phases in a mixed phase state. The band gap in CRO has been shown to be sensitive to crystalline defects [258]. Since CRO on LAO is at the verge between a metallic and insulating state and stays in a metastable state between the MIT and the FM-phase, it is likely to be even more prone to defects than bulk CRO. A natural unavoidable macroscopic defect is the twin boundary of the LAO substrate, which is transferred to the film [234]. In order to elucidate the influence of defects on the system, again a SNOM study could give insights.

In light of the unusual magnetic moment direction in CRO on NCAO (sec. 5.2.3), it would be interesting to perform O-K-edge XAS measurements on this system. Such experiments could clarify the octahedral compression, which is predicted to be tuning the magnetic moment direction in the strong SOC picture [106].

X-ray structural refinement studies on thin films have not yet evolved to a regular technique as for bulk systems. However, pioneering work has shown that a structural refinement can yield valuable information despite the restricted usable reciprocal space for thin films [259]. A similar study might be able to quantify the octahedral distortions in the CRO films.

It would be desirable to extend this study to substrates which exert biaxial tensile strain instead of compressive strain. This might stabi-

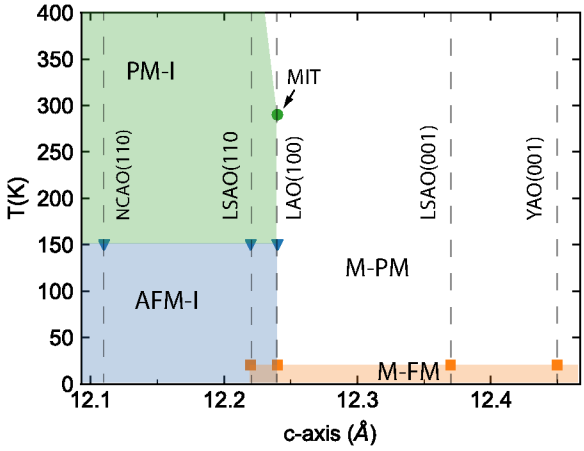

Figure 4.25: Phase diagram c-axis vs. temperature of films on all investigated substrate types. PM-I: Paramagnetic and insulating. AFM-I: Antiferromagnetic and insulating. M-PM: Metallic-paramagnetic. M-FM: Metallic-ferromagnetic.

lize antiferromagnetic insulating states similar to NCAO(110) * and potentially opens up regions in the pressure-phase-diagram which are inaccessible for compressive bulk methods (Fig. 4.25). As mentioned in sec. 4.5, we attempted to grow on LSAT(100) and $NdGaO_3$(001) and (110) using various growth conditions, but this only yielded a mixture of $CaRuO_3$ and Ca_2RuO_4 phases. A possible reason might be that, since the lattice parameters of LSAT and NGO are closer to $CaRuO_3$, that this phase is thermodynamically more favored than on other substrates. We note that, however, the growth of CRO on $NdGaO_3$(110) using molecular-beam epitaxy (MBE) has been reported [144], which suggests that the synthesis is in principle possible and might also be achievable using PLD under the appropriate growth conditions. A large difference between PLD and MBE is the kinetic energy of the arriving particles. Using a high background gas pressure allows deceleration of the ions in the PLD plasma plume and might bring conditions closer to MBE.

*Since the MIT is not suppressed, but the insulating state is enhanced in CRO on NCAO, we classify it as having rather "tensile strain character" compared with the other films and pressurized single crystals.

As an outlook, we also want to suggest routes to improve the growth process using PLD. We realized that even when upholding the growth conditions described above, the growth was not always reproducible. We believe that the narrow temperature window needed for the growth might be responsible for this. The pyrometer used to measure the temperature integrates the infrared radiation within its detection spot and applies basically the Stefan-Boltzmann-law including a material specific emissivity. In our case, the pyrometer senses the infrared radiation coming from the substrate, the Pt-paste and the Ta-block. The surface morphology can have a substantial influence on the emissivity of a material [260]. Since the surface of the Pt-paste squished between substrate and block is always different, because the process is done by hand, we believe that this is likely a source of non-reproducibility. To calibrate the temperature directly on the substrate, we tried to use the sublimation point of RuO_2 as a reference, by depositing a small film before heating the substrate. Surprisingly at $p_{O2} = 60\,\mathrm{mtorr}$, RuO_2 already started sublimating at 570 °C*, which was unusable as a reference for the growth temperature. However, one might be able to monitor the sublimation rate by RHEED and deduce the temperature at higher temperatures. Alternatively, another phase transition might be used for calibration. Ag, Au have melting points close to the growth temperature of 900 °C: (961.78 °C and 1064.18 °C), which might be used for this purpose. However, one needs to make sure that such a calibration does not interfere with the subsequent growth process.

Conceptually, radiant heaters might yield a better temperature homogeneity than the IR-laser heater system used during this work. Here, precautions must be taken to mitigate potential evaporation from heating elements at the high growth temperatures [261].

Finally, we want to acknowledge recent progress in synthesizing single-layer ruthenates by adsorption-controlled molecular beam epitaxy (MBE). Typically, MBE films are grown in a RHEED controlled layer-by-layer fashion [262]. While such a mode allows atomic layer precision, it is difficult to maintain the correct stoichiometry [263]. In

*The RuO_2 was deposited in vacuum at room temperature, where it formed a grey layer on top of a LAO substrate, presumably elemental Ru. The sublimation temperature is measured by using the pyrometer directed at the bare substrate surface after complete evaporation. The temperature is subject to the emissivity $\varepsilon_{\mathrm{LAO}}$.

addition, metallic Ru can only be evaporated with an e-beam heater in an MBE-setup, which provides a relatively unstable flux of atoms. Recently, however, it was shown that working with a codeposition method (PLD-like) with slightly Ru-rich conditions allows to grow in a regime, where $CaRuO_3$ and gaseous RuO_x species are thermodynamically favored [138]. Since the RuO_x excess evaporates, the tight constraints on the Ru-flux are lifted. This so called adsorption-controlled growth method was able to produce superconducting Sr_2RuO_4 thin films [58, 66] underlining the high-quality that is possible using this method. Employing this technique might offer an alternative for synthesizing Ca_2RuO_4 thin films [143].

5 Magnetic Properties

The large magnetostructural coupling in Ca_2RuO_4 single crystals makes the study of the epitaxial strain effect on magnetic properties CRO one of the prime targets of this work. In this chapter, we present the experimental results obtained using magnetometry, magnetoresistance, polarized neutron reflectometry and resonant X-ray scattering (REXS). We show that the effect of epitaxy can indeed be considerable and lead to substantial changes into the magnetic anisotropy of the material.

5.1 Magnetometry and Magnetoresistance

5.1.1 Low-Temperature Ferromagnetic Phase

As it was visible in the transport properties of the films (sec. 4.9), a transition toward a metallic state below 20 K is observed for all the films except CRO on NCAO, which showed an insulating state at the lowest temperatures. Pressure studies on bulk CRO showed the formation of ferromagnetism below the low-temperature transition to the metallic state [42]. The phase is characterized by a low saturated moment $\approx 0.1\,\mu_B$ per Ru compared to the full moment of $2\,\mu_B$ per Ru indicating Stoner-type (itinerant) ferromagnetism (FM), where

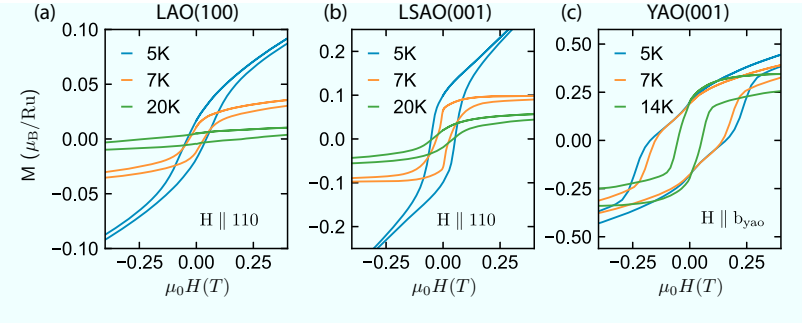

Figure 5.1: Low-temperature ferromagnetic phase studied with SQUID magnetometry. (a) 80 nm thick CRO film on LAO(100) (b) 40 nm thick CRO film on LSAO(001) and (c) 8 nm thick CRO film on YAO(001) . The saturated moment increases with compressive strain from the film on LAO (1 %) to YAO (3 %). The data was corrected for the linear diamagnetic contributions of the substrate and sample holder. Paramagnetic impurities likely cause the remaining linear background visible as an apparent non-saturating moment.

a partially polarized band structure allows for a fraction of the full moment to occur.

To investigate the FM at low-temperatures, we performed SQUID-magnetometry on the c-axis oriented films (LAO (100), LSAO (001) and YAO(001)). Hysteresis loops became visible below 20 K as expected by the FM state. The saturated moment increases with increasing compressive strain from $\approx 0.03\,\mu_B$/Ru on LAO to $\approx 0.1\,\mu_B$/Ru in LSAO and $\approx 0.3\,\mu_B$/Ru in YAO (see Fig. 5.1). The data is in accordance with literature on pressurized CRO single crystals, where increasing pressure led to higher saturated moments [42]. One might speculate that the structural distortions for CRO on YAO (orthorhombicity and large in-plane compressive strain) are favorable for inducing a rotation of the octahedra, which have been linked to FM in the CRO-system (sec. 2.2).

The temperature dependence of the magnetisation of CRO on YAO(001) reveals a clear anisotropy between the in-plane axes. This shows that the film is not twinned unlike CRO on LAO and LSAO(001) as expected from the orthorhombicity of the substrate. The orientation of the film relative to the substrate could not be established due to its thinness and the weak intensity of the X-ray peaks indicating the orthorhombicity. However, the structure of the a-axis oriented films

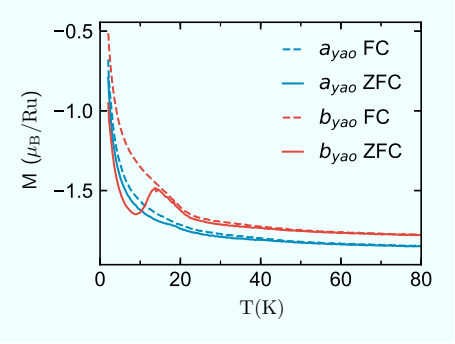

Figure 5.2: Temperature dependent magnetization of a 8 nm thick CRO film on YAO(001). The ferromagnetic transition starting at $T_C \approx 20$ K can be clearly discerned. The crystallographic orientation of CRO could not be determined due to thinness of the film. Substrate axes are given instead.

on NCAO(110) and LSAO(110) suggests that the longer in-plane axis of the film is the a-axis. In this case, the b-axis of YAO (b=5.31 Å vs a=5.18 Å) would correspond to the a-axis of CRO. An easy axis along a corresponds to the situation for pressurized bulk CRO at 1.5 GPa[41]. Measuring low moments ($\approx 1 \times 10^{-6}$ emu) with SQUID-VSM needs to be done carefully, since due to the low mass of thin films (≈ 1 g), ferromagnetic contaminants can easily cause artifacts in the SQUID signal [264, 265]. Indeed, we found that the Pt-backcoating used in the PLD process contains magnetic impurities and needed to be ground off before SQUID-measurements. The raw signal consists of a large signal coming from the diamagnetism of the substrate and sample holder (quartz), a paramagnetic signal from impurities and the signal from the film. The hysteresis loops shown were corrected for the diamagnetic signal by subtracting a linear background fitted the curves at high-fields. At low temperatures, however, the contribution from the paramagnetic impurities becomes comparable due to its Curie-type temperature dependence. This causes the apparent non-saturation in the loops at low temperatures. In these cases, the saturation moment can only be roughly estimated by the coercive field which is imprinted in the shape of the loop. The lower the temperatures one is interested in, the higher the chance that some contaminant becomes ferromagnetic. In order to rule out this possibility, i.e. to probe for true bulk magnetism of the film, we studied an 80 nm thick CRO film on LAO using polarized neutron reflectometry (PNR) at NREX, Garching [266]. (Fig. 5.3) The technique is similar to X-ray reflectometry, but instead of using photons, it is based on the refraction of neutrons. The advantage of the neutron as a probe is its magnetic

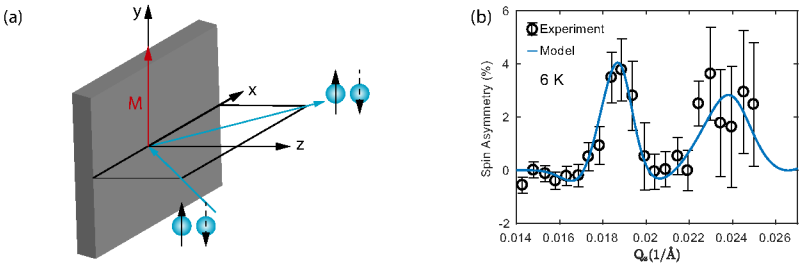

Figure 5.3: (a) Measurement geometry of the polarized neutron reflectometry (PNR) experiment. Based on [269]. (b) Spin asymmetry of CRO on LAO at 6K determined from polarized neutron reflectometry. The sample was cooled in a field of $4.5\,\mathrm{k}$ along the [110] axis of CRO. The line is the result of a model calculation based on a homogeneous layer of CRO with a ferromagnetic moment of $0.08\,\mu_\mathrm{B}$ per Ru.

moment, which can couple to the electron spin through dipolar interaction. This effectively makes a magnetic material birefringent in terms of the spin of the incoming neutron relative to the magnetization of the sample. This is exploited in PNR by using polarized neutrons as a probe: Neutrons are spin-polarized along the magnetization of the sample, refract and then one selects the non-spin-flipped-channel to detect neutrons with the same polarization as the incoming neutrons (*up-up* channel). The same measurement is performed for neutrons polarized in the opposite direction of the magnetization of the sample (*down-down*). The ratio of the two channels is called spin asymmetry $A = (R^{++} - R^{--})/(R^{++} + R^{--})$ and can be modeled to extract the moment size. More detailed treatments of this technique can be found in e.g. [267]. For the measurement, the sample was cooled to 6 K with field of 4.5 kOe applied along the (110) axis of CRO. Modeling of the spin-asymmetry was performed using the SIMULREFLEC software package [268]. Using structural parameters obtained by XRR as initial parameters yields a good fit for $0.08\,\mu_\mathrm{B}$ per Ru, which is in good agreement with the data recorded in the SQUID measurements (Fig. 5.1).

The low-temperature ferromagnetic phase (LT-FM) phase is characterized by a giant positive magnetoresistive (MR) effect in pressurized bulk, when measuring with current $J \| ab$ and $H \| c$ [44]. We also observed a similar effect in the films on LAO measuring in the transverse configuration with $H \| c$ and $J \| 110$. Remarkably, there is already a

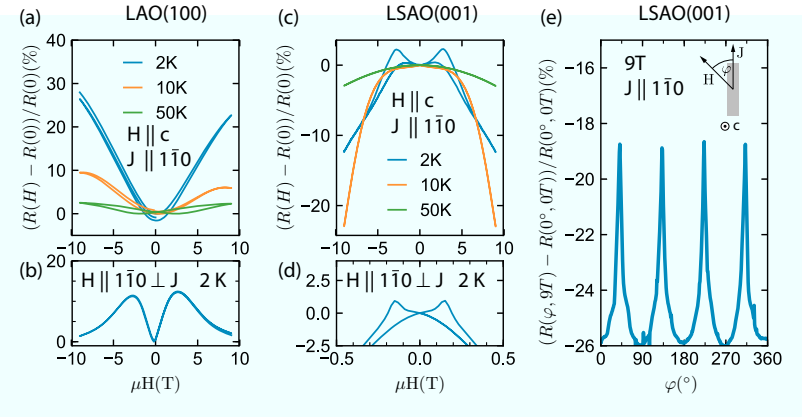

Figure 5.4: Transverse magnetoresistance (MR) in the low-temperature ferromagnetic phase. CRO on LAO: (a) For a field along c, a hysteresis at $50\,\mathrm{K}$ in the antiferromagnetic state can be observed (see also Fig. 5.7), which vanishes and then a giant positive MR effect emerges. (b) For $H \parallel a/b$, the MR is initially positive, but then reverses at higher field. CRO on LSAO(001): (c) For $H \parallel c$, MR stays negative at all temperatures showing the strongest effect close to T_C. At $2\,\mathrm{K}$ a hysteresis can be observed with a coercive field of $2.8\,\mathrm{T}$. (d) For $H \parallel a/b$ at $2\,\mathrm{K}$, the MR stays negative, but the hysteresis is much smaller with a coercive field of $0.15\,\mathrm{T}$ (e) Anisotropic MR at $2\,\mathrm{K}$ showing a characteristic fourfold pattern when rotating $\boldsymbol{H}$ within the ab-plane. The MR is generally higher with an in-plane field than with $H \parallel \boldsymbol{c}$. The peaks are observed, when $H \parallel \mathrm{a/b}$. The small sketch shows the relation between $\boldsymbol{H}, \boldsymbol{J}, \boldsymbol{\varphi}$.

strong MR effect in the $1\,\%$ range at $50\,\mathrm{K}$ suggesting a hysteresis while sweeping the field (Fig. 5.4 and 5.7) suggesting the presence of FM above T_C. We will come back to this feature when discussing the AFM phase. On lowering the temperature deeper into the FM-phase, the MR rises significantly up to $28\,\%$ at $9\,\mathrm{T}$. When we apply the field transversely at $2\,\mathrm{K}$ parallel to the surface of the film along the $(1\bar{1}0)$ direction, initially a positive slope is visible, which then inflects to a negative one. CRO on LSAO(001) on the other hand shows a negative MR in both channels with a hysteresis appearing at low temperatures indicating a correlation with ferromagnetism. The ordinary MR-effect is based on the Lorentz-force, i.e. it is a function of $\boldsymbol{H} \times \boldsymbol{J}$. However, the observed anisotropy and the fact that the largest MR sets in with the FM phase, suggests a different mechanism, namely an effect based on the anisotropic magnetoresistance (AMR), which is a function of

the angle between the magnetization $\boldsymbol{M}$ and $\boldsymbol{J}$ [153]. In general, the function is based on the spin-dependent terms in the electron scattering functions, which is non-trivial and material-specific. Due to the spin-orbit-coupling in CRO, one naturally expects that the effect on the spin of the electron by the magnetic field also effects its orbital motion in some way causing an MR effect. In ferromagnetic metals, however, one can often link a negative MR to the suppression of spin-fluctuations enhancing the electron conduction [270]. Changes in scattering-cross-section of electrons can also be caused by the rotation of $\boldsymbol{M}$ in a magnetic field, which controls the orientation of the Landau orbitals relative to $\boldsymbol{J}$. The rotation of $\boldsymbol{M}$ in a magnetic field $\boldsymbol{H}$ is governed by the magnetocrystalline anisotropy causing it to be mirrored in the MR-effect.

The large positive magnetoresistance in bulk CRO is only poorly understood, but it was suggested that it could be caused by tunnel-MR (TMR). This effect arises when a thin insulating layer is sandwiched between two metallic FM layers. The matrix element for tunneling through the insulating tunnel barrier is dependent on the relative spin orientation of the two FM layers and thus leads to an MR effect. Depending on how the wavefunctions are matched at the interface (the FM layers can be of a different material), this effect can be positive or negative [271]. The argument, why this effect was attributed to TMR was the fact that CRO is driven through the MIT under pressure, which has been characterized as a first-order phase transition. A discontinuous phase transition is naturally characterized by an intermediate region with phase coexistence. In the case of CRO, this would be an FM metallic (FM-M) phase and an AFM insulating (AFM-I) phase. Assuming the right spatial dimensions for both phases, the insulating phase could form the tunnel barrier and a TMR effect could occur [44]. AMR-data presented in previous reports of CRO films on LAO indeed suggest a phase coexistence of the FM-M phase and AFM-I phase, which would corroborate the TMR-scenario [240].

Having the original report on MR of single crystalline CRO at hand, we can see distinct differences. The transverse MR with $\boldsymbol{H}\|\boldsymbol{c}$ for the single crystal at 2 K showed first a positive slope with increasing field, which switched to a negative one similar to $\boldsymbol{H}\|(1\bar{1}0)$ of the film (Fig.5.4a)[44]. The inflection point was correlated to the anisotropy field; If a field higher than this is applied, the magnetization will be fully aligned with the field. In our case, this field would be 2.5 T along

the 110 direction (9.5 T was given in Ref. [44], but this for a field along c, which was determined to be the hard axis). If one assumes that the negative MR at higher fields corresponds to the suppression of spin fluctuations of the FM-M phase, the data indicates that this is more effective along the in-plane 110 direction than the out-of-plane c-direction. FM thin films usually have their the hard-axes out-of-plane due to the shape anisotropy, which would explain the differences between the pressurized bulk and CRO on LAO [153].

CRO on LSAO(001) shows a negative MR with hysteresis with the field aligned along the surface and normal the surface, which suggests that the suppression of spin fluctuations is the main origin of the MR in both channels. A good indicator for this is also the fact, that the MR is actually higher for 10 K than for 2 K. The suppression of spin fluctuations is most effective close to the phase transition due to the diverging correlation length [272]. The magnitude of the MR is higher in-plane with $\Delta R/R(9\,\mathrm{T})=-26\,\%$ at 2 K with $\boldsymbol{H}\|110$ vs. out-of-plane with $\Delta R/R(9\,\mathrm{T})=-12\,\%$ at 2 K. The measurements at 2 K show a pronounced hysteresis. The in-plane coercive field in-plane of 0.15 T is much smaller than the out-of-plane coercive field with 2.8 T. An AMR measurement rotating the magnetic field $\boldsymbol{H} = 9\,\mathrm{T}$ about the 001-axis with $\boldsymbol{J}\|110$ shows a fourfold pattern with peaks, when $H\|110$. The fourfold symmetry indicates that orientation of the magnetization vs. the crystalline directions is governing the effect and not the orientation of $\boldsymbol{J}$ vs $\boldsymbol{H}$. Similar AMR scans on $SrRuO_3$showed cusps at the hard axes of $\boldsymbol{M}$[273]. Translating this result to CRO, this would put the easy axes along the 110 directions of CRO on LSAO, where the MR is most negative. This is different from pressurized bulk, where the easy axis was located along the a-axis [41]. Similar measurements of $Ca_{2-x}Sr_xO_4$ films on LAO show minima along the (010)/(100) directions for $x = 0$ and a switching to (110) at higher x [141]. An isovalent substitution with Sr shows increased metallicity similar to the higher compressive strain on LSAO(001) implying an analogous mechanism of switching the easy axis.

5.1.2 Antiferromagnetic Phase

Films showing an insulating phase, CRO on LAO(100) and LSAO(110), exhibit a zero-field (ZFC) / field-cooled (FC) splitting anomaly around 150 K in SQUID-VSM magnetometry (Fig. 5.5). The data for CRO

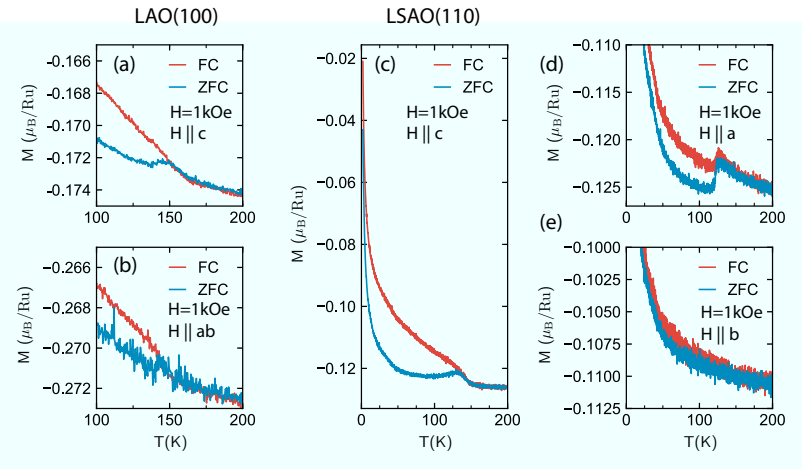

Figure 5.5: Antiferromagnetic phase transitions detected via SQUID VSM for a $80\,\mathrm{nm}$ thick CRO film on LAO(001) and $50\,\mathrm{nm}$ thick film on LSAO(110). (a) Along c-axis of CRO on LAO (b) Along a/b (CRO on LAO is twinned) (c) Along c-axis of CRO on LSAO(110) (d) Along b-axis of CRO on LSAO(110). For all measurements, a magnetic field of $1\,\mathrm{kOe}$ was applied. Cell axes notation is referring to the orthorhombic unit cell of CRO. FC=Field-cooled, ZFC=Zero-field-cooled. The largest contribution of the signal is coming from the substrate, giving a diamagnetic and paramagnetic background. It was assumed that the total signal is coming from the film, when normalizing the data.

on LAO matches previous reports in the literature well [142]. CRO on NCAO cannot be probed due to the high paramagnetic moment of Nd^{+3}, which overwhelms the film signal.

The film on LSAO(110) shows a clear anisotropy between the measurement along both in-plane (referring to the sample surface) directions c and b, whereas the measurements of CRO on LAO(100) exhibit similar splittings in both directions. A striking feature is the monotonous increase with decreasing temperature in the FC data for $H||c$, which is reminiscent of a ferromagnetic transition characterized by increasing moment with decreasing temperature. A simple antiferromagnet perpendicular to the direction of the staggered magnetization would show a plateau as it is the case for stoichiometric CRO with $T_N = 110\,\mathrm{K}$(Fig.5.6). However, single crystalline La-doped CRO with field along the a-axis and oxygen-excess O-CRO powder show a magnetic susceptibility that shows a ferromagnetic trend similar to

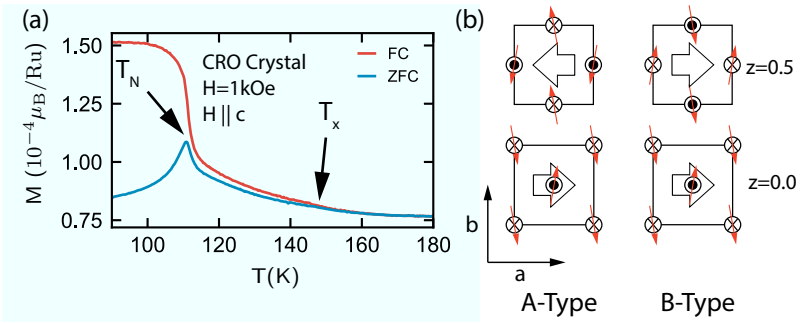

Figure 5.6: (a) SQUID-VSM Magnetometry of a Ca_2RuO_4 single crystal along the c-axis with an applied field of $1\,\mathrm{kOe}$. The AFM-transition around $110\,\mathrm{K}$ can be clearly identified. A weak FC/ZFC splitting, however, is already observed starting at $150\,\mathrm{K}$. FC=Field-cooled, ZFC=Zero-field-cooled. Data taken by J.Bertinshaw. (b) Sketch illustrating the spin-canting in the B-Type structure based on explaining the formation of a weak FM moment along a-axis in B-Type AFM CRO (based on Ref. [274].). The crosses denote a z-component pointing in the negative direction, solid circles in open circles a positive direction. A net momentum along the a-axis results.

the data from the films [90, 274]. The magnetic structure of O-CRO was studied in detail using neutron powder diffraction and determined to be AFM with a B-Type magnetic structure following the notation of Ref. [90] (see sec. 2.3). In contrast to the A-Type of stoichiometric CRO, the symmetry of the magnetic and structural unit cell allows a weak ferromagnetic component along a, which can explain the magnetisation of polycrystalline O-CRO and the ferromagnetic trend along the a-axis of La-doped CRO (Fig. 5.6). The polarization analysis using REXS is most compatible with a B-Type ordering (see also sec. 5.2.2). Due to symmetry constraints, however, B-Type order does not allow for a weak ferromagnetic component along c (see also 5.3). We point out, that a reminiscent feature is observed in magnetometry data for S-CRO single crystals with $\boldsymbol{H} \parallel \boldsymbol{c}$ (see Fig. 5.6 and Ref. [89]), but lacks a conclusive explanation up to this point. In contrast to polycrystals, high-quality CRO single crystals do not show B-Type AFM [32, 40].

Magnetometry measurements of films are highly prone to artifacts. An FM impurity phase can easily overpower effects from AFM. From the growth optimization process, we expect the $CaRuO_3$ phase to

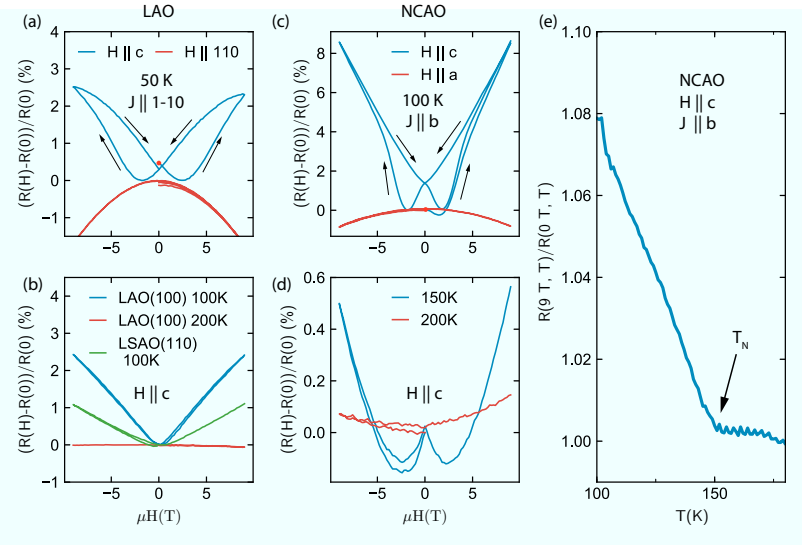

Figure 5.7: Magnetoresistance (MR) Measurements on CRO thin films in the AFM phase. (a) Positive transverse MR of CRO on LAO showing hysteresis when $H \parallel \boldsymbol{c}$ at 50 K (b)Transverse MR of CRO on LAO with $H \parallel c$ and $J \parallel [110]$ at 100 K and 200 K. Green: MR of CRO on LSAO(110) at 100 K with $J \parallel b$ (c) Positive transverse MR of CRO on NCAO showing hysteresis when $H \parallel c$. (d) Positive transverse MR with $H \parallel c$ at 150 K and 200 K (e) Temperature dependence of the MR showing a distinct kink at 150 K.

be the most likely impurity phase, that could be magnetically active. Bulk $CaRuO_3$ powder does not show long-range order [275]. $CaRuO_3$ films on the other hand can indeed become ferromagnetic under epitaxial tensile strain [276, 277]. The compressively strained films on LAO are generally paramagnetic. Since no long-range order was detected in bulk and for strained films on LAO, even partially strained films on LAO are unlikely to show FM. As a reference, magnetometry was conducted on a sample on LAO with all conceivable impurities (Pt-backcoating, $CaRuO_3$ and CaO phases) and no signal at 150 K was detected. An impurity would also be likely to be present in the films on LSAO(001), but no anomaly was detected at 150 K via SQUID-VSM and βNMR(sec. 6.1).

Since we detected AFM in REXS setting in at 150 K, we thus attribute the 150 K signal in the magnetometry to the appearance of a

weak FM coupled to the AFM arising in the Ca_2RuO_4 phase.

Similar to the FM-M phase at low temperatures, the FM component along the c-axis can also be detected in the MR by the observation of a hysteresis when $H \| c$ (Fig. 5.7)* The MR is already relatively large at 100 K. By recording the temperature dependence in zero field and 9 T, we can trace the emergence of the MR back to 150 K. At this temperature, we also detected the AFM transition in REXS, which lets us associate the MR with the AFM ordering. The magnitude of the MR does not seem to be directly correlated to amplitude of the weak FM moment. For CRO on LAO we obtain 2.4 % at 100 K and 9 T for $\boldsymbol{H} \parallel c$, while for CRO on LSAO(110) we obtain 1.1 % under the same experimental conditions although the moment is almost one order of magnitude larger for LSAO(110) at 1 kOe (Fig. 5.5).

5.2 Resonant Magnetic X-ray Scattering

5.2.1 C-Axis oriented CRO on LAO(100)

The 101/011 reflection of CRO on LAO(100) was investigated using X-rays at the Ru-L2-edge at the BM28 beamline at the ESRF. In agreement with SQUID-magnetometry, we observed a strong increase in the intensity at 150 K indicating antiferromagnetic order (Fig. 5.9). Due to twinning, it is not possible to distinguish between the 101/011 reflections, which is preventing an assignment of a magnetic structure (A- or B-Type) to this system. However, the onset temperature would suggest B-Type order, which is known to set in at 150 K instead of 110 K typical for A-Type order [90]. The reflection is still visible at high-temperatures and is resonant to the Ru L2 edge. In sec. 6.2.1 we will study the high-temperature region of the 103/013 reflection, which is equivalent to 101/011. The polarization analysis shows that the high-temperature reflection is compatible with Templeton scattering.

Nominally, a temperature of 10 K was reached, which should be in the ferromagnetic phase, but the peak intensity seems unaltered by the phase transition, indicating that the ferromagnetic and antiferromagnetic phases are indeed coexisting. We note, however, that due to

*As mentioned above, for CRO on NCAO, a SQUID measurement was not feasible due the high moment of the Nd^{+3}, which creates a large paramagnetic background.

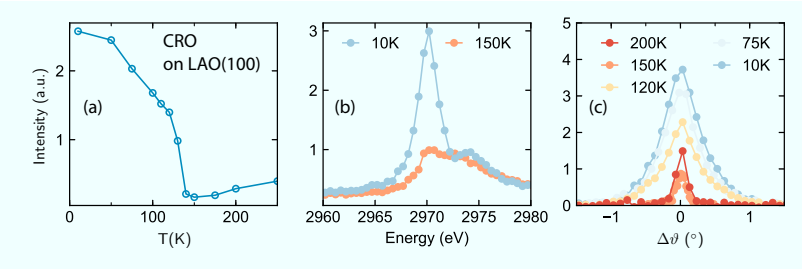

Figure 5.8: Magnetic 101/011 Reflection measured at the Ru L2 edge. (a) Temperature Dependence of the integrated intensity on warming showing a strong increase at 150 K indicating the onset of antiferromagnetic order (b) Energy Scans at 150 K and 10 K (c) Rocking curves at different temperatures. All measurements were conducted at $\psi = 0°$.

the strong absorption at the Ru-L-edges no thermal shield was used. Thus, we cannot state with certainty that this temperature was actually reached. A combined transport and scattering experiment might be able to prove this unambiguously. The energy scan at 10 K in the antiferromagnetic phase shows a two-peak structure. A similar shape was observed in the REXS experiments on bulk CRO [125], where the low-energy peak was identified as the t_{2g}-states, while the higher peak was labeled as the e_g-orbitals. [29]

5.2.2 A-axis oriented CRO on LSAO(110)

Searching for the propagation vector of antiferromagnetism (AFM), we studied the (100) and (101) reciprocal space positions of CRO on LSAO(110) using REXS at the Ru-L2 edge. The experiment for the (100) reflection was conducted at the BM28 beamline and the study of the (101) peak was performed at the P09 beamline. A Ru-L2-REXS study of the (100) reflection for bulk CRO showed an increase of the intensity at 260 K and 110 K. The former was linked to an orbital ordering (OO) transition, while the latter was identified as the A-Type AFM order known from magnetometry and neutron-scattering [125]. The study of the (011) reflection in bulk was shown to behave similarly in agreement with the (100) propagation vector of A-Type AFM. It was thus concluded that the OO-phase has the same propagation vector as the AFM-phase (see sec. 2.3).

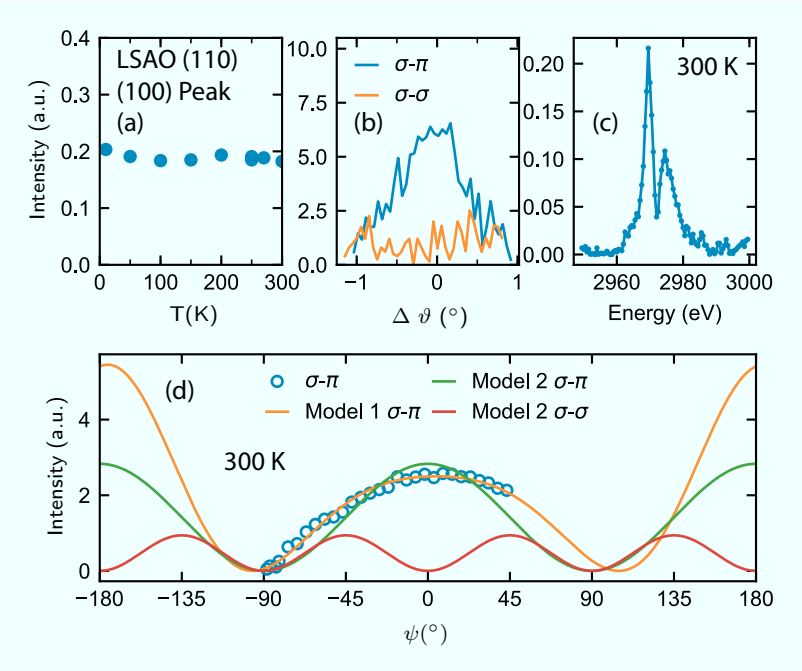

Figure 5.9: Investigation of the (100) reflection of CRO on LSAO(110) at the Ru L2-edge. (a) Temperature Dependence of the total intensity of the resonant (100) reflection of CRO on LSAO(110) (b) Rocking curves of the (101) reflection at $300\,\mathrm{K}$ in $\sigma - \pi$ and $\sigma - \sigma$ (absent). (c) Energy scan at $300\,\mathrm{K}$ in σ-π channel at $\psi = 0°$. d) Data of $\sigma - \pi$ azimuthal scan at $300\,\mathrm{K}$ in comparison with several models. "Model 1" denotes the expected model, "Model 2" gives a better fit, but should give a $\sigma - \sigma$ component, which has not been observed.

We find a resonant peak at the forbidden (100) position of CRO on LSAO(110) already present at room temperature, which only appears in the $\sigma-\pi$-channel (Fig. 5.9). No large intensity changes are observed with temperature. This is reminiscent of the (110) peak studied in bulk, which was identified as Templeton scattering (see sec.3.1.4). Polarization analysis shows that the signal is solely detected in the $\sigma-\pi$ channel. To elucidate the underlying nature of the peak, we conducted azimuthal scans at several temperatures (10 K, 50 K, 200 K, 300 K). All exhibit an angle dependence identical to the one shown in Fig. 5.9c. Based on the Pbca space group, we would expect the scattering tensor to be of the form (eq. 3.35)

$$F_{\alpha\beta} = \begin{pmatrix} 0 & 0 & \mathrm{xz} \\ 0 & 0 & 0 \\ \mathrm{zx} & 0 & 0 \end{pmatrix} \qquad \text{(Model1)}\,. \tag{5.1}$$

The simulated azimuthal dependence of the intensity based on this tensor is in good agreement with the data. It also exhibits no intensity in the $\sigma-\sigma$ channel in accordance with our observations. When exploring alternative tensor configurations, one realizes that

$$F_{\alpha\beta} = \begin{pmatrix} 0 & 0 & \mathrm{xz} \\ 0 & 0 & \mathrm{zy} \\ \mathrm{zx} & \mathrm{zy} & 0 \end{pmatrix} \qquad \text{(Model2)} \tag{5.2}$$

actually can yield a better fit, since it allows for a broader maximum through an additional $\cos(2\psi)^2$ term. However, this term should give non-vanishing $\sigma - \sigma$-contribution, which has not been observed. The absence of $\sigma - \sigma$ scattering poses a hard restriction on the scattering tensor and limits it to the first model. Thus, a different Templeton scattering tensor through e.g. a lower space group symmetry cannot be justified. One might speculate that the small deviations are caused by extrinsic factors such contamination on the surface (similar to other experiments, we found a visible discoloring on the surface after the experiment). We thus conclude that the (100) peak for CRO on LSAO(110) arises through a Templeton scattering mechanism, i.e. purely by the presence of structural distortions. The azimuthal dependence is fully compatible with the tilt pattern of the Pbca space group determined by selection rules (sec. 4.8).

Studying the forbidden (101) position in reciprocal space at the P09 beamline, similar to the other forbidden positions, a weak resonant peak was already found at 300 K. The peak shows no change in

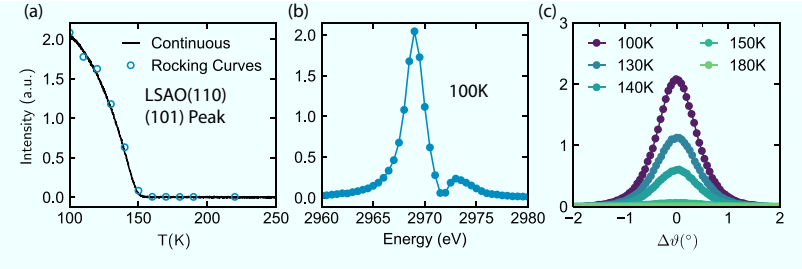

Figure 5.10: a) Temperature Dependence of the 101 of the CRO film on LSAO acquired by integrated rocking curves (on warming) and by monitoring the reflection intensity while cooling (after aligning once at room temperature) at $\psi = 180^\circ$ b) Energy Scan in the antiferromagnetic state c) Temperature evolution of the magnetic peak.

temperature until it exhibits a large increase below 150 K in an order-parameter-like fashion (Fig. 5.10). The onset is in agreement with the magnetometry data, which indicates that the magnetic ordering is being sensed at this position. The (101) peak identifies the ordering as B-Type based on the selection rules for the magnetic unit cell (Ref. [90] and sec. 2.3). B-Type AFM was also suggested for pressurized bulk based on magnetometry measurements in comparison with the oxygen-rich O-CRO phase [43, 90], where neutron scattering was able to identify B-Type AFM. B-Type AFM order in bulk shows typically a higher $T_{\mathrm{Neel}} = 150\,\mathrm{K}$ than the A-type ordering stoichiometric S-CRO with $T_{\mathrm{Neel}} = 110\,\mathrm{K}$, which is also compatible with the data on CRO on LSAO(110). The intensity above 150 K is attributed to Templeton scattering based on the weakness and lack of temperature dependence*. The energy scan in the AFM phase shows the typical two-peak structure similar to CRO on LAO compatible with a splitting of t_{2g} and e_g levels.

To study the impact of epitaxial strain on the magnetic moment anisotropy, an azimuthal scan was performed at 100 K (Fig. 5.11). The geometry correspond to Fig.3.9: The incoming beam was σ-

*In principle, the cryostat would have allowed us to cool further, but we noticed a drop in intensity at lower temperatures for other films at the same beamline. We attributed this to condensation of residual gases due to the bad vacuum of the setup. Cooling further would offer the possibility to study the influence of the ferromagnetic phase on the antiferromagnetic phase at low temperatures.

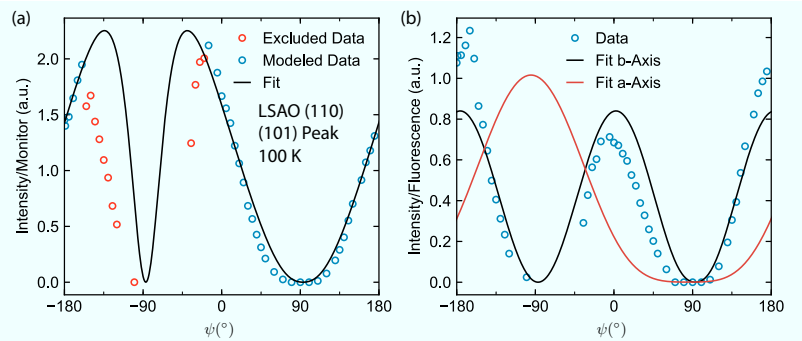

Figure 5.11: Azimuthal Scans of the magnetic 101 peak recording the intensity without polarization analysis at 100 K. Both panels show the same data, but normalized differently. (a) Normalization to Monitor with Model including geometric and absorption correction factors. The blue points denote the data that was used for the fit. The red points denote data excluded from the fit, since the intensity drop is likely caused by beam spillover. (b) Normalization to the Fluorescence signal. This corrects the geometric effects in the proximity of the grazing angles around 90°. The access to this angular sector allows to clearly distinguish between an a-axis and b-axis magnetic moment.

polarized and the sample was mounted on a 24° wedge to access the 101 reflection without having to add offset to the χ and ϑ motors. At each azimuth position, the peak was aligned and the peak intensity was determined by integrating a background-corrected rocking curve after normalizing to the incoming beam intensity (monitor). The scan was conducted without polarization analysis, recording the total intensity of both $\sigma - \sigma$ and $\sigma - \pi$ channels. However, magnetic scattering only yields $\sigma - \pi$ scattering (see sec. 3.1.3). At the Ru-L2 edge the 101 reflection is located at $\vartheta = 25°$, which lets us expect large geometric effects, since, together with the wedge, the incident angle varies between 1° and 49° (see also 3.2).

Using eq. 3.29, we can model the azimuthal dependence arising from a B-Type AFM ordering (sec. 2.3)

$$f_1^{\mathrm{m}} = \begin{pmatrix} 0 & m_z & -m_y \\ -m_z & 0 & m_x \\ m_y & -m_x & 0 \end{pmatrix} \qquad F_{101}^{\mathrm{m}} = f_1^{\mathrm{m}} + f_2^{\mathrm{m}} + f_3^{\mathrm{m}} + f_4^{\mathrm{m}} \,. \tag{5.3}$$

Here, we are assumed a simple alternating antiferromagnetic arrangement without any symmetry constraints for the four Ru-atoms imposed by the crystallographic space group (see 5.3). The structure factor is simple and directly represents the anisotropy of the magnetic moment of a single Ru-atom. Because of the large variance of the incident angle, we have to include a correction factor η for geometrical and absorption effects elaborated in 3.2.3. Integrating eq.3.48, we arrive at

$$\eta(\alpha) = \frac{\csc(\alpha)\delta}{d(\csc(2\vartheta-\alpha)+\csc(\alpha))}\left(1-\exp\left(-\frac{d(\csc(2\vartheta-\alpha)+\csc(\alpha))}{\delta}\right)\right), \tag{5.4}$$

where $\csc(x) = sin(x)^{-1}$ denotes the cosecans, 2ϑ the detector angle and α the incidence angle. Combining eqs.5.4 and 5.3 yields the expression we use to model the polarization dependence including the correction of absorption and geometric effects:

$$I(\psi) \propto \eta(\alpha(\psi))\left|\boldsymbol{\pi}_{\mathrm{f}} \cdot \begin{pmatrix} 0 & m_z & -m_y \\ -m_z & 0 & m_x \\ m_y & -m_x & 0 \end{pmatrix} \cdot \boldsymbol{\sigma}_{\mathrm{i}}\right|^2 \tag{5.5}$$

with

$$m_x = \cos(\varphi)\sin(\vartheta) \qquad m_y = \sin(\vartheta)\sin(\varphi) \qquad m_z = \cos(\vartheta)\,. \tag{5.6}$$

For convenience, we introduced spherical coordinates for the moment direction. The thickness $d = 50\,\mathrm{nm}$ for this sample is derived from the growth rate based on XRR-measurements of similar samples. The penetration depth is estimated to be $\delta \approx 1.75\,\mathrm{m}$ at the Ru L2 edge at the transition into the t_{2g}-states (see appendix A). The penetration depth is damping the scattering signal only at grazing incidence or grazing exiting angles ($\psi = -90°$ and $\psi = 90°$), where in either case no intensity is measured. Thus, inaccuracies in δ can influence the goodness of fit, but have only little impact on the statements regarding the magnetic moment direction extracted from the data.

The position with grazing incidence angle is located at $\psi = -90°$, where we encounter a sudden drop in intensity. It is unclear whether this is due to a beam-spillover effect, absorption effect or even the intrinsic polarization dependence of the Ru-atoms. This prompts us to initially exclude the red data points in fig.5.11 for the data analysis,

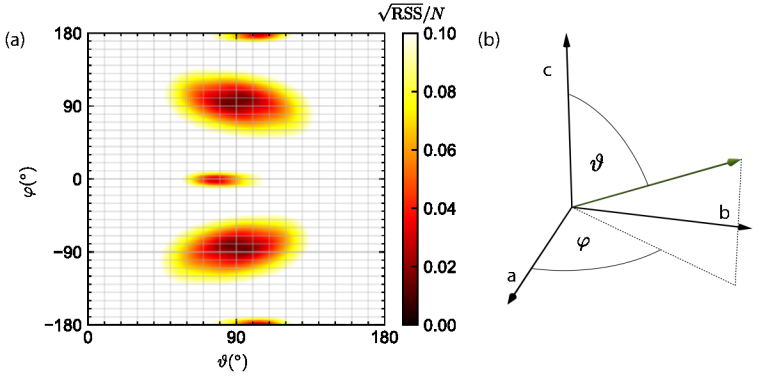

Figure 5.12: Evaluations of fits with fixed magnetic moment direction ϑ and φ using the square root of residual sum squared(RSS) normalized by the total number of data points N. The solution with a moment pointing along the b-axis yields the best fit. However, another minimum for an a-axis oriented magnetic moment is also visible using the data shown in Fig. 5.11a. However, this solution can be identified as artificial by using the fluorescence signal as normalization (see text).

since it is unclear whether they can be modeled (e.g. a beam spillover is not included in our model).

Modelling a b-axis oriented momentum as in bulk based on eq. 5.6 and only applying a scaling factor and a small ψ offset, we already obtain an excellent agreement with the data. To explore possible other solutions, we tested all other moment directions and tested the goodness of fit (GOF). For this, we fitted the data with a fixed ϑ and φ varying a scaling factor and a small ψ offset ($\mp 5°$) to account for slight misalignments. Fig. 5.12 shows the $\sqrt{RSS}/N$, where RSS is the residual sum squared and N the total amount of data points. Minima around $\vartheta = 90°, \varphi = 90°$ and at the point symmetric position $\vartheta = 90°, \varphi = -90°$ can be identified, confirming our expectation of a b-axis oriented momentum. However, a small region around $\vartheta = 0°, \varphi = 0°$ corresponding to an a-axis oriented moment exhibits a second minimum. Assuming a magnetic scattering signal, we expect a term $\propto (\boldsymbol{\pi_f} \times \boldsymbol{\sigma_i}) \cdot \boldsymbol{m}$ (see 3.26). Since $(\boldsymbol{\pi_f} \times \boldsymbol{\sigma_i}) \| \boldsymbol{k_f}$, the signal is $\propto \boldsymbol{k_f} \cdot \boldsymbol{m}$. The ψ reference vector is defined in such a way, that $\psi = 0$, when the b-axis lies within the scattering plane. Thus, at the grazing position, $\boldsymbol{k_f}$ mainly points along the a-direction letting us expect a

maximum in the oscillation at $\psi = 90°$ for an a-axis oriented momentum, but a minimum for a b-axis-momentum. However, the leading $csc(\alpha)$ term in the correction factor η distorts the signal around the grazing positions that it appears in both cases as a maximum in the untreated raw signal.

However, we can leverage the fluorescence signal we obtained simultaneously with a diode (see sec. 3.2.3). Elaborated above, the fluorescence signal (XRF) is subject to the same $\propto csc(\alpha)$ term and is also proportional the illuminated area. Normalizing to its signal thus cancels out possible spillover and geometric effects, allowing us to access the red data points of Fig. 5.11a for modelling the polarization dependence. The XRF-normalized dataset clearly shows a minimum around the grazing position, unambiguously identifying the model with b-axis oriented moments as the only compatible model compared to the case of an a-axis oriented moment (Fig. 5.11b). The fits in Fig. 5.11b were modeled only applying the absorption corrected factors for the outgoing beam.

5.2.3 A-axis oriented CRO on NCAO(110)

CRO on NCAO(110) are certainly the most peculiar films of the series that we were able to synthesize within the course of this thesis. It is distinct from strain states that were reported in the literature (sec. 2.4): The insulating behavior from 400 K to lowest temperatures, the absence of an MIT up to 400 K and the large orthorhombicity in an antiferromagnetic state. This motivated us to conduct a REXS study of the magnetic (101) peak of NCAO at the Ru-L2 edge. The experiment described in the following was conducted at the 4-ID-D beamline. Similar to the film on LSAO(110), we were able to detect a resonant peak at the forbidden (101) position already at room temperature. The intensity weakly changes on cooling until it exhibits a strong enhancement of the intensity at 150 K (Fig. 5.13). The jump coincides with the onset of the magnetoresistance in Fig. 5.7, prompting us to identify it as the onset of antiferromagnetism. The situation thus presents itself similar to LSAO(110): The low temperature region can be ascribed to the AFM in the sample and the intensity at higher temperatures likely to Templeton scattering.

However, the polarization dependence of the magnetic peak taken at 10 K exhibits a quite different behavior. Apart from slight changes

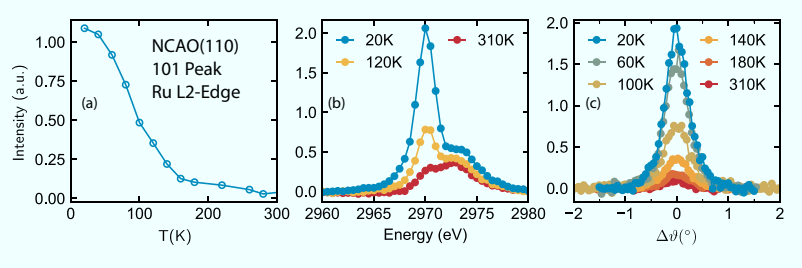

Figure 5.13: Temperature dependence of the resonant (101) reflection of CRO on NCAO(110) at $\psi = -45°$. (a) Temperature dependence of the integrated intensity showing a signal at higher temperatures and a strong increase at $150\,\mathrm{K}$ indicating the onset of AFM. (b) Energy dependence of the reflection exhibiting two peaks - likely originating from the splitting between t2g and eg states (c) Temperature dependence of the rocking curves.

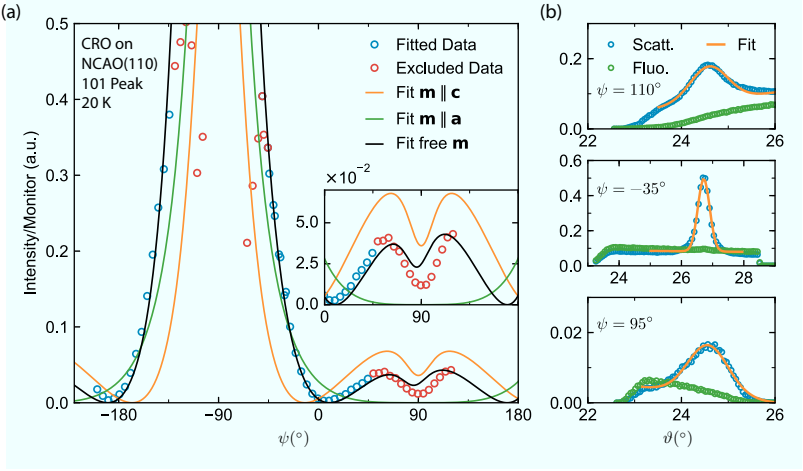

Figure 5.14: Azimuthal scan of the (101) peak of CRO on NCAO(110) at the Ru-L2 edge and exploration of several fitting approaches. (a) Dataset with fits for $\boldsymbol{m}$ along high-symmetry axes (fitting scaling factor and offset for the intensity) and free $\boldsymbol{m}$. All cases with fixed penetration depth $\delta = 1.75\,\mathrm{m}$ (b) Rocking curves used to integrate the intensity with corresponding fits (sloped Gaussian) and fluorescence signal. Close to grazing incidence or emergence, the signal is cut making the integrated intensity value questionable. The XRF-signal used for normalization is the averaged value over which the fit (orange) is defined.

in the angles due to the difference in lattice constants, the scattering geometry is identical to the experiment for CRO on LSAO(110): We use the (010) as a reference vector, thus the azimuth with grazing incidence angle is located at $\psi = -90°$ and the position with grazing exiting angle is located at $\psi = 90°$. Similar to CRO on LSAO(110), we excluded data in proximity to the grazing position (Fig. 5.14). The experimental setup did not allow us to attach a diode directly to the vacuum chamber to measure the X-ray fluorescence (XRF), but an energy-discriminating Vortex detector was available, which allowed us to integrate the intensity in different energy windows. To measure the coherent scattering signal, we selected a region of 2.860 eV–3.183 eV around the absorption edge and for the XRF 2.469 eV–2.860 eV was chosen to include the Ru L-β and L-α lines. Thus, the coherent scattering from the magnetic peak and the XRF was measured at the same angle.

The rocking curves used to obtain the integrated intensity of the scattering signal show that the signal is being cut off close to the extremal positions at $\psi = 90°$ and $\psi = -90°$ (Fig. 5.14). The incidence or emergence angle becomes so shallow, that the detector is at least partially moving below the sample horizon either at the outgoing edge (grazing out) or at the edge close to the incoming beam (grazing in). Thus, for the initial analysis, we excluded the parts where this was the case, since we could not reliably state that the azimuthal dependency of the intensity is actually the intrinsic one.

At $\psi = -90°$, the scattering signal is again strongly boosted since we are accessing more volume of the film due to the shallow incidence angle. Around $\psi = 90°$, a maximum with a dip is observed. Since the beam is exiting with a grazing emergence angle, the path length within the sample is dramatically increased to a multiple of the penetration depth, giving rise to a substantial loss of the signal due to absorption in the sample. Expecting magnetic scattering, the signal is again assumed to be $\propto \boldsymbol{m} \cdot \boldsymbol{k_f}$. Around $\psi = 90°$, the b-axis, the reference vector, is perpendicular to the scattering plane and the (101) plane is coinciding with the scattering plane. Thus, the presence of a maximum at this position – in contrast to CRO on LSAO(110) and to bulk CRO with both their moments aligned along b – shows us that a significant moment must lie within the (101)-plane. In order to fit the data, we employ the model defined in eq.5.6. Only applying an additional scaling factor for the intensity while keeping the

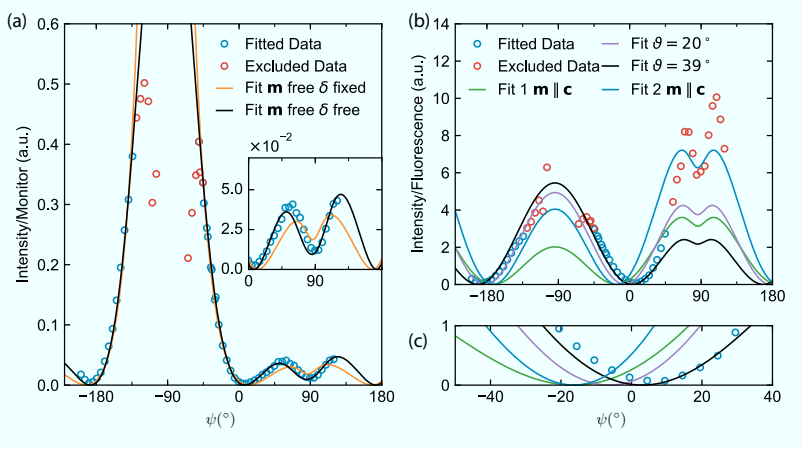

Figure 5.15: (a) Fits of the azimuthal scan of the magnetic 101 reflection of CRO on NCAO fitted including the data around the grazing emergence region. A fit with a fixed penetration depth of $\delta = 1.75\,\mathrm{m}$ and a fit a free δ is shown. (b) Fluorescence-normalized scattering signal in comparison with various fits with fixed moment directions. Fits with fixed canting angles ϑ of the moment away from the c-axis ($\psi = 180°$) and fits with a moment fixed along the c-axis are shown. All fits except Fit 2 are fitting only the blue data points. (c) Magnification of the region close to $\psi = 0°$ to compare the zero positions of the fits with the data.

moment fixed along $\boldsymbol{c}$ or $\boldsymbol{a}$ gives non-satisfactory fits. Qualitatively, the presence of intensity around $\psi = 90°$ has to be intrinsic, since all extrinsic effects (absorption, geometric factor) lead to a reduction of the intensity in this region, which makes a solution with a moment purely aligned along a incompatible. Only a fit allowing the moment to be arbitrarily chosen allows us to reproduce the shape well. All fits weighed the data points with a factor $1/I(\psi)$ to not overly emphasize the high intensity points around the grazing position. For the modeling, we again used the penetration depth $\delta = 1.75\,\mathrm{m}$ and the thickness $d = 59\,\mathrm{nm}$, which was determined via X-ray reflectivity. The iteration converges at $\vartheta = 45°$ and $\phi = 180°$ giving equal z and x elements in the scattering tensor.

Despite only fitting the range between $-45°$–$45°$, the model follows the excluded part around $\psi = 90°$ quite well. If we include this part in our fitting routine, we obtain $\vartheta = 49°$ and $\phi = 180°$ agreeing well with the initial result (Fig. 5.15a). The fit can be further improved by

unfixing the penetration depth δ and including it in the fitting process. This is justified by the fact that we expect considerable surface contamination, which might change the penetration power of the beam. Using this model, the fit converges at $\vartheta = 39°$ and $\phi = 180°$ with $\delta = 0.3\,\mathrm{m}$, which is still in good agreement with the initial result. An additional check is the XRF-normalized signal that directly corrects the absorption and geometric factors. As value of the XRF-signal used for normalization we used an the average over an angular range, where the scattering-signal shows a flat plateau (Fig. 5.14). the average over the plateau A difference relative to the experiment on LSAO(110) is the location of the XRF-detector. During this experiment, the detector for the XRF and the scattering signal is identical, which makes the influence of absorption on the XRF-signal for grazing emergence angles non-negligible. To account for this effect, the correction factor applied to the XRF-normalized signal is the following

$$\eta_{\text{fl}}(\alpha) = \frac{1}{d}\int_0^d \exp\left(\frac{x_{\text{out}}(\alpha)}{\delta_{\text{Fl}}}\right)\exp\left(-\frac{x_{\text{out}}(\alpha)}{\delta_{\text{L2}}}\right)dz\,. \tag{5.7}$$

Here, we are "uncorrecting" the fluorescence signal for the absorption at the emission lines and then correcting the scattering signal for its absorption under grazing emergence angle. If we take the same moment orientation from the monitor-corrected fit ($\vartheta = 39°$ and $\phi = 180°$) and use $\delta_{\text{L2}} = 1.75\,\mathrm{m}$ and $\delta_{\text{Fl}} = 3\,\mathrm{m}$ and apply a scaling factor to the XRF-corrected data we can model the region around $\psi = -90°$ quite well, but in the sector with grazing emergence angle, the model cannot reproduce the intensity satisfactorily (Fig. 5.15b). Rotating the moment closer to the c-axis ($\vartheta = 20°$) and along the c-axis ($\vartheta = 0°$) allows us to better fit the intensity ratio of the maxima, but the zero positions of the model curves are shifted beyond a reasonable experimental error ($\approx 20°$) relative to the experimental data (Fig. 5.15c). If we assume that the XRF-signal in the sector with grazing emergence angle is unreliable, both datasets are consistent and compatible with $\vartheta \approx 45°$. One effect that affects the XRF, but not the intensity of the diffraction peak, could be their difference in divergence: The XRF-signal is filling the whole detector, while the diffraction peak fills only a solid angle smaller than the detector. A shadowing of the XRF-signal by the sample horizon might thus occur before it has an effect on the scattering signal.

As for CRO on LSAO(110), we tested the parameter space of the

moment directions for local minima by performing fits with various fixed moment directions and only fitting a scaling factor (Fig. 5.16). Since the fit minimized a weighed RSS (residual sum of squares), the goodness of fit is represented by

$$Q = \frac{1}{N}\sqrt{\sum_{i=1}^{N}\left(\frac{u_i - v_i}{u_i}\right)^2}. \tag{5.8}$$

Here, u_i denotes a data point, while v_i is the corresponding value from the fit. The result clearly shows a single minimum around $\vartheta = 45°$ and $\phi = -180°$ and the symmetry-equivalent solution.

Our analysis thus concludes that the data can be well described by the anisotropy of a tensor approximately of the form

$$F_{\mathrm{mag}} = \begin{pmatrix} 0 & m & 0 \\ -m & 0 & -m \\ 0 & m & 0 \end{pmatrix}. \tag{5.9}$$

This corresponds to a magnetic moment pointing approximately along the $(\bar{1}02)$ direction in the orthorhombic unit cell of CRO.

As we discussed in sec.3.1.3, the symmetry of the crystal field surrounding the Ru-atom breaks the spherical symmetry of the scattering tensor in addition to the presence of a magnetic moment. This effect is negligible, when the moment is pointing along a high symmetry direction, which, however, does not seem to be the case here. Thus, a more detailed analysis might be required, since the azimuthal dependence of the intensity $|(\varepsilon \times \varepsilon') \cdot \boldsymbol{m}|^2$ needs to be replaced by [157] $|F_{\mathrm{eu}}(\boldsymbol{\varepsilon} \times \boldsymbol{\varepsilon'}) \cdot \boldsymbol{m_{xy}} + F_{\mathrm{a2u}}(\boldsymbol{\varepsilon} \times \boldsymbol{\varepsilon'}) \cdot \boldsymbol{m_z}|^2$. Here, F_{a2u} and F_{eu} are coefficients of an spherical harmonics expansion of the magnetic moment direction. However, the basic result, that we are sensing substantial a and c components of the magnetic moment remains unchanged.

5.3 Discussion

While the result for CRO on LSAO(110) is in good agreement with the bulk magnetic structure, the result for CRO on NCAO(110) appears puzzling, since the high spin-orbit-coupling in CRO should lead to a high single-ion-anisotropy and thus the spin should be preferably

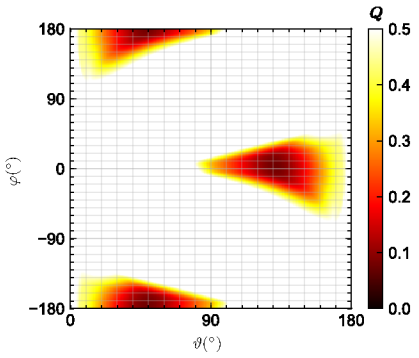

Figure 5.16: Evaluation of the goodness of fit for modeling the azimuthal dependence of the magnetic peak at 101 of CRO on NCAO. The fitted range corresponds to the one depicted in Fig.5.15. The moment direction is fixed along the (ϕ,ϑ) coordinates and the data is fitted by only varying a scaling factor. The penetration depth is fixed with $\delta = 1.75\,\mathrm{m}$. $Q = 1/N\sqrt{\sum_{i=1}^{N}((u_i - v_i)/u_i)^2}$ with u_i being the data and v_i being the fit value at the same azimuth.

aligned along a high-symmetry direction. The ferromagnetic signal detected by SQUID-VSM and MR along the c-axis is also at odds with the usual description of the spin ordering in bulk CRO. Here, we want to provide a more detailed discussion and discuss symmetry constraints to evaluate possible solutions to these questions. The symmetry of a magnetically ordered system is lower than the space group of the chemical unit cell due to time-reversal symmetry breaking. This adds a "color" to atomic positions expanding the possible symmetry elements. A powerful tool to study the implications of crystal symmetry on the spin arrangement is the use of group representation theory. One method to rationalize the description of a magnetic structure is by invoking the concept of a propagation vector $\boldsymbol{k}$. Then the magnetic lattice can be described by [278]

$$\boldsymbol{m_{ls}} = \boldsymbol{S}_s e^{-2\pi i \boldsymbol{k} \boldsymbol{R}_l} . \tag{5.10}$$

Here, the $\boldsymbol{m_{ls}}$ describes the magnetic moments $\boldsymbol{S}_s$ within the unit cell l with an origin R_l occupying the position s (usually a subsite of a Wyckoff-position). As we can see, $\boldsymbol{k}$ describes how the spin arrangement is translated from one unit cell to the next. We assume that only only propagation vector can be used to describe the structure, which is the case for most magnetic systems. The question now becomes, which symmetry operations g of a group $\mathcal{G}$ leave the propagation vector $\boldsymbol{k}$ invariant. In mathematical terms, we are looking for a set g

that fulfills [278]

$$\mathcal{G} = \{g \in \mathcal{G} | g\boldsymbol{k} = \boldsymbol{k} + \boldsymbol{G}, \boldsymbol{G} \in \boldsymbol{L}*\}\,, \tag{5.11}$$

where $\boldsymbol{L}*$ represents the reciprocal lattice. In order to organize the symmetry operations, group representation theory was developed. A representation of a group is the set of square matrices $D(g_i)$ associated with each group symmetry element that satisfy [279]

$$D(g_j)D(g_i) = D(g_k) \qquad \text{given that} \qquad g_j g_i = g_k\,. \tag{5.12}$$

The relation between representations and group elements does not necessarily have to be one-to-one. A symmetry element can have multiple representations. The most trivial example is the identity operation, which can be represented by

$$D_1(E) = \begin{pmatrix} 1 & 0 \\ 0 & 1 \end{pmatrix} \quad \text{in 2D and} \quad D_2(E) = 1 \quad \text{in 1D} \tag{5.13}$$

One can construct another representation of a symmetry operation by combining representations:

$$D_3(g_i) = \begin{pmatrix} D_1(g_i) & 0 \\ 0 & D_2(g_i) \end{pmatrix}\,. \tag{5.14}$$

A representation of such a shape is said to be *reducible*, since it can be decomposed into two other representations. This may seem trivial, but the reducibility of such a matrix might be hidden. A equivalence transformation might be needed to achieve such a block-diagonal form. If there is no reduction possible, the representation is called *irreducible*. As an abbreviation, often *irrep* is being used. We can define a set of independent elements $\{\psi_1, \psi_2, \ldots \psi_\nu\}$ in a vector space, which form a group $\mathcal{G}$. We call this set *basis* for a representation, if [279]

$$g_i \psi_\nu = \sum_{\mu=1}^{d} \psi_\mu D_{\mu\nu}(g_i)\,. \tag{5.15}$$

This forces the set to be closed within a group. Initially, $D_{\mu\nu}(g_i)$ is just a coefficient matrix, but it can be shown it actually also forms a representation of the group operation g_i[279]. The members of the basis are called *basis vectors* or *basis functions* The space that is spanned by the basis is called *invariant subspace*.

The idea of representation analysis is now to construct all possible spin arrangements using the symmetry relations of the space group. This includes the permutation of the atomic positions and rotational effects on the magnetic moment vectors [280]. During the collection of all the symmetry operations, the propagation vector will enter as a phase factor, if one of the operations results in a position outside the zeroth unit cell. Each of the generated spin arrangements is can be labeled as a basis function. The resulting representation $D_{\mu\nu} = \Gamma_{\mathrm{mag}}$ connecting all the basis functions is the so called *magnetic representation* Γ_{mag}. Now Γ_{mag} can be decomposed into several irreducible representations

$$\Gamma_{\mathrm{mag}} = \Gamma_1 \oplus \Gamma_2 \oplus \Gamma_3 \oplus \ldots \oplus \Gamma_n \,. \tag{5.16}$$

Each of the irrep forms an irreducible invariant subspace of orthonormal basis vectors [281]. These sets of basis vectors offer now a sensible way of classifying the magnetic structure. This is similar to the classification of Raman modes in terms of their irreducible representation.

A fundamental result from Landau's theory of second order phase transitions is the fact, that a continuous phase transition breaks symmetry and that only a single irrep becomes critical [282]. This is a dramatic simplification, since possible solutions of the spin structure are now much more constrained. Calculating irrep with a given space group and propagation vector can be an arduous task. Several computer programs were developed to facilitate the calculation. In this work, the program BASIREPS [283] was used.

Simply based on selection rules, we can state the observation of a magnetic peak at the (101) position must be caused by a magnetic moment component that orders antiferromagnetically within the RuO planes. There are only two possibilities for such a commensurate ordering on the 4a-Wyckoff-position for $Ca_2RuO_4$and only one would give intensity at this position (B-Type)[90](Fig. 5.17). This mode of magnetic order exhibits a $\boldsymbol{k} = (0, 1, 0)$ propagation vector. As we discussed in sec. 4.8, the selection rules of all CRO films are compatible with the bulk space group Pbca. Equipped with the space group and the propagation vector $\boldsymbol{k}$, one can then create a magnetic representation and its irrep for the four Ru-atoms on the 4a-Wyckoff-position. In general, Γ_{mag} is composed of the irrep of all symmetry elements of the space group. In total, Γ_{mag} of the Pbca space group with $\boldsymbol{k} = (0, 1, 0)$ can be decomposed into eight irrep. However, at

IR	B-V	Ru1			Ru2			Ru3			Ru4		
		m_x	m_y	m_z	m_x	m_y	m_z	m_x	m_y	m_z	m_x	m_y	m_z
Γ_1	ψ_1	1	0	0	-1	0	0	-1	0	0	1	0	0
	ψ_2	0	1	0	0	-1	0	0	1	0	0	-1	0
	ψ_3	0	0	1	0	0	1	0	0	-1	0	0	-1
Γ_3	ψ_4	1	0	0	-1	0	0	1	0	0	-1	0	0
	ψ_5	0	1	0	0	-1	0	0	-1	0	0	1	0
	ψ_6	0	0	1	0	0	1	0	0	1	0	0	1
Γ_5	ψ_7	1	0	0	1	0	0	-1	0	0	-1	0	0
	ψ_8	0	1	0	0	1	0	0	1	0	0	1	0
	ψ_9	0	0	1	0	0	-1	0	0	-1	0	0	1
Γ_7	ψ_{10}	1	0	0	1	0	0	1	0	0	1	0	0
	ψ_{11}	0	1	0	0	1	0	0	-1	0	0	-1	0
	ψ_{12}	0	0	1	0	0	-1	0	0	1	0	0	-1

Table 5.1: Non-zero irreducible representations calculated using BASIREPS after decomposing the magnetic representation of the Pbca space group with a propagation vector of $\boldsymbol{k} = (0, 1, 0)$. IR: Irreducible representation. B-V: Basis vector.

the Wyckoff-4a site only four of them apply (Tab. 5.1). The table then gives possible configurations of the magnetic moments for each Ru-atom and how they are coupled to obey the symmetry operations. Based on these relations we can then calculate the structure factor of the 101 peak to evaluate which elements should be visible at this position. With

$$F_{101} = f_1 + f_2 - f_3 - f_4 \tag{5.17}$$

and assuming a magnetic scattering tensor based on eq.5.3 in combination with the relations from each irrep (Tab. 5.1), we yield

$$F_{101}^{\Gamma 1} = \begin{pmatrix} 0 & -4z & 0 \\ 4z & 0 & 0 \\ 0 & 0 & 0 \end{pmatrix} \qquad F_{101}^{\Gamma 7} = \begin{pmatrix} 0 & 0 & 4y \\ 0 & 0 & 0 \\ -4y & 0 & 0 \end{pmatrix} \tag{5.18}$$

$$F_{101}^{\Gamma 3} = \begin{pmatrix} 0 & 0 & 0 \\ 0 & 0 & 0 \\ 0 & 0 & 0 \end{pmatrix} \qquad F_{101}^{\Gamma 5} = \begin{pmatrix} 0 & 0 & 0 \\ 0 & 0 & -4x \\ 0 & 4x & 0 \end{pmatrix}. \tag{5.19}$$

Comparing these theoretical predictions with our experimental results, it is readily seen that Γ_7 is in good agreement with the REXS result of the CRO film on LSAO(110) and corresponds to the B-Type

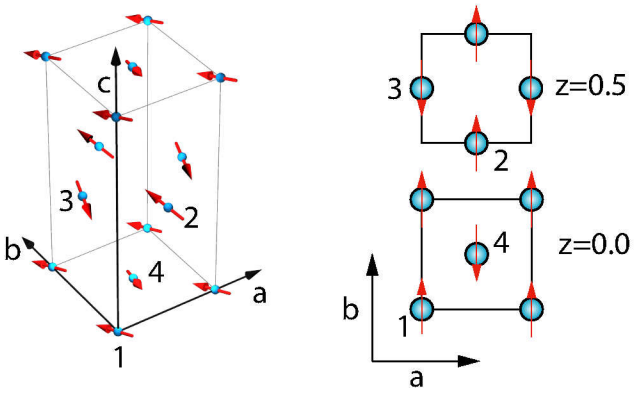

Figure 5.17: Magnetic Structure of B-Type CRO corresponding to Γ_7. For clarity, only Ru-atoms are shown and the canting of the spins has been exaggerated. The numbers correspond to the ordering of the Ru-atoms on the 4a-site in Tab. 5.1.

AFM found in bulk CRO. The magnetometry-data indicates that the moment aligns along the b-axis, since no moment was detected along this axis. However, one can see that this irrep does not exhibit a ferromagnetic component along the c-direction as measured via SQUID. The analysis of the data of CRO on NCAO(110) shows roughly equal x and z elements, which cannot be explained by a single irrep in the Pbca space group. The MR-data with field along the c-axis shows also a clear hysteresis for CRO on NCAO and LAO implying the FM along the c-axis is an inherent property of the AFM in the CRO films. The only irrep that would allow a ferromagnetic component along the c-axis would be Γ_3, but it should not result in an intensity at 101-position. In light of the apparent incompatibility with the representation analysis we want to discuss aspects which could help explaining the discrepancy.

5.3.1 Surface Ferromagnetism

The surface portion, i.e. the topmost layer, comprises a relative large portion of a thin film. The symmetry arguments laid out above only hold for an infinite lattice. The surface and also the interface between substrate and film breaks symmetry and thus does not need to obey the same constraints as the bulk. Indeed, surface ferromagnetism has

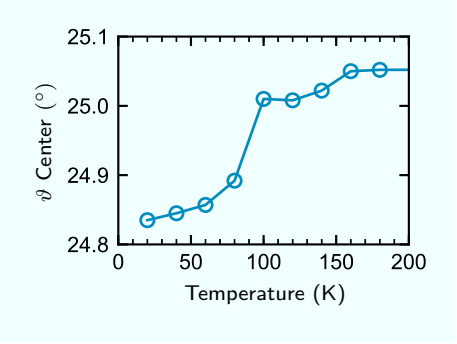

Figure 5.18: Temperature dependence of the ϑ-position of the 101 magnetic peak corresponding to the scans in Fig. 5.13. A kink at $\approx 100\,\mathrm{K}$ is visible that could be related to the hysteresis in the transport properties (sec. 4.9).

been proposed for ruthenates [284]. If we assume a ferromagnetic surface with the full moment ($2\,\mu_\mathrm{B}$) per Ru and normalize by the amount of RuO_2 layers (≈ 100 in a typical film), we find a moment size consistent with our data for the ferromagnetism along the c-axis. However, the surface orientation is fundamentally different for the c-axis oriented CRO on LAO and a-axis oriented CRO on LSAO(110) and NCAO(110). Despite this fact, all of them show weak ferromagnetism along the c-axis. It is unlikely, that surface ferromagnetism would be insensitive towards such large changes in the surface truncation.

5.3.2 Reduced Symmetry

Transport and the ϑ-positions (Fig. 5.18) during the REXS measurement of CRO on NCAO indicate a phase transition at $\approx 100\,\mathrm{K}$. The exact nature needs to be clarified, but a structural phase transition is certainly a possibility. Such a transition could lead to a reduced symmetry of the crystal. However, one would expect a structural transition also to be visible in the temperature dependence of the magnetic peak, of the structural phase transition is coupled to the magnetic one, but we did not observe a clear anomaly. Apart from a phase transition, a reduced symmetry could already be present at room temperature and be just too small to be observable during the structural characterization experiments. Thus, in any case, it is worthwhile to discuss the influence of a possible lowering of the crystal symmetry on the scattering tensor. In principle, the symmetry could be lowered to a point, where all symmetry constraints are lifted, but it is more realistic to start from the bulk Pbca space group, which is also compatible

with our X-ray data and investigate how slight reduction in symmetry would affect the symmetry constraints. A change in symmetry would dephase the form factors in the structure factor (eq. 5.20). The next lowest symmetry reduction of the lattice would invoke a monoclinic distortion that splits the 4a-Wyckoff-position of the Ru-sites into two separate ones. This is the case for example in the $P2_1/c$ subgroup of Pbca, which was suggested for the O-CRO oxygen-excess bulk phase at high temperatures [90]. Generally, for $P2_1/c$, the four Ru-sub-sites of the 4a-Wyckoff-position are split into the Wyckoff 2d and 2a sites, which would lift the symmetry constraints between the sub-site pairs (Ru1,Ru3) and (Ru2,Ru4).*Assuming a structure factor that approximates this dephasing would then be

$$F_{101} = f_1 + \epsilon f_2 - f_3 - \epsilon f_4 \,. \tag{5.20}$$

For Γ_1 and Γ_5 (of Pbca), the scattering tensor would then result in

$$F_{101}^{\Gamma 1} = \begin{pmatrix} 0 & -2z - 2\epsilon z & 0 \\ 2z + 2\epsilon z & 0 & -2x + 2\epsilon x \\ 0 & 2x - 2\epsilon x & 0 \end{pmatrix} \tag{5.21}$$

$$F_{101}^{\Gamma 5} = \begin{pmatrix} 0 & -2z + 2\epsilon z & 0 \\ 2z - 2\epsilon z & 0 & -2x - 2\epsilon x \\ 0 & 2x + 2\epsilon x & 0 \end{pmatrix} \tag{5.22}$$

If we assume that a major component of the magnetic moment aligns along one axis, the other component could then be caused by a small canted component. Canted components are naturally expected for CRO, since the RuO_6 octahedra exhibit substantial tilting and rotation. For the Γ_1 irrep, the small canted component would have to be along $\boldsymbol{c}$ and the major component along $\boldsymbol{a}$ to be compatible with the observed tensor. In the case of Γ_5, the major component would have to be along $\boldsymbol{c}$ and the small canted component would be along $\boldsymbol{a}$. The distortion ϵ reduces the contribution of the major component and could explain why both x and z components are similar in size. Within this scenario, the weak ferromagnetism would arise from a canted component of the magnetic moment, which does not compensate in the symmetry-reduced version of Pbca. The size of the weak ferromagnetism along the c-direction would be difficult to combine

*We note, that while this space group was suggested, Ref. [90] could not find evidence for a splitting of the 4a-position.

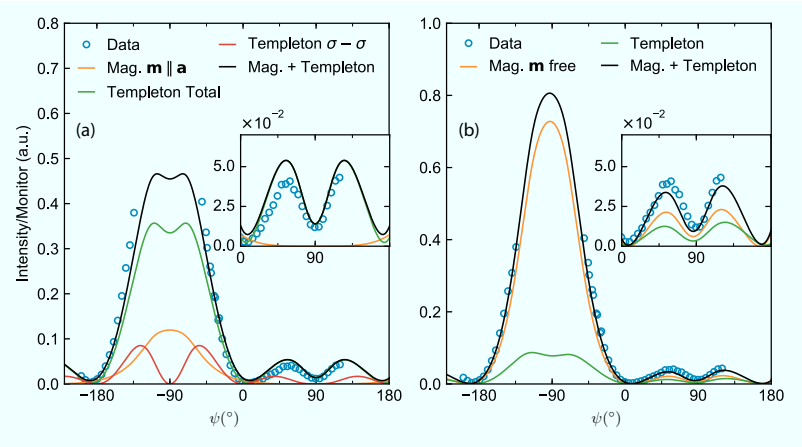

Figure 5.19: Azimuthal Scan of the 101 reflection of CRO on NCAO interpreted with a large Templeton scattering contribution. (a) Model with largely Templeton-scattering contribution and an a-axis oriented magnetic moment. (b) Model with free magnetic moment direction and a Templeton scattering contribution fixed to 1/4 based on its temperature dependence at $\psi = -45°$ (Fig. 5.13).

with a moment pointing mainly along the c-axis, which would favor Γ_1 with the major moment along $\boldsymbol{a}$.

In order to distinguish between both scenarios, one could investigate the polarization dependence of the (110) reflection. At this reciprocal space position, the situation reverses

$$F_{101}^{\Gamma 1} = \begin{pmatrix} 0 & -2z + 2\epsilon z & 0 \\ 2z - 2\epsilon z & 0 & -2x - 2\epsilon x \\ 0 & 2x + 2\epsilon x & 0 \end{pmatrix} \tag{5.23}$$

$$F_{101}^{\Gamma 5} = \begin{pmatrix} 0 & -2z - 2\epsilon z & 0 \\ 2z + 2\epsilon z & 0 & -2x + 2\epsilon x \\ 0 & 2x - 2\epsilon x & 0 \end{pmatrix}. \tag{5.24}$$

The major component of the moment would be dominant compared to the 101 reflection.

5.3.3 Contribution due to Templeton Scattering

First let us recall the Templeton scattering tensor we constructed for the (101) reflection (sec. 3.1.4)

$$F_{101}^{\text{Templeton}} = \begin{pmatrix} 0 & 4\text{xy} & 0 \\ 4\text{yx} & 0 & 0 \\ 0 & 0 & 0 \end{pmatrix} \tag{5.25}$$

Here, the xy refers to the general xy-element of the scattering tensor of the Ru-atom at the (0,0,0) position. This lets us expect that a contribution from Templeton scattering could appear similar to a c-axis oriented magnetic moment. Indeed, on inspection of the temperature dependence of the (101) peak in Fig. 5.13, we notice that the high temperature intensity could account for up to 25 % of the signal at low temperatures, if we roughly extrapolate the shallow increase in the high temperature region. If we model the acquired data using a contribution from eq. 5.25 and a magnetic moment along the a-axis, the data can be modeled well (Fig. 5.19). However, for the least-squares-fit, the Templeton scattering signal would need to be approx. four times larger than the total intensity. Such a large variation in the intensity of the Templeton peak would imply a large change in the tilt or rotation of the RuO_6-octahedra setting in at the magnetic transition at 150 K. Bulk CRO exhibits a considerable change in the tilt starting at 260 K, which is concomitant with an approx. tenfold increase in intensity of the resonant (100) and (011) reflections. [90, 125, 176] Our data in sec. 6.2.3 indicates that the underlying origin for the resonant intensity at these positions might also be Templeton scattering. The tilt order peak we investigated in LSAO(001) shows approximately a threefold rise in intensity (sec. 6.2.2). Both cases show that a Templeton peak can change considerably with temperature.

If one keeps the ratio of Templeton scattering to magnetic scattering fixed to 25 % assuming a continuation of the trend above the magnetic transition and allows the magnetic moment to rotate freely during the fitting, we again obtain roughly equal x and z components in the magnetic scattering tensor validating the analysis above in case the Templeton scattering is not a major contributor to the intensity at lower temperatures.

In order to rule out this scenario, a measurement of a pure Templeton scattering signal would be insightful to probe for changes inde-

pendent of a magnetic contribution. In contrast to magnetic scattering, Templeton scattering should also exhibit scattering in the $\sigma-\sigma$-channel, which could be tracked separately in temperature with a polarization analyzer.

However, even if significant Templeton scattering would be observed in the AFM phase of CRO on NCAO, it would still not explain the weak FM along the c-axis. Thus, another mechanism for explaining the incompatibility with the representation analysis is indicated.

5.3.4 Multiple critical irreducible Representations

Similar to a soft-phonon-mode for structural transitions, Landau-theory predicts a single critical irreducible representation [281] for magnetic phase transitions [281]. This is true for many magnetic structures, but exemptions have been found, where the magnetic moment direction cannot be reconciled with a reduced symmetry and one has to resort to a description via multiple irreps [285]. In fact, it can be shown that the constraint to a single critical irrep is only given, if the free energy Φ used in Landau theory has only terms up to second order. If higher order terms are important, a phase transition involving multiple irreps can occur [286]. For magnetic systems, this translates to the fact that the exchange Hamiltonian involves terms higher in order than the usual $\boldsymbol{S} \cdot \boldsymbol{S}$ [287]. In such a case, all constraints would be lifted and we could describe the AFM by a combination of irreps. The weak FM along the c-axis would be generally described by Γ_3, while the scattering tensor for NCAO could be described by a combination of Γ_1 and Γ_5. We note that a similar issue arose in the investigation of the magnetic moment for the Ru-site in $RuSr_2GdCu_2O_8$, where a moment direction along the $(102)^*$ direction was found [288].

5.4 Conclusion and Outlook

We studied low-temperature ferromagnetic phases and antiferromagnetic phases of epitaxial CRO films using SQUID-VSM magnetometry, magnetoresistance measurements, polarized neutron reflectometry and REXS techniques. The impact of strain on the ferromagnetic

*This refers to the tetragonal unit cell of $RuSr_2GdCu_2O_8$ and thus does not correspond to the (102) direction for CRO.

phase shows an increasing saturated moment with increasing compressive strain: We found $\approx 0.1\,\mu_B$ for CRO on LAO, $\approx 0.2\,\mu_B$ for CRO on LSAO and $\approx 0.3\,\mu_B$ for CRO on YAO at 5 K. This is in line with observations on pressurized single crystals, where the moment increases from $0.1\,\mu_B$–$0.3\,\mu_B$ in the pressure range of 0.3 GPa–1.5 GPa. Measurements of the anisotropic magnetoresistance suggest a switching of the easy-axis under compressive strain emphasising the strong response of the magnetic anisotropy of CRO towards strain.

The REXS studies presented here constitutes -to the best of our knowledge- one of the first studies of AFM in Ruthenate thin films using Ru-L-edge light (besides [289]). The element-sensitivity of REXS and the ability to sense the symmetry reduction of the AFM, confirms the occurrence of antiferromagnetism in the films. So far, the assumption of AFM relied on magnetometry, which is not able to detect the propagation vector of a magnetic system. The polarization analysis and magnetometry data of the magnetic peak CRO on LSAO(110) is fully compatible with the situation for pressurized single crystals with a (010) propagation vector and a magnetic moment pointing along the b-axis. The REXS investigation of CRO on NCAO(110) however revealed a surprising finding: The polarization analysis suggests a so far unreported switching of the moment direction to the (101) plane. Fits show a magnetic moment pointing approximately along the $\bar{1}02$ direction. A representation analysis suggests either a space group lower than Pbca or a more exotic Hamiltonian involving terms higher in order than the typical bilinear $\boldsymbol{S_\alpha} \cdot \boldsymbol{S_\beta}$ coupling. Further REXS studies investigating more forbidden reflection such as e.g. (110) and better off-resonant structural characterization might shed more light on this. A clarification of the magnetic structure could help in the quest of elucidating the role of the crystal-field-splitting on the magnetic anisotropy [106].

Magnetometry and Magnetoresistance data suggests weak ferromagnetism along the c-axis as a common feature in the antiferromagnetic phase of the films on LAO(100), LSAO(110) and NCAO(110). The effect is incompatible with the current understanding of the magnetic structure of bulk CRO and with a representation analysis of the CRO space group Pbca. Although we cannot fully exclude surface or interface effects, the quite different surface orientations of the c-axis oriented films and a-axis oriented films suggest an effect coming from the bulk of the film. The signal could not be attributed to any con-

ceivable impurity. Experiments using e.g. Ru-L edge X-ray magnetic circular dichroism or polarised neutron reflectometry are techniques that might be able to clarify this effect. Studying the magnetization and magnetoresistance of pressurized single crystals along the c-direction might be worthwhile to revisit.

6

The Search for Quadrupolar Ordering

In this chapter, we present a study of the spin-lattice-relaxation rate (SLR) of c-axis oriented CRO films on LAO(100), LSAO(001) and YAO(001) via βNMR. Besides confirming the ferromagnetic and antiferromagnetic transitions, we detected an internal field at high-temperatures above any magnetic transition. The field is also detected in a CRO polycrystal setting in below the MIT indicating an electric origin, since it cannot be detected by μSR measurements. Detailed investigations of CRO on LSAO(001) show a temperature dependence that might be compatible with critical behavior despite the absence of an MIT or structural transition. Orbital ordering in CRO single crystals was suggested at high temperatures, creating the intriguing prospect of a possible detection of orbital ordering in the films. Moreover, CRO on LSAO(001) is metallic suggesting an exotic quadrupolar ordering scenario. A caveat for such a scenario, Li-diffusion, is discussed.

Subsequent REXS studies probing at the propagation vector known for antiferro orbital order (AFO) in bulk CRO are discussed. The polarization analysis of found resonances can be interpreted in terms of Templeton scattering. We show that the polarization analysis of the antiferro-orbital-ordered phase in bulk can also be interpreted within

a Templeton scattering scenario and provide an alternative scenario purely based on structural distortions.

6.1 The $300\,\mathrm{K}$ β-NMR Anomaly

6.1.1 Zero Field Measurements

In order to explore the low-energy spin dynamics and to probe for fluctuations coupling to the electric quadrupole of the 8 Li-ion, we conducted zero field spin lattice relaxation measurements on the c-axis oriented CRO films on LAO(100), LSAO(001) and YAO(001) at the βNQR-endstation at ISAC, TRIUMF described in sec. 3.3.2. Zero-field (ZF) measurements have the advantage that any effect on the asymmetry must come from the intrinsic internal fields of the sample. The films on LSAO and LAO are 40 nm and 50 nm thick, while the film on YAO is 9 nm thick due to constraints of the large compressive strain. In order to implant most of the ions within the film and not the substrate, ion penetration profiles were calculated using the SRIM software package [195]. Based on the calculations, ion energies of 1 keV for CRO on YAO and 3 keV for CRO on LSAO and LAO were chosen (Fig. D.1). The ion energies were set by adapting the high-voltage bias of the sample endstation relative to ground. We expect in general most of the ions to decay within the film, while for CRO on YAO a significant fraction is expected to penetrate the film and stop within the substrate.

CRO on LAO (100)

We first conducted SLR measurements on the CRO film on LAO with the ^{8}Li-polarization $\boldsymbol{P} \parallel 110$ of the CRO unit cell. Surprisingly, we already found a measurable asymmetry at high temperatures (Fig. 6.2). In the absence of an internal field (paramagnetic without an electric field gradient), the polarization of ^{8}Li is very unstable and gets quickly destroyed by random fields usually leaving no signal within the time resolution of the setup. This suggests that there is already an internal field present at high temperatures. Its nature (electric or magnetic) is a priori unclear. To extract the relaxation rate, we used a single

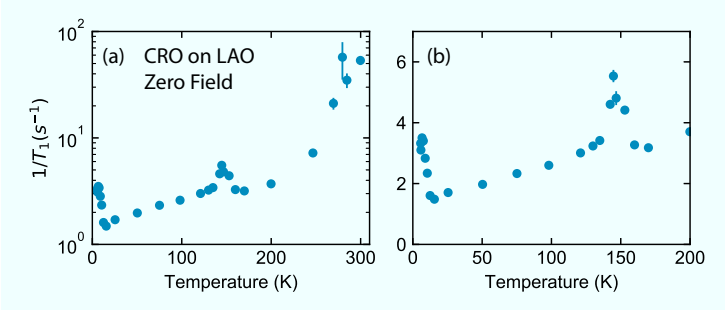

Figure 6.1: Spin-Lattice-Relaxation time measurements of CRO on LAO in zero field. (a) Complete temperature range showing three features at $10\,\mathrm{K}$, $150\,\mathrm{K}$ and $300\,\mathrm{K}$ (b) Magnification of the FM and AFM transitions.

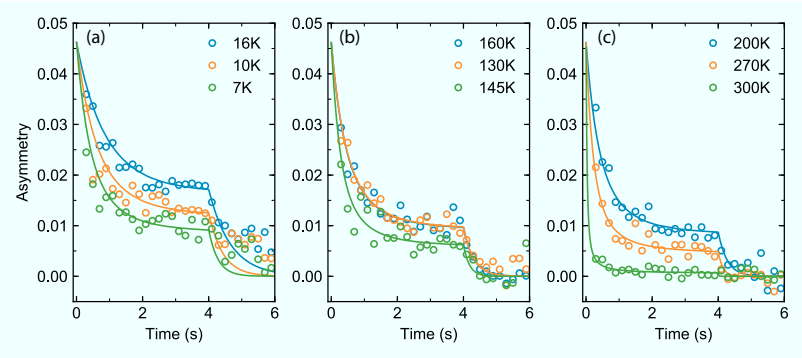

Figure 6.2: Asymmetries around the three features seen in the relaxation time measurements. (a) FM-transition (b) AFM-transition and (c) High-temperature feature. The solid lines depict the single-exponential fits used to extract the relaxation time. Error bars of the individual data points are omitted for clarity.

exponential fit with a fixed amplitude $A_0 = 0.0462$ (eq.3.75) corresponding to the highest observed initial asymmetry. The fits show drop in the SLR down to a plateau around 200 K and then a small peak around 150 K corresponding to the critical fluctuations close to antiferromagnetic transition. The anomaly is relatively small indicating a certain robustness of the signal against magnetic fluctuations, i.e. little spectral weight of the fluctuations at the Larmor frequency. Remarkably, the asymmetry is almost identical above and below the transition corroborating that the freeze out of the spin dynamics below the transition has only little effect on the signal (Fig. 6.2). A similar effect is visible at low temperatures within the ferromagnetic phase: Only a slightly faster relaxation is observed. The dynamics of the high temperature internal field appear to dominate the polarization of the ^{8}Li.

In between the AFM and FM transitions, a linear decrease in the SLR can be observed. Since we did not observe this behavior in the metallic systems on LSAO(001) and YAO(001), we can attribute it tentatively to the AFM in this material. A $1/T_1 \propto T$ is expected in an itinerant antiferromagnet below T_N[290]. This is consistent with our findings from transport measurements that a substantial fraction of the quasiparticles responsible for the magnetism in this material is also delocalized (sec. 4.9), Ref. [142]).

CRO on LSAO(001)

Similar to CRO on LAO, 3 keV-^{8}Li were implanted in to the CRO on LSAO(001) film with a polarization along the 110-direction of the CRO orthorhombic cell. At high temperatures, an asymmetry signal can already be detected despite the absence of an external field. To extract T_1 from the asymmetry, a single exponential with a fixed amplitude of $A_0 = 0.0492$ (the maximum encountered value in the set) allows us to describe the data well. The high-temperature range exhibits a similar phenomenology as the measurement of CRO on LAO(100): The extracted $1/T_1$ decreases on cooling and stabilizes around 250 K (Fig. 6.3). The SLR stays constant until $\approx$ 20 K, where the increasing fluctuations indicate the onset of the FM phase. However, the fluctuations associated with the FM phase are much more effective in suppressing the asymmetry than in CRO on LAO. The critical slow-

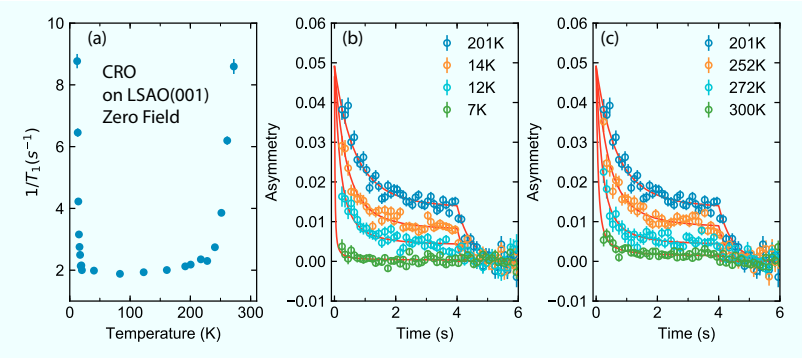

Figure 6.3: (a) Spin lattice relaxation rate of 50 nm of CRO on LSAO(001) with $\boldsymbol{P} \parallel 110$ of the orthorhombic CRO unit cell. (b) Dynamics of the asymmetry close to the ferromagnetic transition (c) Evolution of the asymmetry close to the high-temperature feature.

ing at the phase transition completely destroys the asymmetry signal, which is known as the *wipeout*-effect in NMR-parlance [291].

CRO on YAO(001)

For CRO on YAO(001), the polarization was aligned along the b-axis of YAO(001). As for the other films, we were able to detect an asymmetry although no external field was applied suggesting the presence of a stabilizing internal field (Fig. 6.4). We extracted the SLR using a function with a single exponential relaxation keeping the amplitude fixed at the maximum detected value of $A_0 = 0.0191$ in the same fashion as for the other films measured in zero field. After sweeping from low to high temperatures and determining T_1, a picture similar to CRO on LSAO(001) is found: A well-resolved asymmetry is observed at intermediate temperatures (50 K–200 K), which is subject to an increase in fluctuations at low and high temperatures. Similar to CRO on LAO, there is no wipeout of the signal in the FM phase, while the relaxation becomes sufficiently fast at high temperatures to cause an almost complete quenching of the signal.

As shown in Fig. D.1, we expect a non-negligible portion of the ions to stop within the substrate. Measurements delivering ions intentionally into the substrate by using 19 keV ^{8}Li instead of 1 keV did not show any asymmetry. Together with the data with the other films,

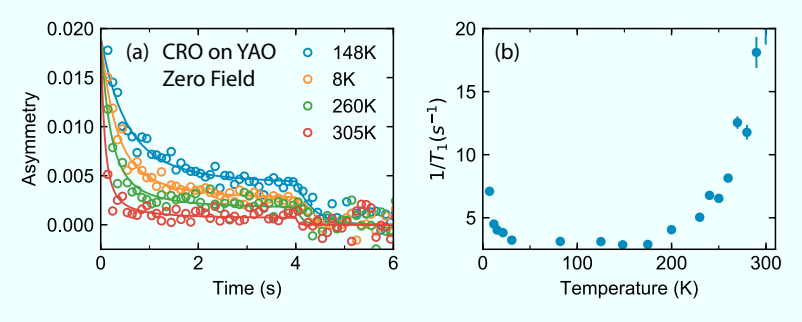

Figure 6.4: (a) Evolution of the asymmetry for CRO on YAO(001) toward high and low temperatures relative to the signal at $148\,\mathrm{K}$. The error bars were omitted for clarity. (b) Extracted SLR from the asymmetry. An upturn at low temperatures related to the ferromagnetic phase and a vanishing signal at high temperatures is visible.

this suggests that the sensed internal field and its suppression at high temperatures indeed originate from the film.

6.1.2 Measurements at $50\,\mathrm{G}$

The high-temperature-anomaly in the SLR observed in zero field in the films was investigated in CRO on LSAO(001) and a CRO Polycrystal using a longitudinal field applied along the polarization of the ^{8}Li-ions, the reasoning being that the observed fluctuations might originate from a phase transition, which should show a characteristic maximum in the relaxation rate. In zero-field measurements, one expects the fields tied to the order parameter to be randomly fluctuating in the disordered phase, which typically depolarizes the ^{8}Li ensemble faster than the time resolution of the measurement.* Thus, one expects not to be able to probe the disordered phase, since the static internal field of the ordered phase vanishes at the transition.† Instead, one would expect a divergence in $1/T_1$ when going from the ordered phase

*μSR spectroscopy has a much higher time-resolution and is regularly used to perform zero-field SLR measurements in paramagnetic phases, see e.g. [292]

†We assume it has a component along the polarization direction in the ordered phase, transverse components would lead to a precession and destruction of the signal.

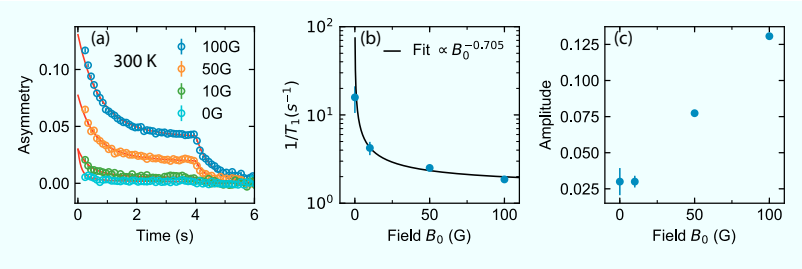

Figure 6.5: (a) Field dependence of the asymmetry and fits at 300 K of CRO on LSAO(001). (b) Extracted SLR vs. field. The trend can be fitted well by a power law $\propto B_0^{-0.705}$. (c) Extracted Amplitude vs. field. The signal is quickly recovered by only applying small fields.

to the disordered phase until the signal disappears- matching the phenomenology of the ZF-measurements presented above (sec. 3.3.3). By applying a static external magnetic field, the random internal fields are superseded and the polarization along the field is stabilized by introducing a Zeeman-gap allowing to measure also within in the disordered phase.

In order to evaluate which field should be used, we conducted a field dependence of the asymmetry and relaxation rate by varying the longitudinal field at 300 K between 0 G–100 G (Fig.6.5). Fitting the measured asymmetries with a single exponential and allowing the SLR and the amplitude to be fitted, shows that the asymmetry lost at temperatures above 200 K can be quickly recovered. If we assume a pure Zeeman-Hamiltonian, the ^{8}Li is sensing only the dynamics at its Larmor-frequency ω_L. In this picture, the effect that already weak fields result in regaining a signal, implies that the fluctuations reside mainly at low frequencies, i.e. are relatively slow. The field-dependence can be fitted well with a power-law $1/T_1 \propto B_0^{-\alpha}$ with $\alpha = 0.705$. Diffusion processes are linked with power law dependences, but typically with $\alpha > 1$ [293]. Based on the measurement, we choose 50 G as an intermediate value to probe the fluctuations at high temperature and try to access a possibly disordered phase.

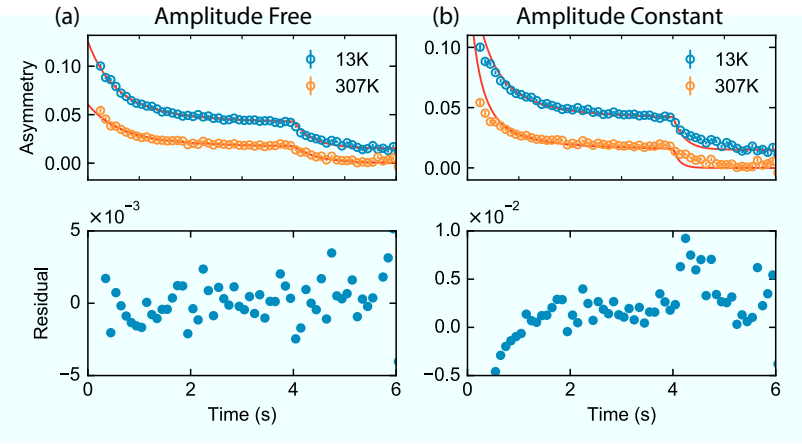

Figure 6.6: Fitting the asymmetry of CRO on LSAO(001) using a single exponential relaxation function with two different methods: (a) Allowing the amplitude and the SLR to be fitted (b) Fixing the amplitude to A_0=0.185, the highest in the temperature series (Fig. 6.7) and only fitting the SLR. Allowing the amplitude to be varied,a better fit with only random residuals can be achieved.

CRO on LSAO(001)

Based on the field dependence (Fig. 6.5) we probed the evolution of the asymmetry of CRO on LSAO(001) in a field of 50 G within the same temperature range 6 K–307 K as the measurement in zero field. Using a single exponential function and fixing the amplitude to $A_0 = 0.185$, the highest value achieved between high and low temperatures, as we did for the ZF measurements resulted in unsatisfactory fits (Fig.6.6). If we allow the amplitude to be varied as well, a better description of the data can be achieved. At low temperatures, the fits reveal the divergence upon entering the ferromagnetic phase and a concomitant drop in the amplitude. The loss of amplitude is likely caused by a relaxation process faster than the time resolution of the spectrometer resulting in an apparent loss of initial asymmetry. The observation of two relaxation processes in contrast to the data in zero-field, might originate from several scenarios depending on whether the internal field observed in the zero-field data is electric or magnetic. The ^{8}Li-ion in a magnetic field resonates at ω_L, so the application of a weak field of $B_0 = 50$ G would only shift this reso-

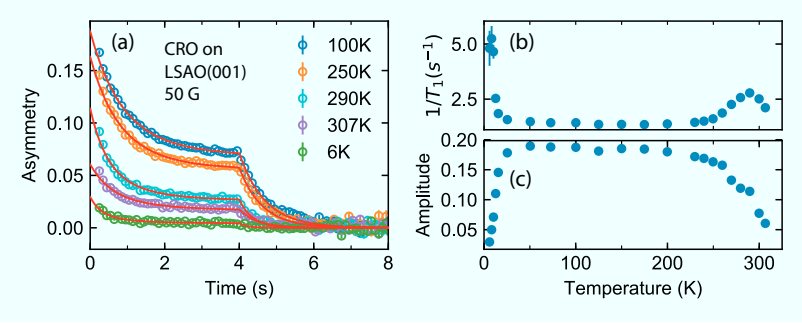

Figure 6.7: SLR-Measurement of CRO on LSAO(001) with applied static longitudinal field $B_0 = 50\,\mathrm{G}$. (a) Exemplary asymmetry curves at various temperatures. The solid lines depict the single-exponential fits to extract the SLR and the amplitude of the signal. (b) Temperature dependence of the relaxation rate $1/T_1$ showing the critical fluctuations at low temperature at the transition to a ferromagnetic state and a high temperature peak. (c) Amplitude (initial asymmetry) vs. temperature. At both anomalies, a dramatic loss of asymmetry is visible.

nance by γB_0. This can change the sensitivity of the asymmetry to certain fluctuations in the spectral density, but should not open up new decay channels for the spin population. Having two stopping sites for the ^{8}Li, one of which is sensed in zero field and 50 G and another one only at 50 G due to different internal field directions, would be a scenario compatible with the observations. A quadrupole Hamiltonian intrinsically yields multiple resonances (Fig. 3.13). Dipolar transitions ($m = \pm 1$) and quadrupolar transitions ($m = \pm 2$) can be of the same order of magnitude [294]. This allows multiple relaxation channels and thus naturally one expects a multiexponential relaxation [189]. Especially when the Quadrupole-Hamiltonian and the Zeeman-Hamiltonian from an applied field do not commute, a small magnetic field can create new relaxation channels, which result in dramatic changes of the asymmetry under an applied field [295]. As we will discuss below, the field sensed in the zero-field measurements is probably electric making the picture of an EFG mixed with the external magnetic field (which might be similar in size) more likely.

Using the discussed fitting procedure, the extracted SLR and amplitude can be again divided into three distinct temperature regions: The ferromagnetic phase transition at low temperatures, an intermediate

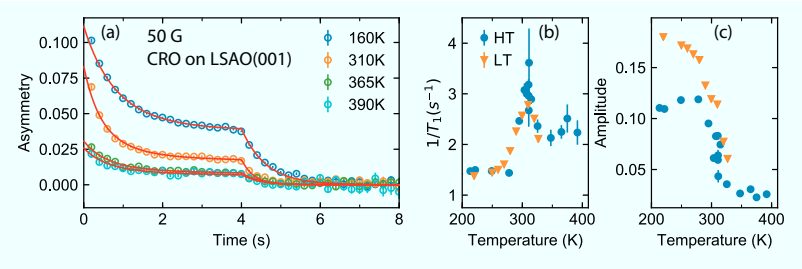

Figure 6.8: High-temperature SLR measurement of CRO on LSAO(001) expanding the range of the previous measurement up to 400 K. (a) Asymmetry evolution upon heating. Solid lines depict the fits to extract $1/T_1$ and the amplitude. (b) SLR measured with the high-temperature setup in comparison with the data measured with the low-temperature setup. Adding an offset of 20 K to the low-temperature allows to match the data well. (c) Amplitude of both measurement runs. The data from the LT-run is also offset by +20 K.

region with flat SLR and amplitude and the high-temperature region with an increase in $1/T_1$ and a drop in amplitude. Most interesting is the observed maximum in the SLR around 300 K, which has not been observed in the ZF-measurement. It is tempting to ascribe the peak to an overall slowing of the relaxation. However, the amplitude does not mirror the same behavior. Overall, the average relaxation of the system might still be increasing. The initial experiment did not allow us to go higher in temperature at this point.

A second measurement using a prototypical cryo-oven at the BNQR setup allowed us to expand the temperature range up to 400 K (Fig.6.8). At the time of the measurement, the temperature control had not been fully optimized yet, which can explain the discrepancy in the two data sets. However, shifting the data from the previous run by 20 K allows matching the sets quite well in the SLR. Since the two runs were conducted at different times with different setups, the discrepancy in amplitude can be well explained by changes in the instrumental parameters [189, 295]. The temperature range 300 K–400 K reveals a salient point: the flattening of the relaxation rate to a plateau - higher than the SLR below 300 K. This is reminiscent of a phase transition, where fluctuations associated with the order parameter freeze out below the critical temperature [296]. The drop in the amplitude, which we associate with a fast relaxation process, approaches a constant value as well following the slow relaxation.

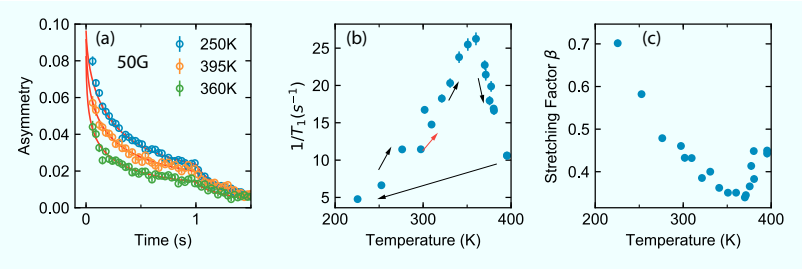

Figure 6.9: Temperature evolution of the SLR of a S-CRO polycrystal with $B_0 = 50\,\mathrm{G}$ applied field. (a) Temperature dependence of the asymmetry below, at and above the MIT. (b) SLR vs. temperature. The red arrow indicates the first data point measured and the direction of the sweep. The points after cooling to 200 K and warming are slightly shifted, which might indicate a hysteresis connected with the MIT. (c) Temperature evolution of the stretching factor β of the stretched exponential function used to fit the data. The experiment was conducted using 1s-pulses instead of 4s-pulses due to the low incoming ^{8}Li-flux.

CRO Polycrystal

As a reference for the measurements in the high-temperature region of the film, we performed an SLR study on a S-CRO polycrystal using 25 keV ^{8}Li. The pellet was made by crushing Ca_2RuO_4 single crystals to avoid the inclusion of the O-CRO phase. After pestling the crystals to a fine powder, it was uniaxially pressed at 120 MPa in a $\varnothing$10 mm-mold and subsequently densified using cold isostatic pressing at 810 MPa. No sintering step was conducted to avoid the formation of the O-CRO phase. The single crystals were synthesized by M. Krautloher following the procedure described in Ref. [107]. A clear signal can be measured at 200 K in zero field providing evidence for the presence of an internal field(Fig. 6.10). In contrast to the film, the spin dynamics of CRO bulk systems have been extensively studied. μSR data does not show any internal field above 120 K[32]. Since muons are not sensitive to electric fields, this indicates that the internal field being sensed by the ^{8}Li is electric. The measured asymmetry was best described by a stretched exponential (eq.3.77). For fitting, the amplitude was kept fixed to the highest observed value of $A_0 = 0.0989$ at 225 K. The relaxation rate shows a maximum around 350 K, which can be associated with the MIT in bulk (Fig. 6.9). The stretching factor β shows also a significant temperature dependence. A $\beta = 1$

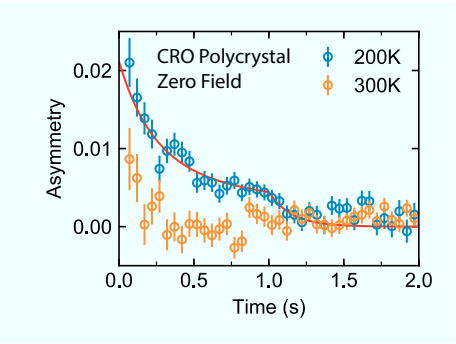

Figure 6.10: Asymmetry of the S-CRO polycrystal measured in zero field. A signal at low temperature becomes visible revealing the presence of an internal field.

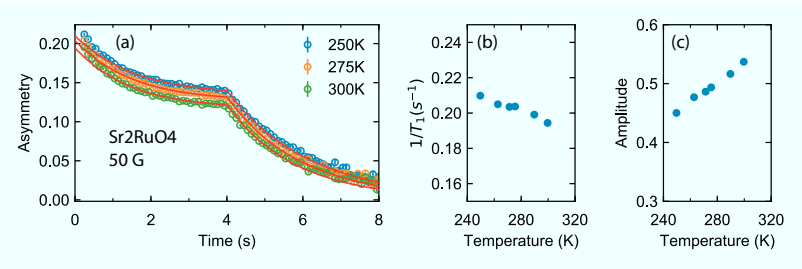

Figure 6.11: Spin Lattice Relaxation Sr_2RuO_4 with a static external field $B_0 = 50\,\mathrm{G}$ applied. (a) Exemplary asymmetry curves at several temperatures showing only weak changes. (b) and (c) $1/T_1$ and amplitude temperature dependence showing a nearly constant or only slightly increasing value.

indicates a homogeneous single-exponential, whereas $\beta < 1$ is associated with a distribution of multiple exponential relaxations. The MIT has been identified as a first-order transition, which is naturally characterized by a mixed-phase region, which would imply at least the presence of two relaxation processes corresponding to the two phases. As discussed in sec. 6.1.2, quadrupolar relaxations are known to be multiexponential. Both aspects are likely contributing to the fact that a distribution of relaxation processes is being sensed.

Sr_2RuO_4 Single Crystal

To explore the relaxation of a structurally similar material without any known long-range magnetic or orbital order, we performed low-field

SLR measurements on Sr_2RuO_4 using $B_0 = 50\,G$. The ^8Li was implanted with the polarization within the ab-plane. NMR-experiments and βNMR measurements at high fields did not reveal any feature at high temperatures in SRO [297, 298]. The SLR and the amplitude was extracted from the asymmetries using a single exponential fit varying the SLR and the amplitude. The results show essentially a featureless temperature dependence (Fig.6.11) corroborating the absence of any low-frequency activity in Sr_2RuO_4 at room temperature.

6.1.3 Discussion

The presence of substantial asymmetry in zero field and the anomaly at high temperatures in the CRO films potentially indicate interesting physics. Especially, experimental findings that suggest that single crystalline CRO hosts quadrupolar order (sec. 2.6) around room temperature (260 K and 350 K concomitant with the MIT were suggested [124, 125]) make it tempting to associate the measured βNMR-anomalies with quadrupolar order in the films. However, since βNMR is a local probe, it is sensitive to a variety of effects , which creates caveats that have to be discussed within this context. The internal field, which was detected in all the films is likely an electric field gradient (EFG), since we did not detect any magnetic order above 150 K with other techniques. The evidence is even more compelling for the single crystal, where μSR can exclude magnetic fields above the Neel temperature. An EFG forms, if the crystal field symmetry at the ^8Li-stopping site is lower than cubic. [295] Due to structural distortions in CRO, one would expect naturally that a cubic symmetry is not fulfilled. Sr_2RuO_4 being higher in symmetry than CRO already exhibits an EFG measurable with βNMR [298]. A certainly more interesting scenario would be that the EFG is caused by effects in the Ru valence shell, namely the deformation of the 4d-orbitals driven by a correlation effect such as quadrupolar ordering. This is especially intriguing in light of the feature at 300 K, which might indicate a phase transition. Ru-NMR data on bulk CRO indeed suggests that the electric quadrupolar interaction of the Ru-atoms can sense the ferro-orbital order below the MIT in S-CRO(Fig. 6.12). Our ^8Li-βNMR measurement on the S-CRO polycrystal is compatible with the formation of an EFG below the MIT-consistent with the report, although the probing sites of ^8Li and Ru should certainly be subject

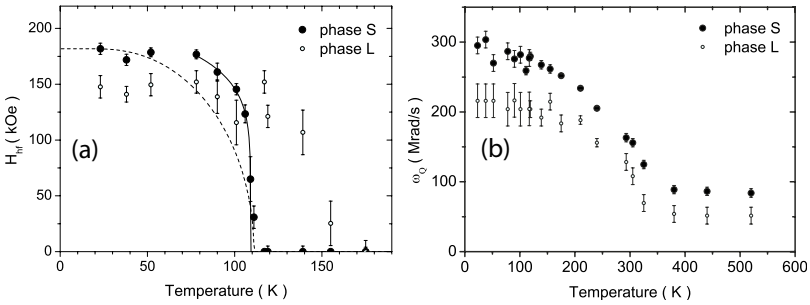

Figure 6.12: Hyperfine field (a) and Quadrupolar frequency (b) of a CRO polycrystal measured via 99 Ru-perturbed angular correlation technique(PAC). A signal at the MIT in stoichiometric CRO (phase S) is sensed, which was associated with orbital order. The polycrystal also contains the oxygen-excess phase (phase L) identified by the different T_N seen in the magnetic channel. Interestingly, the phase-L shows a signal at $300\,\mathrm{K}$ in the quadrupolar channel similar to the CRO films, although the MIT is at much lower temperatures ($150\,\mathrm{K}$[90]). Taken from [123].

to different crystal fields. The data is consistent with the ferro-orbital picture put forward by reports using Ru-K edge REXS and O-K-edge XAS [124, 248]. This would create the enticing possibility that the feature at 300 K measured in the films indicates a correlation-driven phenomenon. We also note that the literature Ru-NMR data also suggests the formation of an EFG at 300 K connected to orbital order for the oxygen-enriched O-CRO phase, although the MIT is suppressed to 150 K in this material and no structural phase transition has been reported at this temperature [90]. However, due to the lack of single crystals, further studies using e.g. REXS were not conducted.

The appearance of the feature at similar temperature scales despite the substantial strain difference and changes in the electronic properties would let one intuitively suspect a magnetic impurity phase. Since the growth conditions of CRO are so stringent (sec. 4.5), $CaRuO_3$ is expected to be present in minute quantities, but no long-range order above 150 K has been reported in strained films or bulk systems [277, 299]. Surprisingly, RuO_2 was reported to host itinerant antiferromagnetism [300]. The authors of the report could not determine the Neel temperature, since their study lacked a temperature dependence of the magnetic peaks, but it was stated to be $\geq 300\,\mathrm{K}$. We used an excess of the precursor RuO_2 for the preparation of the PLD-target,

so it appears reasonable to assume that a small amount of (likely amorphous) RuO_2 becomes transferred onto the sample. However, the Ca_2RuO_4 and Sr_2RuO_4 single crystals are similarly grown with excess RuO_2. [107, 301] Thus, a small percentage of RuO_2 is likely to be embedded in the crystals as well, but no anomaly was found for SRO and the feature in the polycrystal is clearly connected with the MIT located at a higher temperature. In addition, a recent REXS study found the AFM in RuO_2 persisting up to 400 K[289].

The transition temperatures that can unequivocally can be associated with magnetism (low-temperature FM-phase and AFM-phase) show a strongly non-linear strain-dependence, i.e. they are either present or not. This agrees with pressurized CRO single crystals [43] indicating that, despite the lacking sensitivity to strain, it is still sensible to link the anomaly at 300 K to a correlated phenomenon.

If we indeed observe a phase transition, one might wonder why the critical fluctuations would be so strongly damped and only a small feature in the SLR was observed at 300 K. One possibility, might be that the onset of a spin-nematic phase is sensed, which is predicted in the strong SOC-picture of CRO (sec. 2.6). It has indeed been shown, that spin-nematic phases can show substantially slower relaxation at the transition than e.g. typical AFM transitions. [132]

Using muons and the ^{8}Li as probes, one needs to be aware of the influence of diffusion effects on the polarization - especially at the relatively high temperatures that have been investigated. In our case, diffusion is essentially the effect that the ^{8}Li ion starts jumping between stopping sites due to thermal motion. While the ion is in motion, the sensed internal fields transform from static values to a distribution function in time. Staying within the simple picture of an ^{8}Li within a static magnetic field, the polarization of the ^{8}Li is mainly affected by fluctuations at the Larmor frequency ω_L (sec. 3.3.1). The timescale of the ion motion between sites is represented by the correlation time τ_c. The definition for τ_c in the literature is somewhat loose, but in our context it suffices to state that the autocorrelation of the polarization function in time $G(t)$ of the ^{8}Li is very small for $t \gg \tau_c$[103]. It is of the same order of magnitude as the mean site residence time between jumps [293]. The frequency of the hopping and thus of the fluctuations is consequently $\propto \tau_c^{-1}$. For low temperatures, $\omega_L \tau_C \gg 1$, the spectral density function exhibits the most spectral weight at frequencies lower than ω_L (Fig.6.13) Increasing the

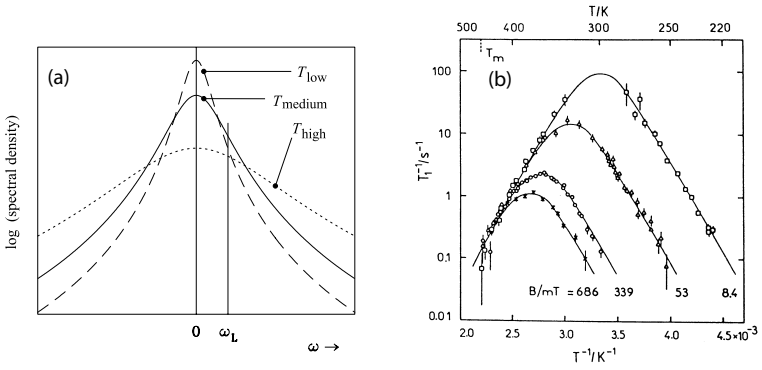

Figure 6.13: Relaxation effects due to diffusion. (a) Qualitative picture of the spectral density of the fluctuations sensed by a diffusing particle at different temperatures. The Larmor frequency defined by the field at the probe is denoted as ω_L. Taken from [293]. (b) SLR measurement using ^{8}Li-βNMR in polycrystalline Li illustrating effects due to diffusion on the relaxation time $1/T_1$. Taken from [302].

temperature, the spectral density increases at ω_L, causing the system to relax faster, i.e. an increase in $1/T_1$. At $\tau_C\omega_L \approx 1$, the spectral weight at ω_L is the highest during the temperature sweep. Increasing the temperature further pushes more fluctuations above ω_L letting the system relax slower. Thus, for a given static external magnetic field B_0, one expects a peak in the temperature dependence of the SLR (Fig. 6.13). Since ω_L is field-dependent, the peak moves in temperature with varying the external magnetic field. A distinct difference between a phase transition and a diffusion-related peak is the recovery of the SLR after sweeping through the maximum. In case of a phase transition, the order parameter fluctuations freeze out, which gives a lower SLR in the ordered state than in the disordered state. Under this aspect, the measurement of CRO on LSAO(001) in a field of 50 G is more compatible with a phase transition than a diffusion-related peak. In addition, comparing the zero-field data and the 50 G-data, the observed maximum appears to have been shifted to lower temperatures, which is the opposite from what would one expect from a diffusion process.

A feature facilitating diffusion is essentially the "dead space" of a unit cell, where guest ions can form diffusion paths. Typical ion con-

ductors are thus materials which have large internal interfaces, where guest ions can easily be intercalated and move freely [293]. A typical example is graphite or even bilayer graphene [303]. Bulk Sr_2RuO_4 and Ca_2RuO_4 are similar in structure and, although quite different in their electronic properties, should be comparable in terms of their ability to allow Li-ion diffusion. Within that reasoning, the lack of a feature in SRO suggests that the SLR upturn for the CRO films is not linked to a diffusion process (Fig. 6.11). It has to be noted, however, that bulk CRO has a higher propensity to accept interstitial oxygen indicating that more intercalation space might be present [90]. A previous report of CRO films on LAO suggests on the other side that CRO films do not accept excess oxygen (see suppl. of [142]).

6.2 Resonant Elastic X-Ray Scattering

The anomaly observed with βNMR suggests the intriguing prospect of a phase transition at high temperatures. The fact that the feature sits above T_N in the antiferromagnetic CRO on LAO and that it appears in a temperature range that has been linked to quadrupolar order [124, 125], motivates us to investigate the films using REXS to directly probe for signatures of such order of the Ru-atoms. Antiferro-orbital-order with the same propagation vector as the AFM was suggested for the S-CRO single crystal by using REXS at the Ru L-edges [125], which made the confirmation of the same type of order our initial prime target. The original report described an orbital order phase transition above T_N observed at the 100 and 011 reflections, which are also the magnetic peaks for the A-Type AFM magnetic symmetry found in stoichiometric CRO. Thus, we studied the films with the same methodology. Resonant peaks were found, but in all cases could be explained by Templeton scattering. Revisiting the single crystal, we find that many key features of the orbital ordered phase can also be interpreted in terms of Templeton scattering.

6.2.1 CRO on LAO(100)

Having the goal in mind to perform a temperature dependence and azimuthal scans at the same reflection that have been linked to AFO in bulk, we chose the 013/103 reflection to probe for a possible phase

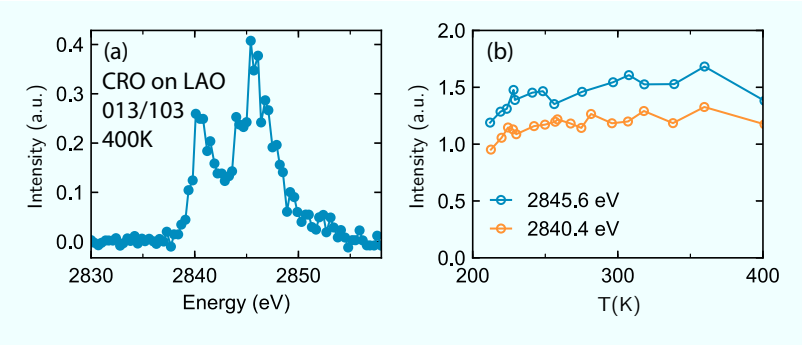

Figure 6.14: (a)Energy scan in the σ-π channel of the 013/103 (twinned) peak at $400\,\mathrm{K}$ at the Ru L3 edge showing the characteristic two peak structure. The low quality resulted from the fact that the backslash correction of the analyzer motors was flawed, which was found out only after the experiment. (b) Temperature dependence of the same peak at both energies showing a featureless dependence.

transition around 300 K. The 100 reflection lies in-plane for the c-axis oriented films and is thus not accessible in a typical geometry for azimuthal scans. The 013 peak is assumed to be symmetry-equivalent to the 011 and thus should have the same underlying scattering tensor as the 011 in bulk, which showed AFO. We confirmed this by conducting a reference measurement on a single crystal (sec. 6.2.3). To be able to conduct polarization analysis, we performed the experiment at the Ru L3 edge, since the scattering angle for the Si-111 analyzer is closer to 90°*. We do not expect significant leakage between channels, but large deviations from 90° are technically not possible at the beamline, which was used for these experiments. The CRO film on LAO is twinned,thus we expect intensity from 013/103 reflection at the same position in reciprocal space. At the Ru L3 edge (2837 eV), the peak is located at $2\vartheta = 85°$ requiring a wedge angle of 37°. This results in a variance of the incidence angle between 5.5° and 79.5° letting us again expect significant geometric effects (sec. 3.2) when performing an azimuthal scan. For all REXS experiments below, the all-in-vacuum setup at P09 was again used to mitigate air-absorption. We note that the edges of the substrate are 45° rotated w.r.t. to the orthorhombic

*At the L3 edge(2837 eV), $2\vartheta = 84°$ vs $2\vartheta = 88°$ at the L2 edge (2968 eV)

unit cell of CRO, which necessitates the rotation of the substrate of 45° to bring the h0l or 0kl plane in the scattering plane [54]. Thus the scattering plane lies in the diagonal of the substrate other than shown for the case in Fig. 3.9.

The 013/103 is structurally forbidden, but similarly to the magnetic peaks investigated in ch. 5, we already detect intensity at room temperature. Energy scans show a resonance with two peak structure (Fig. 6.14), similar to the datasets obtained at the L2 edge during the study of the magnetic peaks, which we ascribe tentatively again to the $t_{2g} - e_g$ splitting of the 4d shell of CRO. The temperature dependence of the integrated intensity in the σ-π channel at both energies does not show any large changes, which could be associated with a phase transition.

In order to probe the origin of the resonant intensity at this position and to test whether a possible transition around 300 K alters the electronic anisotropy of the Ru valence shell, we performed azimuthal scans at 200 K and 400 K including polarization analysis (Figs. 6.15 and 6.16). The lack of temperature dependence of intensity lets us assume that the signal originates from Templeton scattering. Indeed, as we will show below, the signal can be well modeled at both temperatures using the scattering tensors we derived for tilt order in sec.3.1.4. Since both 013 and 103 are contributing to our signal, we expect a priori two modes to be present to our signal:

$$\boldsymbol{F_{013}} = \begin{pmatrix} 0 & 0 & \mathrm{xz} \\ 0 & 0 & 0 \\ \mathrm{xz} & 0 & 0 \end{pmatrix} \qquad \boldsymbol{F_{103}} = \begin{pmatrix} 0 & \mathrm{xy} & 0 \\ \mathrm{xy} & 0 & 0 \\ 0 & 0 & 0 \end{pmatrix} \tag{6.1}$$

Each tensor is associated with specific reference vector for defining the azimuth origin. They are both 90° rotated with respect to each other corresponding to the relative orientation of the twin domains. As in ch. 5, we choose the (010) for $\boldsymbol{F_{103}}$ automatically implying (100) for $\boldsymbol{F_{013}}$. Thus, when $\psi = 0°$, the (010) is in the scattering plane for $\boldsymbol{F_{103}}$ and (100) for $\boldsymbol{F_{013}}$ respectively.

Structurally, the two twin domains are assumed to be present in equal proportions. However, the tensor elements xz and xy are expected to be of different magnitude. Based on the simple estimate from sec. 3.1.4, we predict the xz to be the largest assuming the Pbca spacegroup and tilt and rotation angles comparable to single-crystalline CRO.

We first discuss the approach that was used to analyze the data at 400 K (Fig. 6.15) and then apply the same methodology to the data at 200 K. For modeling the polarization dependence we can use the following expressions derived in the last chapter:

$$I_{\sigma\sigma}(\psi) = \eta(\psi)\left(\left|\boldsymbol{\sigma_f}\cdot\boldsymbol{F_{103}}\cdot\boldsymbol{\sigma_i}\right|^2 + \left|\boldsymbol{\sigma_f}\cdot\boldsymbol{F_{013}}\cdot\boldsymbol{\sigma_i}\right|^2\right) \tag{6.2}$$

$$I_{\sigma\pi}(\psi) = \eta(\psi)\left(\left|\boldsymbol{\pi'_f}\cdot\boldsymbol{F_{103}}\cdot\boldsymbol{\sigma'_i}\right|^2 + \left|\boldsymbol{\sigma'_f}\cdot\boldsymbol{F_{013}}\cdot\boldsymbol{\sigma'_i}\right|^2\right). \tag{6.3}$$

Here, $\eta(\psi)$ denotes the geometric correction factor and $\boldsymbol{\sigma}$ and $\boldsymbol{\pi}$ the azimuth-dependent polarization vectors calculated according to sec. 3.2.2. The subscripts i and f denote whether the vector is incoming or outgoing. The prime distinguishes the polarization vectors from their twin domain counterparts. We first focus on the polarization dependence normalized to the monitor signal depicted in Fig. 6.15a. Here $\eta(\psi)$ corrects for the varying diffraction volume within the film and absorption effects. We estimated an attenuation length of 1.5 m for the penetration depth based on Fig.A.2. However, the absorption effects have only minor impact on the model due to the relatively steep incidence angles (see flattening of the maximum of the σ-π fit around $\psi = 90°$). Fitting both channels (σ-σ and σ-π) simultaneously and assuming that both xy and xz modes contribute to the signal, we arrive at a ratio of $|xz|/|xy| = 80$. A fit only using the xy-mode fails to describe the data in the σ-π channel. The σ-σ channel shows the same dependence for both tensors yielding thus good fits for both approaches. However, in the grazing emergence region around $\psi = 90°$, we observe some significant deviations from our model. Inspecting the rocking curves used to obtain the integrated intensity, we find that the scans above $\psi = 50°$ contain two peaks, which likely arise from the twin domain structure of the LAO substrate which is translated to the film (sec. 4.8.1) [234]. Thus, the intensity in this region is probably less reliable, since the incoming intensity is now distributed on two domains, but only the fully optimized signal of one domain is measured. During the experiment, we recorded simultaneously the fluorescence(XRF) by a diode offset from the detector. The setup is identical to the setup used for studying the magnetic peak of CRO on LSAO(110) (see sec. 5.2.2 and Fig. 3.9). The XRF-signal is subject to the same geometric effects on the incoming beam as the scattering signal and also includes absorption effects e.g. due to surface contamination, which are not included for the model of the monitor-

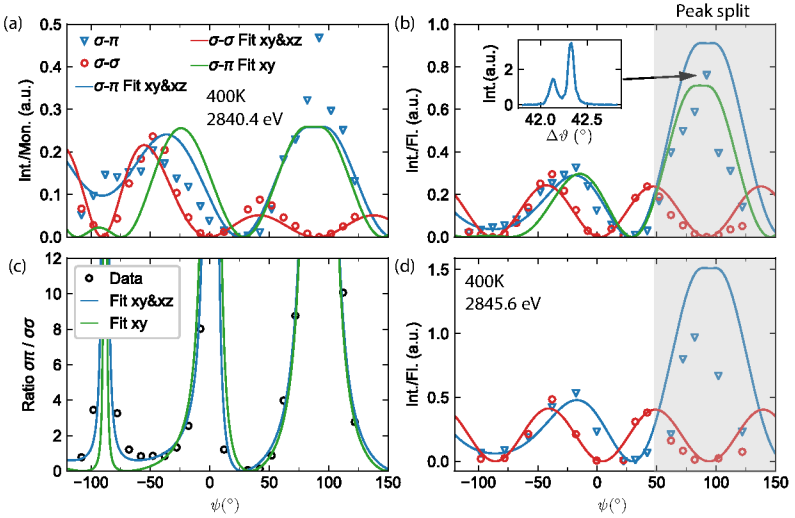

Figure 6.15: Polarization analysis of the 013/103 peak of CRO on LAO(100) at $400\,\mathrm{K}$. Each twin domain contributes to the signal through a different tilt mode (103 with xy, 013 with xz, see text). (a) Integrated intensity normalized to the monitor signal showing both σ-σ and σ-π channels including fits assuming both (xy and xz) or only xy tilt modes. The σ-σ dependency is identical for both channels, thus only one fit is shown. (b) XRF-normalized azimuthal dependence including fits retaining the same color code as (a). Gray areas depict ranges that were excluded from the fit, due the peak splitting (inset). The XRF signal corrects for geometric and absorption effects, which gives rise to the different shapes. (c) Ratio of σ-σ to σ-π and corresponding fits confirming the xz-mode as the dominant contribution to the signal. (d) Polarization dependence at the energy of the peak associated with the eg-orbitals showing an identical signal.

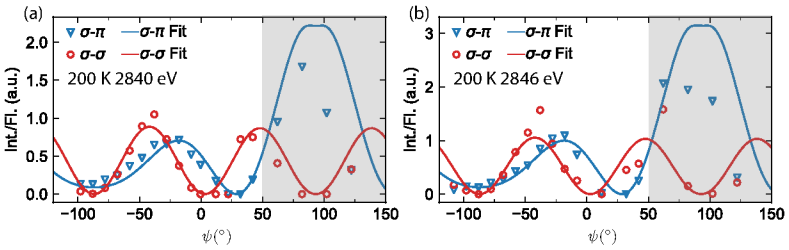

Figure 6.16: Polarization analysis of the 013/103 peak of CRO on LAO(100) 200 K using the XRF-corrected signal at the two peaks in the energy scan (Fig. 6.14). The fits assumed solely a xz-type contribution. The good agreement confirms the identity of the data taken at 400 K and 200 K. As in Fig.6.15, the gray regions denote data excluded from the fit due to varying contributions from twin domains.

normalized data. The geometric correction factor $\eta(\psi)$ is only correcting for the absorption of the outgoing beam of the scattering signal in this case. The detection angle of the XRF, i.e. the angle between the line of sight of the diode and the sample surface, stays relatively large such that absorption effects on the XRF signal not more than 1 % are estimated. This is negligible in comparison with typical systematic errors encountered during the experiment. Here, we assume again that the fluorescence signal from the diode is mainly coming for the Ru-atoms, since we are in proximity of the absorption edge. We observed a significant discrepancy between η and the XRF-signal, which we conjectured to be an effect of the typical surface contamination when using the all-in-vacuum setup. Generally, we expect the effect of any contamination to be stronger for the weaker Templeton scattering peaks in comparison with the magnetic peaks. This prompted us to examine the XRF-normalized signal(Fig. 6.15b) to assure the assignment to the xz-mode is accurate, since the difference between the modes is relatively subtle. The resulting signal was again fitted assuming the presence of both xy and xz modes. Using the full range in ψ, the fitting only yielded unsatisfactory results. However, when we exclude the range with $\psi > 50°$ based on the double peak showing up in the rocking curves, we achieve a good fit of the residual finite range with practically zero xy contribution. As a last check we fit the ratio σ-π / σ-σ in the full range, since all mentioned extrinsic effects (surface contamination, geometric effects, twin domains) should

affect both channels equally and thus should cancel out for the ratio. At the positions, where the σ-σ is zero, the ratio diverges to infinity and is unusable. However, fitting the remaining data points assuming both modes results in an excellent fit with exclusively xz contribution (Fig. 6.15c). The difference to the xy-mode is subtle, but the combination of all three methods and the agreement with our prediction, strongly suggests that the major contribution to the observed data is indeed the xz-mode. We also conducted a coarser azimuthal scan at 2845.6 eV associated with the eg-orbitals and find the same xz-type dependency. The data at 200 K is in good agreement with the data taken at 400 K showing that we likely only sense Templeton scattering. No phenomenon linked to the anomaly observed in βNMR can be detected. Additionally, this implies that the weak MIT for CRO on LAO at $\approx$ 290 K observed in transport is apparently not connected to any large structural changes.

6.2.2 CRO on LSAO(001)

The indication of an electronic phase transition at 300 K by the βNMR data -possibly of electronic origin- make the study of CRO on LSAO(001) especially interesting due to its metallicity. Correlated phenomena such as quadrupolar order are typically associated with localized electrons with small bandwidth and spatially well separated orbitals. However, it has been shown that correlation effects still play a role in metallic ruthenates (sec. 2.6). Finding evidence for a correlation-driven phase transition in a metallic state would certainly give crucial input for the theoretical understanding of the system. Guided by the report of antiferro-orbital order(AFO) in bulk CRO [125], we set out to probe for anomalies linked to the 300 K-SLR-feature at the 101/011 peak. CRO forms two twin domains on the tetragonal LSAO(001) substrate, thus , similar to CRO on LAO, we cannot distinguish between H0L and 0KL peaks. Initially, we measured the temperature dependence of the 101/011 peak at the Ru L2 edge at the beamlines BM28 and 4-ID-D, which revealed a curve that resembles an order-parameter-like shape. However, during these experiments, the maximum temperature of the cryostat was limited to 320 K not allowing us to probe a substantial range above the suspected transition at 300 K (Fig.6.17). To expand the temperature range, we employed a cryostat with higher maximum temperature for

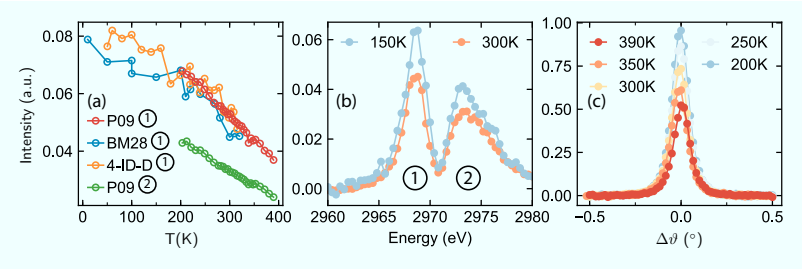

Figure 6.17: (a) Temperature dependence of the resonant 101/011 reflection of CRO on LSAO(001) extracted using integrated intensities of rocking curves. The data acquired at the beamline BM28 and 4-ID-D could not be extended to higher temperatures leaving room for interpretation, whether the shape represents an order-parameter-like behavior. A subsequent experiment at P09 using a high-temperature setup allowed to extend the range and showed no anomalies around 300 K. The circles numbers relate to the different energies depicted in the energy scan. (b) Energy dependence at the reflection around the Ru L2 edge showing the characteristic doublet. (c) Temperature evolution of the rocking curves used to extract the integrated intensity.

the final experiment at P09. Here, we observed a continuation of the linear trend toward higher temperatures without any flattening. Energy scans show again a two-peak shape similar to all the other CRO systems presented in this work. One key feature of the AFO in bulk CRO were the different temperature dependences of the two peaks. This prompted us to study the temperature dependence at the higher-energy peak as well, which shows that the behavior of both peaks is practically identical.

For the c-axis oriented CRO film on LSAO, the 101/011 position is reachable at all of the mentioned beamlines, but it is not favorable for conducting azimuthal scans. In order to reach this reflection in a specular fashion for an azimuthal scan (Fig. 3.9), the geometry necessitates $\vartheta = 25.4°$ and a wedge angle of 66.8°, which would render a large portion of the azimuthal range inaccessible due to the sample horizon. In order to probe for any changes in the anisotropy of the valence shell of the Ru-atoms connected to the feature observed in βNMR, we conducted azimuthal scans at the 013/103 position at the Ru L3 edge at the beamline P09 using the same procedures as for CRO on LAO (sec. 6.2.1). The presence of two twin domains lets us expect a contribution from a xy- and a xz-mode Templeton

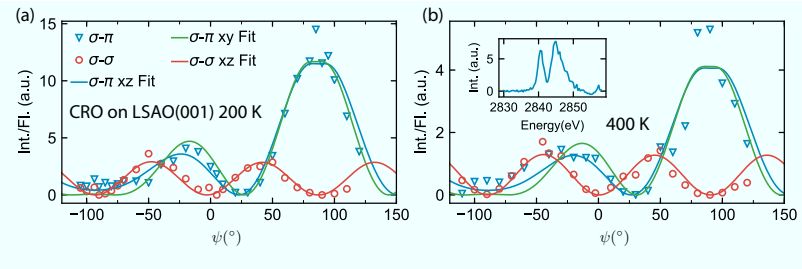

Figure 6.18: Polarization analysis of the 013/103 of CRO on LSAO(001) at (a) $200\,\mathrm{K}$ and b) $400\,\mathrm{K}$ with a photon energy of $2845\,\mathrm{eV}$. The fits for models based on two possible types of Templeton scattering (xy- or xz-type) are shown. The presence of intensity below $\psi = -50°$ indicates a predominantly xz-mode contribution. The inset of panel (b) shows an energy scan at $300\,\mathrm{K}$ at $\psi = -80°$ with σ-π analysis.

scattering (eq.6.1). Going through the same analysis illustrated in Fig. 6.15, we find that the polarization analysis is again agreeing well with a xz-type Templeton scattering at $200\,\mathrm{K}$ and $400\,\mathrm{K}$ (Fig. 6.18). A simplification is the fact that LSAO does not have a corrugated surface as LAO, so only a single peak is observed when collecting the integrated intensity via rocking curves. Combined with the lack of features in the temperature dependence, we can state that no major changes in the scattering tensor can be observed and that the peak is likely purely caused by structural distortions. The agreement with tilt order caused by the arrangement of the octahedra in the Pbca space group constitutes additional evidence that the assignment to the Pbca space group is indeed valid.

Although the temperature dependence of the resonant 101/011 reflection does not exhibit an order-parameter-like-behavior or an anomaly, it still shows a remarkable intensity increase with temperature (Fig.6.17). In order to definitely separate structural effects from a possible ordering phenomenon, we decided to take additional data of off-resonant peaks. Using X-rays at $11.2\,\mathrm{keV}$, we recorded the temperature dependence of the (1,0,10)/(0,1,10) peak. This peak was deliberately chosen, since it has a structure factor, where mainly oxygen atoms contribute, which move under the tilt and rotation of the RuO_6 octahedron. For peaks arising from Thomson-scattering, we expect intensity variations predominantly coming from a change in the atomic positions and a subsequent phase change in the structure fac-

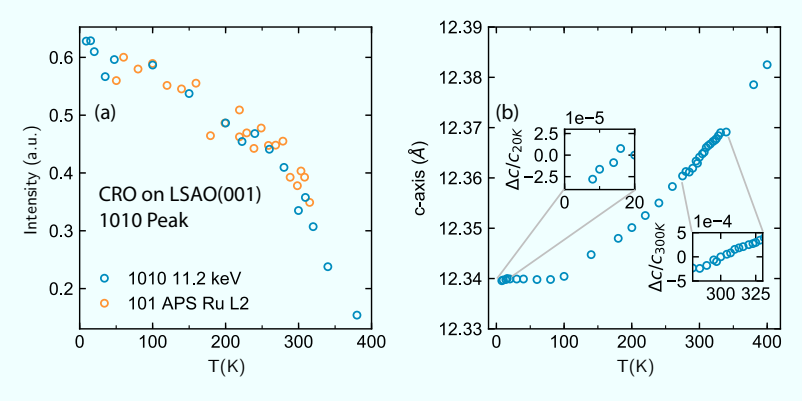

Figure 6.19: Studying charge peaks at a photon energy of $11.2\,\mathrm{keV}$ as a reference for the observed effects at the 101/011 reflection of CRO on LSAO(001). (a) Integrated intensity of the 1010/0110 peak vs. temperature in comparison with the trend of the resonant 101/011 peak observed at the Ru L2 edge. The similar behavior confirms the structural origin of the intensity variations. (b) Temperature dependence of the C-axis lattice constant by tracking the 2ϑ-value of the 0018 reflection. No distinct feature around room temperature can be observed. However, small changes at low temperature might indicate magnetostructural coupling upon entering the ferromagnetic phase.

tor. The sensitivity to the oxygen positions should allow us to monitor tilt and rotation activity of the RuO_6 octahedra. Indeed, the resulting temperature dependence is in good agreement with the trend of the resonant 101/011 reflection (Fig. 6.19). An intensity change purely arising from thermal vibrations of the atoms, a.k.a the *Debye-Waller factor*, is unlikely, since we do not see the typical changes in the diffuse background surrounding the Bragg reflection [304].

Using the same energy, we tracked the 2ϑ position of the (0,0,18) peak to study any anomalies in the out-of-plane c-axis lattice constant. The reasoning being, that the in-plane lattice constants are assumed to be pinned to the substrate due the epitaxial relationship, which should cause any thermodynamical drive to change the unit cell volume by e.g. a phase transition to be relieved by expanding or contracting the c-axis. The data shows typical phononic thermal expansion without any features around $300\,\mathrm{K}$. However, a minute decrease at low temperatures might be connected to magnetoelastic coupling when entering the low-temperature ferromagnetic state.

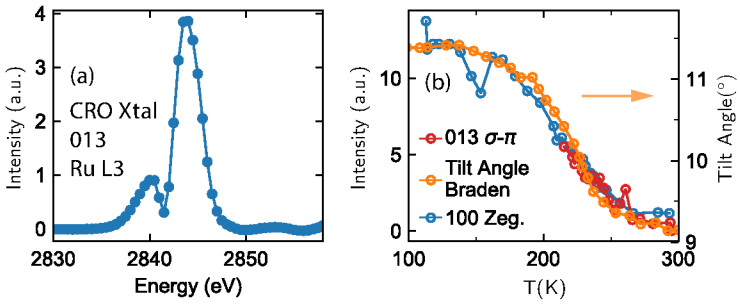

Figure 6.20: Investigation of the 013 peak of a CRO single crystal. (a) Energy scan at the 013 reflection close to the Ru L3 edge at $\psi = -30°$ and $T = 210\,\mathrm{K}$ acquired in the σ-π channel. Similar to the findings from previous reports at the 100 and 011 at the Ru L2 edge, the peak at $2845\,\mathrm{eV}$ is significantly larger than the one at $2840\,\mathrm{eV}$. The scan was not corrected for absorption. (b) Temperature dependence of the 013 reflection acquired with σ-π polarization analysis at $\psi = 0°$. The data is compared with the dependence of the (100) recorded in the previous REXS-study of CRO crystals [176] and the tilt angle measured with Neutron powder diffraction [90]. The similarity of the tilt and the intensity trend is striking and seems to have been missed in the previous study.

Altogether, the X-ray scattering dataset of CRO on LSAO(001) can be fully explained by distortions of the RuO_6 octahedra: The presence of resonant peaks at forbidden positions is consistent with a Templeton-scattering mechanism. Combined with the off-resonant data, the temperature dependences can be interpreted as activity of the tilt, rotation or compression of the octahedron.

6.2.3 CRO Single Crystal

The bulk CRO system has been intensively investigated using REXS at the Ru L-edges and K-edge [124, 125, 176]. A key finding of the Ru-L-edge study was the antiferro-orbital order (AFO) evidenced by an order-parameter-like intensity trend of the 100 and 011 reflections above the Neel-temperature, which has been one of the key motivations to perform similar studies on the CRO thin films. The 110 peak was also studied, but identified as Templeton-scattering due to its polarization dependence and lack of features in its trend vs. temperature. However, attempts to obtain an azimuthal dependence

of the AFO phase only seemed to have been successful in limited ranges [176], which was likely due to the inherent low crystalline integrity of CRO single crystals. Bulk CRO undergoes an MIT at 350 K with extreme concomitant structural changes. The volume change and the orthorhombicity change is so dramatic that the crystals shatter when they are cooled through the transition. The crystals therefore typically consist of several macroscopic crystallites, which are relatively loosely connected and aligned to each other. Due to the multiple angular adjustments during an azimuthal scan, it cannot be avoided that the beam spot moves on the sample, illuminating different crystallites at different azimuths and thus obscuring the inherent polarization dependence. The crystals appear to preferentially fracture along the (110) twin boundaries, which might explain why the (110) azimuthal scan (with $\boldsymbol{q}$ perpendicular to the (110) face) resulted in higher quality data than other reflections. This motivated us to to retry an azimuthal scan within the AFO phase using the (001) face. The (001) plane is a natural cleavage plane of CRO and also typically the largest face of the crystal. To this end, analogous to geometry used for the c-axis oriented films studied above, we conducted an investigation of the 013 peak of a CRO single crystal scattering off the 001 face using light tuned to the Ru-L3 edge. The crystal was grown by M. Krautloher using the floating-zone technique. Details regarding the synthesis can be found in Ref. [107]. The characterization of the sample in a lab-source with a beam covering the whole sample indicated the presence of two twinning domains. However, the orthorhombicity of CRO yields $2\vartheta = 85.4°$ for the (013) and $2\vartheta = 85.8°$ for the (103) at the Ru L3 edge, which lets us distinguish between the two domains. Since we only observed the peak corresponding to the (013) during the synchrotron experiment, we assume to only have detected a single domain. Recording the intensity of the 013 reflection while cooling down to 210 K* shows the same intensity as the 100 in the CRO single crystal [125] confirming that we are sensing the same trend associated with the setting in of the AFO phase (Fig. 6.20). We noticed that the tilt angle of the RuO_6-octahedra determined by neutron powder diffraction matches the temperature trend of the reflection almost perfectly [90]. This promted us to reevaluate the existing data in terms of Templeton scattering.

*A defective thermal switch of the cryooven used did not allow us to cool further.

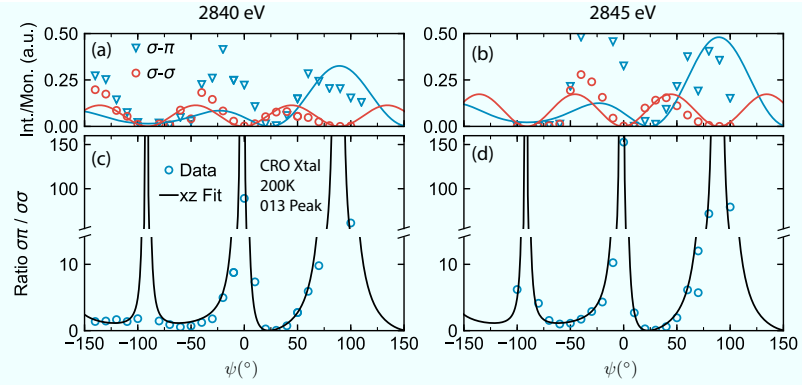

Figure 6.21: Polarization analysis of the 013 peak of a CRO single crystal taken at $210\,\mathrm{K}$. (a) Intensity vs. azimuth tuned to the first maximum in the energy scan at $2840\,\mathrm{eV}$. The solid lines depict fits based on Templeton scattering (red: σ-σ, blue: σ-π). (b) Intensity vs. azimuth at $2845\,\mathrm{eV}$ with fits using the same model. (c) Ratio σ-π/σ-σ of the data shown in (a) with a fit of the ratio based on Templeton scattering. (d) Same ratio and fit for the dataset shown in (b).

We performed a polarization analysis at $210\,\mathrm{K}$ of the 013 reflection at the two maxima in the energy scan, $2840\,\mathrm{eV}$ and $2845\,\mathrm{eV}$. Initially, it was difficult to unify the expected xz-type azimuthal dependence (eq. 6.1) arising from Templeton scattering (Fig. 6.21) with the data.* The minima and maxima of the measured data and the simulation, however, agree well indicating that systematic influences might distort the true intensity variation. Most likely, effects due to the "hopping" of the beam between crystallites are still present despite using the rather well-defined 001-face. This prompted us to study the ratio of the two channels, since this should cancel out any effects that alter both channels equally. Fitting the ratio of σ-π to σ-σ with the predicted xz-mode for the 013 gives an excellent agreement for both energies.

*For the simulations, the geometric correction factor $\eta(\psi)$ was neglected, since the crystal is much thicker than the penetration depth. In order to calculate q, we used the lattice constants given for $180\,\mathrm{K}$ in Ref. [45].

6.2.4 Discussion

The REXS study of the 013/103 reflections of the c-axis oriented CRO films on LAO(100) and LSAO(001) is fully consistent with a Templeton scattering mechanism. The temperature dependence of the reflections or the corresponding 011/101 peak does not show any anomalies around 300 K rendering us unable to link them to the feature observed in βNMR. It is noteworthy that despite the weak MIT of CRO on LAO at 290 K, no changes in the resonant peaks were observed. Although the trend cannot be linked to an order-parameter-like behavior, the intensity change of the resonant 101/011 of CRO on LSAO is significant. In view of complementary off-resonant measurements at the 1010/0110 position and 0018, however, changes in the RuO_6-octahedra distortions can be identified as the most likely origin.

The polarization analysis of the 013/103 peak of the films at 200 K and 400 K can be well described with a scattering tensor resulting from Templeton scattering. Due to twinning, both, the 013 and the 103, are expected to contribute to the measured intensity. Comparing with simulations, we have shown that mainly the xz-mode coming from the 013 is responsible for the polarization dependence, which is in accordance with our prediction based on the estimate laid out in sec. 3.1.4. While no connection to the feature in βNMR can be drawn either, it confirms that the tilt/rotation pattern matches the Pbca spacegroup consistent with our hard X-ray studies . While investigating the single crystal as a reference for the thin films, we found that the intensity increase at 260 K suggested to be the onset of an AFO order can be explained in many aspects with changes in the tilt of the RuO_6-octahedra. Simply overlaying the measured tilt from the neutron powder diffraction structural refinement with the previously reported intensity changes at the (100) and (011) reflection already gives an excellent agreement, which seemed to have been missed in Refs. [125, 176]. We also note that the flattening at high temperatures, which is crucial to distinguish the new phase from Templeton scattering consists essentially only of two data points between 260 K and 300 K. Our polarization analysis of the resonant 013 at 210 K is consistent with the anisotropy of Templeton-scattering expected at this position. In fact, all of the azimuthal scans of the CRO single crystal within the AFO phase presented in Ref. [176] appear to be

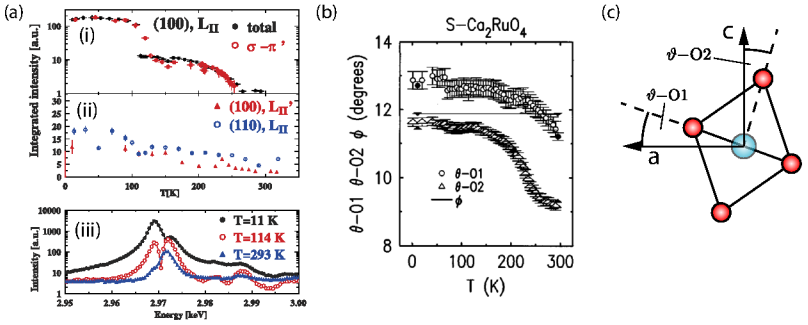

Figure 6.22: Previous report of Ru-L2-REXS of a CRO single crystals compared with tilts of the octahedra. (a) i. Intensity vs. temperature of the 100 peak at $2968.5\,\mathrm{eV}$ indicating a transition at $260\,\mathrm{K}$ ii. Temperature dependence of the 110 at $2968.5\,\mathrm{eV}$ and the 100 at $2972.5\,\mathrm{eV}$ iii. Energy scans at the 100 position around the Ru-L2 edge. Taken from Ref. [125]. (b) Rotation ϕ, Basal-plane tilt $\vartheta - \mathrm{O1}$ and apical oxygen tilt $\vartheta - \mathrm{O2}$ of the RuO_6 octahedron of bulk CRO determined by neutron powder diffraction. Taken from Ref. [90]. (c) Sketch illustrating the basal-plane and apical oxygen tilt. The blue sphere denotes a Ru-atom, red spheres oxygen atoms. The rotation about the c-axis is not included for clarity.

compatible with a Templeton scattering (TS) based mechanism (see appendix B). Furthermore, we want to address additional arguments against tilt order as the underlying origin for the 260 K-anomaly put forward by the original report. A point arguing against TS as the main reason for the observed signal was the fact that the two peaks observed in the energy scan showed different temperature trends(Fig. 6.22aii and aii). Based on the behavior at the magnetic transition and the matching energy splitting, it was suggested that the lower energy peak corresponds to the t_{2g}-orbitals and the higher energy peak to the e_g-orbitals of the $4d$-shell (Fig. 6.22aiii). Since the lower peak shows an order-parameter-like behavior below 260 K, but the upper one does not, it is assumed that it mirrors a phenomenon connected to the $t2g$ shell and higher-energy peak is connected to the tilt of the e_g-shell, which is taken to be the same as for the $t2g$-shell. However, structural distortions can have a large impact on the shape of REXS energy spectra (Fig. 6.23). Comparing the energy scans of the 100 peak of CRO on LSAO(110) with the crystal at room temperature or the 011 of CRO on LSAO(001) shows that the system under epi-

taxial strain can show a profoundly different ratio of the two peaks.* Assuming that both the film peaks and the crystal peaks at room temperature arise solely from Templeton scattering suggests that the distortions induced by epitaxial strain can indeed influence the ratio of the two peaks. This indicates that the various changes in the octahedral distortions below the MIT at 350 K might be responsible for the line-shape changes. Due to the matching temperature dependence, this might be the $\vartheta{-}O2$ itself. It was was pointed out that the 110 peak of the CRO single crystal does not show a large variance in temperature without any anomaly at 260 K in contrast to the 011 or 100 position. Since the polarization dependence of the 110 agreed well with Templeton scattering, it was thus concluded that TS cannot be the origin for the order-parameter-like increase. However, the 011 and 100 probe xz/zx-type TS, while the 110 reflection is mainly sensitive to the xy/yx elements of an TS based scattering tensor, which do not necessarily have to show the same trends. As we have shown in sec. 3.1.4, off-diagonal elements can arise in the unit-cell reference frame due to the tilt and rotation of the RuO_6-octahedra. Since the rotation was found to be practically constant for the single-crystal (Fig. 6.22), any structurally-driven REXS dynamics should mainly arise from the tilt or the changes in the Ru-O distances below the MIT. An important aspect is the fact that the basal-plane oxygen atoms (often denoted as O-1) are independent of the apical oxygen atoms (O2) in the Pbca space group. It was indeed found that the basal-plane tilt $\vartheta{-}$O1 has quite different dynamics than the apical-oxygen tilt $\vartheta{-}$O2(Fig.6.22). It still shows a substantial change (13 % vs. 23 % of the ϑ-O2) from 300 K down to 11 K, however the change is more gradual than the Ru-O2-tilt and it does not show any anomaly around 260 K. Indeed, it was suggested that the shape indicates a tilt transition at higher temperatures [90]. Together with the dynamics

*The energy scans of the (100) and (011) reflections of the single crystal show identical trends [176]. Relating the mixed 011/101 of CRO on LSAO(001) to the 100 of the crystal is justified by the fact that the polarization analysis suggests mainly a contribution from the 011 reflection. We note, that we did not apply an absorption correction to the energy scans of the thin films, since absorption effects for the thin films at the relatively high energies of the Ru-L edges are only relevant for grazing incidence or emergence as we have seen during the analysis of the azimuthal dependences. This is different from single crystals, where the beam path within the sample is always similar to the penetration depth [176].

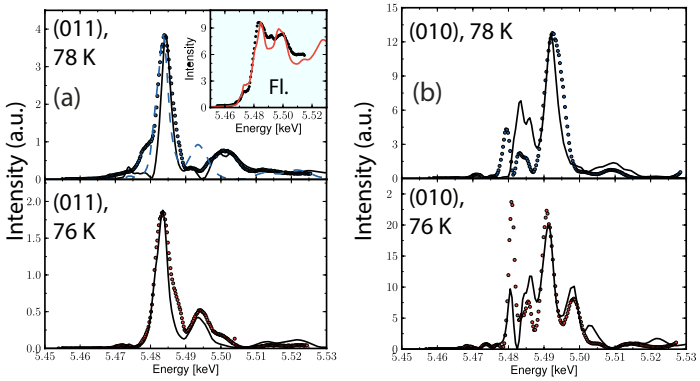

Figure 6.23: Line shape variations of the REXS energy spectra at the V-K-edge of YVO_3 across a magnetic phase transition concomitant with structural changes. At 78 K the system exhibits small monoclinic distortions, which vanish across a magnetic phase transition. This structural change can explain entirely the line shape changes without being connected to any ordering phenomenon in the 3d-shell. Dots denote experimental data, the solid lines simulations using the FDMNES code [305]. The dashed line shows a simulation of the spectrum using a structural refinement based of the structure without assuming a monoclinic spacegroup. (a) REXS energy spectra at the (011) reflection. The inset shows a energy scan of the fluorescence signal. (b) REXS energy spectra at the (010) reflection. Adapted from [306].

in the octahedral compression starting at 350 K and distortion of the basal plane of the octahedra, the situation is thus undoubtedly more complex than our simple model presented in sec. 3.1.4 and it requires likely DFT-studies to calculate the sensitivity of each tensor element to the octahedral distortions. It might be that the xy elements of the tensor (corresponding to 110) are more sensitive to $\vartheta-$O1. Applying the empirical proportionality between $\vartheta-$O2 and the intensity of the 100/011 would roughly match: In the single crystal, the 110 shows approx. a fourfold increase from 300 K to 10 K, so roughly half of the tenfold increase at the 100/011. Thus, we believe that the absence of a kink at 260 K in the temperature evolution of the 110 does not automatically allow to exclude tilt order as the underlying origin of the behavior of the 100/011 intensity.

A similar discussion surrounds the REXS data of orbitally ordered states in $YTiO_3$ and YVO_3[307, 308]. Here, issues arose about the interpretation of K-edge REXS data, since it was unclear whether inten-

sity changes originate from an orbital ordering or effects of structural distortions. Indeed, simulations show that REXS spectral changes can be completely explained by structural effects in YVO_3 and that the impact on the intensity and line shape varies substantially between reflections(Fig. 6.23). Here, at the (011) only small changes in the line shape and roughly a 2.5 times larger intensity are observed when heating through a transition associated with structural distortions. On the other hand, the (010) shows a decrease of about 40 % and quite dramatic spectral shape changes. This illustrates that the effect of purely structural effects can differ significantly. The effects seen in YVO_3 appear to be connected to a small monoclinic distortion setting in at a phase transition, which constitutes likely more severe changes to the structure than in CRO across 260 K. However, we are not aware of any REXS studies on a system with similar tilt dynamics like CRO that might serve as a better-fitting reference. Within this context, we also would like to note, that ,to the best of our knowledge, no single-crystal structural refinement of CRO has been conducted. Such an experiment might be able to catch small monoclinic distortions connected to ϑ-$O2$, which might be too weak to be observed by powder diffraction refinements [285].

To conclusively reconcile the line shape variations in the energy scans with purely structural effects, DFT-studies such as Ref. [148] would be insightful. An experimental approach could consist in controlling the structural distortions in a systematic fashion, e.g. by a small Sr-substitution and study the impact on the resonance spectra [45] above any known order phenomenon.

Based on the REXS data, the analysis also allows the possibility that a quadrupolar order exists which has the same propagation vector as the AFM order and the same scattering tensor as Templeton scattering. In this scenario, the quadrupolar order would likely be the driving mechanism for the ϑ-$O2$ change observed with neutrons. However, it is difficult to classify such a mechanism as phase transition as no symmetry is broken. If we assume a strong link between tilt and the quadrupolar order, REXS alone might not be able to disentangle the two mechanisms. We note that our βNMR data of the polycrystal does not detect any feature at 260 K (Fig. 6.9) in line with the findings reported using Ru-NMR [123]. No structural parameter besides $\vartheta-\mathrm{Ru}-\mathrm{O2}$ appears to show an anomaly around 260 K in CRO single crystals [90].

To the best of our knowledge, the only evidence for the 260 K-feature found by other experimental techniques is a paramagnetic broad hump around the same temperature in magnetization measurements along the c-axis of CRO single crystals (see e.g. suppl. of [39]). The correlation with the tilt changes was quickly noticed upon the discovery, but no conclusive mechanism for its origin was provided [309]. If quadrupolar order is indeed absent, one might speculate that it be connected to a peculiarity of the paramagnetic state of excitonic magnetism (sec. 2.6).

6.3 Conclusion and Outlook

In this chapter, we have presented spin-lattice-relaxation (SLR) measurements of CRO films using ^{8}Li as a NMR probe. Previously detected ferromagnetic and antiferromagnetic transitions were observed. More interestingly, we found a feature around room-temperature, which shows properties of a phase transition. Since quadrupolar order was detected at similar temperatures in the single crystals and we do not have evidence for any structural phase transition at this temperature, the finding possibly constitutes the detection of quadrupolar order in the CRO thin films as well. Especially the fact that the feature survives in the metallic state of CRO on LSAO(001) could be evidence for localization effects in the metallic phase of CRO. This could provide new intriguing input for the discussion about correlation effects in proximity of the insulator-metal boundary. The data shows to potential of βNMR as a technique to investigate orbital fluctuations in thin films.

While definite proof of an electronic nature of the SLR-anomaly still needs to be provided, an alternative scenario based on ^{8}Li-diffusion is rendered unlikely due to the absence of the feature in the structurally very similar SRO. In view of the tight-packed crystal structure of single-layer ruthenates, it is difficult to uphold an interpretation based on long-range motion of guest ions. The temperature dependence of the SLR in zero field and 50 G show properties distinct from typical diffusion effects and suggest an ordering phenomenon. Additional data on the feature at 300 K also involving different techniques than βNMR would certainly be desirable for clarifying its nature. Indeed, careful electrical transport measurements might detect a feature in

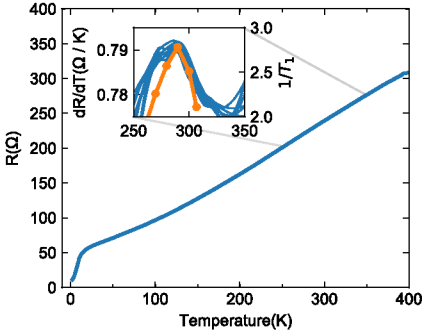

Figure 6.24: Probing the transport of CRO on LSAO(001) for anomalies around 300 K. The inset shows smoothed derivatives of multiple sweeps from 250 K to 300 K together with the SLR measurement in 50 G. An weak anomaly around 300 K could be connected to the βNMR-feature.

the metallic CRO on LSAO(001) (Fig. 6.24). Acquiring resonance spectra of the ^{8}Li above and below 300 K in the films should allow to directly probe the strength of the suspected internal field, which might be associated with an order parameter(similar to Fig. 3.19).

Despite not being able to find evidence for features around room temperature in the CRO films connected to the anomaly in βNMR, the REXS study of the films at the Ru-L edges provides important microscopic structural information as the studied peaks can be explained by Templeton scattering confirming the tilt pattern of the Pbca space group. Since crystallographic refinement is generally not feasible for thin films, this adds valuable information to the understanding of the structure. The absence of antiferro-quadrupolar order at the 101/011 positions of the films does not exclude other quadrupolar order patterns. Especially ferro-order is a promising candidate based on the evidence found in bulk. The βNMR-SLR-measurements on the CRO-polycrystal are consistent with Ru-K-edge REXS [124], XAS [29], NMR [123] and optical spectroscopy [89] experiments suggesting that a similar type of ordering might also be applicable for the films.

Revisiting the single crystal using REXS at the Ru-L-edges, we found considerable evidence that resonant reflections linked to the previously reported AFO order are strongly related to tilt of the RuO_6-octahedra. Templeton scattering can explain much of their phenomenology. While pure tilt changes as the underlying origin are a viable mechanism to explain the intensity changes, the order-parameter-like trend and the line-shape changes in the energy scans

of the associated resonant peaks still need to be clarified. Our findings suggest a more complicated picture of the previously reported antiferro-quadrupolar (AFO) order, where a possible electronic ordering phenomenon might only have been observed indirectly via the structural response of the system. In such a scenario, the true propagation vector of the ordered phase would be obfuscated as the observed resonant peaks arise from Templeton scattering and are not directly linked to the translation symmetry breaking of the ordering phenomenon. The findings provide crucial information about the role of orbital degrees of freedom in pristine CRO as the reported orbital order cannot unambiguously be classified as an AFO ordering. This is especially of relevance in the context of the recently proposed strong spin-orbit coupling picture for the electronic states in the system.

A

X-ray Penetration Depth of Ca_2RuO_4 Thin Films

X-ray absorption spectroscopy (XAS) measurements at the Ru-L-edges were performed at ALBA, Barcelona, to probe for a possible X-ray linear dichroism (XLD) arising from orbital or magnetic order. No significant dichroism, temperature dependence or differences between samples on LAO and LSAO(110) could be detected within the sensitivity of the instrument (Fig. A.2). This also held for $E \parallel c$ vs $E \parallel b$, which is the direction, one would expect the largest natural dichroism. In contrast, measurements for bulk showed a relatively large change in the relative occupation of the t_{2g}-orbitals with temperature.[310] While the Ru-L-edge spectra are more direct, since they directly probe the 4d-shell, the spectra are dominated by the empty eg-orbitals, which are split by only 4 eV from the valence t_{2g} shells making it difficult to probe effects in the t_{2g} states. Thus, usually these orbitals are probed at the O-K-edge via their hybridization with the O-2p-orbitals (see 4.8.4). Despite not being sensitive any of the electronic properties probed via REXS or transport, the measurements can be used to estimate the absorption coefficient μ in eq.3.46 for CRO films at the L edges. For a single atom, the optical theorem (eq. 3.19) can be used to connect the imaginary part of the scattering length to the absorption

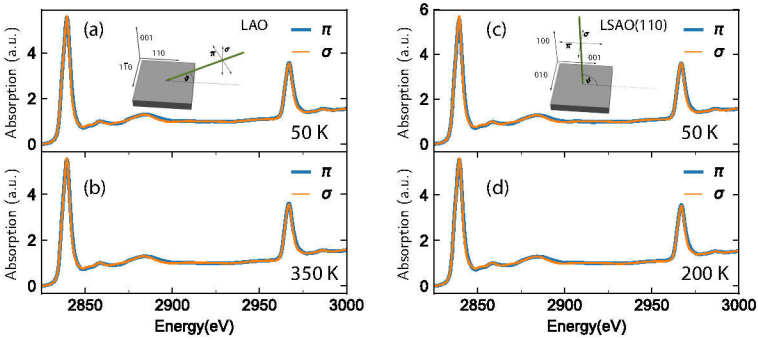

Figure A.1: Left: XAS spectra at the Ru-L edges at an incident angle of $\vartheta = 30°$ for CRO on LAO at (a) $50\,\mathrm{K}$ and (b) $350\,\mathrm{K}$ for σ- and π-polarization. Right: XAS spectra at normal incidence($\vartheta = 90°$) for CRO on LSAO(110) at (c) $50\,\mathrm{K}$ and (d) $200\,\mathrm{K}$ for σ- and π-polarization. No significant dichroism, temperature dependence or differences between the samples could be detected.Top: Illustration showing the geometry of the XAS-experiment.

cross-section

$$\frac{d\sigma_{\mathrm{abs}}}{d\Omega} = 2\lambda f'' \,. \tag{A.1}$$

The absorption coefficient μ is simply related to the cross section by

$$\mu = \frac{d\sigma_{\mathrm{abs}}}{d\Omega} n = \frac{d\sigma_{\mathrm{abs}}}{d\Omega} \frac{\rho}{M} N_A \,, \tag{A.2}$$

where n represents the number density of the probed atoms, ρ its mass density, M the molar mass and N_A Avogadro's number. Off-resonant values for the atomic scattering lengths are tabulated in Ref. [311] were used to calculate the absorption coefficient in eq. A.2. The film densities can be determined via X-ray reflectivity measurements via the critical angle ($\approx 4.5\,\mathrm{g\,cm^{-3}}$). The XAS spectra can then be fitted to the step jumps in the XAS via the procedure described in Ref.[312]. The resulting modified spectrum allows to extract the absorption coefficient μ and the penetration depth $\delta = \mu^{-1}$ close to the absorption edges (Fig. A.2).

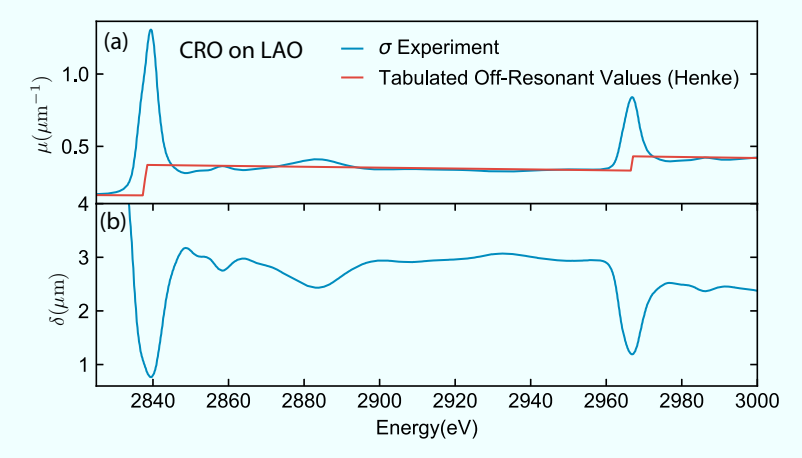

Figure A.2: (a) Absorption coefficient and (b) X-ray attenuation length close to the Ru-L edges derived by scaling an XAS spectrum of CRO on LAO to off-resonant absorption data calculated using eq. A.2.

B

Single Crystal AFO Phase Azimuthal Dependences

We extracted the azimuthal dependences of the (100) and (011) peak within the claimed antiferro-orbital ordered phase below 260 K from the thesis of Zegkinoglou[176] and compared them with the polarisation dependences expected from Templeton scattering. In the thesis, the polarisation dependence of the 100 reflection of an oriented CRO single crystal was investigated with X-rays tuned to the Ru-L2 edge at 175 K (Fig.B.1). It was reported that the strong intensity fluctuations likely arise due to hopping between grains of the crystal under the azimuthal rotation. However, on average a maximum at $\psi = 0°$ and a minimum at $\psi = -90°$ is discernible. Assuming a scattering tensor correspond to xz-type Templeton scattering (eq. 3.35), we yield a $\propto \cos(\psi)^2$ with no intensity in the σ-π channel, which is in good agreement with the data and corresponding to the azimuthal dependence that was guessed in the thesis.

A higher quality azimuthal dependence in the antiferro-orbital ordered phase was accomplished at the (011) reflection at 144 K using again light at the Ru-L2 edge (Fig.B.2). Repeating the procedure from above, we use the appropriate xz-type Templeton scattering tensor. The scan was acquired without polarisation analyzer, thus we fit the sum of σ-π and σ-σ intensities. Allowing different amplitudes

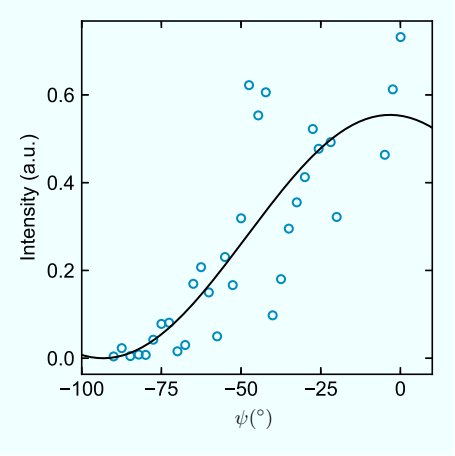

Figure B.1: Fitting the azimuthal dependence data of the 100 peak acquired at the Ru-L2 edge at $175\,\mathrm{K}$ within the suspected AFO phase. The data was extracted from the thesis of Zegkinoglou[176]. Using a xz-Templeton scattering model gives a good fit.

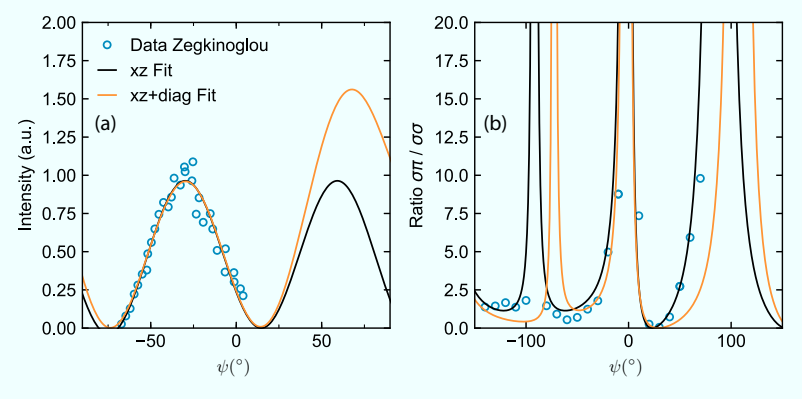

Figure B.2: Modeling the polarization dependence of the 011 peak of a CRO single crystal recorded at the Ru L2-edge without analyzer, which was presented in the thesis of Zegkinoglou[176]. (a) The expected tensor from Templeton scattering gives a good agreement, but only when using large ψ offset of $\psi_0 = -15^\circ$. Using diagonal elements in the tensor, a large ψ_0 can be avoided, but including these elements in the model for the ratio of σ-π vs. σ-σ at the equivalent 013 results in a clear disagreement with the data prompting us to assign the ψ_0-offset indeed to a misalignment. (b) Data and fits from Fig.6.21. Using the xz-element from the original fit, but adding the diagonal elements in the same ratio relative to the xz element as the orange fit in panel a disagrees clearly with the data.

for each channel, we yield an excellent agreement with mainly the $\propto \cos(2(\psi+\psi_0))^2$ dependence of the σ-σ channel. However, the offset ψ_0 needed to achieve an agreement is concerningly large ($\psi_0 \approx -15°$, typically $|\psi_0| \leq 5°$). We found that a large shift in ψ_0 can be avoided by introducing diagonal elements in the tensor (xx,yy and zz), which gives fits indiscernible with our previous fit within the measured range. However, we would expect the same elements at the 013, which was investigated within this work (6.2.3). Introducing diagonal elements with the same ratio relative to the xz in our model for the ratio of σ-π vs. σ-σ of the 013 yields a clear disagreement with the data. In addition, diagonal elements should result in a σ-σ-contribution at the 100 peak, which was not observed. Thus, we attribute the large ψ_0 offset to misalignment.

C

Low-Magnification TEM

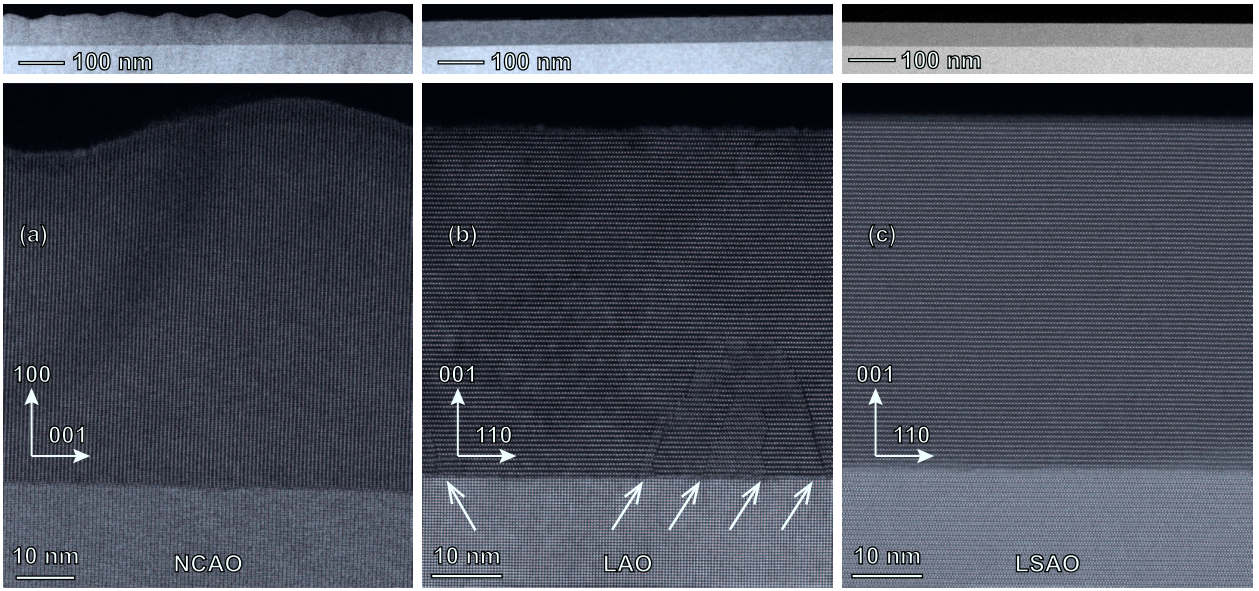

Figure C.1: Low-magnification HAADF images of the same films shown in Fig.4.19. (a) CRO on NCAO. A wavy surface can be seen, which corresponds well to the island growth observed via RHEED (sec. 4.6). (b) CRO on LAO. Here, typical out-of-phase boundary defects are observed (indicated by arrows). (c) CRO on LSAO(001). No defects can be observed indicating a high-quality microstructure.

D

SRIM Penetration Profiles

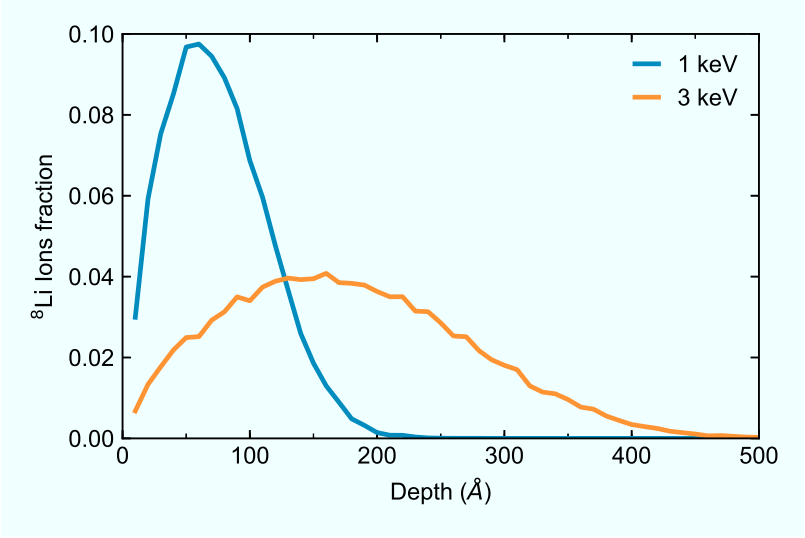

Figure D.1: 8Li penetration profile for the ion energies $1\,\mathrm{keV}$ and $3\,\mathrm{keV}$ modeled using the SRIM software package[195].

References

[1] D. I. Khomskii, *Transition Metal Compounds* (Cambridge University Press, Cambridge, 2014).

[2] J. Heber, *Nature* **459**, 28–30 (2009).

[3] C. N. R. Rao, *Annual Review of Physical Chemistry* **40**, 291–326 (1989).

[4] J. G. Bednorz and K. A. Müller, *Zeitschrift für Physik B Condensed Matter* **64**, 189–193 (1986).

[5] M. Imada, A. Fujimori, and Y. Tokura, *Reviews of Modern Physics* **70**, 1039–1263 (1998).

[6] S. Jin, T. H. Tiefel, M. McCormack, R. A. Fastnacht, R. Ramesh, and L. H. Chen, *Science* **264**, 413–415 (1994).

[7] Y. Murakami, J. P. Hill, D. Gibbs, M. Blume, I. Koyama, M. Tanaka, H. Kawata, T. Arima, Y. Tokura, K. Hirota, and Y. Endoh, *Physical Review Letters* **81**, 582–585 (1998).

[8] J. H. de Boer and E. J. W. Verwey, *Proceedings of the Physical Society* **49**, 59–71 (1937).

[9] V. Potapkin, L. Dubrovinsky, I. Sergueev, M. Ekholm, I. Kantor, D. Bessas, E. Bykova, V. Prakapenka, R. P. Hermann, R. Rüffer, V. Cerantola, H. J. Jönsson, W. Olovsson, S. Mankovsky, H. Ebert, and I. A. Abrikosov, *Physical Review B* **93**, 20–24 (2016).

[10] N. F. Mott and R. Peierls, *Proceedings of the Physical Society* **49**, 72 (1937).

[11] J. Hubbard, *Proceedings of the Royal Society A: Mathematical, Physical and Engineering Sciences* **276**, 238–257 (1963).

[12] F. J. Morin, *Physical Review Letters* **3**, 34–36 (1959).

[13] M. Nakano, K. Shibuya, D. Okuyama, T. Hatano, S. Ono, M. Kawasaki, Y. Iwasa, and Y. Tokura, *Nature* **487**, 459–462 (2012).

[14] J. Jeong, N. Aetukuri, T. Graf, T. D. Schladt, M. G. Samant, and S. S. P. Parkin, *Science* **339**, 1402–1405 (2013).

[15] M. Lorenz, M. S. Ramachandra Rao, T. Venkatesan, E. Fortunato, P. Barquinha, R. Branquinho, D. Salgueiro, R. Martins, E. Carlos, A. Liu, F. K. Shan, M. Grundmann, H. Boschker, J. Mukherjee, M. Priyadarshini, N. DasGupta, D. J. Rogers, F. H. Teherani, E. V. Sandana, P. Bove, K. Rietwyk, A. Zaban, A. Veziridis, A. Weidenkaff, M. Muralidhar, M. Murakami, S. Abel, J. Fompeyrine, J. Zuniga-Perez, R. Ramesh, N. A. Spaldin, S. Ostanin, V. Borisov, I. Mertig, V. Lazenka, G. Srinivasan, W. Prellier, M. Uchida, M. Kawasaki, R. Pentcheva, P. Gegenwart, F. Miletto Granozio, J. Fontcuberta, and N. Pryds, *Journal of Physics D: Applied Physics* **49**, 433001 (2016).

[16] W. Eerenstein, N. D. Mathur, and J. F. Scott, *Nature* **442**, 759–765 (2006).

[17] M. Ogata and H. Fukuyama, *Reports on Progress in Physics* **71**, 036501 (2008).

[18] B. A. Bernevig, T. L. Hughes, and S.-C. Zhang, *Science* **314**, 1757–1761 (2006).

[19] W. Witczak-Krempa, G. Chen, Y. B. Kim, and L. Balents, *Annual Review of Condensed Matter Physics* **5**, 57–82 (2014).

[20] B. J. Kim, H. Jin, S. J. Moon, J.-Y. Kim, B.-G. Park, C. S. Leem, J. Yu, T. W. Noh, C. Kim, S.-J. Oh, J.-H. Park, V. Durairaj, G. Cao, and E. Rotenberg, *Physical Review Letters* **101**, 076402 (2008).

[21] X. Wan, A. M. Turner, A. Vishwanath, and S. Y. Savrasov, *Physical Review B - Condensed Matter and Materials Physics* **83**, 1–9 (2011).

[22] J. Chaloupka, G. Jackeli, and G. Khaliullin, *Physical Review Letters* **105**, 027204 (2010).

[23] A. Kitaev, *Annals of Physics* **321**, 2–111 (2006).

[24] B. Keimer and J. E. Moore, *Nature Physics* **13**, 1045–1055 (2017).

[25] A. Jain, M. Krautloher, J. Porras, G. H. Ryu, D. P. Chen, D. L. Abernathy, J. T. Park, A. Ivanov, J. Chaloupka, G. Khaliullin, B. Keimer, and B. J. Kim, *Nature Physics* **13**, 633–637 (2017).

[26] Y. Maeno, S. Kittaka, T. Nomura, S. Yonezawa, and K. Ishida, *Journal of the Physical Society of Japan* **81**, 011009 (2012).

[27] A. P. Mackenzie and Y. Maeno, *Reviews of Modern Physics* **75**, 657–712 (2003).

[28] G. Khaliullin, *Physical Review Letters* **111**, 197201 (2013).

[29] T. Mizokawa, L. H. Tjeng, G. a. Sawatzky, G. Ghiringhelli, O. Tjernberg, N. B. Brookes, H. Fukazawa, S. Nakatsuji, and Y. Maeno, *Physical Review Letters* **87**, 077202 (2001).

[30] T. Giamarchi, C. Rüegg, and O. Tchernyshyov, *Nature Physics* **4**, 198–204 (2008).

[31] S.-M. Souliou, J. Chaloupka, G. Khaliullin, G. Ryu, A. Jain, B. J. Kim, M. Le Tacon, and B. Keimer, *Physical Review Letters* **119**, 067201 (2017).

[32] J. P. Carlo, T. Goko, I. M. Gat-Malureanu, P. L. Russo, a. T. Savici, a. a. Aczel, G. J. MacDougall, J. a. Rodriguez, T. J. Williams, G. M. Luke, C. R. Wiebe, Y. Yoshida, S. Nakatsuji, Y. Maeno, T. Taniguchi, and Y. J. Uemura, *Nature Materials* **11**, 323–328 (2012).

[33] S. Nakatsuji and Y. Maeno, *Physical Review Letters* **84**, 2666–2669 (2000).

[34] S. Nakatsuji and Y. Maeno, *Physical Review B* **62**, 6458–6466 (2000).

[35] S. Nakatsuji, D. Hall, L. Balicas, Z. Fisk, K. Sugahara, M. Yoshioka, and Y. Maeno, *Physical Review Letters* **90**, 137202 (2003).

[36] A. P. Mackenzie, T. Scaffidi, C. W. Hicks, and Y. Maeno, *npj Quantum Materials* **2**, 40 (2017).

[37] C. N. Veenstra, Z.-H. Zhu, M. Raichle, B. M. Ludbrook, A. Nicolaou, B. Slomski, G. Landolt, S. Kittaka, Y. Maeno, J. H. Dil, I. S. Elfimov, M. W. Haverkort, and A. Damascelli, *Physical Review Letters* **112**, 127002 (2014).

[38] M. Haverkort, I. Elfimov, L. Tjeng, G. Sawatzky, and a. Damascelli, *Physical Review Letters* **101**, 026406 (2008).

[39] C. Sow, S. Yonezawa, S. Kitamura, T. Oka, K. Kuroki, F. Nakamura, and Y. Maeno, *Science* **358**, 1084–1087 (2017).

[40] P. Steffens, O. Friedt, P. Alireza, W. G. Marshall, W. Schmidt, F. Nakamura, S. Nakatsuji, Y. Maeno, R. Lengsdorf, M. M. Abd-Elmeguid, and M. Braden, *Physical Review B* **72**, 094104 (2005).

[41] F. Nakamura, *Journal of the Physical Society of Japan* **76**, 96–99 (2007).

[42] F. Nakamura, T. Goko, M. Ito, T. Fujita, S. Nakatsuji, H. Fukazawa, Y. Maeno, P. Alireza, D. Forsythe, and S. R. Julian, *Physical Review B* **65**, 220402 (2002).

[43] H. Taniguchi, K. Nishimura, R. Ishikawa, S. Yonezawa, S. K. Goh, F. Nakamura, and Y. Maeno, *Physical Review B* **88**, 205111 (2013).

[44] F. Nakamura, R. Nakai, T. Takemoto, M. Sakaki, T. Suzuki, P. L. Alireza, S. Nakatsuji, and Y. Maeno, *Physical Review B* **80**, 193103 (2009).

[45] O. Friedt, M. Braden, G. André, P. Adelmann, S. Nakatsuji, and Y. Maeno, *Physical Review B* **63**, 174432 (2001).

[46] D. Dijkkamp, T. Venkatesan, X. D. Wu, S. A. Shaheen, N. Jisrawi, Y. H. Min-Lee, W. L. McLean, and M. Croft, *Applied Physics Letters* **51**, 619–621 (1987).

[47] D. G. Schlom, L.-Q. Chen, C. J. Fennie, V. Gopalan, D. A. Muller, X. Pan, R. Ramesh, and R. Uecker, *MRS Bulletin* **39**, 118–130 (2014).

[48] H. Y. Hwang, Y. Iwasa, M. Kawasaki, B. Keimer, N. Nagaosa, and Y. Tokura, *Nature Materials* **11**, 103–113 (2012).

[49] N. Reyren, S. Thiel, A. D. Caviglia, L. F. Kourkoutis, G. Hammerl, C. Richter, C. W. Schneider, T. Kopp, A.-S. Ruetschi, D. Jaccard, M. Gabay, D. A. Muller, J.-M. Triscone, and J. Mannhart, *Science* **317**, 1196–1199 (2007).

[50] A. Ohtomo and H. Y. Hwang, *Nature* **427**, 423–426 (2004).

[51] Y.-Y. Xiang, F. Wang, D. Wang, Q.-H. Wang, and D.-H. Lee, *Physical Review B* **86**, 134508 (2012).

[52] S. He, J. He, W. Zhang, L. Zhao, D. Liu, X. Liu, D. Mou, Y.-B. Ou, Q.-Y. Wang, Z. Li, L. Wang, Y. Peng, Y. Liu, C. Chen, L. Yu, G. Liu, X. Dong, J. Zhang, C. Chen, Z. Xu, X. Chen, X. Ma, Q. Xue, and X. J. Zhou, *Nature materials* **12**, 605–10 (2013).

[53] S. Middey, J. Chakhalian, P. Mahadevan, J. Freeland, A. Millis, and D. Sarma, *Annual Review of Materials Research* **46**, 305–334 (2016).

[54] A. Frano, "Spin Spirals and Charge Textures in Transition-Metal-Oxide Heterostructures", PhD thesis (Technische Universität Berlin, Max Planck Institute for Solid State Research, 2014).

[55] M. Hepting, "Ordering Phenomena in Rare-Earth Nickelate Heterostructures", PhD thesis (University of Stuttgart, Max Planck Institute for Solid State Research, Stuttgart, 2016).

[56] D. G. Schlom, Y. Jia, L. N. Zou, J. H. Hanei, S. Briczinski, M. A. Zurbuchen, C. W. Leitz, S. Madhavan, S. Wozniak, Y. Liu, M. E. Hawley, G. W. Brown, A. Dabkowski, H. A. Dabkowska, R. Uecker, and P. Reiche, *Proceedings of the Society of Photo-Optical Instrumentation Engineers (SPIE)* **3481**, 226–240 (1998).

[57] M. A. Zurbuchen, Y. Jia, S. Knapp, A. H. Carim, D. G. Schlom, and X. Q. Pan, *Applied Physics Letters* **83**, 3891 (2003).

[58] M. Uchida, M. Ide, H. Watanabe, K. S. Takahashi, Y. Tokura, and M. Kawasaki, *APL Materials* **5**, 106108 (2017).

[59] T. Ohnishi and K. Takada, *Applied Physics Express* **4**, 025501 (2011).

[60] Y. Krockenberger, M. Uchida, K. S. Takahashi, M. Nakamura, M. Kawasaki, and Y. Tokura, *Applied Physics Letters* **97**, 082502 (2010).

[61] W. Tian, J. H. Haeni, D. G. Schlom, E. Hutchinson, B. L. Sheu, M. M. Rosario, P. Schiffer, Y. Liu, M. A. Zurbuchen, and X. Q. Pan, *Applied Physics Letters* **90**, 022507 (2007).

[62] S. Madhavan, D. G. Schlom, A. Dabkowski, H. A. Dabkowska, and Y. Liu, *Applied Physics Letters* **68**, 559 (1996).

[63] B. Burganov, C. Adamo, A. Mulder, M. Uchida, P. D. C. King, J. W. Harter, D. E. Shai, A. S. Gibbs, A. P. Mackenzie, R. Uecker, M. Bruetzam, M. R. Beasley, C. J. Fennie, D. G. Schlom, and K. M. Shen, *Physical Review Letters* **116**, 197003 (2016).

[64] J. Cao, D. Massarotti, M. E. Vickers, A. Kursumovic, A. D. Bernardo, J. W. A. Robinson, F. Tafuri, and M. G. Blamire, *Superconductor Science and Technology* **29**, 1–6 (2016).

[65] D. Reisinger, B. Blass, J. Klein, J. Philipp, M. Schonecke, A. Erb, L. Alff, and R. Gross, *Applied Physics A: Materials Science & Processing* **77**, 619–621 (2003).

[66] H. Nair, N. Schreiber, J. Ruf, M. Grandon, D. Low, G. Ferguson, K. Nowack, K. Shen, and D. Schlom, "Demystifying the growth of superconducting Sr_2RuO_4 thin films", APS March Meeting, 2018.

[67] V. Vakaryuk and V. Vinokur, *Physical Review Letters* **107**, 037003 (2011).

[68] P. Gentile, M. Cuoco, A. Romano, C. Noce, D. Manske, and P. M. R. Brydon, *Physical Review Letters* **111**, 097003 (2013).

[69] Y. Maeno, H. Hashimoto, K. Yoshida, S. Nishizaki, T. Fujita, J. G. Bednorz, and F. Lichtenberg, *Nature* **372**, 532–534 (1994).

[70] M. Rice, *Nature* **396**, 627–628 (1998).

[71] G. M. Luke, Y. Fudamoto, K. M. Kojima, M. I. Larkin, J. Merrin, B. Nachumi, Y. J. Uemura, Y. Maeno, Z. Q. Mao, Y. Mori, H. Nakamura, and M. Sigrist, *Nature* **394**, 558–561 (1998).

[72] K. Ishida, H. Mukuda, Y. Kitaoka, K. Asayama, Z. Q. Mao, Y. Mori, and Y. Maeno, *Nature* **396**, 658–660 (1998).

[73] Y. Maeno, T. M. Rice, and M. Sigrist, *Physics Today* **54**, 42 (2001).

[74] S. NishiZaki, Y. Maeno, and Z. Mao, *Journal of the Physical Society of Japan* **69**, 572–578 (2000).

[75] K. Ishida, H. Mukuda, Y. Kitaoka, Z. Q. Mao, Y. Mori, and Y. Maeno, *Physical Review Letters* **84**, 5387–5390 (2000).

[76] K. Izawa, H. Takahashi, H. Yamaguchi, Y. Matsuda, M. Suzuki, T. Sasaki, T. Fukase, Y. Yoshida, R. Settai, and Y. Onuki, *Physical Review Letters* **86**, 2653–2656 (2001).

[77] M. A. Tanatar, S. Nagai, Z. Q. Mao, Y. Maeno, and T. Ishiguro, *Physical Review B* **63**, 064505 (2001).

[78] I. Bonalde, B. D. Yanoff, M. B. Salamon, D. J. Van Harlingen, E. M. E. Chia, Z. Q. Mao, and Y. Maeno, *Physical Review Letters* **85**, 4775–4778 (2000).

[79] C. Lupien, W. A. MacFarlane, C. Proust, L. Taillefer, Z. Q. Mao, and Y. Maeno, *Physical Review Letters* **86**, 5986–5989 (2001).

[80] A. Damascelli, D. H. Lu, K. M. Shen, N. P. Armitage, F. Ronning, D. L. Feng, C. Kim, and Z. Shen, **4**, 2–5 (2000).

[81] A. P. Mackenzie, S. R. Julian, A. J. Diver, G. J. McMullan, M. P. Ray, G. G. Lonzarich, Y. Maeno, S. Nishizaki, and T. Fujita, *Physical Review Letters* **76**, 3786–3789 (1996).

[82] T. Nomura and K. Yamada, *Journal of the Physical Society of Japan* **71**, 404–407 (2002).

[83] M. E. Zhitomirsky and T. M. Rice, *Physical Review Letters* **87**, 057001 (2001).

[84] P. W. Anderson and W. F. Brinkman, *Physical Review Letters* **30**, 1108 (1973).

[85] Y. Sidis, M. Braden, P. Bourges, B. H. S. Nishizaki, Y. Maeno, and Y. Mori, *Physical Review Letters* **83**, 3320–3323 (1999).

[86] J. Spałek, *Physical Review B* **63**, 104513 (2001).

[87] T. Takimoto, *Physical Review B* **62**, R14641–R14644 (2000).

[88] B. Keimer, S. A. Kivelson, M. R. Norman, S. Uchida, and J. Zaanen, *Nature* **518**, 179–186 (2015).

[89] J. H. Jung, Z. Fang, J. P. He, Y. Kaneko, Y. Okimoto, and Y. Tokura, *Physical Review Letters* **91**, 056403 (2003).

[90] M. Braden, G. André, S. Nakatsuji, and Y. Maeno, *Physical Review B* **58**, 847–861 (1998).

[91] S. Nakatsuji, S.-i. Ikeda, and Y. Maeno, *Journal of the Physical Society of Japan* **66**, 1868–1871 (1997).

[92] C. S. Alexander, G. Cao, V. Dobrosavljevic, S. McCall, J. E. Crow, E. Lochner, and R. P. Guertin, *Physical Review B* **60**, R8422–R8425 (1999).

[93] H. Müller-Buschbaum and J. Wilkens, *Zeitschrift für anorganische und allgemeine Chemie* **591**, 161–166 (1990).

[94] T. Vogt and D. J. Buttrey, *Physical Review B* **52**, R9843–R9846 (1995).

[95] Z. Fang and K. Terakura, *Physical Review B* **64**, 020509 (2001).

[96] S. Blundell, *Magnetism in Condensed Matter* (Oxford University Press, Oxford, 2001).

[97] Y. Takahashi, *Spin Fluctuation Theory of Itinerant Electron Magnetism*, Vol. 253, Springer Tracts in Modern Physics (Springer, Berlin, Heidelberg, 2013).

[98] E. Wohlfarth, *Journal of Magnetism and Magnetic Materials* **7**, 113–120 (1978).

[99] L. D. Landau and E. M. Lifshitz, *Quantum Mechanics: Non-Relativistic Theory*, Course of Theoretical Physics (Elsevier Science, 1981).

[100] Y. Lu, "From itinerant to localized : an x-ray spectroscopic study of transition metal oxides", PhD thesis (University of Stuttgart, Max Planck Institute for Solid State Research, 2017).

[101] C. J. Ballhausen, *Introduction to the Ligand field theory.* English (McGraw-Hill, New York, 1962).

[102] J. S. Griffith, *The Theory of Transition-Metal Ions* (Cambridge University Press, Cambridge, 1971).

[103] A. Abragam, *Principles of Nuclear Magnetism* (Oxford University Press, 1961).

[104] E. Gorelov, M. Karolak, T. O. Wehling, F. Lechermann, A. I. Lichtenstein, and E. Pavarini, *Physical Review Letters* **104**, 226401 (2010).

[105] N. W. Ashcroft and N. D. Mermin, *Solid State Physics* (Holt, Rinehart and Winston, New York, 1976).

[106] A. Akbari and G. Khaliullin, *Physical Review B* **90**, 035137 (2014).

[107] A. Jain, M. Krautloher, J. Porras, G. H. Ryu, D. P. Chen, D. L. Abernathy, J. T. Park, A. Ivanov, J. Chaloupka, G. Khaliullin, B. Keimer, and B. J. Kim, *Nature Physics* **13**, 633–637 (2017).

[108] S. Kunkemöller, D. Khomskii, P. Steffens, A. Piovano, A. A. Nugroho, and M. Braden, *Physical Review Letters* **115**, 247201 (2015).

[109] G. Zhang and E. Pavarini, *Physical Review B* **95**, 075145 (2017).

[110] T. Nomura and K. Yamada, *Journal of the Physical Society of Japan* **69**, 1856–1864 (2000).

[111] S. Okamoto and A. J. Millis, *Physical Review B* **70**, 195120 (2004).

[112] M. Cuoco, F. Forte, and C. Noce, *Physical Review B* **74**, 195124 (2006).

[113] T. Hotta and E. Dagotto, *Physical Review Letters* **88**, 017201 (2001).

[114] L. M. Woods, *Physical Review B* **62**, 7833–7838 (2000).

[115] V. Anisimov, I. Nekrasov, D. Kondakov, T. Rice, and M. Sigrist, *The European Physical Journal B* **25**, 191–201 (2002).

[116] Z. Fang, N. Nagaosa, and K. Terakura, *Physical Review B* **69**, 045116 (2004).

[117] G. Q. Liu, *Physical Review B - Condensed Matter and Materials Physics* **88**, 1–5 (2013).

[118] G. Q. Liu, *Physical Review B - Condensed Matter and Materials Physics* **84**, 1–5 (2011).

[119] A. Koga, N. Kawakami, T. M. Rice, and M. Sigrist, *Physical Review Letters* **92**, 1–4 (2004).

[120] A. Liebsch, *Physical Review Letters* **91**, 226401 (2003).

[121] S. Biermann, L. De'Medici, and A. Georges, *Physical Review Letters* **95**, 1–4 (2005).

[122] J. S. Lee, Y. S. Lee, T. W. Noh, S.-J. Oh, J. Yu, S. Nakatsuji, H. Fukazawa, and Y. Maeno, *Physical Review Letters* **89**, 257402 (2002).

[123] M. Rams, M. Krużel, A. Zarzycki, K. Królas, and K. Tomala, *Physical Review B* **80**, 045119 (2009).

[124] M. Kubota, Y. Murakami, M. Mizumaki, H. Ohsumi, N. Ikeda, S. Nakatsuji, H. Fukazawa, and Y. Maeno, *Physical Review Letters* **95**, 026401 (2005).

[125] I. Zegkinoglou, J. Strempfer, C. S. Nelson, J. P. Hill, J. Chakhalian, C. Bernhard, J. C. Lang, G. Srajer, H. Fukazawa, S. Nakatsuji, Y. Maeno, and B. Keimer, *Physical Review Letters* **95**, 136401 (2005).

[126] M. Neupane, P. Richard, Z.-H. Pan, Y.-M. Xu, R. Jin, D. Mandrus, X. Dai, Z. Fang, Z. Wang, and H. Ding, *Physical Review Letters* **103**, 097001 (2009).

[127] A. Shimoyamada, K. Ishizaka, S. Tsuda, S. Nakatsuji, Y. Maeno, and S. Shin, *Physical Review Letters* **102**, 086401 (2009).

[128] N. Arakawa and M. Ogata, *Physical Review B* **86**, 125126 (2012).

[129] K. Penc and A. M. Läuchli, "Spin nematic phases in quantum spin systems", in *Introduction to frustrated magnetism: materials, experiments, theory*, edited by C. Lacroix, P. Mendels, and F. Mila (Springer, Berlin, Heidelberg, 2011).

[130] L. Savary and T. Senthil, *arXiv:1506.04752* **02139** (2015).

[131] B. J. Kim and G. Khaliullin, *Physical Review B* **96**, 085108 (2017).

[132] A. Smerald, *Theory of the Nuclear Magnetic 1/T1 Relaxation Rate in Conventional and Unconventional Magnets*, Springer Theses (Springer International Publishing, Cham, 2013).

[133] G. Koster, L. Klein, W. Siemons, G. Rijnders, J. S. Dodge, C.-B. Eom, D. H. A. Blank, and M. R. Beasley, *Reviews of Modern Physics* **84**, 253–298 (2012).

[134] Y. Liu, J. A. Mitchell, S. Madhavan, D. G. Schlom, A. Dabkowski, and H. A. Dabkowska, *Czechoslovak Journal of Physics* **46**, 1113–1114 (1996).

[135] F. Yang, N. Kemik, M. D. Biegalski, H. M. Christen, E. Arenholz, and Y. Takamura, *Applied Physics Letters* **97**, 092503 (2010).

[136] A. Mackenzie, R. Haselwimmer, A. Tyler, G. Lonzarich, Y. Mori, S. Nishizaki, and Y. Maeno, *Physical Review Letters* **80**, 161–164 (1998).

[137] M. Schneider, D. Geiger, S. Esser, U. S. Pracht, C. Stingl, Y. Tokiwa, V. Moshnyaga, I. Sheikin, J. Mravlje, M. Scheffler, and P. Gegenwart, *Physical Review Letters* **112**, 206403 (2014).

[138] H. P. Nair, Y. Liu, J. P. Ruf, N. J. Schreiber, S.-L. Shang, D. J. Baek, B. H. Goodge, L. F. Kourkoutis, Z.-K. Liu, K. M. Shen, and D. G. Schlom, *APL Materials* **6**, 046101 (2018).

[139] X. Wang, Y. Xin, P. A. Stampe, R. J. Kennedy, and J. P. Zheng, *Applied Physics Letters* **85**, 6146 (2004).

[140] Y. Xin, X. Wang, Z. X. Zhou, and J. P. Zheng, *Thin Solid Films* **515**, 3946–3951 (2007).

[141] L. Miao, W. Zhang, P. Silwal, X. Zhou, I. Stern, T. Liu, J. Peng, J. Hu, D. H. Kim, and Z. Q. Mao, *Physical Review B* **88**, 115102 (2013).

[142] L. Miao, P. Silwal, X. Zhou, I. Stern, J. Peng, W. Zhang, L. Spinu, Z. Mao, and D. Ho Kim, *Applied Physics Letters* **100**, 052401 (2012).

[143] J. Ruf, H. Nair, Y. Liu, D. Schlom, and K. Shen, "Controlling the electronic ground state of Ca_2RuO_4 thin films with epitaxial strain", APS March Meeting, 2017.

[144] N. Shukla, M. Jerry, H. Nair, M. Barth, D. G. Schlom, and S. Datta, "Electrically driven reversible insulator-metal phase transition in Ca_2RuO_4", 74th Annual Device Research Conference (DRC), 2016.

[145] P. Willmott, *An Introduction to Synchrotron Radiation* (John Wiley & Sons, Ltd, Chichester, UK, July 2011).

[146] J. Als-Nielsen and D. McMorrow, *Elements of Modern X-ray Physics* (John Wiley & Sons, Inc., Hoboken, NJ, USA, Mar. 2011).

[147] E. Benckiser, M. W. Haverkort, S. Brück, E. Goering, S. Macke, A. Frañó, X. Yang, O. K. Andersen, G. Cristiani, H.-U. Habermeier, A. V. Boris, I. Zegkinoglou, P. Wochner, H.-J. Kim, V. Hinkov, and B. Keimer, *Nature Materials* **10**, 189–193 (2011).

[148] Y. Lu, A. Frano, M. Bluschke, M. Hepting, S. Macke, J. Strempfer, P. Wochner, G. Cristiani, G. Logvenov, H.-U. Habermeier, M. W. Haverkort, B. Keimer, and E. Benckiser, *Physical Review B* **93**, 165121 (2016).

[149] S. P. Collins and A. Bombardi, *Magnetism and Synchrotron Radiation*, Springer Proceedings in Physics (Springer, Berlin, Heidelberg, 2010).

[150] J. Fink, E. Schierle, E. Weschke, and J. Geck, *Reports on Progress in Physics* **76**, 056502 (2013).

[151] L. J. P. Ament, M. Van Veenendaal, T. P. Devereaux, J. P. Hill, and J. Van Den Brink, *Reviews of Modern Physics* **83**, 705–767 (2011).

[152] M. Blume, *Journal of Applied Physics* **57**, 3615–3618 (1985).

[153] J. Stöhr and H. C. Siegmann, *Magnetism* (Springer, Berlin, Heidelberg, 2006).

[154] Y. Joly, S. D. Matteo, and O. Bunău, *The European Physical Journal Special Topics* **208**, 21–38 (2012).

[155] S. P. Collins and A. Bombardi, *Magnetism and Synchrotron Radiation*, edited by E. Beaurepaire, H. Bulou, F. Scheurer, and K. Jean-Paul, Vol. 133, Springer Proceedings in Physics (Springer, Berlin, Heidelberg, 2010).

[156] S. Hess, *Tensors for Physics*, Undergraduate Lecture Notes in Physics (Springer International Publishing, Cham, 2015).

[157] M. W. Haverkort, N. Hollmann, I. P. Krug, and A. Tanaka, *Physical Review B* **82**, 094403 (2010).

[158] J. P. Hannon, G. T. Trammell, M. Blume, and D. Gibbs, *Physical Review Letters* **61**, 1245–1248 (1988).

[159] D. H. Templeton and L. K. Templeton, *Acta Crystallographica Section A Foundations of Crystallography* **42**, 478–481 (1986).

[160] M. I. Aroyo, ed., *International Tables for Crystallography*, Vol. A (International Union of Crystallography, Chester, England, Dec. 2016).

[161] F. De Bergevin and M. Brunel, *Physics Letters A* **39**, 141–142 (1972).

[162] D. Gibbs, D. R. Harshman, E. D. Isaacs, D. B. McWhan, D. Mills, and C. Vettier, *Physical Review Letters* **61**, 1241–1244 (1988).

[163] D. H. Tomboulian and P. L. Hartman, *Physical Review* **102**, 1423–1447 (1956).

[164] H. Wiedemann, *Synchrotron Radiation*, Advanced Texts in Physics (Springer, Berlin, Heidelberg, 2003).

[165] S. Mobilio, F. Boscherini, and C. Meneghini, *Synchrotron Radiation* (Springer, Berlin, Heidelberg, 2015).

[166] H. Kitamura, *Journal of Synchrotron Radiation* **5**, 184–188 (1998).

[167] C. Schmitz-Antoniak, *Reports on Progress in Physics* **78**, 62501 (2015).

[168] J. A. Bearden and A. F. Burr, *Reviews of Modern Physics* **39**, 125–142 (1967).

[169] T. Matsumura, H. Nakao, and Y. Murakami, *Journal of the Physical Society of Japan* **82**, 1–18 (2013).

[170] A. Stunault, F. de Bergevin, D. Wermeille, C. Vettier, T. Brückel, N. Bernhoeft, G. J. McIntyre, and J. Y. Henry, *Physical Review B* **60**, 10170–10179 (1999).

[171] S. Macke, J. E. Hamann-Borrero, R. J. Green, B. Keimer, G. A. Sawatzky, and M. W. Haverkort, *Physical Review Letters* **117**, 115501 (2016).

[172] A. Frano, E. Schierle, M. W. Haverkort, Y. Lu, M. Wu, S. Blanco-Canosa, U. Nwankwo, A. V. Boris, P. Wochner, G. Cristiani, H. U. Habermeier, G. Logvenov, V. Hinkov, E. Benckiser, E. Weschke, and B. Keimer, *Physical Review Letters* **111**, 3–7 (2013).

[173] A. Thompson and D. Vaughan, eds., *X-Ray Data Booklet* (Lawrence Berkeley National Laboratory, 2001).

[174] S. D. Brown, L. Bouchenoire, D. Bowyer, J. Kervin, D. Laundy, M. J. Longfield, D. Mannix, D. F. Paul, A. Stunault, P. Thompson, M. J. Cooper, C. A. Lucas, and W. G. Stirling, *Journal of Synchrotron Radiation* **8**, 1172–1181 (2001).

[175] J. Strempfer, S. Francoual, D. Reuther, D. K. Shukla, A. Skaugen, H. Schulte-Schrepping, T. Kracht, and H. Franz, *Journal of Synchrotron Radiation* **20**, 541–549 (2013).

[176] I. Zegkinoglou, "Resonant and High-Energy X-Ray Scattering Studies on Strongly Correlated Electron Systems in Transition Metal Oxides", PhD thesis (University of Stuttgart, Max Planck Institute for Solid State Research, 2007).

[177] B. Bohnenbuck, "Resonant X-Ray Scattering Studies of Ruthenium Oxides and Ruthenocuprates", PhD thesis (University of Stuttgart, Max Planck Institute for Solid State Research, 2009).

[178] E. Gullikson, *X-Ray Interactions With Matter Tools*, (2018) `http://henke.lbl.gov/optical_constants/`.

[179] A. Chatzichristos, R. M. L. McFadden, V. L. Karner, D. L. Cortie, C. D. P. Levy, W. A. MacFarlane, G. D. Morris, M. R. Pearson, Z. Salman, and R. F. Kiefl, *Physical Review B* **96**, 014307 (2017).

[180] C. P. Slichter, *Principles of Magnetic Resonance*, Vol. 1, Springer Series in Solid-State Sciences (Springer, Berlin, Heidelberg, 1990).

[181] B. Cowan, *Nuclear Magnetic Resonance and Relaxation* (Cambridge University Press, Cambridge, 1997).

[182] E. D. Commins, *Journal of the Physical Society of Japan* **76**, 111010 (2007).

[183] J. H. Smith, E. M. Purcell, and N. F. Ramsey, *Physical Review* **108**, 120–122 (1957).

[184] M. Brodeur, "First direct mass measurement of the two and four neutron halos ^{6}He and ^{8}He using the TITAN Penning trap mass spectrometer", PhD thesis (University of British Columbia, 2010).

[185] T. D. Lee and C. N. Yang, *Physical Review* **104**, 254–258 (1956).

[186] C. S. Wu, E. Ambler, R. W. Hayward, D. D. Hoppes, and R. P. Hudson, *Physical Review* **105**, 1413–1415 (1957).

[187] R. L. Garwin, L. M. Lederman, and M. Weinrich, *Physical Review* **105**, 1415–1417 (1957).

[188] E. Morenzoni, R. Khasanov, H. Luetkens, T. Prokscha, A. Suter, N. Garifianov, H. Glückler, M. Birke, E. Forgan, H. Keller, J. Litterst, C. Niedermayer, and G. Nieuwenhuys, *Physica B: Condensed Matter* **326**, 196–204 (2003).

[189] W. MacFarlane, *Solid State Nuclear Magnetic Resonance* **68-69**, 1–12 (2015).

[190] Qun Song, "β-Detected NMR of $^{8}Li^{+}$ in Spintronic Materials", PhD thesis (University of British Columbia, 2012).

[191] H. Saadaoui, "Magnetic properties near the surface of cuprate superconductors studied using Beta-Detected NMR", PhD thesis (University of British Columbia, 2009).

[192] J. Govaerts, M. Kokkoris, and J. Deutsch, *Journal of Physics G: Nuclear and Particle Physics* **21**, 1675–1699 (1995).

[193] C. Levy, M. Pearson, G. Morris, J. Lassen, K. Chow, M. Hossain, R. Kiefl, R. Labbé, W. MacFarlane, T. Parolin, L. Root, H. Saadaoui, M. Smadella, and D. Wang, *Physica B: Condensed Matter* **404**, 1010–1012 (2009).

[194] K. Olive, *Chinese Physics C* **40**, 100001 (2016).

[195] J. F. Ziegler, M. Ziegler, and J. Biersack, *Nuclear Instruments and Methods in Physics Research Section B: Beam Interactions with Materials and Atoms* **268**, 1818–1823 (2010).

[196] G. D. Morris, *Hyperfine Interactions* **225**, 173–182 (2014).

[197] Z. Salman, R. F. Kiefl, K. H. Chow, M. D. Hossain, T. A. Keeler, S. R. Kreitzman, C. D. P. Levy, R. I. Miller, T. J. Parolin, M. R. Pearson, H. Saadaoui, J. D. Schultz, M. Smadella, D. Wang, and W. A. MacFarlane, *Physical Review Letters* **96**, 147601 (2006).

[198] A. Yaouanc and P. de Réotier, *Muon spin rotation, relaxation, and resonance: applications to condensed matter* (Oxford University Press, Oxford, 2011).

[199] J. Ziolo, S. Torre, A. Rigamonti, and F. Borsa, *Journal of Applied Physics* **63**, 3095–3097 (1988).

[200] R. J. Christianson, R. L. Leheny, R. J. Birgeneau, and R. W. Erwin, *Physical Review B - Condensed Matter and Materials Physics* **63**, 2–5 (2001).

[201] S. Krämer and M. Mehring, *Physical Review Letters* **83**, 396–399 (1999).

[202] S. Kawasaki, Y. Tani, T. Mabuchi, K. Kudo, Y. Nishikubo, D. Mitsuoka, M. Nohara, and G.-q. Zheng, *Physical Review B* **91**, 060510 (2015).

[203] K. Binder, *Reports on Progress in Physics* **50**, 783–859 (1987).

[204] M. Pleimling and F. Iglói, *Europhysics Letters (EPL)* **79**, 56002 (2007).

[205] I. V. Markov, *Crystal Growth for Beginners*, 2nd Edition (World Scientific, Singapore, 2011).

[206] K. Oura, M. Katayama, A. V. Zotov, V. G. Lifshits, and A. A. Saranin, *Surface Science* (Springer, Berlin, Heidelberg, Oct. 2003).

[207] K. Yamaguchi, K. Yujobo, and T. Kaizu, *Japanese Journal of Applied Physics* **39**, L1245–L1248 (2000).

[208] A. Ichimiya and P. I. Cohen, *Reflection High-Energy Electron Diffraction* (Cambridge University Press, Cambridge, 2004).

[209] J. Li, W. Peng, K. Chen, P. Wang, H. Chu, Y. Chen, and D. Zheng, *Science China Physics, Mechanics and Astronomy* **56**, 2312–2326 (2013).

[210] D. P. Norton, *Pulsed Laser Deposition of Complex Materials: Progress Toward Applications* (John Wiley & Sons, Inc., Hoboken, NJ, USA, Mar. 2006).

[211] P. Schaaf, ed., *Laser Processing of Materials*, Springer Series in Materials Science (Springer, Berlin, Heidelberg, 2010).

[212] A. Kumatani, T. Ohsawa, R. Shimizu, Y. Takagi, S. Shiraki, and T. Hitosugi, *Applied Physics Letters* **101**, 1–5 (2012).

[213] M. Hiratani, C. Okazaki, K. Imagawa, and K. Takagi, *Japanese Journal of Applied Physics* **35**, 6212–6216 (1996).

[214] J. C. Chaston, *Platinum Metals Review* **19**, 135–140 (1975).

[215] G. W. C. Kaye and T. H. Laby, *Kaye & Laby Tables of physical & chemical constants.* English (National Physical Laboratory, Middlessex, England, 2005).

[216] D. R. Lide, *CRC Handbook of Chemistry and Physics, 85th Edition* (Taylor & Francis, 2004).

[217] S. Nakatsuji and Y. Maeno, *Journal of Solid State Chemistry* **156**, 26–31 (2001).

[218] H. Samata, Y. Saeki, S. Mizusaki, Y. Nagata, T. Ozawa, and A. Sato, *Journal of Crystal Growth* **311**, 623–626 (2009).

[219] D. B. Chrisey and G. K. Hubler, *Pulsed laser deposition of thin films* (Wiley New York, Hoboken, New Jersey, 1994).

[220] Y. Li, X. Yao, and K. Tanabe, *Physica C: Superconductivity* **304**, 239–244 (1998).

[221] G. Cao, S. McCall, J. E. Crow, and R. P. Guertin, *Physical Review Letters* **78**, 1751–1754 (1997).

[222] X. U. Wang, "Pulsed Laser Deposition Growth and Property Studies of $Ca_{2-x}La_xRuO_4$ and RuO_2 Thin Films", PhD thesis (The Florida State University, 2004).

[223] S. Nakatsuji, "Quasi-two-dimensional Mott transition system $Ca_{2-x}Sr_xRuO_4$", PhD thesis (Kyoto University, 2001).

[224] P. L. Alireza, F. Nakamura, S. K. Goh, Y. Maeno, S. Nakatsuji, Y. T. C. Ko, M. Sutherland, S. Julian, and G. G. Lonzarich, *Journal of Physics: Condensed Matter* **22**, 052202 (2010).

[225] Z. A. Munir, U. Anselmi-Tamburini, and M. Ohyanagi, *Journal of Materials Science* **41**, 763–777 (2006).

[226] N. Keawprak, R. Tu, and T. Goto, *Materials Science and Engineering: B* **161**, 71–75 (2009).

[227] H. Schraknepper, C. Bäumer, F. Gunkel, R. Dittmann, and R. A. De Souza, *APL Materials* **4**, 126109 (2016).

[228] J. W. Arblaster, *Journal of Phase Equilibria and Diffusion* **39**, 255–272 (2018).

[229] R. Speiser, P. Blackburn, and H. L. Johnston, *Journal of The Electrochemical Society* **106**, 52 (1959).

[230] R. Berktold, "Kapazitätsmessungen an Feldeffekttransistoren auf $LaAlO_3$-$SrTiO_3$-Basis", PhD thesis (University of Stuttgart, Max Planck Institute for Solid State Research, 2017).

[231] A. Stierle, A. Steinhäuser, A. Rühm, F. U. Renner, R. Weigel, N. Kasper, and H. Dosch, *Review of Scientific Instruments* **75**, 5302 (2004).

[232] H. Heinke, M. Möller, D. Hommel, and G. Landwehr, *Journal of Crystal Growth* **135**, 41–52 (1994).

[233] J. B. Nelson and D. P. Riley, *Proceedings of the Physical Society* **57**, 160–177 (1945).

[234] S. Bueble, K. Knorr, E. Brecht, and W. W. Schmahl, *Surface Science* **400**, 345–355 (1998).

[235] K. Kawamura, M. Yashima, K. Fujii, K. Omoto, K. Hibino, S. Yamada, J. R. Hester, M. Avdeev, P. Miao, S. Torii, and T. Kamiyama, *Inorganic Chemistry* **54**, 3896–3904 (2015).

[236] H. B. Premkumar, D. V. Sunitha, H. Nagabhushana, S. C. Sharma, B. Daruka Prasad, B. M. Nagabhushana, C. Shivakumara, J. L. Rao, N. O. Gopal, K. R. Prabhakara, S. C. Ke, and R. P. S. Chakradhar, *Journal of Alloys and Compounds* **591**, 337–345 (2014).

[237] K. Nishio, H. Y. Hwang, and Y. Hikita, *APL Materials* **4**, 036102 (2016).

[238] T. Ohnishi and K. Takada, *Applied Physics Express* **4**, 025501 (2011).

[239] K. Shibuya, S. Mi, C.-L. Jia, P. Meuffels, and R. Dittmann, *Applied Physics Letters* **92**, 241918 (2008).

[240] L. Miao, P. Silwal, X. Zhou, I. Stern, J. Peng, W. Zhang, L. Spinu, Z. Mao, and D. Ho Kim, *Applied Physics Letters* **100**, 052401 (2012).

[241] M. Renninger, *Zeitschrift für Physik* **106**, 141–176 (1937).

[242] Y. S. Terminasov and L. V. Tuzov, *Soviet Physics Uspekhi* **7**, 434 (1964).

[243] S. L. Morelhão and J. Z. Domagala, *Journal of Applied Crystallography* **40**, 546–551 (2007).

[244] E. H. Smith, P. D. C. King, A. Soukiassian, D. G. Ast, and D. G. Schlom, *Applied Physics Letters* **111**, 131903 (2017).

[245] M. Zurbuchen, W. Tian, X. Pan, D. Fong, S. Streiffer, M. Hawley, J. Lettieri, Y. Jia, G. Asayama, S. Fulk, D. Comstock, S. Knapp, A. Carim, and D. Schlom, *Journal of Materials Research* **22**, 1439–1471 (2007).

[246] H. Rho, S. L. Cooper, S. Nakatsuji, H. Fukazawa, and Y. Maeno, *Physical Review B* **68**, 100404 (2003).

[247] M. Hepting, M. Minola, A. Frano, G. Cristiani, G. Logvenov, E. Schierle, M. Wu, M. Bluschke, E. Weschke, H.-U. Habermeier, E. Benckiser, M. Le Tacon, and B. Keimer, *Physical Review Letters* **113**, 227206 (2014).

[248] T. Mizokawa, L. H. Tjeng, H.-J. Lin, C. T. Chen, S. Schuppler, S. Nakatsuji, H. Fukazawa, and Y. Maeno, *Physical Review B* **69**, 132410 (2004).

[249] H.-J. Noh, S.-J. Oh, B.-G. Park, J.-H. Park, J.-Y. Kim, H.-D. Kim, T. Mizokawa, L. H. Tjeng, H.-J. Lin, C. T. Chen, S. Schuppler, S. Nakatsuji, H. Fukazawa, and Y. Maeno, *Physical Review B* **72**, 052411 (2005).

[250] C. G. Fatuzzo, M. Dantz, S. Fatale, P. Olalde-Velasco, N. E. Shaik, B. Dalla Piazza, S. Toth, J. Pelliciari, R. Fittipaldi, A. Vecchione, N. Kikugawa, J. S. Brooks, H. M. Rønnow, M. Grioni, C. Rüegg, T. Schmitt, and J. Chang, *Physical Review B* **91**, 155104 (2015).

[251] R. Okazaki, Y. Nishina, Y. Yasui, F. Nakamura, T. Suzuki, and I. Terasaki, *Journal of the Physical Society of Japan* **82**, 103702 (2013).

[252] J. Thompson, J. Nichols, S. Lee, S. Ryee, J. H. Gruenewald, J. G. Connell, M. Souri, J. M. Johnson, J. Hwang, M. J. Han, H. N. Lee, D.-W. Kim, and S. S. A. Seo, *Applied Physics Letters* **109**, 161902 (2016).

[253] G. Bergmann, *Physica Scripta* **1986**, 99 (1986).

[254] P. A. Lee and T. V. Ramakrishnan, *Reviews of Modern Physics* **57**, 287–337 (1985).

[255] A. S. McLeod, E. Van Heumen, J. G. Ramirez, S. Wang, T. Saerbeck, S. Guenon, M. Goldflam, L. Anderegg, P. Kelly, A. Mueller, M. K. Liu, I. K. Schuller, and D. N. Basov, *Nature Physics* **13**, 80–86 (2017).

[256] R. G. Moore, J. Zhang, V. B. Nascimento, R. Jin, J. Guo, G. Wang, Z. Fang, D. Mandrus, and E. W. Plummer, *Science* **318**, 615–619 (2007).

[257] L. Pauw, *Philips Tech. Rev* **20**, 220–224 (1958).

[258] R. Okazaki, Y. Ikemoto, T. Moriwaki, F. Nakamura, T. Suzuki, Y. Yasui, and I. Terasaki, *Journal of the Physical Society of Japan* **83**, 084701 (2014).

[259] S. J. May, J.-W. Kim, J. M. Rondinelli, E. Karapetrova, N. a. Spaldin, A. Bhattacharya, and P. J. Ryan, *Physical Review B* **82**, 014110 (2010).

[260] C. D. Wen and I. Mudawar, *International Journal of Heat and Mass Transfer* **47**, 3591–3605 (2004).

[261] L. Miao, "Epitaxial Strain Effect on the Physical Properties of Layered Ruthenate and Iridate Thin Films", PhD thesis (Tulane University, 2014).

[262] J. Haeni, C. Theis, and D. Schlom, *Journal of Electroceramics* **4**, 385–391 (2000).

[263] F. Wrobel, A. F. Mark, G. Christiani, W. Sigle, H.-U. Habermeier, P. A. van Aken, G. Logvenov, B. Keimer, and E. Benckiser, *Applied Physics Letters* **110**, 041606 (2017).

[264] T. Dubroca, J. Hack, and R. Hummel, *Physical Review B* **74**, 026403 (2006).

[265] M. Sawicki, W. Stefanowicz, and A. Ney, *Semiconductor Science and Technology* **26**, 064006 (2011).

[266] Y. Khaydukov, O. Soltwedel, and T. Keller, *Journal of large-scale research facilities JLSRF* **1**, A38 (2015).

[267] J. Daillant and A. Gibaud, eds., *X-ray and Neutron Reflectivity*, Vol. 770, Lecture Notes in Physics (Springer, Berlin, Heidelberg, 2009).

[268] *SIMULREFLEC—Reflectivity Curves Simulations and Fitting*, (2011) `http://www-llb.cea.fr/prism/programs/simulreflec/simulreflec.html`.

[269] H. Zabel, *Journal of Applied Physics* **116** (2014) `10.1063/1.4902960`.

[270] H. Yamada and S. Takada, *Progress of Theoretical Physics* **48**, 1828–1848 (1972).

[271] H. Béa, M. Bibes, S. Cherifi, F. Nolting, B. Warot-Fonrose, S. Fusil, G. Herranz, C. Deranlot, E. Jacquet, K. Bouzehouane, and A. Barthélémy, *Applied Physics Letters* **89**, 242114 (2006).

[272] H. H. Potter, *Proceedings of the Royal Society A: Mathematical, Physical and Engineering Sciences* **132**, 560–569 (1931).

[273] M. Ziese, I. Vrejoiu, and D. Hesse, *Physical Review B* **81**, 184418 (2010).

[274] H. Fukazawa and Y. Maeno, *Journal of the Physical Society of Japan* **70**, 460–467 (2001).

[275] I. Felner, I. Nowik, I. Bradaric, and M. Gospodinov, *Physical Review B* **62**, 11332–11335 (2000).

[276] M. Wissinger, D. Fuchs, L. Dieterle, H. Leiste, R. Schneider, D. Gerthsen, and H. V. Löhneysen, *Physical Review B* **83**, 144430 (2011).

[277] S. Tripathi, R. Rana, S. Kumar, P. Pandey, R. S. Singh, and D. S. Rana, *Scientific Reports* **4**, 3877 (2015).

[278] J. Rodríguez-Carvajal and F. Bourée, *EPJ Web of Conferences* **22**, 00010 (2012).

[279] T. Inui, Y. Tanabe, and Y. Onodera, *Group Theory and Its Applications in Physics*, Springer Series in Solid-State Sciences (Springer, Berlin, Heidelberg, 1990).

[280] E. Bertaut, *Journal of Magnetism and Magnetic Materials* **24**, 267–278 (1981).

[281] Y. A. Izyumov, V. E. Naish, and R. P. Ozerov, *Neutron Diffraction of Magnetic Materials* (Springer US, Boston, MA, 1991).

[282] J. O. Dimmock, *Physical Review* **130**, 1337–1344 (1963).

[283] J. Rodríguez-Carvajal, *Physica B: Condensed Matter* **192**, 55–69 (1993).

[284] R. Matzdorf, *Science* **289**, 746–748 (2000).

[285] M. Reehuis, C. Ulrich, P. Pattison, B. Ouladdiaf, M. C. Rheinstädter, M. Ohl, L. P. Regnault, M. Miyasaka, Y. Tokura, and B. Keimer, *Physical Review B* **73**, 094440 (2006).

[286] J. O. Dimmock, *Physical Review* **130**, 1337–1344 (1963).

[287] E. F. Bertaut, *Acta Crystallographica Section A* **24**, 217–231 (1968).

[288] B. Bohnenbuck, I. Zegkinoglou, J. Strempfer, C. S. Nelson, H.-H. Wu, C. Schüßler-Langeheine, M. Reehuis, E. Schierle, P. Leininger, T. Herrmannsdörfer, J. C. Lang, G. Srajer, C. T. Lin, and B. Keimer, *Physical Review Letters* **102**, 037205 (2009).

[289] Z. H. Zhu, J. Strempfer, R. R. Rao, J. Pelliciari, Y. Choi, T. Kawaguchi, H. You, Y. Shao-Horn, and R. Comin, *arXiv:1806.02036* (2018).

[290] Y. Kitaoka and H. Yasuoka, *Journal of the Physical Society of Japan* **48**, 1460–1469 (1980).

[291] W. A. MacFarlane, Q. Song, N. J. C. Ingle, K. H. Chow, M. Egilmez, I. Fan, M. D. Hossain, R. F. Kiefl, C. D. P. Levy, G. D. Morris, T. J. Parolin, M. R. Pearson, H. Saadaoui, Z. Salman, and D. Wang, *Physical Review B* **92**, 064409 (2015).

[292] B. A. Frandsen, L. Liu, S. C. Cheung, Z. Guguchia, R. Khasanov, E. Morenzoni, T. J. S. Munsie, A. M. Hallas, M. N. Wilson, Y. Cai, G. M. Luke, B. Chen, W. Li, C. Jin, C. Ding, S. Guo, F. Ning, T. U. Ito, W. Higemoto, S. J. L. Billinge, S. Sakamoto, A. Fujimori, T. Murakami, H. Kageyama, J. A. Alonso, G. Kotliar, M. Imada, and Y. J. Uemura, *Nature Communications* **7**, 12519 (2016).

[293] P. Heitjans, A. Schirmer, and S. Indris, "NMR and β-NMR Studies of Diffusion in Interface-Dominated and Disordered Solids", in *Diffusion in condensed matter* (Springer, Berlin, Heidelberg).

[294] E. R. Andrew and D. P. Tunstall, *Proceedings of the Physical Society* **78**, 1–11 (1961).

[295] Z. Salman, E. P. Reynard, W. A. MacFarlane, K. H. Chow, J. Chakhalian, S. R. Kreitzman, S. Daviel, C. D. P. Levy, R. Poutissou, and R. F. Kiefl, *Physical Review B* **70**, 104404 (2004).

[296] A. Yaouanc, P. Dalmas de Réotier, P. C. M. Gubbens, A. M. Mulders, F. E. Kayzel, and J. J. M. Franse, *Physical Review B* **53**, 350–353 (1996).

[297] H. Mukuda, K. Ishida, Y. Kitaoka, K. Asayama, Z. Mao, Y. Mori, and Y. Maeno, *Journal of the Physical Society of Japan* **67**, 3945–3951 (1998).

[298] D. L. Cortie, T. Buck, M. H. Dehn, R. F. Kiefl, C. D. P. Levy, R. M. L. McFadden, G. D. Morris, M. R. Pearson, Z. Salman, Y. Maeno, and W. A. MacFarlane, *Physical Review B* **91**, 241113 (2015).

[299] I. M. Gat-Malureanu, J. P. Carlo, T. Goko, A. Fukaya, T. Ito, P. P. Kyriakou, M. I. Larkin, G. M. Luke, P. L. Russo, A. T. Savici, C. R. Wiebe, K. Yoshimura, and Y. J. Uemura, *Physical Review B* **84**, 224415 (2011).

[300] T. Berlijn, P. C. Snijders, O. Delaire, H.-D. Zhou, T. A. Maier, H.-B. Cao, S.-X. Chi, M. Matsuda, Y. Wang, M. R. Koehler, P. R. C. Kent, and H. H. Weitering, *Physical Review Letters* **118**, 077201 (2017).

[301] S. I. Ikeda, U. Azuma, N. Shirakawa, Y. Nishihara, and Y. Maeno, *Journal of Crystal Growth* **237-239**, 787–791 (2002).

[302] P. Heitjans, A. Korblein, H. Ackermann, D. Dubbers, F. Fujara, and H. .-.-J. Stockmann, *Journal of Physics F: Metal Physics* **15**, 41–54 (1985).

[303] M. Kühne, F. Paolucci, J. Popovic, P. M. Ostrovsky, J. Maier, and J. H. Smet, *Nature Nanotechnology* **12**, 895–900 (2017).

[304] R. Gross and A. Marx, *Festkörperphysik*, 2. Auflage (De Gruyter, Berlin, 2014).

[305] O. Bunău and Y. Joly, *Journal of Physics: Condensed Matter* **21**, 345501 (2009).

[306] T. A. W. Beale, R. D. Johnson, Y. Joly, S. R. Bland, P. D. Hatton, L. Bouchenoire, C. Mazzoli, D. Prabhakaran, and A. T. Boothroyd, *Physical Review B* **82**, 024105 (2010).

[307] M. Takahashi and J. Igarashi, *Physical Review B* **65**, 205114 (2002).

[308] M. Takahashi and J. Igarashi, *Physical Review B* **64**, 075110 (2001).

[309] H. Fukazawa, S. Nakatsuji, and Y. Maeno, *Physica B: Condensed Matter* **281-282**, 613–614 (2000).

[310] T. Burnus, "Study of Charge, Spin, and Orbital States in Novel Transition-Metal Oxides Using X-Ray Absorption Spectroscopy", PhD thesis (University of Cologne, 2008).

[311] B. Henke, E. Gullikson, and J. Davis, *Atomic Data and Nuclear Data Tables* **54**, 181–342 (1993).

[312] S. Brück, "Magnetic Resonant Reflectometry on Exchange Bias Systems", PhD thesis (University of Stuttgart, Max Planck Institute for Solid State Research, 2009).

Acknowledgements

I had the pleasure to meet and work with many fantastic people during my PhD years. In the following, I want thank everybody who has helped me along the way and contributed in some form or another:

First, I want to thank my supervisor, Prof. Keimer, for his guidance, trust and support throughout the PhD years. His group and its work environment with excellent intellectual and technical resources was essential for this project. I appreciate the many opportunities to attend conferences, summer schools, and workshops I was given during my PhD.

I would also like to thank Prof. Wrachtrup for accepting the position as a second reviewer and Prof. Daghofer for chairing the exam.

Thanks to my day-to-day supervisor Eva Benckiser for guiding me through the initial cuprate project, teaching me the careful analysis of soft X-ray reflectivity and always being there for any kind of question. I am very grateful to Bum–joon Kim, who became my day-to-day supervisor for the Ruthenate project, during which I could profit greatly from his knowledge about spin-orbit systems. Special thanks to Jone Zabaleta for being the external advisor on my PhD committee and conducting CAFM measurements.

I want to particularly thank my office mate Matthias Hepting who has a miraculous ability to spot promising projects. You became a true friend over the years and always gave honest advice when difficult decisions were demanded. I also have to thank Juan Porras for a myriad of good advice. You will make an excellent PI one day. Many thanks to Friederike Wrobel, who got me started in all aspects related to thin film growth. Special thanks to my office mate Gideok Kim for the good scientific and non-scientific discussions and teaching me the meaning of OTL. Thanks also to the rest of the growth team, each of whom contributed with their unique knowledge about film growth: Federico Baiutti, Padma Radhakrishnan, and Daniel Putzky. It was also a pleasure to have discussions with the Takagi thin film group Hiro Nakamura, Avaise Mohammed, Ulrike Niemann, and Deba Samal. Thanks also to my fellow office mates Sebastian Macke, Roberto Ortiz, and Jorge Sauceda. 7C16 has truly a great spirit and I enjoyed my time there.

During the ANKA beamtimes and the setup of the in-house diffractometers, I profited from the immense knowledge about scattering and technical details from Peter Wochner. I also would like to thank Shyjumon Ibrahimkutty for his support at the ANKA beamline.

I am very grateful to my trusted beamtime partner Joel Bertinshaw and his amazing Python scripts which analyzed the data pretty much "on-the-fly" during the experiment. Especially the strenuous and legendary Ru-L beamtime during June 2017 at Sec-4 would not have been possible without your help.

Thanks to "Prof." Yi Lu for having always good answers to all questions regarding X-ray scattering. To Martin Bluschke for always being willing to squeeze in an oxygen K-edge XAS during this beamtimes at UE46. To Katrin Fürsich for beamtime support and for proofreading my abstract. To Max Krautloher for nice Ca_2RuO_4 single crystals. To Meng Wu for helping me with the reflectometry analysis and for the help during the UE56 beam times.

Thanks to all the great engineers and mechanics at MPI. I would like to thank Manfred Ohl for making sure that my orders went smoothly through the purchasing department. I greatly appreciate the maintenance of the PPMS and SQUID by Michael Schulz and his help regarding all radiation safety issues. Thanks to Benjamin Bruha for designing the wedges for the ALBA experiment and Heiko Uhlig for fixing the PPMS rotator insert for me. Here I also have to thank Thomas Frey and Karl Seel of the central mechanical workshop, who managed to meet the sometimes very tight deadlines I set them. In particular, I would like to thank Kathrin Gülck for the high-quality machining of the sample holders I used for many beamtimes.

Thanks to all other members of the Keimer department, it was a pleasure to work with you: Ayman Akil, Santi Blanco-Canosa, Alexander Boris, Paul Butler, Sungkyun Choi, Robert Dawson, Nadir Driza, Alex Frañó, Gerd Friemel, Giorgi Ghambashidze, Hlynur Gretarsson, Namrata Gung, Marc Höppner, George Jackeli, Thomas Keller, Giniyat Khalliulin, Hun-ho Kim, Timofei Larkin, Emilie Lefrancois, Huimei Liu, Toshinao Loew, Matteo Minola, Suguru Nakata, Darren Peets, Daniel Pröpper, Ksenia Rabinovich, Armin Schulz, Olaf Soltwedel, Michaela Souliou, Nakheon Sung, Hakuto Suzuki, Kentaro Ueda, Youngje Um, Alexander Yaresko, and Luca Zanotti. For handling all kinds of organizational matters, I would like to thank Sonja Balkema and Hans-Georg Libuda.

I am very grateful for the support from the thin film technology group at MPI regarding all kinds of aspects related to thin film deposition and characterization. For synthesis and technical details, I relied heavily on the support of Georg Cristiani, who shared many of his growth secrets with me. The same holds for MBE-guru Gennady Logvenov, whose MBE-knowledge helped tremendously for the first MBE projects. Many thanks to Benjamin Stuhlhofer for reviving many of the vacuum machines critical for my project and ion-milling my samples. To Peter Specht for technical support. To Yvonne Stuhlhofer, Birgit Lemke, and Stephan Schmid for sputtering contacts and wirebonding many samples. To Petar Yordanov for letting me join the Cobaltate project.

Thanks also go to the STEM group of Prof. van Aken: To Shyam Kanta Sinha and Yi Wang for the excellent TEM images, to Eren Suyolcu for good advice, and to Ute Salzberger for the technical support.

For the XPS measurements, I would like to thank Dr. Konuma and Dr. Kathrin Müller.

When synthesizing polycrystals, I greatly profited from the know-how of Prof. Dinnebier's and Prof. Maier's group at MPI. I am grateful for the support of Rotraut Merkle, Annette Fuchs, Christine Stefani, Frank Adams, and Luzia Germann.

I am also very indebted to all the beamline scientists maintaining the instruments I used to investigate my samples: Laurence Buchenoire, Paul Thompson from BM28 at the ESRF, Yongseong Choi and Joerg Strempfer from 4-ID-D at the APS, Sonia Francoual from P09 at DESY, Manuel Valvidares and Pierluigi Gargiani from BL29 at ALBA, and Willy Mahler at the UE56 beamline at BESSY. Thanks also go to Yury Khaydukov for the support at NREX and for his unforgiving Russian directness.

Thanks to the βNMR-Team in Vancouver for their amazing support and keeping my experiments staffed 24/7: Profs. Rob Kiefl and Andrew McFarlane, Ryan McFadden, Gerald Morris, Iain McKenzie, Martin Dehn, Victoria Karner, Derek Fujimoto and Aris Chatzichristos. I would like to thank David Cortie in particular, who conducted the initial experiments and introduced us to this technique.

Thanks to all my friends outside the MPI world. To my friends Michael Lohse and Simon Faller from Würzburg, my friends from my studies in Würzburg Frank Schwemmer, Phil Holzmeister, Bernhard Schmitzer and Tobias Staudacher, and from my studies in Heidelberg

Thomas Nikodem, Fabian Bock, Andreas Korzowski, and Simon Murmann. Thank you all for your support, great weekends, and skype sessions. Particularly, I would like to thank Michael for good PhD advice, thesis corrections, and for coaching me for the defense. Also, thanks for being a great hiking and skiing partner!

I am very grateful to my family, which I could always rely on. Especially to my parents: Thank you for your unconditional support throughout the years.

To my girlfriend Katharina: Thank you for your patience, encouragement and understanding, especially during the last demanding weeks of the PhD.